



QUENCH - LOCA - REPORTS Nr. 5

**Results of the LOCA bundle test QUENCH-L4
with pre-hydrogenated M5[®] claddings (SR-7712)**

J. Stuckert, M. Große, A. Pshenichnikov , C. Rössger,
M. Steinbrück, M. Walter

Karlsruher Institut für Technologie

in der Helmholtz-Gemeinschaft

Wissenschaftliche Berichte

QUENCH – LOCA – REPORTS Nr. 5

Results of the LOCA bundle test QUENCH-L4
with pre-hydrogenated M5[®] claddings (SR-7712)

J. Stuckert*, M. Große*, A. Pshenichnikov*, C. Rössger*,
M. Steinbrück*, M. Walter**

Institut für Angewandte Materialien:

* Angewandte Werkstoffphysik (IAM-AWP)

** Werkstoff- und Biomechanik (IAM-WBM)

Programm Nukleare Entsorgung und Sicherheit

Karlsruher Institut für Technologie

Mai 2018

Impressum

Karlsruher Institut für Technologie (KIT)

Institut für Angewandte Materialien

Angewandte Werkstoffphysik IAM-AWP-KOR

Nukleare Sicherheitsforschung

Hermann-von-Helmholtz-Platz 1

76344 Eggenstein-Leopoldshafen

www.iam.kit.edu/awp/666.php

DOI: 10.5445/IR/1000083094

Zusammenfassung

Ergebnisse des unter Bedingungen eines LOCA-Störfalls ausgeführten Versuches QUENCH-LOCA-4 mit hydrierten M5[®]-Hüllrohren

Der QUENCH-L4-Bündelversuch wurde im Rahmen der QUENCH-LOCA-Testserie durchgeführt. Das Ziel der Testreihe ist die Untersuchung von Dehnung, Bersten, Oxidation und sekundärer Hydrierung der Hüllrohre unter repräsentativen Auslegungsstörfallbedingungen sowie der Einfluss dieser Parameter auf die mechanischen Eigenschaften dieser Rohre. Mit den Versuchen dieser Serie wird das Verhalten von verschiedenen Hüllrohrmaterialien mit und ohne Vorhydrierung untersucht. Für den QUENCH-L4-Versuch wurden M5[®]-Hüllrohre (Außendurchmesser: 10,75 mm) mit etwa 100 gew. ppm Wasserstoff vorbelastet. Die Bündelkonfiguration und das Testprotokoll waren ähnlich dem Referenztest QUENCH-L2, der mit nicht vorbehandelten M5[®]-Hüllrohren durchgeführt wurde. Spezifisches Ziel des QUENCH-L4-Tests war die Untersuchung des Verhaltens der vorhydrierten Hüllrohre, mit speziellem Fokus auf die Auswirkungen des Berstens dieser Rohre auf deren sekundäre Hydrierung. Der Test wurde am Karlsruher Institut für Technologie (KIT) am 30. Juli 2014 erfolgreich durchgeführt.

Zu Beginn des Experiments wurde zunächst die Teststrecke stabilisiert. Hierzu wurde das Bündel erwärmt mit einer elektrischen Leistung von 3,6 kW, einer Gasströmung von 6 g/s Argon sowie 2 g/s überhitzten Dampfes bis eine maximale Hüllrohrtemperatur von etwa 850 K erreicht war. Während dieser Stabilisierungsphase (mit einer Dauer von 1700 s) wurden die Stäbe bis auf 55 bar mit Krypton beaufschlagt. In der sich anschließenden Aufheizphase wurde die elektrische Leistung auf 60 kW erhöht, und diese Testphase dauerte 82 s. Während dieser Zeit stiegen die Temperaturen von ihren Anfangswerten (d.h. denen am Ende der Stabilisierungsphase) bis zu einem Maximum von 1352 K. Die durchschnittliche Aufheizgeschwindigkeit betrug 6,7 K/s. Die erhöhte Duktilität der erwärmten Hüllrohre führte zu deren fortschreitender Dehnung und anschließendem Bersten aller Rohre. Die Bersttemperatur betrug 1107 ± 27 K (etwa 30 K niedriger als im QUENCH-L2-Test). Das Experiment wurde mit einer Leistungsreduzierung auf 3,5 kW (Modellierung der Zerfallswärme) und Einführung von Dampf bei einem Nennwert von 20 g/s fortgesetzt (Abkühlphase). In dieser Phase fand eine Abkühlung auf etwa 980 K statt. Die darauf folgende Abschreckphase erfolgte vom Bündelboden aus mit einer Wassereinspeisung von bis zu 100 g/s (entspr. 3,3/g/s/Effektivstab). Das vollständige Abschrecken wurde nach 300 s erreicht.

Aufnahmen nach dem Versuch mit einem Videoskop vom Bündelinneren zeigen Ballooning-Bereiche typischerweise in den heißesten Bündelebenen zwischen 900 und 950 mm. Das Bündel wurde demontiert und die geometrischen Parameter aller Stäbe wurden mit einem Laserscanner bestimmt; die gemessenen Hüllrohr-Umfangsdehnungen im Berstbereich lagen zwischen 18% und 30%. Bei allen Stäben konnten kleine Verbiegungen in den radialen Ebenen, die durch die Berstöffnungen gingen, festgestellt werden. Mit Ultraschallmessungen wurde die Verminderung der Hüllrohrwandstärke in der Nähe von Berstöffnungen bestimmt. Die axiale und radiale Verteilung sowie die Stärke von Oxidschichten an den Hüllrohren wurden durch Wirbelstromverfahren ermittelt; die maximale Dicke von ZrO₂ - in Kombination mit α -Zr(O) -Schichten - betrug etwa 25 μ m. Die Bestimmung der Konzentration und Verteilung von absorbiertem Wasserstoff wurde mit Hilfe der Neutronentomographie durchgeführt; eine maximale Wasserstoffkonzentration von ca. 1500 wppm wurde oberhalb der Berstöffnung (sekundäre Hydrierung) des zentralen Stabes gemessen. Die Messung der mechanischen Eigenschaften und die Bestimmung der Restduktilität wurden durch Zugversuche mit Hüllrohrsegmenten von ca. 800 mm bewerkstelligt; bei den äußeren Stäben zeigten sich Sprödbrüche bei Spannungen von etwa 500 MPa hauptsächlich aufgrund der Spannungskonzentration an den Spitzen von Berstöffnungen. Die Mehrheit der inneren Stäbe versagte durch Einschnürung in weitem Abstand von der Berstöffnung; nur drei innere Hüllrohre brachen aufgrund sekundärer Hydrierung. Mikrostrukturuntersuchungen von Hüllrohren und Hydriden-Verteilung wurden mittels XRD- und EBSD-Verfahren durchgeführt.

Abstract

The QUENCH-L4 experiment was performed in the framework of the QUENCH-LOCA test series. The overall objective of this bundle test series is the investigation of ballooning, burst, degree of oxidation and secondary hydrogen uptake of the cladding under representative design-basis accident conditions and their influence on the mechanical properties. The various experiments of the series examine the behavior of different cladding materials and the effect of pre-hydriding. For the QUENCH-L4 test, M5[®] claddings pre-loaded with approximately 100 wppm hydrogen and with an outside diameter of 10.75 mm have been used. Like in all experiments of the QUENCH-LOCA series, the fuel rod simulators were separately pressurized with krypton to 55 bar. Bundle configuration and test protocol were similar to the reference test QUENCH-L2 with as-received M5[®] claddings. Specific objectives of QUENCH-L4 were to provide information about the behavior of pre-hydrided M5[®] alloy on the response to a best-estimate large-break LOCA sequence, with special focus on the impact of burst parameters on secondary hydrogenation of the cladding. The test was successfully conducted at the Karlsruhe Institute of Technology (KIT) on July 30, 2014.

The experiment started by stabilizing the bundle conditions with an application of electrical bundle power of 3.6 kW and gas flows of 6 g/s argon plus 2 g/s superheated steam resulting in maximum bundle temperatures of about 850 K. During this stabilization phase (lasting 1700 s) the rods were refilled with krypton to 55 bar. The transient stage was initiated by increasing of electrical power to 60 kW and lasted 82 s. During this period the temperatures increased from their initial values to a maximum of 1352 K. The average heatup rate at the maximum temperature location was 6.7 K/s. The increased ductility of the heated cladding resulted in a progressive ballooning and consequent burst of all rods. The burst temperature is 1107 ± 27 K (about 30 K lower in comparison to the QUENCH-L2 test). The experiment continued with power decrease to 3.5 kW to simulate decay heat and injection of steam at a nominal of 20 g/s (cool-down stage). In this stage mostly steady cooling to about 980 K occurred. The cooling phase was followed by up to 100 g/s (3.3 /g/s/effective rod) water injection from bundle bottom (quench stage). Complete quench was achieved at 300 s.

Post-test videoscope inspections showed typical ballooning pictures at the hottest bundle elevations between about 900 and 950 mm. The bundle was dismounted and geometric parameters of all rods were determined by laser scanning; the range of circumferential strains measured was between 18% and 30%. A small bending of all rods was detected in the plane going radially through the burst opening. Ultrasound measurements were used to determine thinning of cladding wall in vicinity of burst openings. Axial and radial distribution of oxidation rate was measured by eddy current methods; maximal combined thickness of ZrO₂ and α -Zr(O) layers was about 25 μ m. Determination of concentration and distribution of absorbed hydrogen was performed by neutron imaging methods; a maximal hydrogen concentration of about 1500 wppm was measured above the burst opening (secondary hydrogenation) of the central rod of the bundle. Measurement of mechanical properties and determination of residual ductility were carried out by tensile tests with cladding tube segments and showed fracture of claddings at engineering stress of about 500 MPa mostly due to stress concentration at burst opening tips for the outer bundle rods. Majority of the inner rods was fractured due to necking far away from the burst for the inner rods; only three claddings were fractured due to secondary hydrogenation. Micro-structure examinations of claddings and distribution of hydrides were performed by means of XRD and EBSD methods.

Contents

Zusammenfassung.....	i
Abstract	iii
List of tables.....	vi
List of figures	vii
Introduction.....	1
1 Description of the Test Facility.....	3
1.1 The test bundle	3
1.1.1 Claddings.....	3
1.1.2 Heaters.....	4
1.2 Bundle surroundings	4
1.3 Rod pressurization	5
2 Test Bundle Instrumentation	5
2.1 Thermocouples	6
2.2 Gas measurement system.....	6
3 Data Acquisition and Process Control	7
4 Test Performance and Results of Online Measurements	7
5 Posttest Examinations.....	9
5.1 Optical Observation of Cladding Surfaces.....	9
5.2 Profilometry of Claddings with Laser Scanner	10
5.2.1 Linear Laser Scanning.....	10
5.2.2 Main Characteristics of the Measuring Device and Procedures.....	10
5.2.3 Results of the Scans	11
5.3 Nondestructive Ultrasound and Eddy Current Measurements	11
5.4 Results of Neutron Radiography and Tomography; Analysis of Absorbed Hydrogen.	12
5.4.1 Basic Principles.....	12
5.4.2 Technique.....	13
5.4.3 Results of Radiography	13
5.4.4 Results of Tomography: Hydrogen Content.....	13
5.4.5 Cladding Cross Sections Reconstructed by Tomography	14
5.5 Mechanical Tests.....	14
5.5.1 Tensile Test Set-up.....	15
5.5.2 Results of the Tensile Tests.....	15
5.6 SEM investigations	15
5.7 Metallographic Examination	16
5.8 XRD investigations.....	16
5.9 EBSD analysis.....	17
6 Summary and Conclusions	18
7 Acknowledgments.....	19
8 References.....	20
Tables and Figures.....	23

List of tables

Table 1	QUENCH Test Matrix 1997 – 2014	24
Table 2	Design characteristics of the QUENCH-L4 test bundle	26
Table 3	Properties of M5 [®] cladding tubes.....	27
Table 4	Main characteristics of the ZrO ₂ pellet material, yttria-stabilized (type FZY) *	28
Table 5	QUENCH-L4; Electrical resistances of rods [mΩ] at 20 °C.....	29
Table 6	Properties of zirconia fiber insulating boards*	30
Table 7	List of instrumentation for the QUENCH-L4 test	31
Table 8	QUENCH-L4; Rod thermocouple positions.....	38
Table 9	QUENCH-L4; Sequence of events.....	39
Table 10	QUENCH-L4; Burst parameters	40
Table 11	Burst time and temperature of all rods for the experiments: QL2 (left and QL4 (right).....	41
Table 12	Burst geometrical parameters : QL2 (left) and QL4 (right).	42
Table 13	QUENCH-L4; Content of hydrogen absorbed by secondary hydrogenation (post-tensile n0- tomography): axial maximum averaged for cross section and axial absolute local maximum	43
Table 14	QUENCH-L4: average hydrogen content in hydrogen bands (results of hot extraction with LECO TCH600 device, cladding segments with h=11 mm, d=5 mm)	43
Table 15	QUENCH-L4: average hydrogen content in the vicinity of burst openings (hot extraction with LECO TCH600 device, cladding segments with h=11 mm, d=5 mm)	43
Table 16	QUENCH-L4; Wetting of TFS thermocouples	44
Table 17	QUENCH-L4; Strain parameters	45
Table 18	QUENCH-L4; Results of tensile tests	46

List of figures

Figure 1	QUENCH Facility - Main components.	47
Figure 2	Flow diagram of the QUENCH test facility.	48
Figure 3	QUENCH Facility; Containment and test section.	49
Figure 4	QUENCH-L4; Test section with flow lines.	50
Figure 5	QUENCH-L4; Fuel rod simulator bundle (cross section, top view) including rod type indications corresponding to table “List of Instrumentation”	51
Figure 6	QUENCH-L4; Heated fuel rod simulator.....	52
Figure 7	QUENCH-L4; Hydrides inside the prototype cladding with 100 wppm H (as etched).	53
Figure 8	QUENCH-L4; Ballooning test of welded prototype cladding (both parts hydrogenated to about 100 wppm) pressurized to 55 bar; burst after 1 hour at constant T=650 °C.	54
Figure 9	QUENCH-L4; Tensile test of welded prototype cladding (only lower part hydrogenated to about 100 wppm) at 650 °C; inner pressure was decreased from 55 to 4 bar after holding time of 1800 s at 650 °C.....	55
Figure 10	QUENCH-L4; Tensile diagram for prototype sample composed (welded) of hydrogenated and not hydrogenated claddings (shown in Fig. 9).....	56
Figure 11	QUENCH-L4; Welding of pre-hydrogenated claddings.	57
Figure 12	QUENCH-L4; Axial distribution of hydrogen in the pre-hydrogenated central part (bundle elevation 50 – 1250 mm) of the claddings #1 - #6 estimated by cladding diameter change. (Please note: sample numbers do not match the rod numbers.)	58
Figure 13	QUENCH-L4; Axial distribution of hydrogen in the pre-hydrogenated central part (bundle elevation 50 – 1250 mm) of the claddings #7 - #12 estimated by cladding diameter change. (Please note: sample numbers do not match the rod numbers.)	59
Figure 14	QUENCH-L4; Axial distribution of hydrogen in the pre-hydrogenated central part (bundle elevation 50 – 1250 mm) of the claddings #13 - #18 estimated by cladding diameter change. (Please note: sample numbers do not match the rod numbers.)	60
Figure 15	QUENCH-L4; Axial distribution of hydrogen in the pre-hydrogenated central part (bundle elevation 50 – 1250 mm) of the claddings #19 - #21 estimated by cladding diameter change. (Please note: sample numbers do not match the rod numbers).	61
Figure 16	QUENCH-L4; Rod pressure control and measurement panel.....	62
Figure 17	QUENCH-L4; Rod pressurization.	63
Figure 18	QUENCH-L4; Rod pressurization process at $T_{pct}=550$ °C.	64
Figure 19	QUENCH-L4; Concept for TC fastening at the test rod.	65
Figure 20	Axial temperature measurement locations in the QUENCH-L4 test section.....	66
Figure 21	QUENCH-L4; Test bundle; TC instrumentation and rod designation (top view).	67
Figure 22	QUENCH-L4; Arrangement of the thermocouples inside the corner rods.	67
Figure 23	QUENCH Facility; H2 measurement with the GAM 300 mass spectrometer.	68
Figure 24	Mass spectrometer sampling position at the off-gas pipe of the QUENCH test facility.....	68
Figure 25	QUENCH-L4; Test progress, comparison with QUENCH-L2 temperature.....	69
Figure 26	QUENCH-L4; Voltage and current of two DC-generators.	69
Figure 27	QUENCH-L4; Temperatures measured by gas inlet thermocouple (T 511) at -412 mm and rod cladding (TFS 7/1) thermocouple at -250 mm elevation.....	70
Figure 28	QUENCH-L4; Temperatures measured by rod cladding (TFS 7/2) thermocouple at -150 mm elevation.....	70

Figure 29	QUENCH-L4; Temperatures measured by rod cladding (TFS 7/3) and shroud (TSH 3/0) thermocouples at -50 mm elevation.....	71
Figure 30	QUENCH-L4; Temperatures measured by rod cladding (TFS 7/4) and shroud (TSH 4/90) thermocouples at 50 mm elevation.....	71
Figure 31	QUENCH-L4; Temperatures measured by rod cladding (TFS 7/5) and shroud (TSH 5/180) thermocouples at 150 mm elevation.....	72
Figure 32	QUENCH-L4; Temperatures measured by rod cladding (TFS) and shroud (TSH 6/270) thermocouples at 250 mm elevation.....	72
Figure 33	QUENCH-L4; Temperatures measured by rod cladding (TFS) and shroud (TSH 7/0) thermocouples at 350 mm elevation.....	73
Figure 34	QUENCH-L4; Temperatures measured by rod cladding (TFS) and shroud (TSH 8/90) thermocouples at 450 mm elevation.....	73
Figure 35	QUENCH-L4; Temperatures measured by rod cladding (TFS) and shroud (TSH 9/180) thermocouples at 550 mm elevation.....	74
Figure 36	QUENCH-L4; Temperatures measured by rod cladding (TFS) and shroud (TSH 10/270) thermocouples at 650 mm elevation.....	74
Figure 37	QUENCH-L4; Temperatures measured by rod cladding (TFS) and shroud (TSH 11/0), and corner rod internal (TIT D/11) thermocouples at 750 mm elevation.....	75
Figure 38	QUENCH-L4; Temperatures measured by rod cladding (TFS), shroud (TSH 12/90), and corner rod internal (TIT C/12) thermocouples at 850 mm elevation.....	75
Figure 39	QUENCH-L4; Temperatures measured by rod cladding (TFS), shroud (TSH 13/180), and corner rod internal (TIT A/13) thermocouples at 950 mm elevation.....	76
Figure 40	QUENCH-L4; Temperatures measured by rod cladding (TFS) and shroud (TSH 14/270) thermocouples at 1050 mm elevation.....	76
Figure 41	QUENCH-L4; Temperatures measured by rod cladding (TFS) and shroud (TSH 15/0) thermocouples at 1150 mm elevation.....	77
Figure 42	QUENCH-L4; Temperatures measured by rod cladding (TFS) thermocouples at 1250 mm elevation.....	77
Figure 43	QUENCH-L4; Temperatures measured by rod cladding (TFS 7/17) thermocouple at 1350 mm elevation and gas temperature (T 512) at 1360 mm between shroud and rod #20; T511 depicts the gas temperature at the bundle inlet.....	78
Figure 44	QUENCH-L4; Overview of the TCI (inner cooling jacket).	78
Figure 45	Comparison of radial temperature difference at rod #7 for bundles QUENCH-L2 and QUENCH-L4.	79
Figure 46	QUENCH-L4; Axial temperature profile TFS internal and external rod group together with TSH (left) and axial temperature profile of all TFS (right) at 48 s (first cladding burst).....	80
Figure 47	QUENCH-L4; Axial temperature profile TFS internal and external rod group together with TSH (left) and axial temperature profile of all TFS (right) at 68 s (last cladding burst).	81
Figure 48	QUENCH-L4; Axial temperature profile TFS internal and external rod group together with TSH (left) and axial temperature profile of all TFS (right) at 76 s (end of transient).	82
Figure 49	QUENCH-L4; Axial temperature profile TFS internal and external rod group together with TSH (left) and axial temperature profile of all TFS (right) at 87 s (max bundle temperature).....	83
Figure 50	Similar axial temperature distribution for rod #7 for bundles QUENCH-L2 and QUENCH-L4 on the first cladding burst (48 s) and on the end of transition (76 s).	84

Figure 51	Similar axial temperature distribution for shroud of bundles QUENCH-L2 and QUENCH-L4 on the first cladding burst (48 s) and on the end of transition (76 s).	85
Figure 52	QUENCH-L4; Mass spectrometer measurements: steam during reflow.....	86
Figure 53	QUENCH-L4; Sequence of wetting of surface thermocouples for rod #7 by 2-phase fluid formed above collapsed water front (L 501).	87
Figure 54	QUENCH-L4; System pressure measured at test section inlet P 511, at outlet P 512, and in the off-gas pipe P 601.	88
Figure 55	QUENCH-L4; Argon pressure between shroud and cooling jacket P 406 demonstrates tightness of the shroud (pressure change is independent from system pressure oscillations).	88
Figure 56	QUENCH-L4; Quench measurement of collapsed water level (L 501), top, water mass flow rate (Fm 104), center, condensed water (L 701), bottom.	89
Figure 57	QUENCH-L4; Steam rate (top), hydrogen rate (center), krypton concentration (bottom) measured by mass spectrometry (MS).	90
Figure 58	QUENCH-L4; Pressure change during the heating phase, cladding ballooning and burst.....	91
Figure 59	QUENCH-L4; Mass spectrometer measurements: krypton as burst indicator.	92
Figure 60	QUENCH-L4; Videoscope observations with camera inserted from the bundle bottom at position of corner rod A.....	93
Figure 61	QUENCH-L4; Videoscope observations with camera inserted from the bundle bottom at position of corner rod B.	94
Figure 62	QUENCH-L4; Videoscope observations with camera inserted from the bundle bottom at position of corner rod C.	95
Figure 63	QUENCH-L4; Videoscope observations with camera inserted from the bundle bottom at position of corner rod D.....	96
Figure 64	QUENCH-L4; Videoscope observations of weld seams at elevations 50 and 1250 mm at the position of corner rod D.	97
Figure 65	QUENCH-L4; Views of bundle at angle positions of 0° and 90°: negligible rod bending and intact thermocouples.....	98
Figure 66	QUENCH-L4; Views of bundle at angle positions of 180° and 270°: negligible rod bending and intact thermocouples.....	99
Figure 67	QUENCH-L4; Post-test overview of inner rods: no bending, localized ballooning region.	100
Figure 68	QUENCH-L4; Post-test overview of outer rods: no bending, localized ballooning region.....	101
Figure 69	QUENCH-L4; Post-test inner rods (burst side view): bending about 2°, kink in burst region, burst opening always at concave side.	102
Figure 70	QUENCH-L4; Post-test outer rods (burst side view): bending about 2°, kink in burst region, burst opening always at concave side.	103
Figure 71	Burst openings of QUENCH-L2 and QUENCH-L4 bundles.	104
Figure 72	Burst opening orientations of QUENCH-L2 and QUENCH-L4 bundles.....	105
Figure 73	Vertical positions of burst openings for QUENCH-L2 and QUENCH-L4 bundles.....	106
Figure 74	QUENCH-L4; Overview of burst structures of rods #1 - #3, #5.....	107
Figure 75	QUENCH-L4; overview of burst structures of rods #6 - #9.	108
Figure 76	QUENCH-L4; Overview of burst structures of rods #10 - #13.....	109
Figure 77	QUENCH-L4; Overview of burst structures of rods #14 - #16, #18.....	110
Figure 78	QUENCH-L4; Overview of burst structures of rods #19 - #21.....	111

Figure 79	QUENCH-L4; Cladding surface structure (“tree bark”) at elevations 938 mm (top) and 933 mm (bottom) of rod #8: formation of longitudinal surface cracks in oxide during ballooning.....	112
Figure 80	QUENCH-L4; Videoscope observations of cladding inner surface.....	113
Figure 81	QUENCH-L4; Tube scanner laser profilometry.....	114
Figure 82	QUENCH-L4, Rod #1; longitudinal changing of circumferential strain (top): QL4 main balloon region is longer than QL2 one; azimuthal diameter downwards from burst (bottom).....	115
Figure 83	QUENCH-L4, Rod #2; longitudinal changing of circumferential strain (top): QL4 main balloon region is longer than QL2 one; azimuthal diameter downwards from burst (bottom).....	116
Figure 84	QUENCH-L4, Rod #3; longitudinal changing of circumferential strain (top): QL4 main balloon region is longer than QL2 one; azimuthal diameter downwards from burst (bottom).....	117
Figure 85	QUENCH-L4, Rod #4; longitudinal changing of circumferential strain (top); azimuthal diameter downwards from burst (bottom). Spikes: thermocouple.....	118
Figure 86	QUENCH-L4, Rod #5; longitudinal changing of circumferential strain (top): QL4 main balloon region is longer than QL2 one; azimuthal diameter downwards from burst (bottom).....	119
Figure 87	QUENCH-L4, Rod #6; longitudinal changing of circumferential strain (top): QL4 main balloon region is longer than QL2 one; azimuthal diameter downwards from burst (bottom).....	120
Figure 88	QUENCH-L4, Rod #7; longitudinal changing of circumferential strain (top): QL4 main balloon region is longer than QL2 one; azimuthal diameter downwards from burst (bottom).....	121
Figure 89	QUENCH-L4, Rod #8; longitudinal changing of circumferential strain (top): QL4 main balloon region is longer than QL2 one; azimuthal diameter downwards from burst (bottom).....	122
Figure 90	QUENCH-L4, Rod #9; longitudinal changing of circumferential strain (top); azimuthal diameter downwards from burst (bottom).....	123
Figure 91	QUENCH-L4, Rod #10; longitudinal changing of circumferential strain (top): QL4 main balloon region is longer than QL2 one; azimuthal diameter downwards from burst (bottom).....	124
Figure 92	QUENCH-L4, Rod #11; longitudinal changing of circumferential strain (top); azimuthal diameter downwards from burst (bottom).....	125
Figure 93	QUENCH-L4, Rod #12; longitudinal changing of circumferential strain (top): QL4 main balloon region is longer than QL2 one; azimuthal diameter downwards from burst (bottom).....	126
Figure 94	QUENCH-L4, Rod #13; longitudinal changing of circumferential strain (top); azimuthal diameter downwards from burst (bottom).....	127
Figure 95	QUENCH-L4, Rod #14; longitudinal changing of circumferential strain (top): QL4 main balloon region is longer than QL2 one; azimuthal diameter downwards from burst (bottom).....	128
Figure 96	QUENCH-L4, Rod #15; longitudinal changing of circumferential strain (top); azimuthal diameter downwards from burst (bottom). Spikes: thermocouple.....	129

Figure 97	QUENCH-L4, Rod #16; longitudinal changing of circumferential strain in comparison to corresponding rod of QL2 and side view of the QL4-#16 rod (top); azimuthal diameter downwards from burst (bottom).	130
Figure 98	QUENCH-L4, Rod #17; longitudinal changing of circumferential strain (top); azimuthal diameter downwards from burst (bottom).	131
Figure 99	QUENCH-L4, Rod #18; longitudinal changing of circumferential strain (top): QL4 main balloon region is longer than QL2 one; azimuthal diameter downwards from burst (bottom).	132
Figure 100	QUENCH-L4, Rod #19; longitudinal changing of circumferential strain (top); azimuthal diameter downwards from burst (bottom). Spikes: thermocouples.	133
Figure 101	QUENCH-L4, Rod #20; longitudinal changing of circumferential strain (top); azimuthal diameter downwards from burst (bottom).	134
Figure 102	QUENCH-L4, Rod #21; longitudinal changing of circumferential strain (top); azimuthal diameter downwards from burst (bottom).	135
Figure 103	Comparison of circumferential strain between two rods of bundles QUENCH-L2 and QUENCH-L4.	136
Figure 104	Axial distribution of coolant channel blockage for QUENCH-L2 and -L4 bundles. Cross section of QUENCH-L4 bundle corresponds to the bundle elevation 924 mm with a maximal blockage of 19% (blue lines - ballooned claddings; red lines - original claddings) ..	137
Figure 105	QUENCH-L4; Ultrasound measurement of wall thickness for rod #1 below and above the burst opening.	138
Figure 106	QUENCH-L4: results of eddy-current measurements of axial layer thickness distribution for inner rods	139
Figure 107	QUENCH-L4; Results of eddy-current measurements of axial layer thickness distribution for outer rods (and rod #1 for comparison).....	139
Figure 108	QUENCH-L4; Results of eddy-current measurements for different circumferential positions of rod #1.	140
Figure 109	QUENCH-L4: results of eddy-current measurements for hottest and coolest sides of rod #4.	141
Figure 110	QUENCH-L4; Results of eddy-current measurements for hottest and coolest sides of rod #5	141
Figure 111	QUENCH-L4; Hydrogen bands on neutron radiographs of inner rods and maximum hydrogen content measured by neutron tomography.....	142
Figure 112	QUENCH-L4; Neutron radiographs of outer rods and maximum hydrogen content measured by neutron tomography.....	143
Figure 113	QUENCH-L4, Rod #9; results of n^0 -radio- and tomography.	144
Figure 114	QUENCH-L4; Results of neutron tomography for internal rods fractured during the tensile tests at lower hydrogen spot. Dark blue points correspond to hydrogen bearing material. Rings are colouring markers dished up before tensile tests. The values are local maximal hydrogen concentrations.	145
Figure 115	QUENCH-L4; Results of neutron tomography for internal rods fractured during the tensile tests by necking. Dark blue points correspond to hydrogen bearing material. Rings are colouring markers dished up before tensile tests. The values are local maximal hydrogen concentrations.	146
Figure 116	QUENCH-L4; Results of neutron tomography for some outer rods double fractured during the tensile tests at burst opening tips. Dark blue points correspond to hydrogen	

	bearing material. Rings are colouring markers dished up before tensile tests. The values are local maximal hydrogen concentrations.....	147
Figure 117	QUENCH-L4; correspondence between reconstruction of tomography image and plots of mean and maximal hydrogen concentrations (calculated for each cross section slice of 25.6 μm width) in rod #1: hydrogen band above and hydrogen spot below burst opening.	148
Figure 118	QUENCH-L4; correspondence between reconstruction of tomography image and plots of mean and maximal hydrogen concentrations (calculated for each cross section slice of 25.6 μm width) in rod #3: absence of hydrogen bands and spots.	149
Figure 119	QUENCH-L4; correspondence between reconstruction of tomography image and plots of mean and maximal hydrogen concentrations (calculated for each cross section slice of 25.6 μm width) in rod #6: hydrogen spot below burst opening.	150
Figure 120	QUENCH-L4; correspondence between reconstruction of tomography image and plots of mean and maximal hydrogen concentrations (calculated for each cross section slice of 25.6 μm width) in rod #9: hydrogen band above and hydrogen spot below burst opening.	151
Figure 121	QUENCH-L4; correspondence between reconstruction of tomography image and plots of mean and maximal hydrogen concentrations (calculated for each cross section slice of 25.6 μm width) in rod #10: weak hydrogen band above burst opening, relative homogeneous axial distribution of hydrogen.	152
Figure 122	QUENCH-L4; correspondence between reconstruction of tomography image and plots of mean and maximal hydrogen concentrations (calculated for each cross section slice of 25.6 μm width) in rod #14: hydrogenated zone above burst opening, relative homogeneous axial distribution of hydrogen.	153
Figure 123	QUENCH-L4; correspondence between reconstruction of tomography image and plots of mean and maximal hydrogen concentrations (calculated for each cross section slice of 45.9 μm width) in rod #2: hydrogenated zone <i>below</i> burst opening.	154
Figure 124	QUENCH-L4; correspondence between reconstruction of tomography image and plots of mean and maximal hydrogen concentrations (calculated for each cross section slice of 45.9 μm width) in rod #3: no hydrogenated zones.	155
Figure 125	QUENCH-L4; correspondence between reconstruction of tomography image and plots of mean and maximal hydrogen concentrations (calculated for each cross section slice of 45.9 μm width) in rod #5: hydrogenated zone <i>below</i> burst opening.	156
Figure 126	QUENCH-L4; correspondence between reconstruction of tomography image and plots of mean and maximal hydrogen concentrations (calculated for each cross section slice of 45.9 μm width) in rod #7: hydrogenated zone above burst opening.	157
Figure 127	QUENCH-L4; correspondence between reconstruction of tomography image and plots of mean and maximal hydrogen concentrations (calculated for each cross section slice of 45.9 μm width) in rod #8: hydrogenated zones above and below burst opening.....	158
Figure 128	QUENCH-L4; Comparison of tomography images (made after tensile tests) at the axial middle of burst opening with initial (pre-test) cladding cross section (OD=10.75 mm; wall thickness 725 μm); elongation values point the deformation degree after tensile tests.	159
Figure 129	QUENCH-L4; Inner rods after tensile tests; ruptures due to H-embrittlement (rods 1, 6, 9) and necking (rods 2, 3, 5, 7, 8).	160
Figure 130	QUENCH-L4; Inner rods after tensile tests; ruptures due to H-embrittlement for rods 1, 6, 9; necking of the rods 2, 3, 5, 7, 8.	161
Figure 131	QUENCH-L4; Outer rods after tensile tests; ruptures due to stress concentration (rods 10-15, 20, 21) and necking (rods 16, 18, 19).....	162

Figure 132	QUENCH-L4; Outer rods after tensile tests; ruptures due to stress concentration for the rods 10-15, 20, 21; necking of the rods 16, 18, 19.	163
Figure 133	QUENCH-L4; Results of tensile tests with claddings of the inner rod group.	164
Figure 134	QUENCH-L4; Results of tensile tests with claddings of the outer rod group.	165
Figure 135	QUENCH-L4; SEM image of fractured surface of rod #9 at angle 90° after tensile test; top view. Brittle fracture.	166
Figure 136	QUENCH-L4; SEM image of fractured surface of rod #9 at angle 200° after tensile test; top view. Ductile fracture.	167
Figure 137	QUENCH-L4; SEM image of fractured surface of rod #9 at angle 290° after tensile test; top view. Ductile fracture.	168
Figure 138	QUENCH-L4; SEM image of fractured surface of rod #9 at angle 20° after tensile test; top view. Ductile fracture.	169
Figure 139	QUENCH-L4, Rod #9, rupture surface after tensile test (as-etched after polishing). SEM/EDX results: no oxygen in metallic part of the clad.	170
Figure 140	QUENCH-L4; SEM images of fractured surface of rod #10 after tensile test; top view. Ductile fracture.	171
Figure 141	QUENCH-L4; Thicknesses of ZrO ₂ and α-Zr(O) layers at outer and inner surfaces of cladding #1 at burst elevation 918 mm; top view, as polished.	172
Figure 142	QUENCH-L4; Thicknesses of ZrO ₂ and α-Zr(O) layers at outer and inner surfaces of cladding #1 above burst at bundle elevation 935 mm; top view, as polished.	173
Figure 143	QUENCH-L4; Thicknesses of ZrO ₂ and α-Zr(O) layers at outer and inner surfaces of cladding #1 underneath burst at bundle elevation 901 mm; top view, as polished.	174
Figure 144	L4; Thicknesses of ZrO ₂ and α-Zr(O) layers at outer and inner surfaces of cladding #6 at burst elevation 931 mm; top view, as polished.	175
Figure 145	QUENCH-L4; Correspondence between practically absence of inner oxide layer (contact clad ↔ pellet) and hydrogen spot for rod #6.	176
Figure 146	QUENCH-L4, Rod #8 at elevation 950 mm (12 mm above burst opening; SEM observation of cross sections (as etched) at the line of burst opening (bottom) and opposite side (top).	177
Figure 147	QUENCH-L4; XRD analysis of rod #5 at the hydrogen band on the line of the burst opening (161°); indication of {111}γ-hydrides and {110}β-Zr.	178
Figure 148	QUENCH-L4; XRD analysis of rod #5 at the hydrogen band on the line opposite to the burst opening (341°); indication of {110}β-Zr.	178
Figure 149	QUENCH-L4; XRD analysis of rod #8 at the hydrogen band on the line of burst opening (330°); indication of {110}β-Zr.	179
Figure 150	QUENCH-L4; XRD analysis of rod #8 at the hydrogen band on the line opposite to the burst opening (150°); indication of {111}γ-hydrides and {110}β-Zr.	179
Figure 151	QUENCH-L4; EBSD analysis of δ-ZrH _{1.66} and γ-ZrH hydrides (mostly intra-granular) agglomerated inside α-Zr matrix for rod #1 at elevation of 935 mm (area of hydrogen band visualized by neutron tomography) at the burst opening cladding side.	180
Figure 152	QUENCH-L4; EBSD analysis of δ-ZrH _{1.66} and γ-ZrH hydrides (mostly intra-granular) agglomerated inside α-Zr matrix for rod #1 at elevation of 935 mm at the cladding side oppositely to the burst opening side.	181
Figure 153	QUENCH-L4; EBSD analysis of δ-ZrH _{1.66} and γ-ZrH hydrides agglomerated inside α-Zr matrix for rod #5 at elevation of 950 mm.	182

Figure 154	QUENCH-L4; EBSD analysis of cross section 911 mm of rod #6 at hydrogen spot (on the line of burst opening 20 mm below opening).....	183
Figure 155	QUENCH-L4; EBSD analysis of δ -ZrH _{1.66} hydrides (mostly intra-granular) and β Zr (inter- and intra-granular) inside α -Zr matrix for rod #6 at elevation of 911 mm (20 mm below burst opening middle) oppositely to burst opening.	184
Figure 156	QUENCH-L4; EBSD analysis of fractured surface of rod #9 at hydrogen spot (on the line of burst opening 20 mm below opening; after polishing and etching).	185

Introduction

Under the licensing procedures for pressurized water reactors (PWR) evidence must be given that the impacts of all pipe ruptures, hypothetically occurring in the primary loop and implying a loss of coolant, can be controlled when the other cooling lines are not available. The double-ended break of the main coolant line between the main coolant pump and the reactor pressure vessel is considered to constitute the design basis for the emergency core cooling system (ECCS) in a loss-of-coolant accident (LOCA). The break of a coolant line leads to the loss of coolant in the primary circuit of a PWR and the decrease in system pressure from 15.5 MPa to eventually around 0.32 MPa (boiling point, corresponding to 135°C). Consequently, the remaining coolant in the core as well as the emergency cooling water fed into the reactor core evaporate, the temperature of the fuel elements rapidly rises and the fuel rods start to balloon since they contain pressurized filling gas and fission gas products. At temperatures above 700°C, the load within the metallic wall reaches a critical value and the most ballooned cladding tubes finally burst.

Upon rupture of the reactor coolant line the reactor is shut down. However, as the production of decay heat will be continued, reliable sustainment of the reactor core rod geometry and long-term emergency cooling of the core are required. The cladding embrittlement increasing during oxidation in steam has to be limited to an acceptable value to retain the core rod geometry. The current LOCA criteria and their safety goals are applied worldwide with minor modifications since the NRC release in 1973 [1, 2]. The criteria are given as limits on peak cladding temperature ($T_{\text{pct}} \leq 1200 \text{ °C}$) and on oxidation level ECR (equivalent cladding reacted) calculated as a percentage of cladding oxidized ($\text{ECR} \leq 17\%$ using the Baker-Just oxidation correlation). These two items constitute the criterion of cladding embrittlement due to oxygen uptake and, according to the RSK (Reactor Safety Commission) Guidelines, are also included in the current German LOCA criteria [3].

The results elaborated worldwide in the 1980's on the Zircaloy-4 (Zry-4) cladding tubes behavior (oxidation, deformation and bundle coolability) under LOCA conditions constitute a reliable data base and an important input for the safety assessment of LWRs. With respect to the LOCA conditions for German LWRs, different out-of-pile with more prototypical internal heating [4, 8] and outer heating [5, 6], the FR2 in-pile [7] single rod as well as the REBEKA out-of-pile bundle tests [9, 10] were performed. It was concluded that the ECC-criteria established by licensing authorities are conservative and that the coolability of an LWR and the public safety can be maintained in a LOCA [11]. In-pile test data (with burn-up up to 35 MWd/kgU) were consistent with the out-of-pile data and did not indicate an influence of the nuclear environment on cladding deformation.

Due to major advantages in fuel-cycle costs, optimised reactor operation, and waste management, the current trend in the nuclear industry is to increase fuel burn-up. At high burn-up, fuel rods fabricated from conventional Zry-4 often exhibit significant oxidation, hydriding, and oxide spallation. Thus, fuel vendors have developed and proposed the use of new cladding alloys, such as Duplex DX-D4, M5[®], ZIRLO™ and other. Therefore, it is important to verify the safety margins for high burn-up fuel and fuel claddings with advanced alloys. In recognition of this, LOCA-related behaviour of new types of cladding is being actively investigated in several countries [12, 13]. Due to long cladding hydriding period for the high fuel burn-up, post-quench ductility is not only influenced by oxidation, but also significantly depending on the hydrogen concentration. Consequently, the 17% ECR limit is inadequate to ensure post-quench ductility at hydrogen concentrations higher than $\approx 500 \text{ wppm}$ [14]. Due to so-called secondary hydriding (during oxidation of inner cladding surface after burst), which was firstly observed by JAERI [15], the hydrogen content can reach 4000 wppm in Zircaloy cladding regions around the burst [16].

Particularly to investigate the influence of the secondary hydriding phenomena on the applicability of the embrittlement criteria for the German nuclear reactors, it was decided to perform the QUENCH-LOCA bundle test series in the QUENCH facility of KIT, supported by the association of the German utilities (VGB). Additionally, the QUENCH-LOCA bundle tests could support experiments performed in-pile and in-cell, respectively, e.g. single-rod tests as those planned in the OECD SCIP-2 project [17]. Compared to single-rod

experiments, bundle tests have the advantage to study the mutual interference of rod ballooning among fuel rod simulators as well as to take into account the local coolant channel blockages in this more realistic arrangement.

The first test QUENCH-L0 was performed with Zry-4 cladding tubes not pre-oxidised on July 22, 2010 as commissioning test and terminated with reflood immediately after the transient phase [18, 19]. The QUENCH-L1 test was performed on February 02, 2012 as reference test, using a similar bundle compared to the QUENCH-L0 test but including a cool-down phase between transient and reflood [20, 21]. The experiment QUENCH-L2 with as-received M5[®] claddings was conducted on July 30, 2013 [22]. To check the influence of hydrogen absorbed in claddings during the reactor operation, the QUENCH-L4 with M5[®] claddings pre-hydrogenated to about 100 wppm was conducted on July 30, 2014.

1 Description of the Test Facility

The QUENCH facility was constructed 1997 at KIT for the investigation of the hydrogen source term during reflood, i.e. of the measurement of hydrogen release during the reflood of an overheated reactor core. Since then 17 bundle tests were performed as under severe accident conditions ([Table 1](#)). The main components of the QUENCH test facility are presented in [Fig. 1](#). The test section is enclosed by a safety containment with a wall thickness of 5.6 mm and an inner diameter of 801.8 mm. The facility can be operated in two modes: a forced-convection mode depicted in the flow diagram of [Fig. 2](#) and a boil-off mode. In the forced-convection mode (relevant for QUENCH-L4) superheated steam from the steam generator and superheater together with argon as a carrier gas enter the test bundle at the bottom ([Figs. 3 and 4](#)). The system pressure in the test section for the QUENCH-LOCA tests is about 0.3 MPa. The argon, steam and hydrogen produced in the zirconium-steam reaction flow upward inside the bundle and from the outlet at the top through a water-cooled off-gas pipe to the condenser where the remaining steam is separated from the non-condensable gases argon and hydrogen. The water cooling circuits for bundle head and off-gas pipe are temperature-controlled to guarantee that the steam/gas temperature is high enough so that condensation at the test section outlet and inside the off-gas pipe can be avoided. The temperature of the cooling water in the bundle head is kept at 348 K, and the water flow rate is 250 g/s.

The off-gas pipe consists of a water-cooled inner pipe with a counter-current flow and a flow rate of 370 g/s. The water inlet temperature is controlled at 393 K. Between the off-gas pipe and inner cooling jacket there is stagnant off-gas. The main dimensions of the tubes that make up the off-gas pipe are:

Inner pipe: outer diameter 139.7 mm, wall thickness 4.5 mm; total length 3256 mm, material: stainless steel;

Inner cooling jacket: outer diameter 154 mm, wall thickness 2 mm, material: stainless steel;

Outer cooling jacket: outer diameter 168.3 mm, wall thickness 5 mm, material: stainless steel.

The quenching water is injected into the bundle through a separate line marked “bottom quenching” in [Fig. 4](#).

1.1 The test bundle

The design characteristics of the test bundle are given in [Table 2](#). The test bundle is made up of 21 fuel rod simulators, each with a length of approximately 2.5 m, and of four corner rods (see cross section in [Fig. 5](#)). Insertion of four corner rods avoids an atypically large flow cross section at the outer positions and hence helps to obtain a rather uniform radial temperature profile. The fuel rod simulators ([Fig. 6](#)) are held in their positions by five grid spacers, four made of Zry-4, and one of Inconel 718 in the lower bundle zone. This bundle design is applied with a pitch of 14.3 mm. All test rods are heated electrically over a length of 1900 mm (thereof 1024 mm in the middle with W heater and residual length with Mo heaters at rod ends).

1.1.1 Claddings

Unlike the QUENCH-L2 experiment with fresh M5[®] claddings, the QUENCH-L4 test was performed with *pre-hydrogenated* (to hydrogen concentration of 100 wppm) M5[®] claddings. The properties of fresh cladding are listed in [Table 3](#). Before manufacture of hydrogenated tubes for the bundle test, one prototype cladding was prepared by AREVA and tested at KIT. The prototype was welded from three segments: 500 mm hydrogenated, 1200 mm hydrogenated and 500 mm not hydrogenated. This prototype was cut at KIT into three parts: middle part of 200 mm length for the metallographic investigations, lower and upper parts (each 1000 mm) for experiments in tensile machine. [Fig. 7](#) shows results of metallography: the hydrides are oriented in the cladding mostly circumferentially. The lower part of prototype was installed in the tensile machine,

slightly axially loaded with tensile force of 10 N, heated to 650 °C, and pressurized with Kr to 55 bar. After 1 hour heating at constant temperature the sample was burst outside of weld position (Fig. 8). The upper part of the prototype was tested in tensile machine also at temperature of 650 °C, but with increased tensile stress and decreased inner pressure (from 55 bar to 4 bar after 1800 s holding time at temperature). The sample was fractured ductile outside of the weld seam (Fig. 9). The corresponding stress-strain curve is presented in Fig. 10. So, the tests with the prototype showed that failure of the cladding occurred outside of weld seams.

Similar to the prototype, to extend the claddings to full length of used heated rods, the hydrogenated samples were welded to not hydrogenated cladding segments at bundle elevations 50 and 1250 mm (Fig. 11). Whereas the fresh M5[®] cladding of the fuel rod simulator has an outside diameter of 10.75 mm and a wall thickness of 0.725 mm (see also Table 2), the outside diameter of hydrogenated tubes will be increased. This material property was used to determine the hydrogen concentration at each elevation of the pre-hydrogenated segment for each cladding (Figs. 12 - 15).

1.1.2 Heaters

Tungsten (chemically clean tungsten) heating elements of 4.6 mm diameter are installed in the center of rods. W heaters with this small diameter were used for the first time in the QUENCH-L2 experiment. Their higher electrical resistance in comparison to tungsten heaters of 6 mm diameter (used for commissioning test QUENCH-L0) results in higher maximum heating rates, especially during the first transient phase and hence to a more prototypical test conduct. The tungsten heaters with a diameter of 4.6 mm produce a similar heat amount as the tantalum heaters with a diameter of 6 mm (used for the QUENCH-L1 test), but they are more rigid at high temperatures. These heaters are surrounded by annular yttria-stabilized ZrO₂ pellets. The physical properties of the ZrO₂ pellets are described in Table 4.

The tungsten heaters are connected to molybdenum heater (chemically clean molybdenum) and copper electrode (material 2.1293 with Cr 0.8, Zr 0.08 and balance Cu) at each end of the W heater. The molybdenum and copper parts are joined by high-frequency/high-temperature brazing under vacuum (2×10^{-3} mbar) using an AuNi 18 powder (particle size <105 μm). For electrical insulation the surfaces of both Mo and Cu parts are plasma-coated with 0.2 mm ZrO₂. To protect the copper electrodes and the O-ring-sealed wall penetrations against excessive heat, they are water-cooled (lower and upper cooling chambers filled with demineralized water).

The copper electrodes are connected to the DC electric power supply by means of special sliding contacts at the top and bottom. The total heating power is limited by a maximal current of 7200 A and voltage of 9 V. Two DC-generators were used for two groups of rods connected in parallel: 1) 10 internal rods: #1 - #9 and rod #15; 2) 11 external rods: #10 - #14 and #16 - #21. The electrical resistance of the rod heating system, combined of W and Mo heaters as well as Cu alloy electrodes, was measured before (at the end of bundle assembling) and after the test (Table 5). The electric resistance of a single heater (W+Mo+Cu sections) measured at room temperature was about 5 mΩ before the test and about 6 mΩ after the test. The additional resistance of the external electric circuit between the axial end of the single heater and the connection to the generator (sliding contacts, cables, and bolts) is 3.75 mΩ for the inner rod group and 4.05 mΩ for the outer rod group. These values can be taken as constant because the external electric circuit remains at ambient temperature throughout the experiment.

1.2 Bundle surroundings

The bundle is surrounded by a 3.17 mm thick shroud (79.66 mm ID) made of the Zr702 alloy. This part has two functions: 1) The shroud acts as steam and gas guide tube; 2) It simulates an adiabatic surrounding of the reactor core. The consideration of heated rod claddings, corner rods and shroud, manufactured from similar

zirconium alloys, results in the surface of 30.6 effective rod simulators. The shroud is surrounded by a 36 mm thick ZrO_2 fiber insulation (physical properties are given in [Table 6](#)) and an annular cooling jacket made of Inconel 600 (inner tube) and stainless steel (outer tube; see [Fig. 5](#)). The annulus between shroud and cooling jacket was filled (after several cycles of degassing) with stagnant argon of about 0.3 MPa ([Fig. 55](#)) and was connected to a flow-controlled argon feeding system in order to prevent steam access to the annulus after possible shroud failure. The 6.7 mm annulus of the cooling jacket is cooled by an argon flow. Above the W heater, i.e. above the 1024 mm elevation there is no ZrO_2 fiber insulation to allow for higher radial heat losses. This region of the cooling jacket is cooled by a water flow ([Figs. 3 and 4](#)). Both, the lack of ZrO_2 insulation above the W heaters and the water cooling, force the axial temperature maximum downward.

The lower boundary for the lower cooling chamber is a sealing plate made of stainless steel with plastic inlays for electrical insulation, sealed toward the system by O-shaped rings. The upper boundary of the lower cooling chamber is a sealing plate of stainless steel. An insulation plate made of plastic (PEEK) forms the top of the upper cooling chamber, and a sealing plate of Al_2O_3 , functioning as a heat-protection shield, is the lower boundary of the upper cooling chamber (see [Fig. 6](#)).

In the region below the upper Al_2O_3 plate the copper electrode is connected firmly to the cladding. This is done by rotary swaging the cladding onto the electrode. In the swaging region a sleeve of boron nitride is put between electrode and cladding for electrical insulation. The axial position of the fuel rod simulator in the test bundle is fixed by a groove and a locking ring in the top Cu electrodes. Referred to the test bundle the fixing point of the fuel rod simulators is located directly above the upper edge of the upper insulation plate. So, during operation the fuel rod simulators are allowed to expand downwards. Clearance for expansion of the test rods is provided in the region of the lower sealing plate. Also in this region, relative movement between cladding and internal heater/electrode can take place.

1.3 Rod pressurization

All fuel rod simulators were separately pressurized. The gas supply system ([Fig. 16](#)) for individual pressurization of rods consists of pressure controller, 21 valves, 21 pressure transducers, and 21 justified compensation volumes for simulation of prototypic plenum volumes of 31.5 cm^3 . The gas supply is connected with capillary tubes (with inner diameter 1 mm, length ca. 1.2 m) to each rod at its lower end via drill axial holes in the copper electrodes ([Fig. 17](#)). The gas gap between the cladding and the Cu/Mo parts and the W-heater/ ZrO_2 -pellets is 0.15 mm and 0.075 mm, respectively.

Before gas filling, the rods and the gas supply system were evacuated. At the beginning of experiment, the fuel rod simulators were backfilled with Kr gas to 30 bar. Then, before the transient, they were separately pressurized to the target pressure of 55 bar as shown in [Fig. 18](#).

2 Test Bundle Instrumentation

A list of all instruments for the experiment QUENCH-L4, which were installed in the test section and at the test loop is given in [Table 7](#). The distribution of the thermocouples along the bundle is shown in [Table 8](#). No failed thermocouples were detected during the test.

2.1 Thermocouples

The test bundle was instrumented with sheathed thermocouples (TC) attached to the rod claddings ([Fig. 19](#)) at 17 different elevations between -250 mm and 1350 mm and at different orientations according to [Figs. 20 and 21](#). The NiCr/Ni thermocouples (1 mm diameter, stainless steel sheath 1.4541 (X6CrNiTi18-10), MgO insulation) are used for temperature measurement at rod cladding and shroud outer surfaces. The TC tip is held in place by a Zr ferrule welded to the surface. The cables of the rod-thermocouples from the -250 mm to the 850 mm level leave the test section at the bottom whereas those of the TCs above 850 mm are routed out on the top of the test section to prevent TC cables passing the hot zone. For the same reason the cables of the shroud-thermocouples in this region are routed outside the insulation. The thermocouples are designated as following:

- "TFS" for the thermocouples attached to the outer surface of the rod claddings;
- "TSH" for the shroud thermocouples mounted at the outer surface between -250 mm and 1250 mm;
- "TIT" for the thermocouples installed inside the Zry-4 instrumentation rods at the three corner positions of the bundle (positions A, C and D) (see [Fig. 22](#));
- "TCI" for the thermocouples at the cooling jacket are installed inside the wall of the inner cooling tube (from 550 mm to 950 mm, designation).

2.2 Gas measurement system

The flow rates of noble gases (Ar, Kr) are regulated with the BRONKHORST flow controllers. Steam and water flows are controlled with the SIEMENS flow controllers. Numerous pressure transmitters from WIKA measure absolute and differential pressures along the gas supply system, at inlet and outlet of the test section.

The outlet steam and released hydrogen are analyzed by a Balzers mass spectrometer (MS) "GAM 300" ([Fig. 23](#)). Due to its location at the off-gas pipe in the facility the mass spectrometer responds almost immediately (less than 10 s). The "BALZERS GAM 300" is a completely computer-controlled quadrupole MS with an 8 mm rod system which allows reliable quantitative measurement of gas concentrations down to about 10 ppm. For the MS measurement a sampling tube is inserted in the off-gas pipe located approx. 2.7 m downstream from the test section outlet (see [Fig. 2](#) and [4](#)). It has several holes at different elevations to guarantee that the sampling of the gas to be analyzed is representative (see [Fig. 24](#)). To avoid steam condensation in the gas pipes between the sampling position and the MS the temperature of the gas at the MS inlet is controlled by heating tapes to about 150 °C (the upper operating temperature of the MS inlet valves). This allows the MS to analyze the steam production rate. Besides, the concentrations of the following species were continuously measured by the mass spectrometer during all test phases: argon, hydrogen, steam, nitrogen, oxygen, and krypton. The fuel rod simulators are filled with krypton which can be used as an indicator for cladding failure. Additionally, the MS is used to control the atmosphere in the facility, e.g., to monitor the gas composition at the beginning of the test.

The temperature and pressure of the analyzed gas are measured near to the inlet valve of the MS. The MS is calibrated for hydrogen with well-defined argon/gas mixtures and for steam with mixtures of argon and steam supplied by a BRONKHORST controlled evaporator mixing (CEM) device. The MS off-gas is released into the atmosphere because the amount of sampling gas taken out of the system is negligible. A heated measuring gas

pump was used to ensure a continuous flow of the steam-gas mixture from the off-gas pipe to the mass spectrometer.

For the MS the mass flow rate of each gas species is calculated by referring the measured gas concentration to the known argon mass flow rate according to equation (1):

$$\dot{m}_G = \frac{M_G}{M_{Ar}} \cdot \frac{C_G}{C_{Ar}} \cdot \dot{m}_{Ar} \quad (1)$$

with M representing the molecular masses, C the concentrations in vol% and \dot{m} the mass flow rates of the corresponding gases.

3 Data Acquisition and Process Control

A LabView-based control and data acquisition system is used in the QUENCH facility. Data acquisition, data storage, online visualization as well as process control, control engineering and system protection are accomplished by three computer systems that are linked in a network.

During the QUENCH-L4 test the data acquisition system recorded all measurement channels at a frequency of 1 Hz per channel. The experimental data and the date and time of the data acquisition are stored as raw data in binary format. After the experiment the raw data are converted into SI units and stored as ASCII data.

For process control, a system flow chart with the most important actual measurement values is displayed on the computer screen. Furthermore, the operating mode of the active components (pumps, steam generator, superheater, DC power system, valves) is indicated. Blocking systems and limit switches ensure safe plant operation. Operating test phases, e.g. heating or quenching phases, are pre-programmed and can be started on demand during the experiment. The parameter settings of the control circuits and devices can be modified online.

Online visualization allows to observe and to document the current values of selected measurement positions in the form of tables or line graphs. Eight diagrams with six curves each can be displayed as graphs. This means that altogether 48 measurement channels can be selected and displayed online during the course of the experiment.

The data of the main data acquisition system and of the mass spectrometers are stored on different computers. Both computers are synchronized. The data of the mass spectrometer data are recorded at a frequency of approx. 0.8 Hz during the entire test.

4 Test Performance and Results of Online Measurements

The test procedure was based on pre-test calculations for the QUENCH-LOCA series performed by the Paul Scherrer Institute (PSI, Villigen). According to the planned LOCA scenario, the transient phase should be performed with 8 K/s followed by slow cool-down phase and quenching.

The sequence of the test events is represented in [Table 9](#). The experiment began by stabilizing the bundle conditions with an application of electrical bundle power of 3.5 kW (corresponding to a linear heat rate of approx. 1 W/cm) in argon - superheated steam mixture (with rates of 6 g/s argon and 2 g/s steam, or specific rates 0.2 g/s/(effective rod) and 0.07 g/s/(effective rod) correspondingly) resulting in a peak bundle temperatures of 850 K ([Fig. 25](#)). The corresponding current and voltage progression during the test are depicted in [Fig. 26](#).

The transient was initiated by rapidly increasing the electrical power to 42 kW (linear heat rate ≈ 9 W/cm) followed by steady increase to 60 kW (linear heat rate ≈ 13 W/cm) within 42 s and stayed at that level for the rest of the transient (until 78 s). During this period the temperatures increased from their initial values to a maximum in excess of 1352 K, as planned. Due to limitation of the maximal electrical current of the DC generators the average heating rate of about 6 K/s was realised. The readings of thermocouples at each bundle elevation are shown in [Figs. 27 – 43](#). The temperatures of cooling jacket were practically not changed during the whole test ([Fig. 44](#)). The bundle inlet and outlet gas mixture temperatures were registered at -410 mm (T 511) and +135 mm (T 512) correspondingly (showed in [Fig. 27](#) and [Fig. 43](#)). The abrupt gas temperature decrease at bundle outlet 40 s later after reflood initiation ([Fig. 43](#)) is induced by steam condensation at bundle head .

Two additional (in comparison to the reference test QUENCH-L1) thermocouples TFS 7/12i and TFS 7/13i installed at the cladding surface of rod #7 at the azimuthal position adjacent to the central rod #1 (i.e. opposite to thermocouples TFS 7/12 and TFS 7/13) allowed the registration of radial temperature gradients at the hottest elevations ([Fig. 45](#)). According to the REBEKA burst criterion [9], the azimuthal temperature difference has the dominant influence on the circumferential burst strain. Significant azimuthal temperature difference can be developed during the transient not only due to global radial temperature gradient across the bundle (heat loss through the shroud), but due to not coaxial positioning of pellets and cladding [4]. The highest temperature achieved at the contact between pellet and cladding (absence of gas gap with relatively low heat conductivity). The temperature difference between this contact position and opposite cladding side increased during ballooning process, which occurred in such manner that the gas gap at the cold side increased whereas no gas gap formed at the hot side.

The axial temperature profile in the bundle has a pronounced maximum between 850 and 1050 mm ([Figs. 46 – 51](#)). There is also a radial temperature gradient due to two reasons: 1) radial heat flux to the shroud, 2) electrical power supplied to the internal rod group was higher than the power for the external group because both DC generators reached their current limit (~ 3600 A) but the electrical resistance of the 11 external rods connected in parallel is lower than for the 10 internal rods.

The experiment continued with power decrease to 3.5 kW at 82 s to simulate decay heat and injection of steam at a nominal value of 20 g/s. There was an initial minor temporary increase in temperatures at some locations, but this phase was mostly steady cooling to about 980 K.

This cooling phase was followed by 100 g/s (3.3 g/s/ effective rod) water injection at 215 s. There was a period of about 40 s while the lower volume was being filled during which time the temperatures increased somewhat in the absence of significant flow. The first quench occurred at the bottom of the bundle at 248 s. The dependence of evaporation rate of the quench water on the position of collapsed water front is depicted in [Fig. 52](#). Quenching progressed readily toward the top (indicated by wetting of thermocouples at different elevations, [Fig. 53](#), [Table 16](#)), and the first quench in the ballooned region occurred at 270 s. The wetting of thermocouples in upper elevations 1050-1350 mm propagated from the bundle top probably due to counter flow of water condensed at the bundle head (T 512 reading in [Fig. 43](#)). Complete quench was achieved at 300 s.

Oscillation of the gas pressures during the test are presented in [Figs. 54, 55](#). [Fig. 56](#) shows the water flow characteristics. Mass spectrometer data on steam registration (during steam supply and evaporation phases),

hydrogen production (due to oxidation of bundle and shroud) and krypton release (due to failure of claddings) are presented in Fig. 57. Comparison with the QUENCH-L2 results shows increased hydrogen release for QUENCH-L4 initiating on 55 s. At this time point the maximum cladding temperature reached value about 1100 K and all hydrides were completely dissolved in β -Zr. Consequently, the dissolved hydrogen could be partially released from claddings. The development of integral hydrogen production is also illustrated in Fig. 57: 0.8 g hydrogen were measured during the whole test (about 0.2 g more than for QUENCH-L2).

The decreased yield strength and increased ductility of the claddings during the transient phase resulted in a progressive ballooning and consequent burst of all pressurized rods (Table 10). The first burst occurred 48 s after initiation of the transient phase at about 1100 K at rods #1, #5 and #7. All 21 rods failed within 19 s (Fig. 58). The individual rod failures were indicated by internal pressure readings and correlated with krypton peaks measured in the off-gas pipe by the mass spectrometer. The Kr release indicates failure of inner and outer rod groups (Fig. 59). The first failed rod was the internal rod #1, the last failed rods were the peripheral rods #10, #16 and #18 (Table 10). Two rods (#4 and #17) failed non-prototypically at the contact between W heater and lower Mo heater. The temperature range for bursts is estimated from thermocouple readings to be between 1067 and 1151 K. Table 11 gives comparison of burst times and burst temperatures for the tests QUENCH-L2 and -L4. The average burst temperature of hydrogenated claddings (QUENCH-L4) was about 30 K lower in comparison to the same parameter of not hydrogenated claddings (QUENCH-L2). The average geometrical parameters of burst openings are very similar for both bundle tests (Table 12).

5 Posttest Examinations

Posttest Examinations (PTE) included nondestructive methods (optical bundle observations, laser profilometry of all claddings, ultrasound cladding wall thickness measurements, eddy current measurements of outer layers of claddings, neutron radio- and tomography) as well as destructive investigations (tensile tests, metallography, fractography, XRD, EBSD).

5.1 Optical Observation of Cladding Surfaces

First observations of burst positions were performed immediately after the test by means of an OLYMPUS videoscope. The camera of the videoscope (diameter 6 mm, total cable length 9 m) was introduced through the bundle bottom at positions of withdrawn corner rods (Figs. 60 - 64). For the peripheral rods no contacts between adjacent claddings due to ballooning or rod bending were observed. All observed thermocouples remained intact after the test.

The bundle was withdrawn from the shroud for further investigations. No noticeable changes of bundle geometry were indicated (Figs. 65 and 66). Grid spacers were removed for the separation of the single rods. The surface of the claddings is mostly shining black, only the regions around the burst openings are matte black (Figs. 67 and 68) due to surface micro cracks (Fig. 79) formed during ballooning. No rod bending was observed in the plane with overhead view to burst opening. For the plane with the side view of openings only negligible rod bending was observed for the inner rods (Fig. 69) and some of the outer rods (Fig. 70) with values less of 3 mm deviation from original rod axis.

The shape and geometry of burst openings of all rods are very similar among each other (Fig. 71). The lengths of openings varied between 11 and 18 mm, the width between 2.4 and 4.8 mm, and the opening areas determined by image analyses are 17 - 40 mm² (Table 10). The tangential burst positions of all rods correspond to the hottest rod region and are directed mostly to the bundle centre (Fig. 72). All bursts are axially located

between 815 and 960 mm (Fig. 73). No global blockage was formed due to relatively small cladding strengths and due to the variation of the ballooning positions.

Observations of the cladding surface were performed with a Keyence digital microscope equipped with a macroscopic objective. The shapes of burst openings are shown in Figs. 74 - 78. Fig. 79 illustrates the structure of oxidized cladding surfaces near to the opening of rod #1. It can be seen that the cladding surface is covered with a network of crossed longitudinal cracks developed during the ballooning process. A large-scale crack cells network is located near to the burst opening, whereas small-scale cells are typical for the cladding side opposite to burst. The cell sizes change not only circumferentially, but also longitudinally: they decrease with increasing distance to the burst location. The cell size strongly depends on strain: the higher the strain the larger are the cells.

The inner surface of three claddings was investigated by videoscope (Fig. 80). For two claddings typical traces of contact between pellet and cladding slightly below the burst opening were observed. Similar observations were made previously also for some claddings of the QUENCH-L2 bundle and confirmed the early suggestions [4] that relatively often the burst occurs at the position of contact between pellet and cladding. Due to absence of the gas gap, the heat transport from pellet to cladding is at this circumferential position the highest. Concerning the gas penetration to these contact spots, the corresponding surface areas were not oxidised because access of steam was not possible to this area. Because the metal in these areas is not covered by oxide layer, the hydrogen, which has a higher diffusivity than steam penetrating very narrow gaps, can be absorbed at these contacts between pellet and claddings.

5.2 Profilometry of Claddings with Laser Scanner

5.2.1 Linear Laser Scanning

The profilometry of the rods was performed with a Linear Laser Scanner (Fig. 81) made by ANT Antriebstechnik GmbH for quantifying the deformations produced on the rods as a result of the QUENCH-LOCA experiments. The ballooned parts of the bundle rods exposed to LOCA scenarios acquire a variety of shapes and sizes due to different temperature conditions. Therefore a precise method to detect the local variations in diameter along the rods was required.

5.2.2 Main Characteristics of the Measuring Device and Procedures

The measuring mechanism is based upon photocells which compare the amount of laser light blocked by the rod in relation to the portion of light that reaches the sensors. The equipment is mounted vertically and supported on a wall of the experimental hall in order to minimize the effects of shocks and vibrations propagated by the floor. The rod to be measured is placed vertically and linked to a step motor which ensures the precise turning of the rod according to a given number of measurements that should be made during a rotation of 360°. A resolution of 0.25° is provided. The laser scanner itself moves a predetermined length up or down the driving rails in order to cover a specific section of the examined rod. The smallest vertical step is 100 µm and the maximum length which the scanner can handle is 2000 mm.

Automatic settings allow the scanner to work for many hours without the need of supervision. For safety reasons and because of mechanical limitations, the data gathering is quite slow. A total of approximately 5700 points are measured each hour. This means that a scanning of a 1500 mm rod section takes roughly 4 days considering a measurement every 1 mm and 1°.

All data generated can be processed in various ways in order to determine different information. For instance, it allows the exact location and orientation of each burst, determination of radial strain, calculation of cross-

section area reduction and thus blockage. Also, a digital 3D rendered image is generated as a record and for further analysis, since every rod is sooner or later damaged by mechanical testing or cut for metallographic examination.

5.2.3 Results of the Scans

The evaluation of the scans can be divided into azimuthal and longitudinal analysis.

The azimuthal plots ([Figs. 82 - 102, bottom](#)) clearly show the orientation of the bursts and also give an idea of the shape. It was revealed that the bursts were oriented to the center of the bundle, mainly because of the radial thermal gradient which was established in the test section. The maximal cladding diameter was observed in the burst plane, the minimal diameter – in the perpendicular plane. It is also to be seen, that immediately below and above the burst opening the maximal diameter was measured in the plane perpendicular to the burst plane. All azimuthal plots illustrate this fact: the neighboring elevations lower the burst evident the maximal diameter in the plane perpendicular to the burst. I.e. during ballooning and immediately before burst, the cladding extends here more in the directions perpendicular to the burst plane.

The shape of the bursts vary widely, neither size nor symmetry have any apparent correlation to burst temperature.

Also based on these scans, the circumferential strains can be determined ([Table 17](#)), which are depicted on [Figs. 82 - 102, top](#). There is a clear correlation of the burst location (position with a largest strain) and the temperature distribution on the longitudinal axis. Maximum strain of 29.9% was observed on the outer rod #20, minimum strain of 17.5% was observed on the outer rod #15. Comparison with corresponding results of the QUENCH-L2 test shows that the circumferential strain values in ballooning regions outside of burst opening are remarkably higher for the QUENCH-L4. Possible reasons could be 1) other mechanical properties of hydrogenated claddings, 2) smaller circumferential temperature differences for rods of the QUENCH-L4 bundle (according to the REBEKA burst criterion [9]).

For all rods the deformation starts at elevations about 250 mm and ends at 1250 mm. The axial extension of cladding region with more than 5% strain is usually shorter than 185 mm. It is worth to notice that besides the main strain maximum some of the rods (#4, #5, #6, #15, #16, #21) have a second (or sometimes even third) strain maximum located ≈ 100 mm (or ≈ 200 mm) below or above main maximum too. I.e. the ballooning was initiated at many axial locations inside the hot zone. The second balloon regions were observed also for several rods of the QUENCH-L2 test ([Fig. 103](#)). The intensity and extension of ballooning were comparable for both bundle tests. [Table 17](#) gives overview of strain parameters measured at burst position.

The blockage is the quotient of total increase of the rod cross-sections divided by initial empty area inside the inner surface of the shroud. Since the burst locations are scattered between elevations 784 and 963 mm, the blockage wasn't too significant. As shown in [Fig. 104](#), the maximum blockage occurs at about 925 mm and reaches 19% of area reduction. If, hypothetically, all burst were located at the same level, the blockage would be 27%.

5.3 Nondestructive Ultrasound and Eddy Current Measurements

Before cutting the cladding tubes for further investigations, some analyses had to take place. The thinning of the cladding wall along the line of the burst opening in the ballooned region of the central rod was proved by ultrasound measurements ([Fig. 105](#)) performed by Echometer device from Karl Deutsch GmbH. The wall thickness increases from 500 μm in vicinity of the opening tip to the regular thickness of 725 μm at a distance of about 50 mm.

The oxidation degree of each cladding was measured by means of the eddy current measurement device ISOSCOPE FMP30 from Helmut Fischer GmbH. The device was calibrated with two plastic foils of 24.3 and 99.3 μm thicknesses, which were disposed at the surface of hydrogenated M5[®] prototype tube. At least 20 circumferential measurements at each axial position were used to achieve the averaged result. The axial step width was 20 mm. The device shows the distance between the gauge and the internal metallic layer; i.e. the measured values correspond to the sum of the thicknesses of ZrO_2 and $\alpha\text{-Zr(O)}$ layers. The comparison of eddy current results with metallographic results confirms this assumption.

Fig. 106 and Fig. 107 show results of eddy current measurements for the inner and the outer groups of rods respectively. The most oxidized region is between 750 and 950 mm, what corresponds to the axial temperature profile. Figs. 108 – Fig. 110 illustrate clearly the existence of a radial temperature gradient. This radial temperature gradient causes an azimuthal difference in the oxidation of each rod: the side of the cladding oriented to the central (hottest) rod is more oxidized than the cladding side oriented to shroud. Irregular thickness changes were observed inside the axial zone with the pronounced ballooning due to variations of the cladding thickness from the cladding thickness for the original calibration sample.

5.4 Results of Neutron Radiography and Tomography; Analysis of Absorbed Hydrogen.

5.4.1 Basic Principles

Neutron radiography is a powerful tool for the determination of hydrogen concentration and distribution in zirconium alloys [23-27]. Hydrogen can be quantitatively and non-destructively determined with a spatial resolution of up to 25 μm . The method was applied for the post-test hydrogen analysis of selected QUENCH-L4 cladding tubes.

Firstly, a short introduction into neutron radiography will be given. The sample is positioned into a parallel neutron beam. The intensity distribution behind the sample is measured for each pixel. From the intensity the transmission T can be calculated:

$$T(x, y) = \frac{I(x, y) - I_B(x, y)}{I_0(x, y) - I_B(x, y)} \quad (2)$$

where x and y are the coordinates of the pixel position. I , I_0 and I_B are the intensities behind and before the sample and the background intensity, respectively. From the neutron transmission the total macroscopic neutron cross section Σ_{total} can be calculated:

$$\Sigma_{\text{total}}(x, y) = \frac{-\ln(T(x, y))}{s(x, y)} \quad (3)$$

where s is the neutron path length through the material. The total macroscopic neutron cross section is the sum of the total microscopic cross section σ of the isotopes i multiplied with their number density N :

$$\Sigma_{\text{total}}(x, y) = \sum_i \sigma_i \cdot N_i = \underbrace{N_{\text{Zry}}(x, y) \overline{\sigma_{\text{Zry}}}}_{\Sigma_{\text{samples received}}} + N_{\text{O}}(x, y) \sigma_{\text{O}} + N_{\text{H}}(x, y) \sigma_{\text{H}} \quad (4)$$

In the case of steam oxidation of cladding materials it can be assumed that only the amount of oxygen and hydrogen is changed whereas the amount of zirconium and the alloying elements is not influenced significantly.

In order to reconstruct the specimen three-dimensionally, radiography projections have to be taken from different orientations. According to the sampling theorem, the number n of projections is connected with the spatial resolution (pixel size) d and the radius R of the object circle that fully encompasses the object formed by the rotating of the sample:

$$n = \sqrt{2\pi} \frac{R}{d} \quad (5)$$

5.4.2 Technique

The neutron radiography measurements were performed at the ICON facility at the Swiss neutron source SINQ at Paul Scherrer Institute Villigen (PSI). The investigations were performed applying the so called micro-tomography setup providing the highest resolution (pixel distance 13 μm). The field of view is 28 mm x 28 mm. The samples were scanned through the field of view with a step width of 25 mm. Exposure times of 300 s were applied. The specimens were measured horizontally.

The neutron tomography experiments were performed partially at the ANTARES facility at the FRM2 research reactor in Garching. 475 projections were measured with a pixel size of 25.6 μm and an illumination time of 30 s. A field of view of 52 mm (axial direction) x 65 mm (radial direction) was applied.

The rods #2, #3, #5, #7 and #8 were qualitatively investigated at the BOA/SINQ facility with a pixel size of 45.9 μm (due to problem with calibration only local maximal hydrogen concentrations were determined).

5.4.3 Results of Radiography

The investigations comprise measurements of all rods of the QUENCH-L4 test. Because of the uncertainties of the tube wall thickness caused by the plastic deformation as well as the contribution of front and back side of the tube, quantitative information cannot be extracted from one single radiograph alone. However, the radiographies give information about the occurrence of hydrogen enrichments and their positions. [Fig. 111](#) shows the radiographs taken from inner rods, whereas [Fig. 112](#) reveals depicted results for outer rods. For the inner rods, not only the bended hydrogen enriched bands known from the former QUENCH-L0, -L1 and -L2 tests were found but also hydrogen spots corresponding to contacts between pellets and claddings. In the peripheral rods no hydrogen enrichments are obvious.

5.4.4 Results of Tomography: Hydrogen Content

In order to obtain quantitative information about the hydrogen concentrations in the claddings, neutron tomography investigations were performed. For the sample reconstruction the Muhrec3 software of PSI Villigen was used. The reconstructed data set was analyzed for each slice (axial cut) using the macro "Background correction" developed at KIT in the software package ImageJ. The different steps of the analysis are

- Sample identification by background correction (definition of threshold value at which it is assumed that the voxel is part of the sample, dilatation of the marked volume to close the sample area, shrinking of the marked volume by the same numbers)

- Additional shrinking of the sample to neglected sample surface positions with increased cross section as an artefact or surface effects like total reflection and refraction.
- Determination of minimum, mean and maximum values in the marked sample volume.

This procedure was applied on the reconstructions of all rods of QUENCH-L4 given in [Table 13](#). All 8 burst inner rods and several outer rods were investigated after the tensile tests. [Fig. 113](#) shows comparison of optical, radiography and tomography observations for the inner rod #9. It can be seen that the tomography indicated clearly the markers at the outer cladding surface, made with organic colorant, containing hydrogen.

For the experimental setup applied the following correlation was determined:

$$\Sigma_{total} = 0.204 \text{ cm}^{-1} + 2.327 \text{ cm}^{-1} \frac{H}{Zr} \quad (6)$$

[Fig. 114](#) and [Fig. 115](#) illustrate the tomography results for inner rods containing either hydrogen bands or hydrogen spots. The concentration of absorbed hydrogen for relatively cold outer rods ([Fig. 116](#)) was noticeably low (if any) in comparison to outer rods. The axial hydrogen distributions are shown in [Figs. 117-122](#) (with quantitatively determined concentration) and [Figs. 123-127](#) (with hydrogen content determined relatively in relation to the lowest mean hydrogen concentration). Unfortunately, it was not possible to reach the quantitative values for the last five presented claddings (measured separately from other claddings) due to not correct calibration.

[Table 13](#) gives the mean and local maximal hydrogen concentrations determined for each axial slice (cladding cross section with the size of one pixel). A comparison between inner and peripheral rods of tests QUENCH-L4 and QUENCH-L2 indicates that hydrogen enrichments are formed if the temperature exceeds 1273 K. The maximal hydrogen concentrations in both, the inner as well the peripheral rods of the pre-hydrogenated QUENCH-L4 rods are about 300 wppm higher than the concentrations determined for the non-pre-hydrogenated QUENCH-L2 rods.

Comparison of measured maximal hydrogen concentration with average values determined by hot extraction ([Table 14](#)) showed bigger scattering of the concentration values for the rod #1 in comparison to rods #2 and #7. Measurement of hydrogen concentration by hot extraction outside of the hydrogen bands ([Table 15](#)) gives values, which are higher in comparison to the pre-hydrogenation level (of 100 wppm). The reason for the last observation could be redistribution of hydrogen in the cladding near to the burst opening due to local mechanical not homogeneous stresses.

5.4.5 Cladding Cross Sections Reconstructed by Tomography

Tomographic reconstructions allow rebuilding very precisely the shape of cladding tubes at each axial elevation. [Fig. 128](#) compares the initial tube form (given in blue) with the post-test tomography images of burst claddings at the axial position of the maximal burst opening. This comparison shows that claddings were practically not deformed at positions opposite to burst openings. The wall thinning occurred essentially in vicinity of the burst openings.

5.5 Mechanical Tests

Tensile tests on relevant cladding sections were performed at room temperature to determine the residual strength and ductility of QUENCH-LOCA tested claddings, particularly to identify the embrittlement in dependence of the different quench test conditions. Previously, the mechanical properties of axially homogeneous hydrogenated Zircaloy-4 claddings were investigated in 2010 during a single rod test series [28].

5.5.1 Tensile Test Set-up

The tensile tests were carried out using a universal testing machine from INSTRON (type 4505, 50 kN load cell), equipped with specially developed grip holders. The experiments were performed displacement-controlled with a displacement rate of 2 mm/min at room temperature (RT). Exact fitting end plugs were mounted to clamp the tubes without deforming their end sections. Since a cladding tested in a QUENCH experiment usually shows an inhomogeneous $ZrO_2/\alpha-Zr(O)$ layer thickness along the main tube axis, the specimens were optically subdivided with paint markers to determine both the global and the local axial elongation during a test by using a CCD-camera measurement system. Three cameras were used for the tests to increase the resolution of the optical measurement device. Generally, the initial gauge length l_0 of a specimen was 750 mm and a sample was prepared in that way, that the ballooning section was positioned in the axial center. After the tests, the strain was calculated from the captured pictures by using the Digital Image Correlation and Tracing program provided by MATLAB [29] and the stress was calculated by using average values of the measured initial inner and outer diameters from the ends of a tube.

5.5.2 Results of the Tensile Tests

Three inner rods failed at the positions of hydrogen bands ([Fig. 129](#) and [Fig. 130](#)) whereas others failed after necking. During the tensile tests with outer rods ([Fig. 131](#) and [Fig. 132](#)) also typical fracture after necking with fracture surfaces perpendicular to the load direction was observed for several rods. However, mostly was observed fracture from (pre)crack tip to (pre)crack tip at which the final crack propagates around a sample. This fracture mode doesn't occur abruptly. In fact one can observe that the onset of failure is driven by strong local deformations, starting at the (pre)crack tips. It is interesting to note, that only claddings from the outer area of the bundle failed in this mode, in parts with remarkable elongations at fracture up to more than 5 %.

In general, the elongation at fracture varies between 2.7 and 13.5 %, and the strength at fracture of the QUENCH tested cladding was above 500 MPa. An overview of all determined mechanical properties is given in [Table 18](#). [Fig. 133](#) and [Fig. 134](#) depict the stress-strain curves of all inner and outer specimens, respectively.

5.6 SEM investigations

The structure of the material always has an impact on its mechanical properties. After the rupture of the cladding tube all structural features are well observable at the fracture surface. Each structural element, for example, oxide or sub-oxide layer of oxygen-stabilised zirconium, zirconium-needles of Widmanstätten structure, large fields of coalesced grains with precipitates on the grain boundaries and hydrides has its own fracture mechanism that leave the traces on the fracture surface. It can be identified from its appearance in the scanning electron microscope. Usually the material exhibits ductile or brittle fracture. However, in the case of inhomogeneous oxidation together with hydrogen penetration, the embrittlement behaviour could be more complex.

The scanning electron microscopy analysis of the ruptured surface of the cladding tube of the rod #9 near to burst opening is presented in [Fig. 135](#). The general overview of the cladding tube wall shows that the fracture was brittle. The detailed view of the middle part of the tube allowed to observe a needle-like structure of the ex- β -phase region. No sign of ductility dimples was observed in this region.

In contrast to the burst opening region, the investigation left from the position of the burst opening showed ductile fracture. Of course, there were the oxide and the oxygen-stabilised α zirconium sub-oxide layers. In [Fig. 136](#) these phases showed brittle behaviour which is confirmed by the smooth cleavage fracture surface. However, the ex- β -phase region had overall ductile fracture behaviour, which is confirmed by a lot of dimples. There was no needle-like structure detected in this region.

The structure opposite to the burst opening of the cladding tube wall is shown in [Fig. 137](#). The large coalesced region was detected to act as a whole during rupture. It means that the grain boundaries were not able to retain the structure integrity. The boundaries of these regions are the sources of potentially dangerous intergranular fracture because of the tendency to accumulate hard and mostly brittle precipitates and especially hydrides. It leads to the decrease of the tensile stress necessary to rupture this boundary. Though the fracture mode was still mostly ductile, the size of dimples became smaller together with the development of intergranular fracture mechanism. It can be concluded, that this behaviour could be due to hydrogen.

The structure right to the burst opening shows the development of intergranular fracture. [Fig. 138](#) illustrates big regions of intergranular fracture and dimples. This local structure embrittlement should be only due to hydrogen.

[Fig. 139](#) presents the results of energy dispersive X-ray spectrometry (EDX), which was used to get the oxygen content and its possible impact on the embrittlement of the cladding tube. No distinguishable peaks of oxygen were detected inside the α - β -phase. The only place with the well-developed peak of oxygen was at the oxide scale region. Though there were values of the oxygen between 1 and 10 at% detected, taking into account the uncertainty value of this method in detecting oxygen and the absence of distinguishable oxygen peak, it can be concluded, that there was no significant amount of oxygen in the metallic part of the cladding tube.

The tensile test behaviour of the rod #10 ([Fig. 140](#)) is much in common with that of rod #9. There were also dimples detected with a tendency to intergranular fracture development. However, it was not so good developed as in the rod #9.

5.7 Metallographic Examination

The metallographic investigation of the cross section of the claddings at the burst elevation evidences oxide layer growth at the outer cladding surface as well as oxidation of the inner surface. The thickness of the inner oxide layer decreases axially and circumferentially from the burst position.

The internal cladding oxidation is caused by steam penetration through the burst opening after release of filling and fission gases. The hydrogen, produced during the oxidation of the inner cladding surface, propagated in the gap between cladding and pellet up to boundary of the inner oxidised region. Outside of this region there are no more barriers for the absorption of hydrogen by the metal, and this internally oxidised region should be surrounded by hydrided zones. This assumption was confirmed by neutron radiography.

The detailed optical mapping of the inner surface of rod #1 shows a transition from the oxidised inner surface in the ballooning region ([Fig. 141](#)) to a metallic surface outside the ballooning region ([Figs. 142 and 143](#)). A part of inner surface below burst opening was not oxidised due to a close contact between pellets and cladding ([Fig. 137](#)). Similar conclusions could be made for the rod #6 ([Figs. 144 and 145](#)). Some circumferential variations of inner oxide layer thickness were observed for rod #8 between burst opening and hydrogen band ([Fig. 146](#)). In this case the pellet was perhaps shifted to the cladding side opposite to burst opening and the gap pellet-cladding was larger at the side of opening. The next upper pellet surrounded by a hydrogen band could be positioned without shifting to any cladding side.

5.8 XRD investigations

Two rods (#5 and #8) were investigated by XRD in the region of the hydrogen band ([Figs. 147-150](#)). The peak positions corresponding to γ -hydrides were indicated. The other interesting observation was the indication of β -Zr, probably stabilized by Nb.

5.9 EBSD analysis

Heating to the temperatures above the point of phase transformation of zirconium alloy usually leads to the development of coarse grained structure due to recrystallization process. High temperature promotes diffusion with redistribution of alloying elements. Normally, depending on time of heat treatment, the regions of coalesced grains with the same orientation and typical sizes between 30 and 100 μm are forming.

The electron back scattered diffraction (EBSD) analysis of the cladding tubes after QUENCH-L4 experiment has shown the typical microstructure after high temperature heat treatment above the $\alpha \rightarrow \beta$ phase transition point. During cooling the $\beta \rightarrow \alpha$ back transformation occurs. All the hydrogen should be accommodated in the restructured α phase, which is not possible at room temperature. That is why the zirconium hydrides are forming at the hydrogen enriched places. The other material volume fraction is represented by the pure α -zirconium phase in the form of big needle-like structure. These needles were observed after the QUENCH-L4 experiment in rod #1 in the region of the hydrogen band detected by neutron tomography. Relatively large hydride clusters were detected near to boundaries of the region of coalesced grains with the same spatial orientation, as shown in [Fig. 151](#) (bottom right). Both zirconium δ - and γ -hydrides were detected in the structure. The γ -hydrides were always accompanied with δ -hydrides. But sometimes pure δ -hydrides were detected without additional signal from γ -hydride lattice. The EBSD pattern quality decreased in the sequence δ -hydrides $>$ α -Zr $>>$ γ -hydrides which indicate that the detection of γ -hydrides is connected with significant higher error probability than for Zr and δ -hydride.

In [Fig. 152](#) the site opposite to the burst opening of rod #1 is shown. On the orientation map of grains, the regions of the same orientation have indefinite form with clear growth directions. It was the cross-section below the hydrogen band. As a consequence, there were not so much hydrides detected. Nevertheless, the regions with not recognised phase contained areas of hydrides and it could be suggested, that these regions composed completely from δ -hydrides (probably with embedded γ -hydrides).

The significant reduction of the cladding tube wall thickness can be seen in [Fig. 153](#) near to the burst opening of rod #5. The hydrogen enriched side of the cladding has the same type of structure as in rod #1. Needles of α -Zr are inside the big regions divided by δ - and γ -hydride inclusions. The opposite side of the cladding had lower hydrogen content as it was estimated by neutron tomography and consequently lower amount of hydrides was detected.

[Fig. 154](#) represents the tube wall of rod #6. Though there were a lot of not recognised regions, the amount of detected needle-like structures allows to suggest that it are rather hydrogen rich regions. As was observed in two previous cases, the low hydrogen content leads to the formation of large regions of coalesced grains rather than to formation of needles. The neutron radiography supports this data with rather high values of detected hydrogen content.

In [Fig. 155](#) the opposite side to the burst opening of rod #6 shows lower hydrogen content. The big coalesced grains are reflecting this as it was said earlier. Low amount of hydrides of small dimensions was detected. Together with this the β -Zr was detected in this cross-section due to redistribution of Nb (β -stabiliser for Zr) at high temperature.

The fracture surface of the cladding #9 looks brittle ([Fig. 156](#)). The EBSD analysis of this region also revealed the needle-like structure, which is an indicator for hydrogen enriched regions. Unfortunately, the big amount of null-solutions and the small investigated field not allowed to make clear conclusions for the rod #9. Nevertheless, the structure behaviour is much similar to that obtained for hydrogen enriched regions of rods #1, #5 and #6

6 Summary and Conclusions

The QUENCH-LOCA-4 (QUENCH-L4) test with pre-hydrogenated M5[®] claddings ($C_H \approx 100$ wppm H) was performed according to a temperature/time-scenario typical for a LBLOCA in a German PWR with the same parameters as the QUENCH-L2 test with fresh not pre-hydrogenated M5[®] claddings: the maximal heat-up rate was 8 K/s; the cooling phase lasted about 120 s and was terminated by 3.3 g/s/effective rod water flooding.

Similar to QUENCH-L2, a maximum temperature of about 1400 K was reached at the end of the heat-up phase at elevation 950 mm. The tangential temperature gradient across a rod was up to 30 K on the burst onset. This value is lower than the corresponding parameter for the QUENCH-L2 test. As a consequence, a larger ballooning strain could be expected for QUENCH-L4 according to the REBEKA criterion. This fact was confirmed by laser profilometry.

The detailed profilometry for whole length of the rods showed formation of not only main ballooning area (with burst) but also, for several rods, additional two or three ballooning regions. The reason should be the relatively long duration of the ballooning process at the main position and achievement of ballooning conditions ($T > 1000$ K) at other bundle elevations. Another parameter calculated based on profilometry measurements is the bundle blockage. Due to closer axial localisation of the main ballooned regions the maximum blockage ratio of the cooling channel (18% at 925 mm) was slightly higher in comparison to QUENCH-L2 (15% at 960 mm). Due to this only moderate blockages good bundle coolability was kept for both bundles.

Cladding wall thinning from 725 μm to 450 μm due to ballooning was observed at the burst side along 50 mm below and above burst opening (ultrasound measurement). The cladding burst occurred at temperatures between 1067 and 1151 K with an average value of 1107 K (QUENCH-L2: between 1050 and 1195 K, average 1138 K). The reason of this difference between the two bundle tests (early burst for QUENCH-L4) could be a shift of the phase transformation ($\alpha\text{-Zr} \leftrightarrow \beta\text{-Zr}$) to lower temperature for the pre-hydrogenated claddings (fresh Zr has transformation point at about 1120 K). The average burst opening parameters were: width 3.3 ± 0.7 mm; length 13.1 ± 1.9 mm (similar to QUENCH-L2 with not pre-hydrogenated claddings). I.e. the sizes of openings are relatively small and only small fragments of fuel pellets in the reactor case can be released from the claddings.

The inner rod pressure relieved to the system pressure during about 30 s (similar to QUENCH-L2). After this time period the steam penetrated through the burst opening and propagated between pellets and cladding. The hydrogen, produced during oxidation of the inner cladding surface around the burst opening, can be absorbed by metal with formation of hydrogen enrichments around the oxidized area (secondary hydrogenation). Such enrichments were observed for inner rods having seen peak cladding temperatures of more than 1200 K. No hydrogen bands were observed for all outer rods - the peak cladding temperature measured for these rods was less than 1200 K. Neutron tomography analyses showed the maximal hydrogen concentrations inside the hydrogen bands between 730 and 1520 wppm. XRD analysis detected hydrides inside hydrogen bands. Elaborated EBSD analysis showed that the hydrides with μm -sizes are distributed in the matrix intra- as well inter-granular.

The metallographic investigations of the inner cladding surface showed the formation of an oxide layer around the burst opening with a thickness of less than 15 μm decreasing to 3 μm at a distance of about 20 mm from the burst opening. Similar values were measured also for the thickness of the $\alpha\text{-Zr(O)}$ layer. The maximal oxide thickness at the outer cladding surfaces was also less than 15 μm . The integral oxidation of bundle was indicated by a release of 0.8 g hydrogen during the whole test, almost 0.2 g more in comparison to QUENCH-L2 (what can be not explained by a release of maximal 0.1 g hydrogen absorbed in the hot bundle zone during pre-hydrogenation).

During quenching, following the high-temperature test stages, no fragmentation of claddings was observed (residual strengths and ductility was sufficient).

Tensile tests evidenced fracture at hydrogen bands (similar to QUENCH-L0 with Zry-4 claddings): three inner rods were fractured due to this embrittlement. Corresponding maximal hydrogen concentrations measured at the fracture positions were more than 1400 wppm. Eight peripheral rods were fractured due to stress concentration at burst opening edges (similar to ten claddings of QUENCH-L2 test with not pre-hydrogenated claddings). All other tensile tested claddings failed after necking far away from burst region.

7 Acknowledgments

The QUENCH-LOCA experiments are supported and partly sponsored by the association of the German utilities (VGB).

The broad support needed for preparation, execution, and evaluation of the QUENCH-L4 experiment is gratefully acknowledged. In particular, the authors would like to thank Mr. J. Moch for the assembly including instrumentation as well as disassembly of the test bundle, Dr. H. Leiste for the X-ray diffractometry measurements, Mrs. U. Peters for the metallographic examinations and the photographic documentation.

The determination of the test protocol was based on numerous calculations with SCDAP/RELAP5 and SCDAPSIM performed by Dr. J. Birchley and Dr. L. Fernandez-Moguel, Paul Scherrer Institute (PSI), Switzerland.

8 References

- [1] Atomic Energy Commission Rule-Making Hearing, Opinion of the Commission, Docket RM-50-1, 28 December, 1973.
- [2] G. Hache and H. M. Chung, "The History of LOCA Embrittlement Criteria," NUREG/CP-0172, May 2001, pp. 205-237.
- [3] RSK-Leitlinien für Druckwasserreaktoren. Ursprungsfassung (3. Ausgabe vom 14. Oktober 1981) mit Änderungen vom 15.11.1996.
<http://www.rskonline.de/downloads/8110dwr.pdf>
- [4] K. Wiehr, He. Schmidt, Out-of-pile-Versuche zum Aufblähvorgang von Zirkaloy-Hüllen. Ergebnisse aus Vorversuchen mit verkürzten Brennstabsimulatoren. Wissenschaftliche Berichte, KFK-2345. Karlsruhe, 1977.
<http://bibliothek.fzk.de/zb/kfk-berichte/KFK2345.pdf>
- [5] P. Hofmann, S. Raff. Verformungsverhalten von Zirkaloy-4-Hüllrohren unter Schutzgas im Temperaturbereich zwischen 600 und 1200°C. Wissenschaftliche Berichte, KFK-3973, Karlsruhe, 1981.
<http://bibliothek.fzk.de/zb/kfk-berichte/KFK3168.pdf>
- [6] L. Schmidt, H. Lehning, D. Piel. Berstversuche an Zirkaloy-Huellrohren unter kombinierter mechanisch-chemischer Beanspruchung (FABIOLA). In: Projekt Nukleare Sicherheit. Jahresbericht 1982. KFK-3350 (Juli 83) S.4200/69-4200/70.
http://quench.forschung.kit.edu/img/fabiola_kfk_1980_1983_schmidt.pdf
- [7] E. H. Karb, M. Prüßmann, L. Sepold, P. Hofmann, G. Schanz. LWR Fuel Rod Behavior in the FR2 In-pile Tests Simulating the Heatup Phase of a LOCA. Final Report. Wissenschaftliche Berichte, KFK-3346, Karlsruhe, 1983.
<http://bibliothek.fzk.de/zb/kfk-berichte/KFK3346.pdf>
- [8] M. E. Markiewicz, F. J. Erbacher. Experiments on Ballooning in Pressurized and Transiently Heated Zirkaloy-4 Tubes. Wissenschaftliche Berichte, KFK-4343, Karlsruhe, 1988.
<http://bibliothek.fzk.de/zb/kfk-berichte/KFK4343.pdf>
- [9] K. Wiehr. REBEKA-Bündelversuche Untersuchungen zur Wechselwirkung zwischen aufblähenden Zirkaloyhüllen und einsetzender Kernnotkühlung. Abschlußbericht. Wissenschaftliche Berichte, KFK-4407, Karlsruhe, 1988.
<http://bibliothek.fzk.de/zb/kfk-berichte/KFK4407.pdf>
- [10] F. J. Erbacher, H. J. Neitzel, K. Wiehr. Cladding Deformation and Emergency Core Cooling of a Pressurized Water Reactor in a LOCA. Summary Description of the REBEKA Program. Wissenschaftliche Berichte, KFK-4781, Karlsruhe, 1990.
<http://bibliothek.fzk.de/zb/kfk-berichte/KFK4781.pdf>
- [11] F. J. Erbacher, S. Leistikow. A Review of Zirkaloy Fuel Cladding Behavior in a Loss-of-Coolant Accident. Wissenschaftliche Berichte, KFK-3973, Karlsruhe, 1985.
<http://bibliothek.fzk.de/zb/kfk-berichte/KFK3973.pdf>
- [12] J.-C. Brachet, V. Vandenberghe-Maillot, L. Portier, D. Gilbon, A. Lesbros, N. Waeckel, and J.-P. Mardon, Hydrogen Content, Preoxidation, and Cooling Scenario Effects on Post-Quench

- Microstructure and Mechanical Properties of Zircaloy-4 and M5[®] Alloys in LOCA Conditions. J. ASTM Intl., Vol. 5, No. 5 (2008). Available online as JAI101116 at www.astm.org.
- [13] T. Chuto, F. Nagase and T. Fuketa. High Temperature Oxidation of Nb-containing Zr Alloy Cladding in LOCA Conditions. Nuclear Engineering and Technology, Vol.41, No.2, March 2009.
- [14] Hee M. Chung. Fuel Behavior under Loss-of-Coolant Accident Situations. Nuclear Engineering and Technology, Vol.37 No.4, August 2005.
- [15] H. Uetsuka, T. Furuta and S. Kawasaki. Zircaloy-4 Cladding Embrittlement due to Inner Surface Oxidation under Simulated Loss-of-Coolant Condition. Journal of Nuclear Science and Technology, 18[9], pp. 705~717 (September 1981).
- [16] M. Billone, Y. Yan, T. Burtseva, R. Daum. Cladding Embrittlement During Postulated Loss-of-Coolant Accidents, NUREG/CR-6967, July 2008.
- [17] OECD SCIP-2 Project: <http://www.oecd-nea.org/jointproj/scip-2.html>
- [18] J. Stuckert, M. Große, C. Rössger, M. Steinbrück, M. Walter. Results of the commissioning bundle test QUENCH-L0 performed under LOCA conditions. KIT Scientific Reports, KIT-SR 7571 (March 2013).
- [19] J. Stuckert, M. Große, C. Rössger, M. Klimenkov, M. Steinbrück, M. Walter. QUENCH-LOCA program at KIT on secondary hydriding and results of the commissioning bundle test QUENCH-L0. Nuclear Engineering and Design, 255(2013), pp. 185-201. DOI:10.1016/j.nucengdes.2012.10.024.
- [20] J. Stuckert, M. Große, C. Rössger, M. Steinbrück, M. Walter. Results of the LOCA reference bundle test QUENCH-L1 with Zircaloy-4 claddings. KIT Scientific Reports, KIT-SR 7651 (2013).
- [21] J. Stuckert, M. Große, C. Rössger, M. Steinbrück, M. Walter. Influence of the temperature history on secondary Hydriding and mechanical properties of zircaloy-4 claddings - An analysis of the QUENCH-LOCA bundle tests. Proceedings of 22nd International Conference on Nuclear Engineering (ICONE 2014); Vol. 3, Paper 30792; July 7-11, 2014, Prague. DOI: 10.1115/ICONE22-30792. <http://proceedings.asmedigitalcollection.asme.org/proceeding.aspx?articleid=1937123>, Presentation: <http://bibliothek.fzk.de/zb/veroeff/96364.pdf>.
- [22] J. Stuckert, M. Große, C. Rössger, M. Steinbrück, M. Walter. Results of the LOCA reference bundle test QUENCH-L2 with M5[®] claddings. KIT Scientific Reports, KIT-SR 7677 (2015).
- [23] M. Grosse, E. Lehmann, P. Vontobel, M. Steinbrueck: "Quantitative determination of absorbed hydrogen in oxidised Zircaloy by means of neutron radiography", Nucl. Instr. & Methods in Phys. Res. A 566 (2006), 739.
- [24] M. Große, G. Kühne, M. Steinbrück, E. Lehmann, P. Vontobel, J. Stuckert. Determination of the hydrogen uptake of steam-oxidised zirconium alloys by means of quantitative analysis of neutron radiographs. J. Phys.: Condens. Matter 20 (2008), 104263.
- [25] M. Grosse, E. Lehmann, M. Steinbrueck, G. Kühne, J. Stuckert. Influence of oxide layer morphology on hydrogen concentration in tin and niobium containing zirconium alloys after high temperature steam oxidation. J. Nucl. Mater. 385 (2009), 339.

- [26] J. Stuckert, J. Birchley, M. Grosse, B. Jaeckel, M. Steinbrück. Experimental and calculation results of the integral reflood test QUENCH-14 with M5 cladding tubes. *Annals of Nuclear Energy*, 37(2010) S.1036-47, DOI:10.1016/j.anucene.2010.04.015.
- [27] M. Grosse, M. Van den Berg, C. Goulet E. Lehmann, B. Schillinger. In-situ neutron radiography investigations of hydrogen diffusion and absorption in zirconium alloys. *Nuclear Instruments and Methods in Physics Research Section A: Accelerators, Spectrometers, Detectors and Associated Equipment*, Volume 651, Issue 1, 21 September 2011, Pages 253–257.
- [28] J. Stuckert, M. Große, M. Walter. Mechanical properties of pre-hydrogenated (600 – 5000 wppm) cladding segments. 16th International QUENCH-Workshop, Karlsruhe, November 2010, ISBN 978-3-923704-74-3.
- [29] C. Eberl, D.S. Gianola, K. J. Hemker. Mechanical Characterization of Coatings Using Microbeam Bending and Digital Image Correlation Techniques. *Experimental Mechanics*, January 2010, Volume 50, Issue 1, pp 85-97.

Tables and Figures

Table 1 QUENCH Test Matrix 1997 – 2014

Test	Quench medium and injection rate	Temp. at onset of flooding or cool-down ¹⁾	Max. ZrO ₂ before transient ²⁾	Max. ZrO ₂ (X s) before flooding ²⁾	Posttest average ZrO ₂ thickness ³⁾	H ₂ production before / during cooldown, g	Remarks, objectives
QUENCH-00 October 9 - 16, 97	Water 80 g/s	≈ 1800 K			completely oxidized		Commissioning tests.
QUENCH-01 February 26, 98	Water 52 g/s	≈ 1830 K	312 μm		500 μm at 913 mm	36 / 3	COBE Project; partial fragmentation of pre-oxidized cladding.
QUENCH-02 July 7, 98	Water 47 g/s	≈ 2400 K			completely oxidized	20 / 140	COBE Project; no additional pre-oxidation; quenching from high temperatures.
QUENCH-03 January 20, 99	Water 40 g/s	≈ 2350 K			completely oxidized	18 / 120	No additional pre-oxidation, quenching from high temperatures.
QUENCH-04 June 30, 99	Steam 50 g/s	≈ 2160 K	82 μm		280 μm	10 / 2	Cool-down behavior of slightly pre-oxidized cladding by cold steam injection.
QUENCH-05 March 29, 2000	Steam 48 g/s	≈ 2020 K	160 μm		420 μm	25 / 2	Cool-down behavior of pre-oxidized cladding by cold steam injection.
QUENCH-06 December 13, 2000	Water 42 g/s	≈ 2060 K	207 μm ⁵⁾	300 μm, (60 s), SVECHA modeling	670 μm ⁴⁾ (60% metal converted to outer ZrO ₂)	32 / 4	OECD-ISP 45; prediction of H ₂ source term by different code systems.
QUENCH-07 July 25, 2001	Steam 15 g/s	≈ 2100 K	230 μm		completely oxidized	66 / 120	COLOSS Project; impact of B ₄ C absorber rod failure on H ₂ , CO, CO ₂ , and CH ₄ generation.
QUENCH-09 July 3, 2002	Steam 49 g/s	≈ 2100 K			completely oxidized	60 / 400	As QUENCH-07, steam-starved conditions prior to cooldown.
QUENCH-08 July 24, 2003	Steam 15 g/s	≈ 2090 K	274 μm		completely oxidized	46 / 38	As QUENCH-07, no absorber rod.
QUENCH-10 July 21, 2004	Water 50 g/s	≈ 2200 K	514 μm	613 μm (at 850 mm)	completely oxidized	48 / 5	LACOMERA Project; Air ingress.

Test	Quench medium and injection rate	Temp. at onset of flooding or cool-down ¹⁾	Max. ZrO ₂ before transient ²⁾	Max. ZrO ₂ (X s) before flooding ²⁾	Posttest average ZrO ₂ thickness ³⁾	H ₂ production before / during cooldown, g	Remarks, objectives
QUENCH-11 Dec. 08, 2005	Water 18 g/s	≈ 2040 K		170 μm	completely oxidized	9 / 132	LACOMERA Project; Boil-off.
QUENCH-12 Sept. 27, 2006	Water 48 g/s	≈ 2100 K	160 μm, breakaway	300 μm, (110 s) breakaway	completely oxidized	34 / 24	ISTC Project No. 1648.2; VVER bundle with E110 claddings.
QUENCH-13 November 7, 2007	Water 52 g/s	≈ 1820 K		400 μm, after AgInCd rod failure	750 μm	42 / 1	SARNET; impact of AgInCd absorber rod failure on aerosol generation.
QUENCH-14 July 2, 2008	Water 41 g/s	≈ 2100 K	170 μm ⁶⁾	470 μm ⁶⁾ , (30 s)	840 μm ⁴⁾ (74% metal converted to outer ZrO ₂)	34 / 6	ACM series: M5 [®] cladding.
QUENCH-15 May 27, 2009	Water 48 g/s	≈ 2100 K	145 μm ⁶⁾	380 μm ⁶⁾ , (30 s)	630 μm ⁴⁾ (70% metal converted to outer ZrO ₂)	41 / 7	ACM series: ZIRLO [™] cladding.
QUENCH-L0 July 22, 2010	Water, 100 g/s	1330 K	1 μm	≈ 18 μm	20 μm (central rod)	0.748/0.3	VGB Project; Commissioning test with Zry-4.
QUENCH-16 July 27, 2011	Water 53 g/s	≈ 1870 K	135 μm	130 μm at 450-950 mm, breakaway	1075 μm at 550-650 mm	16 / 128	LACOMEKO Project; Air ingress.
QUENCH-L1 Feb. 02, 2012	Water, 100 g/s	1373 K	1 μm	≈ 19 μm	22 μm (central rod)	0.718/0.01	VGB Project; Reference test.
QUENCH-17 January 31, 2013	Water 10 g/s	≈ 1800 K		completely oxidized	completely oxidized	110 / 1	SARNET-2; Debris formation and coolability.
QUENCH-L2 July 30, 2013	Water, 100 g/s	1373 K	1 μm	n.a.	13 μm (central rod)	0.4 total	VGB Project; M5 [®] test.
QUENCH-L3HT March 21, 2014	Water, 100 g/s	1623 K	1 μm	n.a.	70 μm (central rod)	1 total	VGB Project; Opt. ZIRLO test.
QUENCH-L4 July 30, 2014	Water, 100 g/s	1385 K	1 μm	n.a.	13 μm (central rod)	0.8 total	VGB Project; M5 [®] test.

¹⁾ Maximum measured bundle temperature at 950 mm elevation.

²⁾ Measured (or calculated for LOCA tests) at the withdrawn corner rod at 950 mm elevation.

³⁾ Measured posttest at the bundle elevation of maximum temperature, i.e. 950 mm. ⁴⁾ Some claddings were completely oxidized at 950 mm elevation.

⁵⁾ Oxide thickness during transient phase.

⁶⁾ Zircaloy-4 corner rods.

Revised: July 2016

Table 2 Design characteristics of the QUENCH-L4 test bundle

Bundle type		PWR
Bundle size		21 heated rods
Effective number of rods	(considering surface of heated rods, shroud and corner rods)	30.6 rods (21 + 7.4 from shroud + 2.2 from corner rods)
Pitch		14.3 mm
Coolant channel area		29.65 cm ²
Hydraulic diameter		11.5 mm
Cladding material		pre-hydrogenated M5 [®] (100 wppm H) in middle part (length 1200 mm), not hydrogenated end parts (643 and 435 mm)
Cladding outside diameter		10.75 mm
Cladding thickness		0.725 mm
Cladding length	(position in the bundle)	2278 mm (between -593 and 1685 mm)
Rod length	(elevations)	2480 mm (-690 to 1790 mm)
Internal rod pressure	(gas)	5.5 MPa abs. (Kr)
Material of middle heater		Tungsten (W)
	surface roughness	Ra=1.6 μm
Tungsten heater length		1024 mm (between 0 and 1024 mm)
Tungsten heater diameter		4.6 mm
Annular pellet	material dimensions surface roughness	ZrO ₂ ;Y ₂ O ₃ -stabilized; grinded ∅ 9.15±0.05/4.75±0.1 mm; L=11 mm Ra=0.3 μm
Pellet stack		0 mm to ~1020 mm
Corner rod (4)	material instrumented (A, C, D) not instrumented (B)	Zircaloy-4 tube ∅ 6x0.9 (bottom: -1140 mm) rod ∅ 6 mm (top: +1300 mm) rod ∅ 6 mm (-1350 to +1155 mm)
Grid spacer	material length sheet thickness elevation of lower edge	Zircaloy-4, Inconel 718 Zircaloy: 42 mm, Inconel: 38 mm 0.5 mm Inconel: -100 mm; Zircaloy: 150, 550, 1050, 1410 mm
Shroud	material wall thickness outside diameter length (extension)	Zirconium 702 (flange: Zry-4) 3.17 mm 86.0 mm 1600 mm (-300 mm to 1300 mm)
Shroud insulation	material insulation thickness elevation	ZrO ₂ fiber 36 mm -300 to 1000 mm
Molybdenum heaters and copper electrodes	length of upper part length of lower part outer diameter: prior to coating after coating with ZrO ₂ coat. surface roughness borehole of low. Cu-electrodes	766 mm (576 Mo, 190 mm Cu) 690 mm (300 Mo, 390 mm Cu) 8.6 mm 9.0 mm Ra=6-12 μm diameter 2 mm, length 96 mm
Cooling jacket	Material: inner/outer tube inner tube outer tube	Inconel 600 (2.4816) / SS (1.4571) ∅ 158.3 / 168.3 mm ∅ 181.7 / 193.7 mm

Table 3 Properties of M5[®] cladding tubesTable 3.1. Chemical composition of M5[®] in weight-% (delivery specification)

Element	Symbol	<i>Measured value</i>
Niobium	Nb	0.99
Oxygen	O	0.14
Sulfur	S	0.0017-0.0025

Table 3.2. Mechanical properties of M5[®] at RT in tension

Element	<i>Measured value</i>
0.2 Yield strength Rp 0.2	384 MPa
Ultimate tensile stress Rm	516 MPa
Elongation at fracture A ₅₀ mm	38%

Table 3.3. Microstructure of M5[®]

Grain size: 5.6 μm	Nr. 12.0 according to ASTM E 112 (acceptable average grain size shall be < Nr. 11, i.e. < 7.9 μm)
Surface Conditions: Roughness (inside): Ra = 0.15 μm (accepted 0.80 μm) Roughness (outside): Ra = 0.32 μm (accepted 0.80 μm)	

Table 4 Main characteristics of the ZrO₂ pellet material, yttria-stabilized (type FZY) *

Property		Data
Density		5.5-5.8 g/cm ³
Open porosity		0
Mean grain size		50 μm
Hardness (Knoop, 100 g)		17000 N/mm ²
Yield strength under compression		2000 N/mm ²
Bending strength		350 N/mm ²
Elastic modulus		165 GPa
Specific heat at 20 °C		400 J/(kg·K)
Thermal conductivity at 100 °C		2.5 W/(m·K)
Linear expansion, 20-1000 °C		10.5 x 10 ⁻⁶ /K
Specific electric resistance	at 20 °C	10 ¹⁰ Ω cm
	at 500 °C	5000 Ω cm
	at 1000 °C	50 Ω cm
*According to FRIATEC, Mannheim		

Table 5 QUENCH-L4; Electrical resistances of rods [$m\Omega$] at 20 °C

Table 5.1. Internal circuit with 9+1 rods

rod	1	2	3	4	5	6	7	8	9	15	Ave- rage	10 rods parallel
pre- test	5.4	5.2	4.7	4.7	4.6	5.0	4.9	4.8	5.1	4.8	4.9	0.49
post- test	12.0	6.0	5.8	5.0	4.9	4.9	4.8	6.5	5.6	6.0	6.1	0.57

Note: Measured values include the resistance of slide contacts $R_s=0.75 m\Omega$

Table 5.2. External circuit with 11 rods

rod	10	11	12	13	14	16	17	18	19	20	21	Ave- rage	11 rods parallel
pre- test	4.8	5.0	5.1	4.9	4.9	4.9	4.9	4.9	5.0	4.9	4.9	4.9	0.45
post- test	5.2	5.5	5.4	5.5	6.2	5.1	6.1	5.7	5.9	5.8	7.4	5.8	0.52

Note: Measured values include the resistance of slide contacts $R_s=0.75 m\Omega$

Each circuit connected to the DC generator with 4 parallel bonded cables. The resistance of each cable is $R_c=1.2 m\Omega$. Therefore, the external (outside) resistance corresponding to each heated rod (indicated by SCDAP/RELAP as fxwid) is $R_{ie}=R_s+10\cdot R_c/4=3.75 m\Omega$ for the inner rod group and $R_{oe}=R_s+11\cdot R_c/4=4.05 m\Omega$ for the outer rod group.

Table 6 Properties of zirconia fiber insulating boards*

Table 6.1. Chemical composition

Oxide	ZrO ₂	Y ₂ O ₃	HfO ₂	TiO ₂	SiO ₂	CaO	MgO	Fe ₂ O ₃	Al ₂ O ₃	Na ₂ O
typical wt%	88	10	2	0.14	0.12	0.09	0.03	0.04	0.01	0.01

Table 6.2. Physical properties

bulk density	porosity	shrinkage		thermal expansion coefficient at 298-1453K	melting point	max. service temperature	flexural strength	compressive strength at 10% compression
		(1 hour at 1925 K)	(24 hours at 1925 K)					
g/cm ³	%	%		1/K	K	K	MPa	MPa
0.48	92	1.2	2.8	10.7*10 ⁻⁶	2866	2500	0.59	0.29

Table 6.3. Thermal conductivity

temperature, K	673	1073	1373	1673	1923
conductivity, W/(m·K)	0.08	0.11	0.14	0.19	0.24

Table 6.4. Specific heat capacity

temperature, K	366	2644
specific heat capacity, J/(kg·K)	544	754

*According to specifications of manufacturer ZIRCAR PRODUCTS on the ZYFB3 material

Table 7 List of instrumentation for the QUENCH-L4 test

Chan	Designation	Instrument, location	Unit
0	P rod 13	Internal pressure of rod #13	bar
1	P rod 14	Internal pressure of rod #14	bar
2	P rod 15	Internal pressure of rod #15	bar
3	P rod 12	Internal pressure of rod #12	bar
4	P rod 03	Internal pressure of rod #03	bar
5	P rod 04	Internal pressure of rod #04	bar
6	P rod 05	Internal pressure of rod #05	bar
7	P rod 16	Internal pressure of rod #16	bar
8	P rod 11	Internal pressure of rod #11	bar
9	P rod 02	Internal pressure of rod #02	bar
10	P rod 01	Internal pressure of rod #01	bar
11	P rod 06	Internal pressure of rod #06	bar
12	P rod 17	Internal pressure of rod #17	bar
13	P rod 10	Internal pressure of rod #10	bar
14	P rod 09	Internal pressure of rod #09	bar
15	P rod 08	Internal pressure of rod #08	bar
16	P rod 07	Internal pressure of rod #07	bar
17	P rod 18	Internal pressure of rod #18	bar
18	P rod 21	Internal pressure of rod #21	bar
19	P rod 19	Internal pressure of rod #19	bar
20	P rod 20	Internal pressure of rod #20	bar
21..31		20 mA, Reserve	
32..34		TC (W/Re), Reserve	
35	TSH 15/0	TC (NiCr/Ni), shroud outer surface, 1150 mm, 21°, feed cable outside of shroud insulation.	K
36	TSH 14/270	TC (NiCr/Ni), shroud outer surface, 1050 mm, 289°, feed cable outside of shroud insulation.	K

Chan	Designation	Instrument, location	Unit
37		TC (W/Re), Reserve	K
38	TFS 15/13	TC (NiCr/Ni), surface of fuel rod simulator 15, group 5, 950 mm	K
39	TFS 19/12	TC (NiCr/Ni), surface of fuel rod simulator 19, group 5, 850 mm	K
40..41		TC (W/Re), Reserve	
42	TFS 7/12	TC (NiCr/Ni), surface of fuel rod simulator 7, group 3, 850 mm	K
43	TFS 15/12	TC (NiCr/Ni), surface of fuel rod simulator 15, group 5, 850 mm	K
44	TFS 2/12	TC (NiCr/Ni), surface of fuel rod simulator 2, group 2, 850 mm	K
45	TFS 4/12	TC (NiCr/Ni), surface of fuel rod simulator 4, group 2, 850 mm	K
46	TFS 19/13	TC (NiCr/Ni), surface of fuel rod simulator 19, group 5, 950 mm	K
47..57		TC (W/Re), Reserve	K
58	TFS 7/10	TC (NiCr/Ni), surface of fuel rod simulator 7, group 3, 650 mm	K
59..60		TC (W/Re), Reserve	K
61	TFS 11/12	TC (NiCr/Ni), surface of fuel rod simulator 11, group 4, 850 mm	K
62	P 206	Reserve	
63	F 206	Reserve	
64	T 402 b	TC (NiCr/Ni), Ar super heater	K
65..67		TC (W/Re), Reserve	
68	T 512	TC (NiCr/Ni), gas temperature at 1360 mm (bundle outlet) between rod #20 and shroud	K
69..70		TC (W/Re), Reserve	K
71	<i>Ref. T01</i>	<i>Temperature of measuring crate 1 (reference temperature)</i>	K
72	TFS 11/13	TC (NiCr/Ni) surface of fuel rod simulator 11, group 4, 950 mm	K
73	TFS 7/13	TC (NiCr/Ni), surface of fuel rod simulator 7, group 3, 950 mm	K
74	TFS 2/13	TC (NiCr/Ni), surface of fuel rod simulator 2, group 2, 950 mm	K
75	TFS 4/13	TC (NiCr/Ni), surface of fuel rod simulator 4, group 2, 950 mm	K
76	TFS 15/11	TC (NiCr/Ni), surface of fuel rod simulator 15, group 5, 750 mm	K
77	TFS 19/11	TC (NiCr/Ni), surface of fuel rod simulator 19, group 5, 750 mm	K
78	TFS 11/11	TC (NiCr/Ni) surface of fuel rod simulator 11, group 4, 750 mm	K

Chan	Designation	Instrument, location	Unit
79	TFS 7/11	TC (NiCr/Ni), surface of fuel rod simulator 7, group 3, 750 mm	K
80	TFS 2/11	TC (NiCr/Ni) surface of fuel rod simulator 2 group 2, 750 mm	K
81	TSH 12/90	TC (NiCr/Ni), shroud outer surface, 850 mm, 109°	K
82	TFS 2/10	TC (NiCr/Ni); surface of fuel rod simulator 2, group 2, 650 mm	K
83	TSH 10/270	TC (NiCr/Ni), shroud outer surface, 650 mm, 289°	K
84	TSH 9/180	TC (NiCr/Ni), shroud outer surface, 550 mm, 191°	K
85	TSH 8/90	TC (NiCr/Ni), shroud outer surface, 450 mm, 109°	K
86	TSH 7/0	TC (NiCr/Ni), shroud outer surface, 350 mm, 11°	K
87	TSH 6/270	TC (NiCr/Ni) shroud outer surface, 250 mm, 281°	K
88	TSH 5/180	TC (NiCr/Ni), shroud outer surface, 150 mm, 191°	K
89	TSH 4/90	TC (NiCr/Ni), shroud outer surface, 50 mm, 109°	K
90	TSH 11/0	TC (NiCr/Ni), shroud outer surface, 750 mm, 11°	K
91	TCI 9/270	TC (NiCr/Ni), cooling jacket inner tube wall, 550 mm, 270°	K
92	TCI 10/270	TC (NiCr/Ni), cooling jacket inner tube wall, 650 mm, 270°	K
93	TCI 11/270	TC (NiCr/Ni), cooling jacket inner tube wall, 750 mm, 270°	K
94	TCI 13/270	TC (NiCr/Ni), cooling jacket inner tube wall, 950 mm, 270°	K
95	TFS 4/11	TC (NiCr/Ni), surface of fuel rod simulator 4, group 2, 750 mm	K
96	TFS 15/10	TC (NiCr/Ni), surface of fuel rod simulator 15, group 5, 650 mm	K
97	TFS 19/10	TC (NiCr/Ni), surface of fuel rod simulator 19, group 5, 650 mm	K
98	TFS 11/10	TC (NiCr/Ni), surface of fuel rod simulator 11, group 4, 650 mm	K
99	TSH 13/180	TC (NiCr/Ni), shroud outer surface, 950 mm, 191°, feed cable outside of shroud insulation.	K
100	TSH 3/0	TC (NiCr/Ni), shroud outer surface, -50 mm, 11°	K
101	TFS 4/10	TC (NiCr/Ni), surface of fuel rod simulator 4, group 2, 650 mm	K
102	TFS 15/14	TC (NiCr/Ni), surface of fuel rod simulator 15, group 5, 1050 mm	K
103	TFS 19/14	TC (NiCr/Ni), surface of fuel rod simulator 19, group 5, 1050 mm	K
104	TFS 11/14	TC (NiCr/Ni), surface of fuel rod simulator 11, group 4, 1050 mm	K
105	TFS 7/14	TC (NiCr/Ni), surface of fuel rod simulator 7, group 3, 1050 mm	K

Chan	Designation	Instrument, location	Unit
106	TFS 2/14	TC (NiCr/Ni), surface of fuel rod simulator 2, group 2, 1050 mm	K
107	TFS 4/14	TC (NiCr/Ni), surface of fuel rod simulator 4, group 2, 1050 mm	K
108	TFS 15/9	TC (NiCr/Ni), surface of fuel rod simulator 15, group 5, 550 mm	K
109	TFS 11/9	TC (NiCr/Ni), surface of fuel rod simulator 11, group 4, 550 mm	K
110	TFS 7/9	TC (NiCr/Ni), surface of fuel rod simulator 7, group 3, 550 mm	K
111	TFS 4/9	TC (NiCr/Ni), surface of fuel rod simulator 4, group 2, 550 mm	K
112	TFS 15/15	TC (NiCr/Ni), surface of fuel rod simulator 15, group 5, 1150 mm	K
113	TFS 19/15	TC (NiCr/Ni), surface of fuel rod simulator 19, group 5, 1150 mm	K
114	TFS 11/15	TC (NiCr/Ni), surface of fuel rod simulator 11, group 4, 1150 mm	K
115	TFS 7/15	TC (NiCr/Ni), surface of fuel rod simulator 7, group 3, 1150 mm	K
116	TFS 2/15	TC (NiCr/Ni), surface of fuel rod simulator 2, group 2, 1150 mm	K
117	TFS 4/15	TC (NiCr/Ni), surface of fuel rod simulator 4, group 2, 1150 mm	K
118	TFS 11/8	TC (NiCr/Ni), surface of fuel rod simulator 11, group 4, 450 mm	K
119	TFS 7/8	TC (NiCr/Ni), surface of fuel rod simulator 7, group 3, 450 mm	K
120	TFS 4/8	TC (NiCr/Ni), surface of fuel rod simulator 4 group 2, 450 mm	K
121	TFS 11/16	TC (NiCr/Ni), surface of fuel rod simulator 11, group 4, 1250 mm	K
122	TFS 7/16	TC (NiCr/Ni), surface of fuel rod simulator 7, group 3, 1250 mm	K
123	T 601	Temperature off-gas, 2660 mm from test section outlet (flange)	K
124	TFS 11/7	TC (NiCr/Ni), surface of fuel rod simulator 11, group 4, 350 mm	K
125	TFS 7/12i	TC (NiCr/Ni), surface of fuel rod simulator 7, group 3, 850 mm, near to rod #1	K
126	TFS 7/7	TC (NiCr/Ni), surface of fuel rod simulator 7, group 3, 350 mm	K
127	TFS 4/7	TC (NiCr/Ni), surface of fuel rod simulator 4, group 2, 350 mm	K
128	T 104	Temperature quench water	K
129	T 201	Temperature steam generator heating pipe	K
130	TIT C/12	TC (NiCr/Ni), center line of corner rod C, 850 mm	K
131	T 205	Temperature upstream steam flow instrument location 10 g/s	K
132	T 301A	Temperature downstream superheater	K

Chan	Designation	Instrument, location	Unit
133	T 302	Temperature superheater heating pipe	K
134	T 303	Temperature upstream total flow instrument location	K
135	T 401	Temperature upstream Ar flow instrument (orifice) location	K
136	T 403	Temperature of Ar at inlet cooling jacket	K
137	T 404	Temperature of Ar at outlet cooling jacket	K
138	T 501	Temperature in containment (near from bundle head)	K
139	TFS 7/6	TC (NiCr/Ni), surface of fuel rod simulator 7, group 3, 250 mm	K
140	TFS 4/6	TC (NiCr/Ni), surface of fuel rod simulator 4, group 2, 250 mm	K
141	TFS 7/17	TC (NiCr/Ni), surface of fuel rod simulator 7, group 3, 1350 mm	K
142	TFS 7/5	TC (NiCr/Ni), surface of fuel rod simulator 7, group 3, 150 mm	K
143	TFS 7/4	TC (NiCr/Ni), surface of fuel rod simulator 7, group 3, 50 mm	K
144	TFS 7/3	TC (NiCr/Ni), surface of fuel rod simulator 7, group 3, -50 mm	K
145	TFS 7/2	TC (NiCr/Ni), surface of fuel rod simulator 7, group 3, -150 mm	K
146	TFS 7/1	TC (NiCr/Ni), surface of fuel rod simulator 7, group 3, -250 mm	K
147	TFS 7/13i	TC (NiCr/Ni), surface of fuel rod simulator 7, group 3, 950 mm, near to rod #1	K
148	T 511	Gas temperature at bundle inlet	K
149	TIT D/11	TC (NiCr/Ni), center line of corner rod D, 750 mm	K
150	TIT A/13	TC (NiCr/Ni), center line of corner rod A, 950 mm	K
151	<i>Ref. T02</i>	<i>Temperature of measuring crate 2 (reference temperature)</i>	K
152	P 201	Pressure steam generator	bar
153	P 204	Pressure at steam flow instrument location 50 g/s	bar
154	P 205	Pressure at steam flow instrument location 10 g/s	bar
155	P 303	Pressure upstream total flow instrument (orifice) location	bar
156	P 401	Pressure upstream gas flow instrument location	bar
157	P 511	Pressure at bundle inlet, L501 low leg	bar
158	P 512	Pressure at bundle outlet	bar
159	P 601	Pressure upstream off-gas flow instrument (orifice) F 601	bar

Chan	Designation	Instrument, location	Unit
160	P 901	Pressure at bundle inlet, L501 upper leg	bar
161	L 201	Liquid level steam generator	mm
162	L 501	Liquid level quench water	mm
163	L 701	Liquid level condensation vessel	mm
164	Fm 401	Argon (carrier gas) mass flow rate (Bronkhorst device)	g/s
165	P 411	Reserve (Pressure Kr supply for heated rods)	bar
166	P 403	Pressure Ar cooling of cooling jacket	bar
167	P 406	Pressure insulation shroud/cooling jacket	bar
168	Fm 104	Flow rate quench water	g/s
169	Fm 204	Flow rate steam (flow control up to 50 g/s)	g/s
170	Fm 205	Flow rate steam (flow control up to 10 g/s)	g/s
171	F 303	Flow rate at bundle inlet (steam + argon), orifice	mbar
172	F 401	Argon (carrier gas) volumetric flow rate	Nm ³ /h
173	Fm 403	Mass flow rate of cooling gas (Ar)	g/s
174	F 601	Flow rate off-gas (orifice), 2000 mm from test section outlet (flange)	mbar
175	Fm 406	Flow rate argon into room between shroud and cooling jacket	g/s
176	E 201	Electric current steam generator	A
177	E 301	Electric current superheater	A
178	E 501	Electric current of left group of fuel rod simulators	A
179	E 502	Electric current of right group of fuel rod simulators	A
180	E 503	Electric voltage of left group of fuel rod simulators	V
181	E 504	Electric voltage of right group of fuel rod simulators	V
182	Hub_V302	Gas supply valve lift	%
183	<i>Ref. T03</i>	<i>Temperature of buffer amplifier (reference temperature)</i>	K
184..... 199		Binary inputs	
200.....		Analog outputs	

Chan	Designation	Instrument, location	Unit
215			
250	E 505	Electric power inner ring of fuel rod simulators	W
251	E 506	Electric power outer ring of fuel rod simulators	W
252	EP	Gross electrical power	kW

Indications:

TFS - TC at the rod surface;

TIT - TC at the inside of corner rods;

TSH - TC at outer surface of shroud.

Groups of the rods for modeling:

central groups

group 1: rod 1;

group 2: rods 2, 4, 6, 8;

group 3: rods 3, 5, 7, 9;

peripheral groups

group 4: rods 11, 14, 17, 20;

group 5: rods 10, 12, 13, 15, 16, 18, 19, 21.

Table 8 QUENCH-L4; Rod thermocouple positions

Elevation, mm	-250	-150	-50	50	150	250	350	450	550	650	750	850	950	1050	1150	1250	1350
Rod/Elevation	1	2	3	4	5	6	7	8	9	10	11	12	13	14	15	16	17
1																	
2										X	X	X	X	X	X		
3																	
4						X	X	X	X	X	X	X	X	X	X		
5																	
6																	
7	X	X	X	X	X	X	X	X	X	X	X	X, Xi	X, Xi	X	X	X	X
8																	
9																	
10																	
11							X	X	X	X	X	X	X	X	X	X	
12																	
13																	
14																	
15									X	X	X	X	X	X	X		
16																	
17																	
18																	
19										X	X	X	X	X	X		
20																	
21																	

Number per elevation 1 1 1 1 1 2 3 3 4 6 6 6+1 6+1 6 6 2 2

TFS (rod surface, shroud direction), indicated as X in table above	56
TFS (rod surface, central rod direction), indicated as Xi in table above	2
TIT (inside corner rods)	3
TSH (outer shroud surface)	13



Table 9 QUENCH-L4; Sequence of events

Time [s]	Event
-1918 (10:29:52; 30.07.2014)	Start data recording, $T_{max} = TFS\ 7/13i = 822\ K$, el. power at 3.56 kW. L701 = 948 mm. L 501 = -399 mm. System pressure 3 bar. Hot Ar 6 g/s (heated in superheater), superheated steam 2 g/s.
-1918... -175	Pressurization of rods from 30 to 55 bar.
0	Start of transient with max electrical power increase rate.
4; 20; 47; 83	Electrical power 42.4; 55; 60; 58.8 kW.
40...55	Sequential onset of ballooning from inner rod #1 to peripheral rod #10.
48...65	Sequential onset of burst for rods from inner rod #1 to peripheral rod #10. See burst table (Table 10).
83	Reduction of the electrical power from max 58.8 kW to decay heat of 3.5 kW. Initiation of rapid steam supply line (20 g/s) additionally to carrier argon (6 g/s). Switch-off of slow steam supply (2 g/s). $T_{max} = TFS\ 7/13i = 1352\ K$.
88	Cladding surface temperature maximum reached. Maximal hydrogen production rate. $T_{max} = TFS\ 7/13i = 1385\ K$.
88...215	Cool-down of bundle in steam. Decrease of TFS 7/12i reading from 1385 K to 978 K.
215...221	Increase of maximal bundle temperatures to TFS 3/13i $\approx 1015\ K$ due to switch-off of the steam cooling (closing of gas inlet valve at 216 s).
221	Initiation of quench water supply. Switch of argon to bundle top supply.
257	Maximal quench rate (about 100 g/s) reached.
248...298	Wetting of cladding surface thermocouples (TFS) at elevations between -250 and 1350 mm at temperatures between 511 (TFS 7/1; -250 mm) and 826 K (TFS 4/14; 1050 mm). (Table 16).
276...316	Maximal water evaporation rate (about 25 g/s). Collapsed water front at 350..... 1020 mm.
373	Bundle completely filled with water (L 501 = 1307 mm).
545	Electrical power switched off. $T_{max} = TFS\ 15/15 = 321\ K$.
682	End of data recording.

Table 10 QUENCH-L4; Burst parameters

rod	burst time, s	interpolated burst T, K	burst azimuth. position, °	burst middle elev., mm	max burst width, mm	burst length, mm	burst area, mm ²
1	48	1086	123	920	3.0	11	20
2	55	1121	165	953	3.1	12	21
3	50	1106	125	939	3.3	13	25
4	50**		190**	913 (balloon)/ -14**			
5	48	1101	162	928	3.3	12	24
6	50	1108	178	931	3.1	11	20
7	48	1100*	210	926	4.0	16	34
8	53	1125	156	932	3.2	12	21
9	52	1119	117	947	3.4	13	26
10	65	1072	90	910	3.4	16	26
11	62	1067	40	926	3.0	12	20
12	64	1132	134	916	2.4	12	16
13	63	1151	130	928	2.7	12	18
14	62	1149	163	913	4.5	18	40
15	53	1074	205	899	2.8	13	18
16	65	1137	195	832	2.8	13	20
17	67**		234(balloon)/ 290**	926(balloon)/ -8**			
18	65	1137	353	942	4.1	14	34
19	58	1082	329	937	2.6	11	17
20	64	1096	189	934	4.8	16	39
21	62	1077	81	891	2.7	12	19
average		1107 ± 27		921 ± 27	3.3 ± 0.7	13.1 ± 1.9	24.1 ± 7.4

*direct measurement with TFS 7/13i

**burst at position of connection between W and Mo heater parts

Table 11 Burst time and temperature of all rods for the experiments: QL2 (left and QL4 (right).

Rod group	Rod #	Burst time, s	Burst temperature, interpolated, K
Inner rods	1	50	1135
	2	53	1167
	3	53	1168
	4	52	1167
	5	53	1163
	6	50	1121
	7	53	1136
	8	48	1113
	9	53	1162
Outer rods	10	66	1125
	11	65	1145
	12	68	1195 (Max)
	13	67	1178
	14	66	1167
	15	58	1124
	16	64	1143
	17	62	1102
	18	65	1139
	19	67	1093
	20	63	1110
	21	66	1050 (Min)

QL2: average burst T: 1138 ± 34 K = 865 ± 34 °C

Rod group	Rod #	Burst time, s	Burst temperature, interpolated, K
Inner rods	1	48	1086
	2	55	1121
	3	50	1106
	4	50	
	5	48	1101
	6	50	1108
	7	48	1100
	8	53	1125
	9	52	1119
Outer rods	10	65	1072
	11	62	1067 (Min)
	12	64	1132
	13	63	1151 (Max)
	14	62	1149
	15	53	1074
	16	65	1137
	17	67	
	18	65	1137
	19	58	1082
	20	64	1096
	21	62	1077

QL4: average burst T: 1107 ± 27 K = 834 ± 27 °C

Table 12 Burst geometrical parameters : QL2 (left) and QL4 (right).

rod	max burst width, mm	burst length, mm	burst area, mm ²
1	3.4	14	29
2	2.9	11	20
3	2.5	10	15
4	2.9	11,5	21
5	3.0	11,5	21
6	2.6	11	17
7	3.1	12	23
8	3.3	12	24
9	1.7	11	12
10	6.6	22	85
11	2.8	12	21
12	2.5	11	19
13	2.4	10	15
14	3.1	12	23
15	2.4	13	25
16	3.4	13	27
17	3.9	20	66
18	3.3	12	24
19	1.8	11	12
20	5.5	24	94
21	1.5	15	16

QL2 average sizes of burst openings: **width 3.1 ± 1.2 mm;**
length 13.5 ± 4.0 mm; area: 29.0 ± 22.9 mm²

rod	max burst width, mm	burst length, mm	burst area, mm ²
1	3.0	11	20
2	3.1	12	21
3	3.3	13	25
4			
5	3.3	12	24
6	3.1	11	20
7	4.0	16	34
8	3.2	12	21
9	3.4	13	26
10	3.4	16	26
11	3.0	12	20
12	2.4	12	16
13	2.7	12	18
14	4.5	18	40
15	2.8	13	18
16	2.8	13	20
17			
18	4.1	14	34
19	2.6	11	17
20	4.8	16	39
21	2.7	12	19

QL4 average sizes of burst openings: **width 3.3 ± 0.7 mm;**
length 13.1 ± 1.9 mm; area: 24.1 ± 7.4 mm²

)

Table 13 QUENCH-L4; Content of hydrogen absorbed by secondary hydrogenation (post-tensile n0- tomography): axial maximum averaged for cross section and axial absolute local maximum

rod #	C _H above burst opening (H-band), wppm		elevation, mm		C _H below burst opening (H-spot), wppm		elevation, mm	
	averaged	absolute	aver.	abs.	averaged	absolute	aver.	abs.
1	640±20	1720±100	943	940	434±20	1740±90	905	905
2						800±100		940
3	165±20	900±100	915-960	915-960	165±20	900±100	915-960	915-960
5						760±100		915
6	273±15	1330±100	943	943	358±20	1750±90	898	908
7		780±100		946				
8						730±100		916
9	371±15	1490±100	968	966	360±15	1740±80	926	930
10	236±15	1150±100	939	940	n. a.	n. a.		
14	230±15	1340±100	935-968	938	n. a.	n. a.		

Table 14 QUENCH-L4: average hydrogen content in hydrogen bands (results of hot extraction with LECO TCH600 device, cladding segments with h=11 mm, d=5 mm)

rod #	position of sample in cladding	hydrogen content, wppm	measurement deviation, wppm
1	929-940 mm, 123°	580	±112
2	937-948 mm, 165°	561	±156
7	960-971 mm, 30°	572	±102

Table 15 QUENCH-L4: average hydrogen content in the vicinity of burst openings (hot extraction with LECO TCH600 device, cladding segments with h=11 mm, d=5 mm)

rod #	position of sample in cladding	hydrogen content, wppm	measurement deviation, wppm
1	929-940 mm, 303°	256	±27
2	937-948 mm, 345°	196	±9
7	960-971 mm, 210°	178	±19

Table 16 QUENCH-L4; Wetting of TFS thermocouples

Bundle elevation, mm	Wetting time, s	Collapsed water front on wetting, mm
-250	248	-250
-150	250	-250
-50	250	-250
50	259	5
150	260	46
250	262	85
350	263	102
450	264..267	160
550	264..270	160..285
650	264..270	160..285
750	264..275	160..330
850	264..280	160..400
950	291..296	560..695
1050	273...288	316..520
1150	287..297	520..530
1250	278..298	360..530
1350	266*	160

* Condensation of stagnant steam inside the bundle head due to injection of cold Argon.

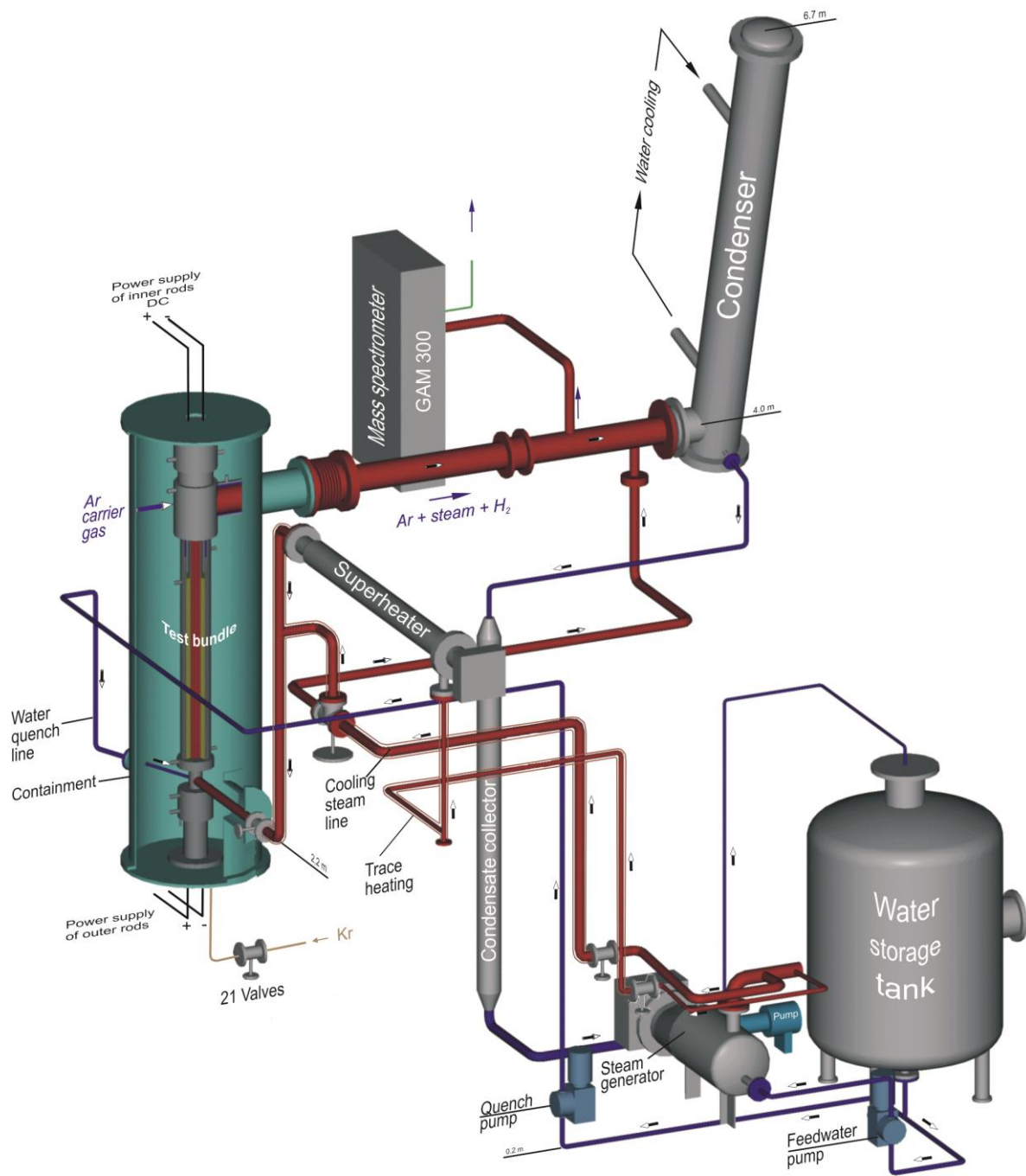
Table 17 QUENCH-L4; Strain parameters

rod group	rod #	elevation of burst middle, mm	max circum. strain, %	max D mm	at azimuth °	min D mm	at azimuth °
central group	1	920	21	13.87	111	12.31	35
	2	954	21.5	14.20	154	12.22	244
	3	940	21	13.88	138	12.19	36
	4*	-14/913(balloon)	37/5	15	191	13.6	101
	5	930	23	14.12	175	12.40	260
	6	931	21.7	14.04	192	12.30	278
	7	926	22.4	14.13	227	12.30	126
	8	933	23	14.28	135	12.46	55
	9	947	23.8	14.32	100	12.52	24
peripheral group	10	911	20	14.00	81	12.1	176
	11	927	18.9	13.75	57	12.00	142
	12	917	17.6	13.54	130	11.95	52
	13	928	18.4	13.63	146	12.02	48
	14	913	23.5	14.40	180	12.32	257
	15	897	17.5	13.57	208	12.00	289
	16	832	19.6	14.00	217	12.10	302
	17*	-8/928(balloon)	35/11.5	15	290	14	202
	18	942	27.5	14.80	337	12.70	257
	19	936	19.1	13.74	341	12.11	60
	20	935	29.9	15.08	165	13.10	85
	21	891	18.60	13.81	73	12.00	170
average		922±27	21.47±3.24	14.15±0.47		12.41±0.54	

*- burst at position of connection between W and Mo heater parts - outside of the hottest region

Table 18 QUENCH-L4; Results of tensile tests

rod l ₀ =800 mm	ultimate tensile strength [MPa]	fracture stress [MPa]	elongation at fracture (graded) [%]	rupture based on
01	522	522	5.7	<i>H-spot</i>
02	516	393	9.7	fracture after necking
03	521	404	7.4	fracture after necking
04				-
05	523	425	8.7	fracture after necking
06	495	495	2.5	<i>H-spot</i>
07	522	407	8.5	fracture after necking
08	518	401	10.3	fracture after necking
09	514	514	5.6	<i>H-spot</i>
10	488	486	4.0	stress concentration at opening tips
11	525	524	5.7	stress concentration at opening tips
12	513	513	6.8	stress concentration at opening tips
13	517	516	9.2	stress concentration at opening tips
14	511	510	6.0	stress concentration at opening tips
15	516	516	6.1	stress concentration at opening tips
16	519	414	10.4	fracture after necking
17				-
18	520	391	13.8	fracture after necking
19	519	377	9.1	fracture after necking
20	516	515	5.6	stress concentration at opening tips
21	506	505	5.3	stress concentration at opening tips
QL4 aver.	520 ± 2	402 ± 15	9.7 ± 1.9	fracture after necking
QL2 aver	507 ± 9	384 ± 33	11.2 ± 4.2	fracture after necking
QL4 aver.	512 ± 11	511 ± 11	6.1 ± 1.5	stress concentration at opening tips
QL2 aver	496 ± 17	454 ± 64	7.8 ± 3.4	stress concentration at opening tips



lage.cdr

Figure 1 QUENCH Facility - Main components.

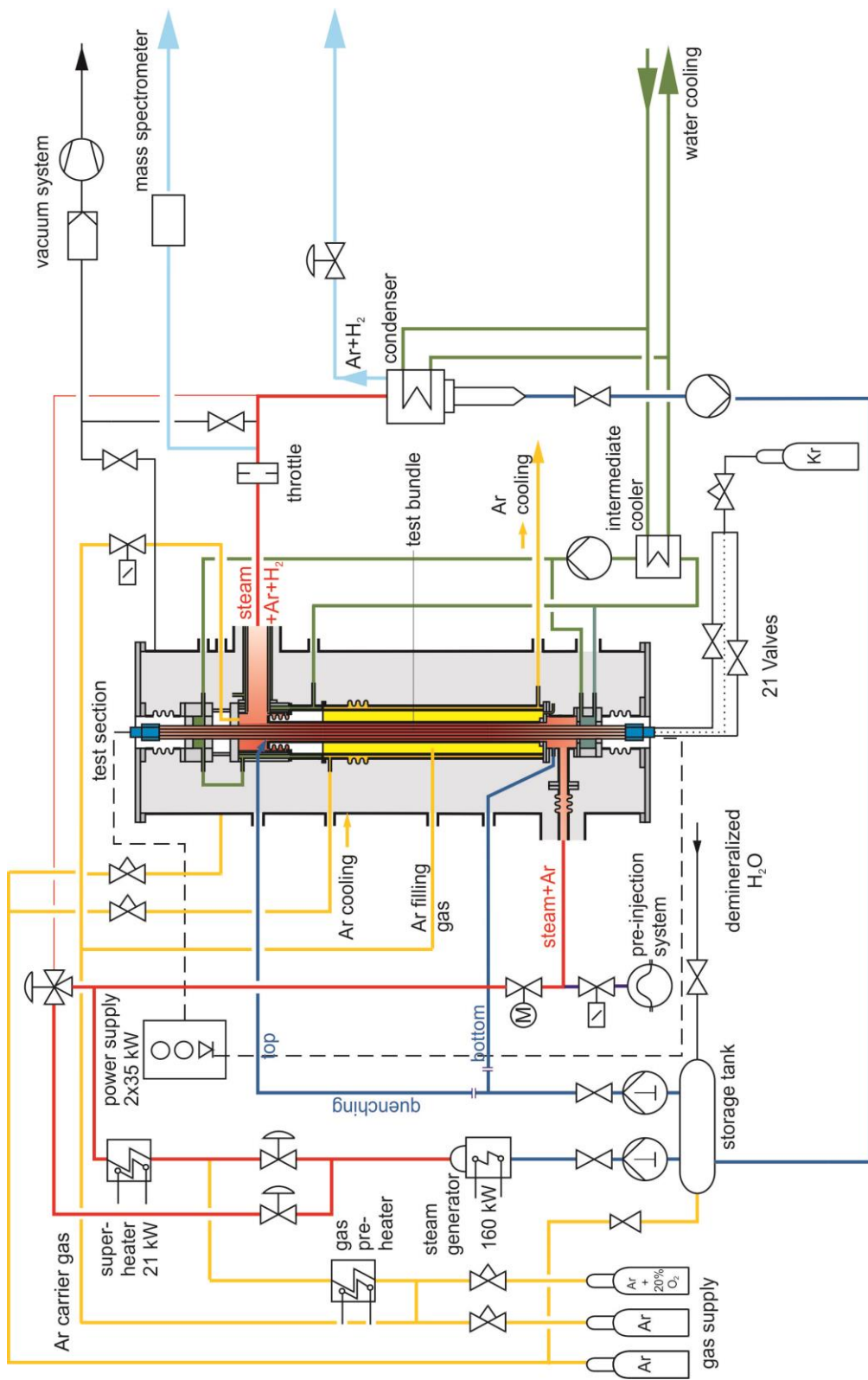


Figure 2 Flow diagram of the QUENCH test facility.

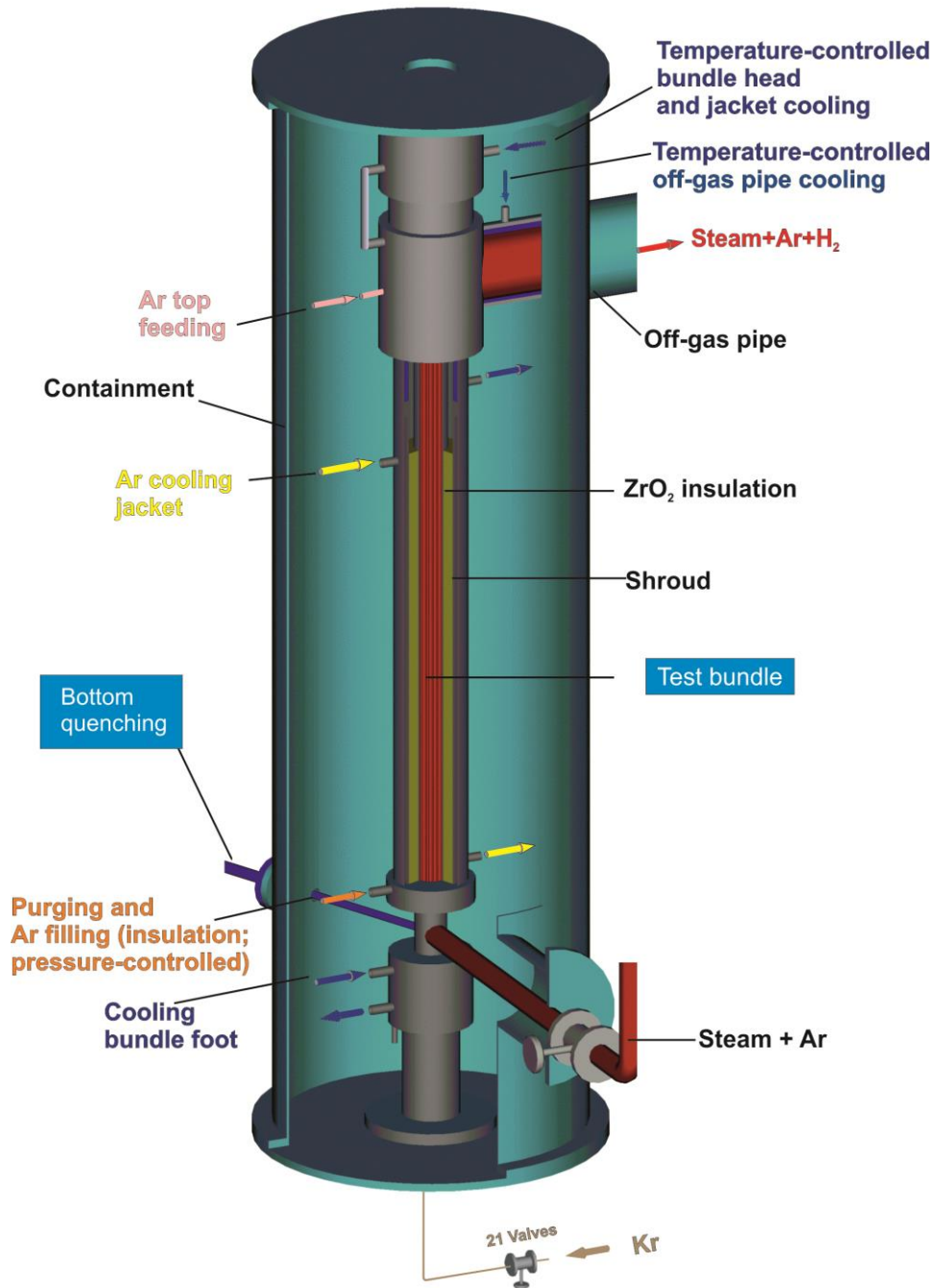


Figure 3 QUENCH Facility; Containment and test section.

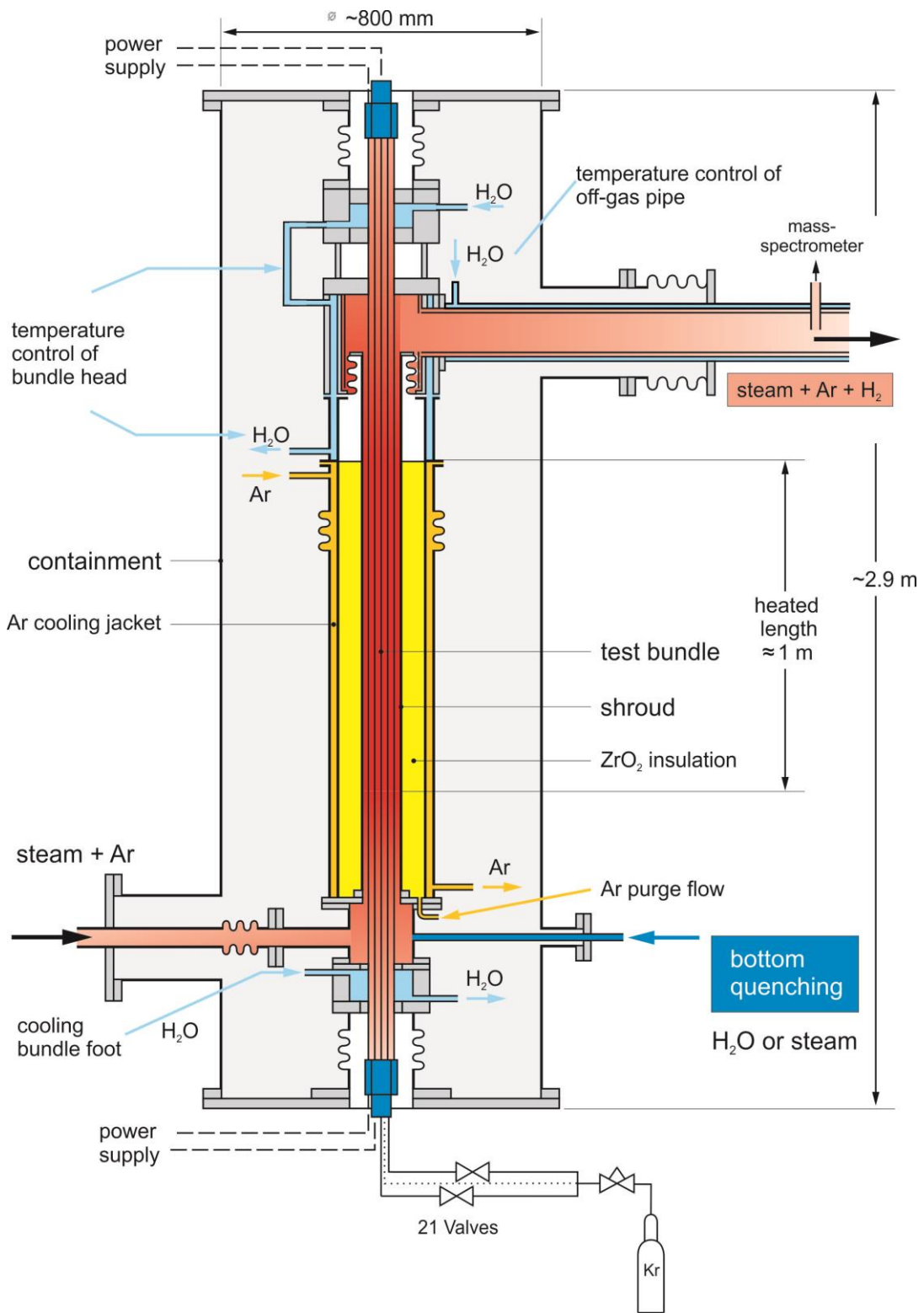


Figure 4 QUENCH-L4; Test section with flow lines.

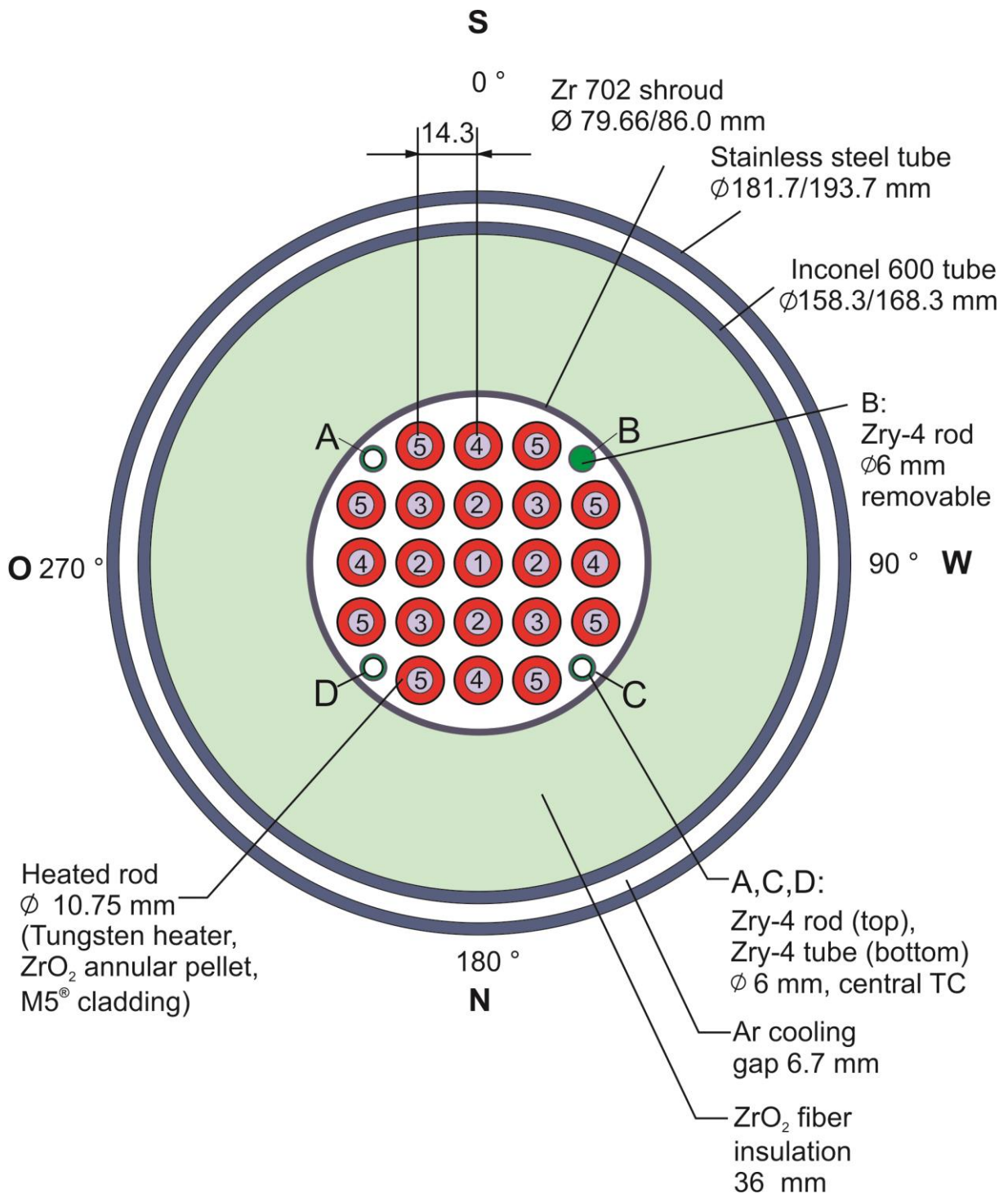


Figure 5 QUENCH-L4; Fuel rod simulator bundle (cross section, top view) including rod type indications corresponding to table “List of Instrumentation”.

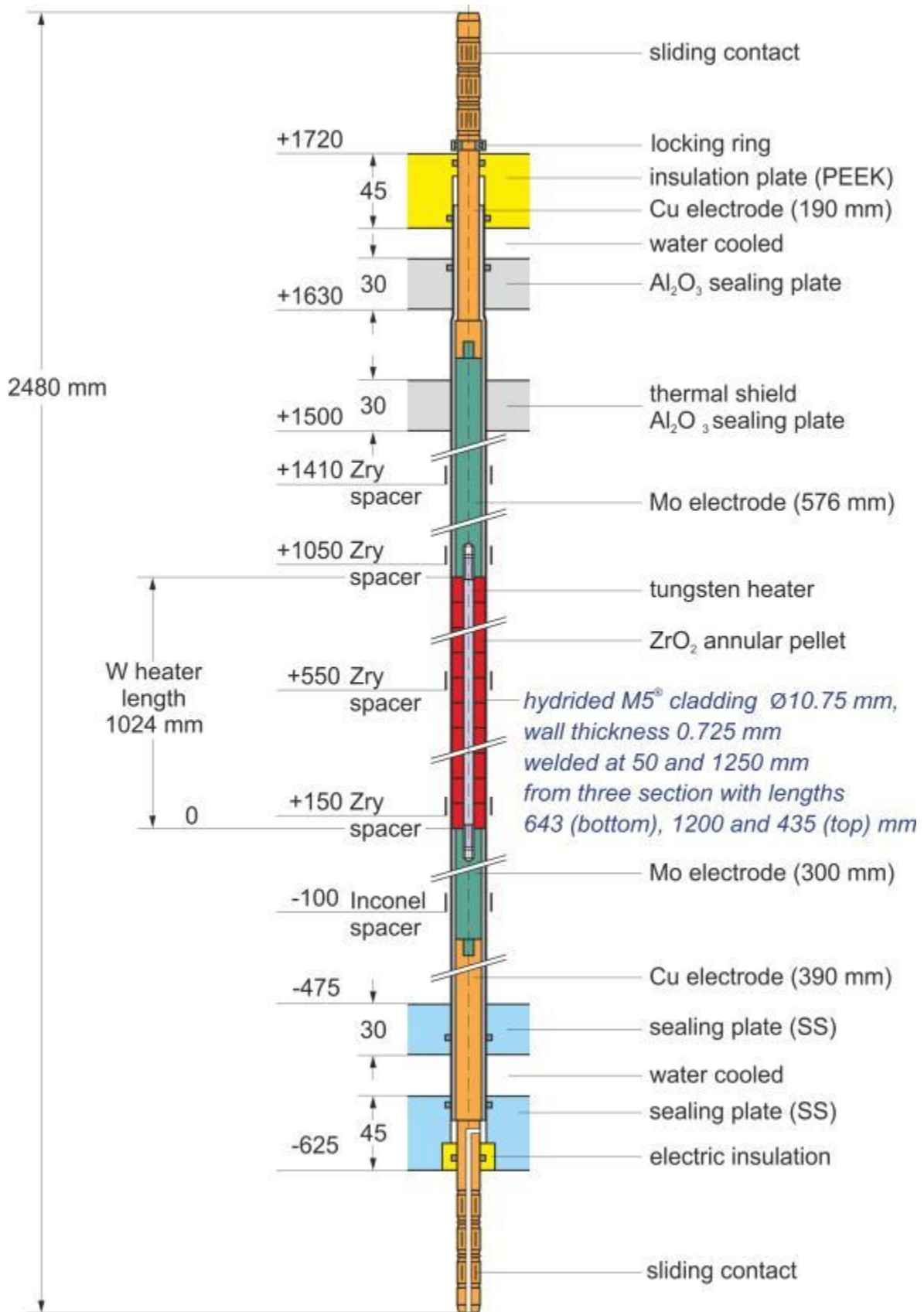


Figure 6 QUENCH-L4; Heated fuel rod simulator.

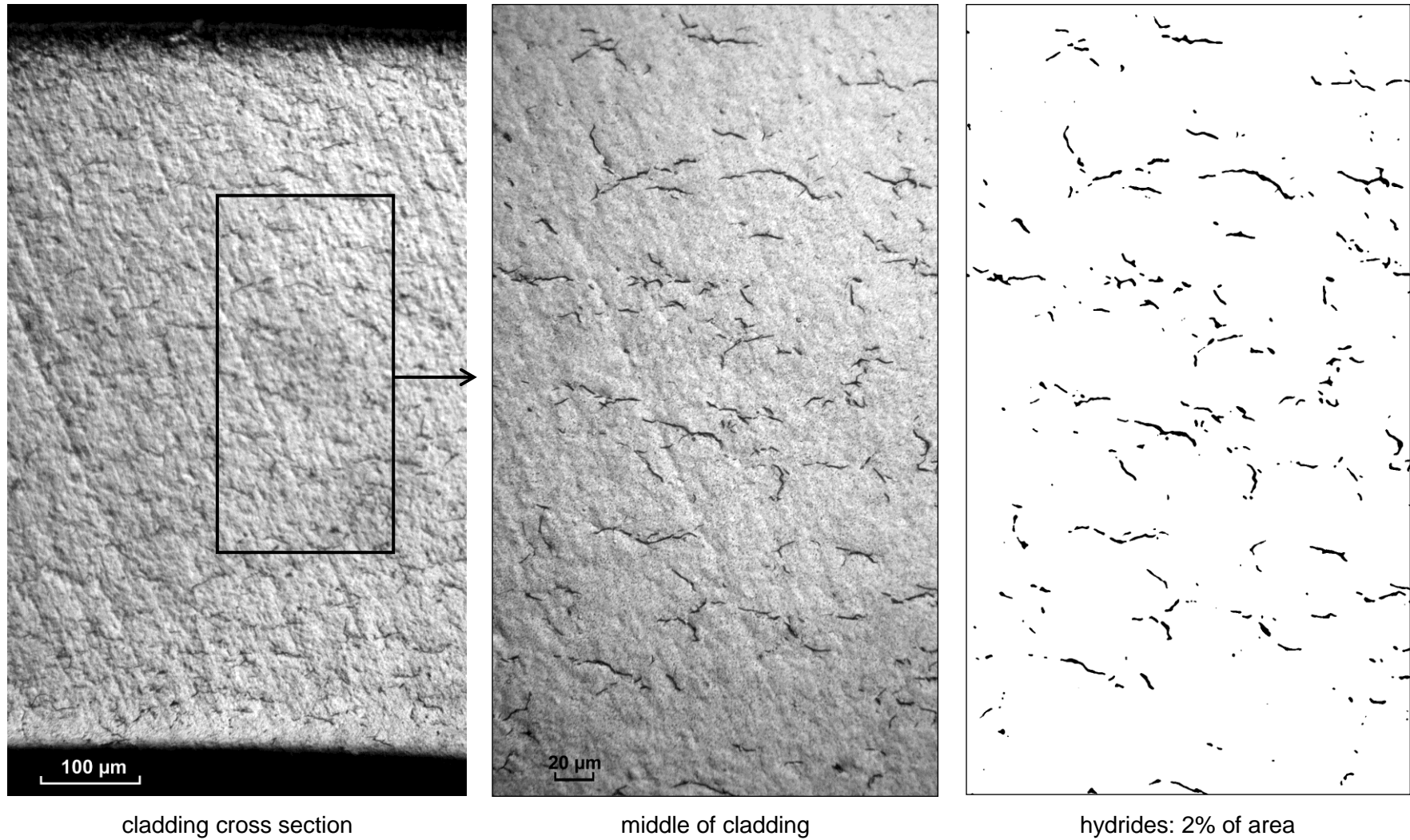


Figure 7 QUENCH-L4; Hydrides inside the prototype cladding with 100 wppm H (as etched).

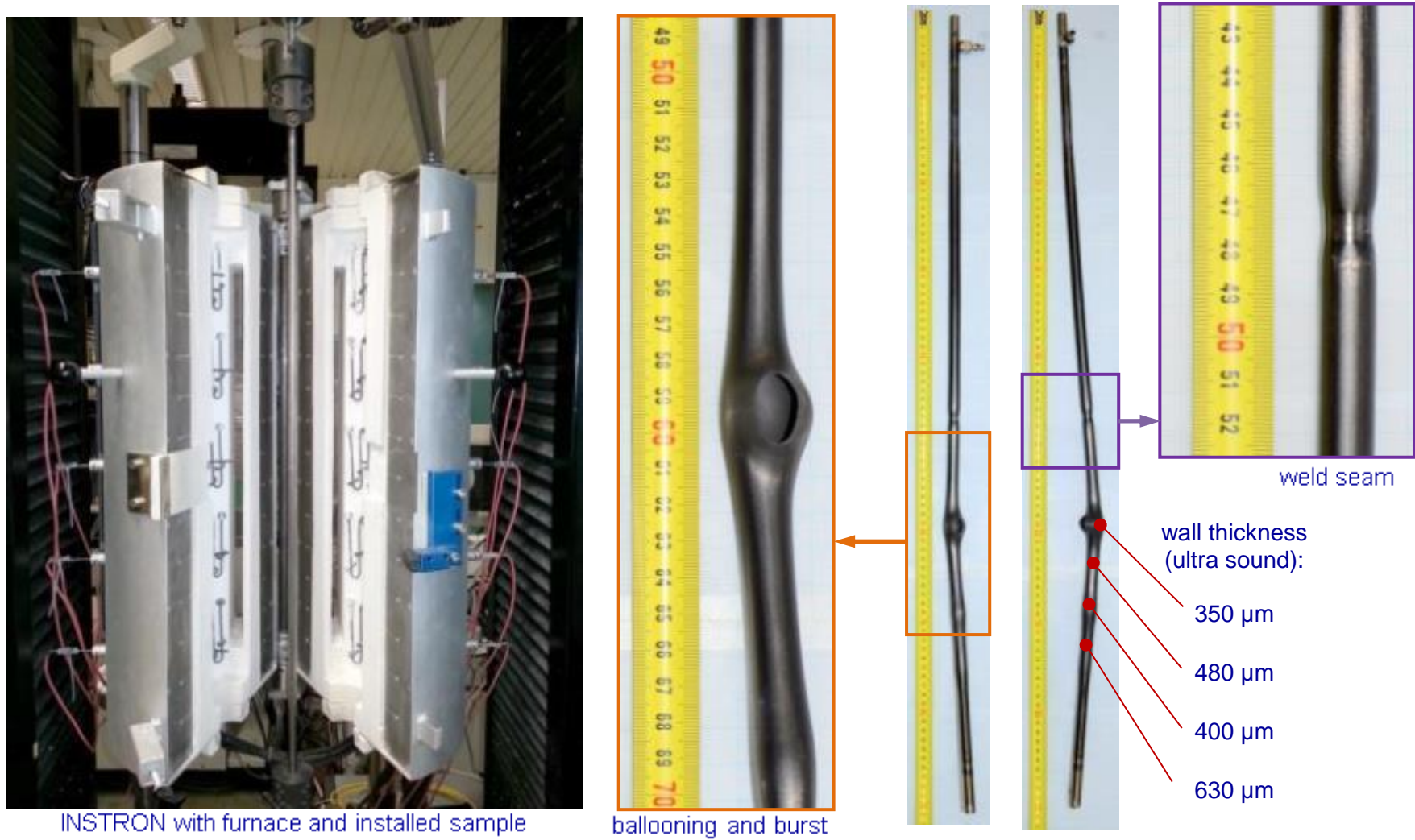


Figure 8 QUENCH-L4; Ballooning test of welded prototype cladding (both parts hydrogenated to about 100 wppm) pressurized to 55 bar; burst after 1 hour at constant $T=650\text{ }^{\circ}\text{C}$.

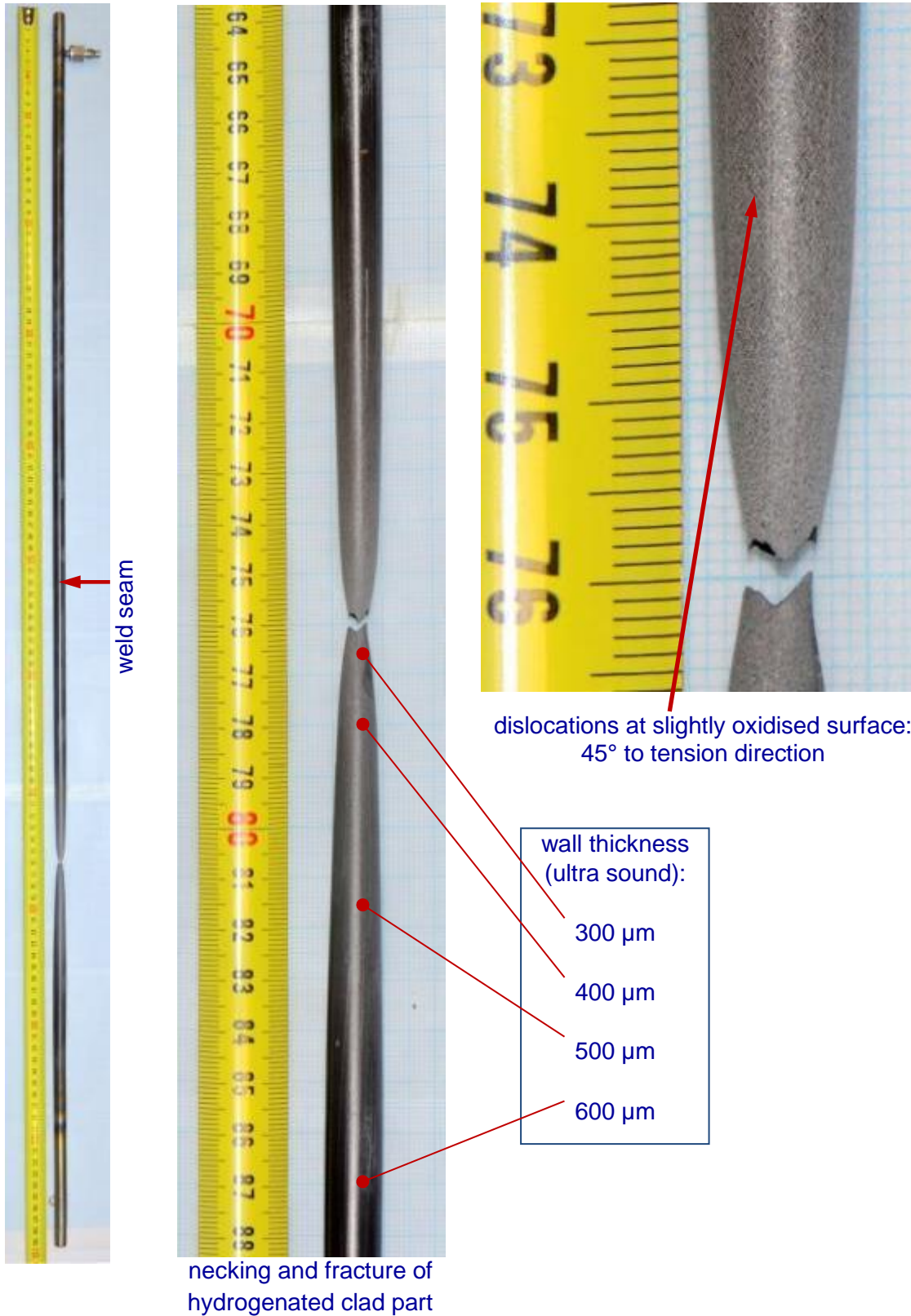


Figure 9 QUENCH-L4; Tensile test of welded prototype cladding (only lower part hydrogenated to about 100 wppm) at 650 °C; inner pressure was decreased from 55 to 4 bar after holding time of 1800 s at 650 °C.

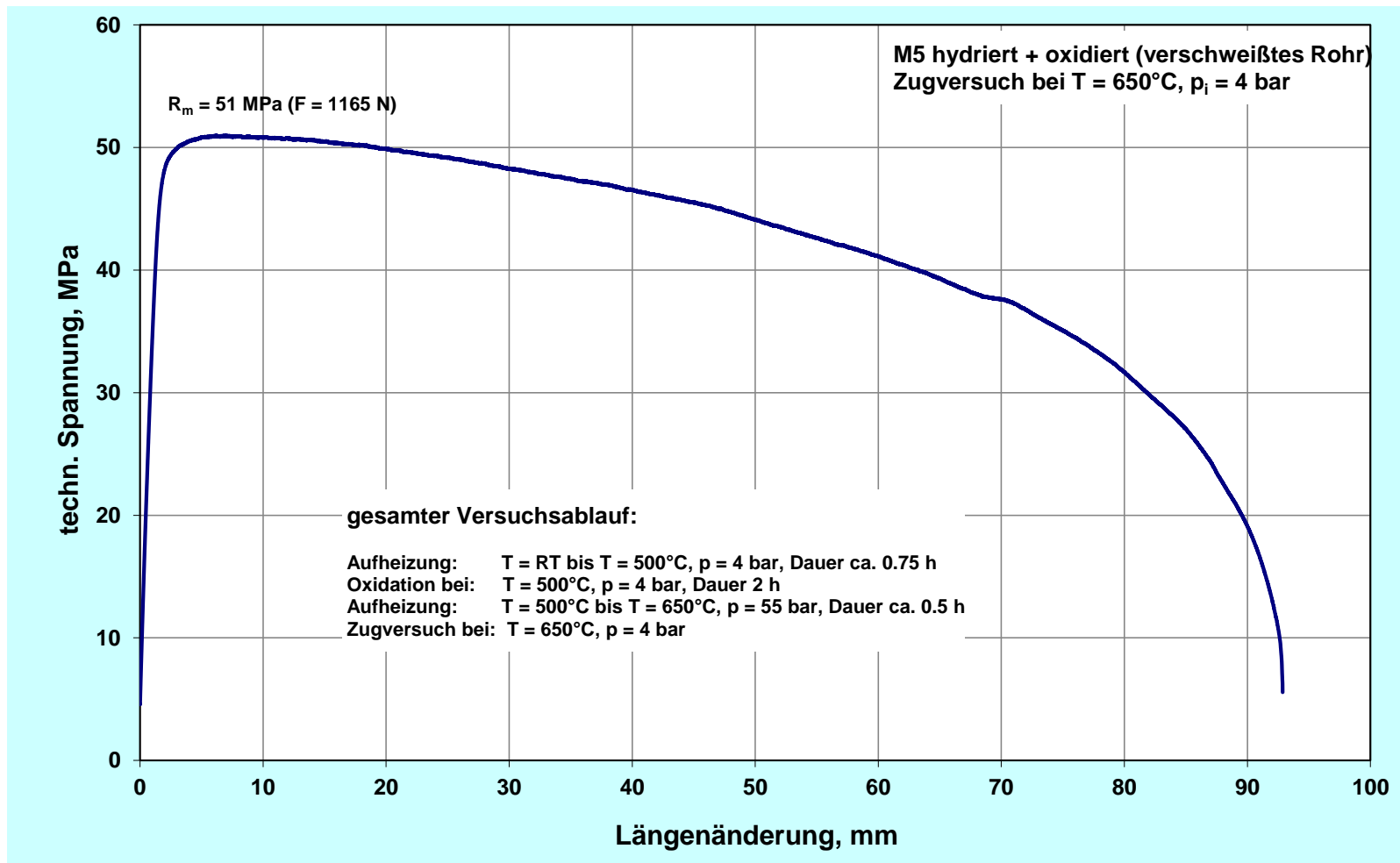


Figure 10 QUENCH-L4; Tensile diagram for prototype sample composed (welded) of hydrogenated and not hydrogenated claddings (shown in Fig. 9).

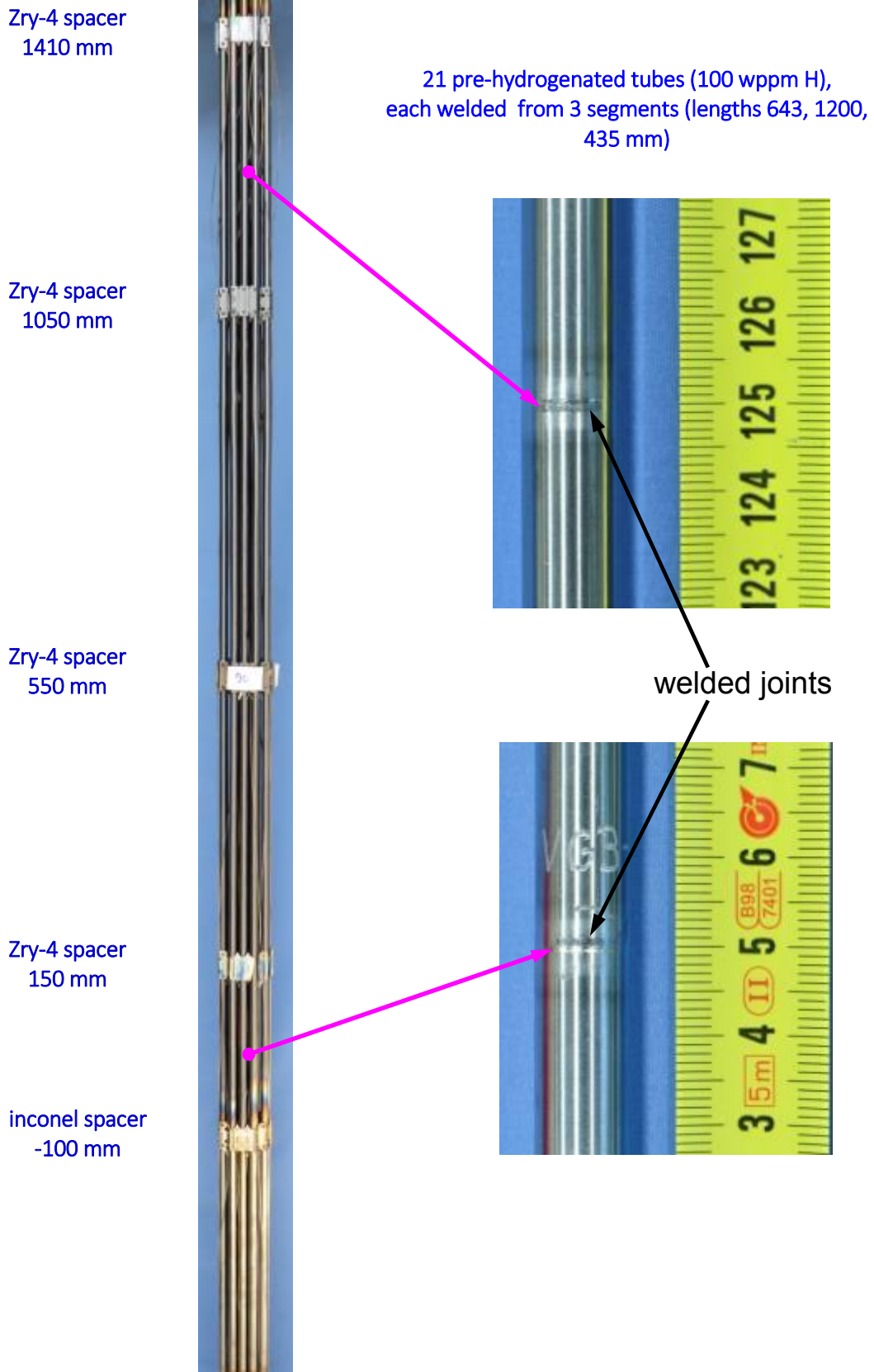
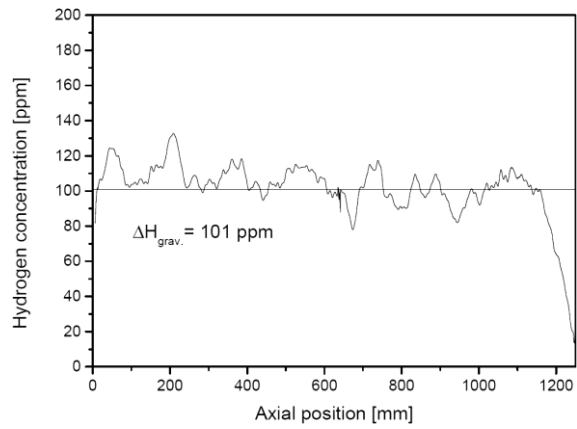
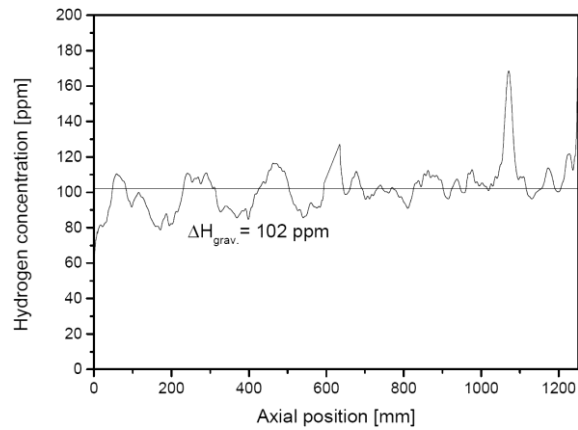


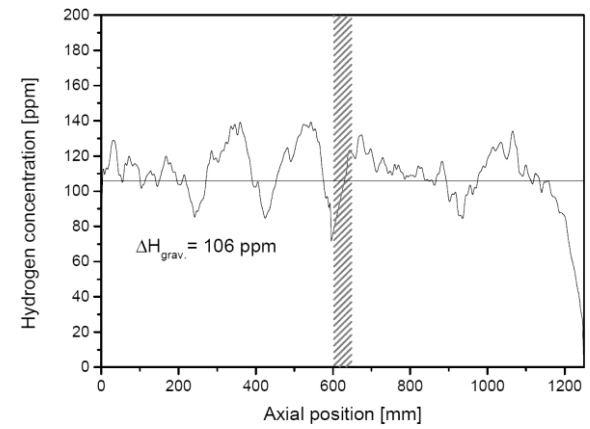
Figure 11 QUENCH-L4; Welding of pre-hydrogenated claddings.



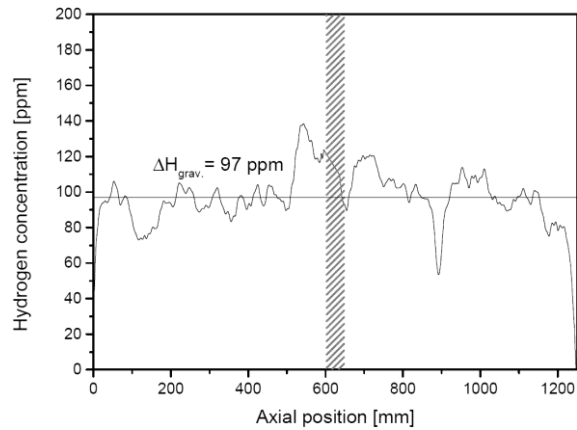
sample 11



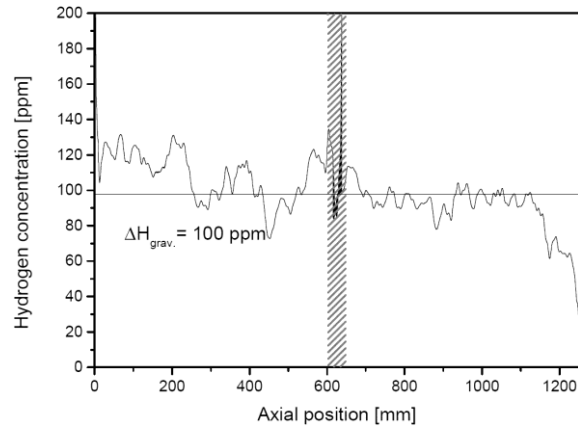
sample 12



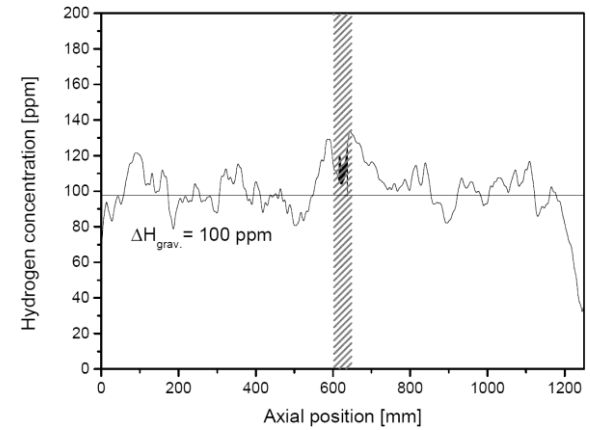
sample 13



sample 14

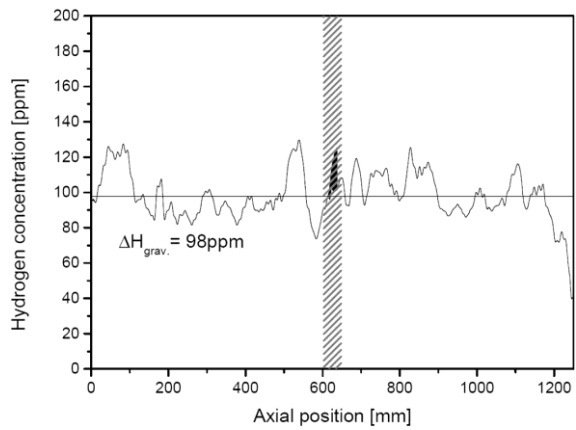


sample 15

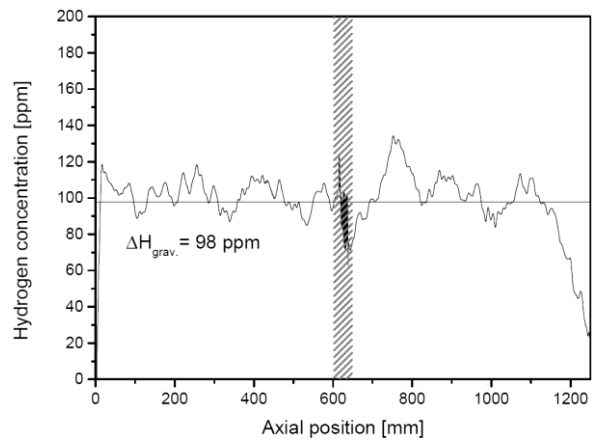


sample 16

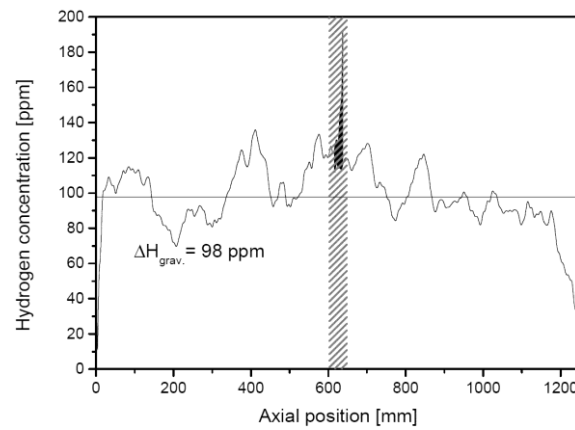
Figure 12 QUENCH-L4; Axial distribution of hydrogen in the pre-hydrogenated central part (bundle elevation 50 – 1250 mm) of the claddings #1 - #6 estimated by cladding diameter change. (Please note: sample numbers do not match the rod numbers.)



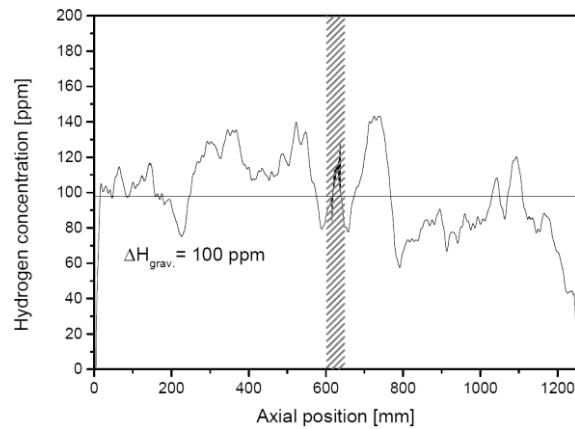
sample 18



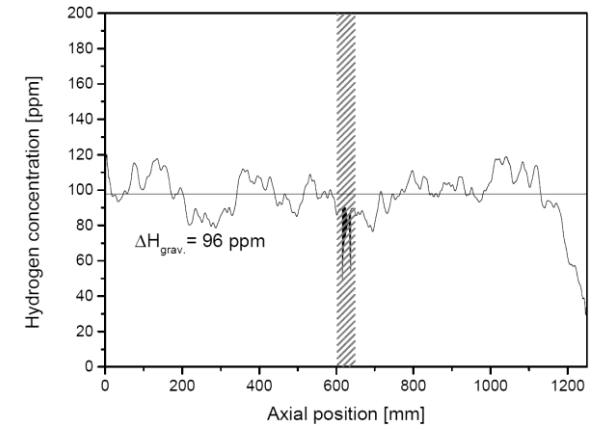
sample 21



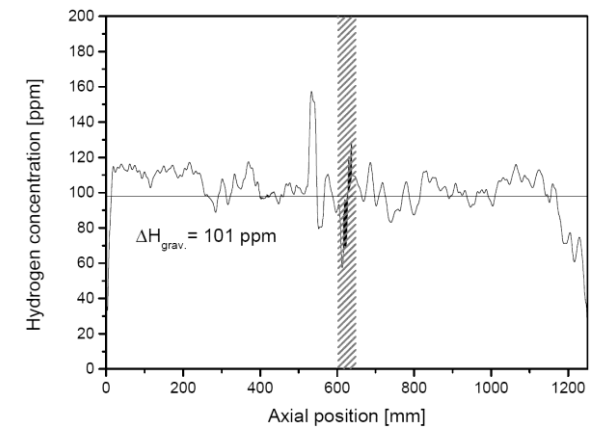
sample 19



sample 22

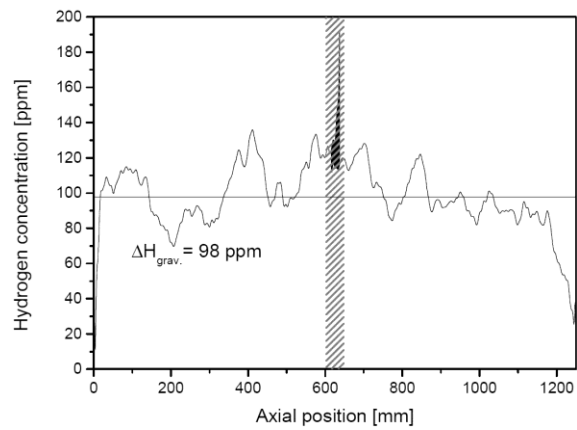


sample 20

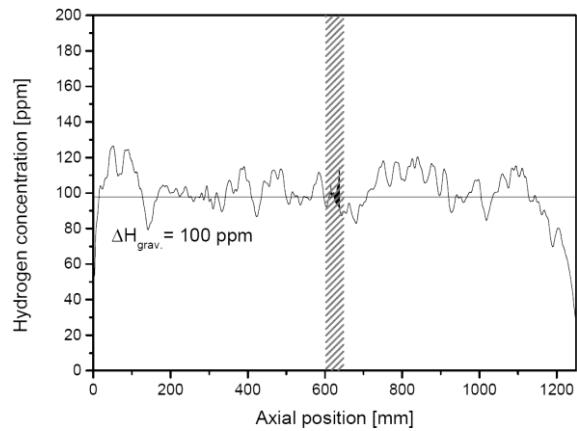


sample 23

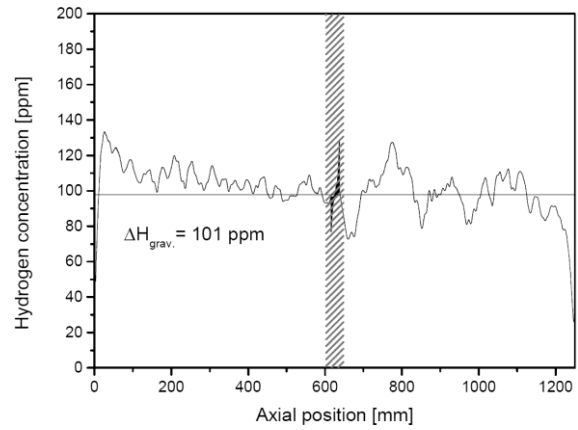
Figure 13 QUENCH-L4; Axial distribution of hydrogen in the pre-hydrogenated central part (bundle elevation 50 – 1250 mm) of the claddings #7 - #12 estimated by cladding diameter change. (Please note: sample numbers do not match the rod numbers.)



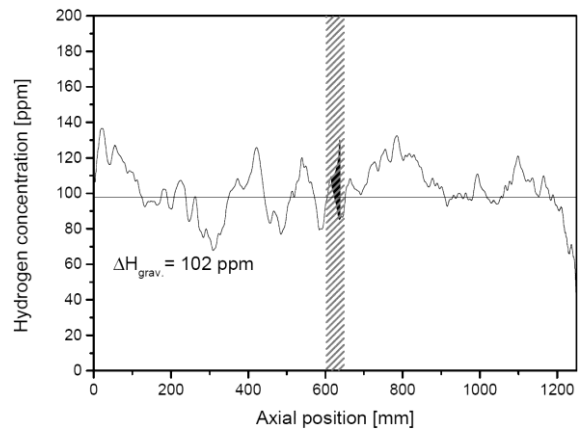
sample 24



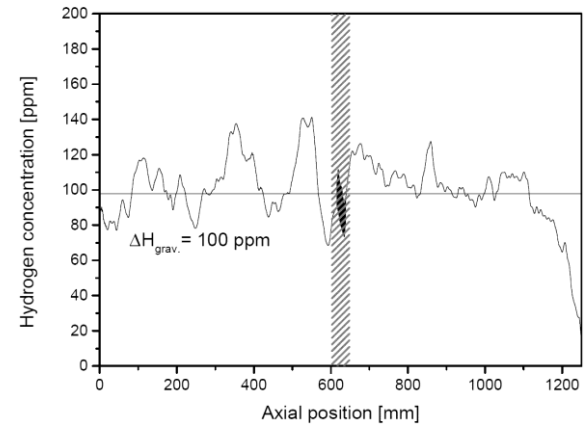
sample 28



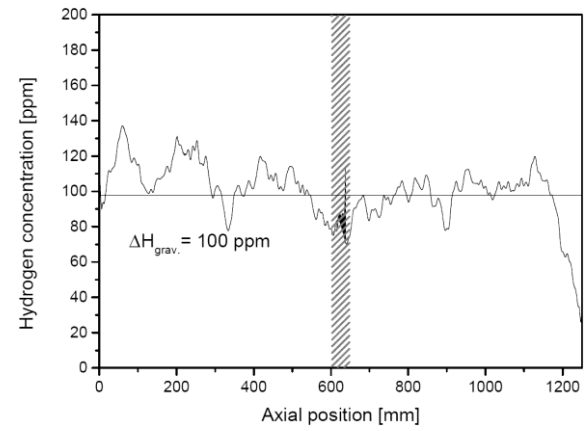
sample 25



sample 29

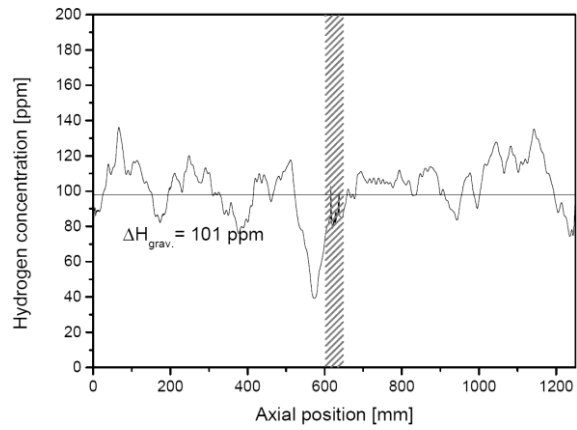


sample 26

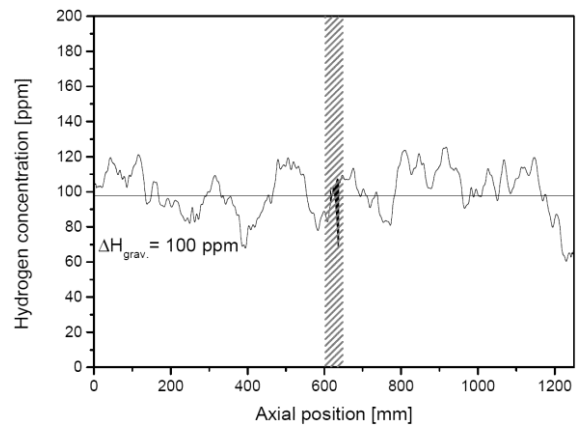


sample 30

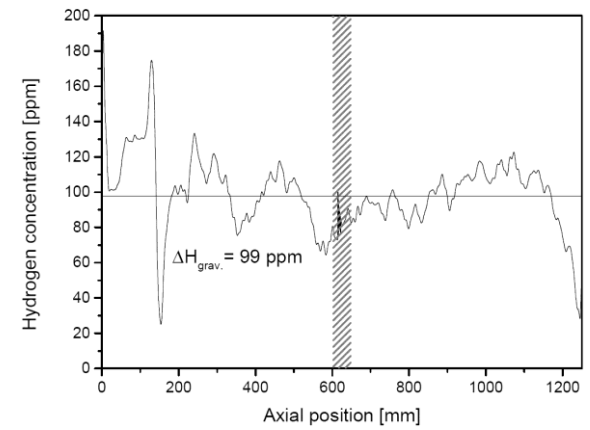
Figure 14 QUENCH-L4; Axial distribution of hydrogen in the pre-hydrogenated central part (bundle elevation 50 – 1250 mm) of the claddings #13 - #18 estimated by cladding diameter change. (Please note: sample numbers do not match the rod numbers.)



sample 31

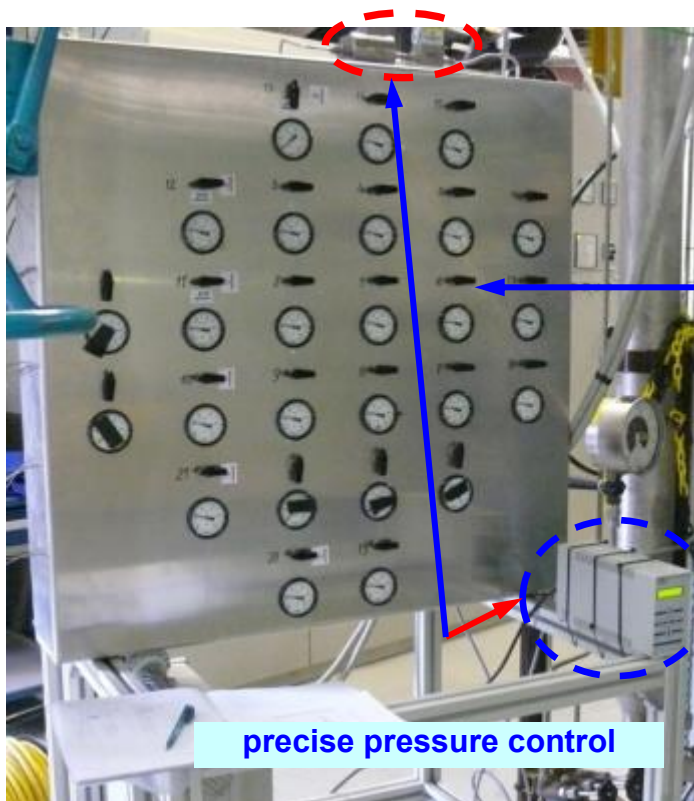


sample 33



sample 34

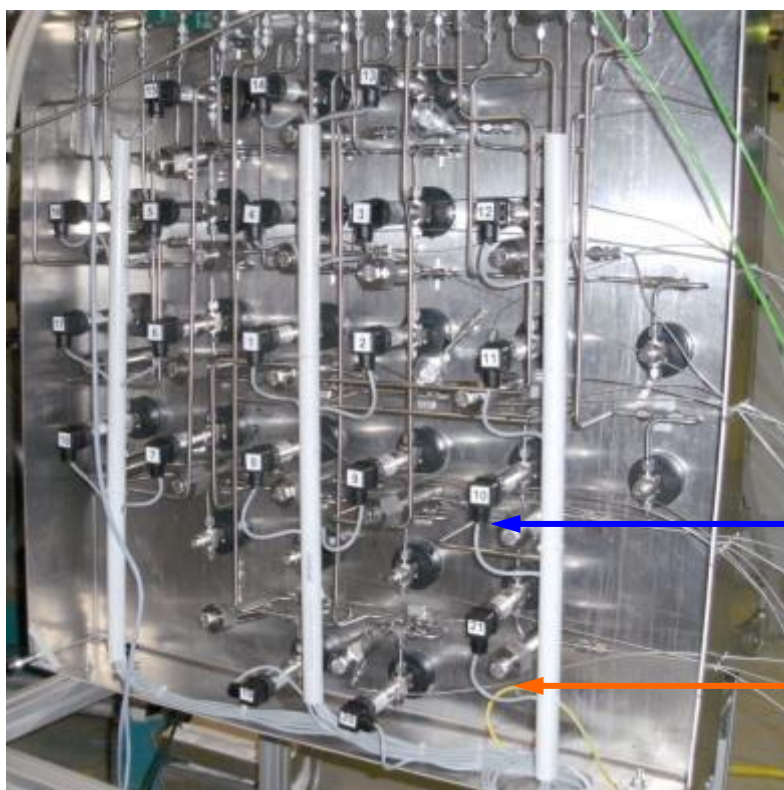
Figure 15 QUENCH-L4; Axial distribution of hydrogen in the pre-hydrogenated central part (bundle elevation 50 – 1250 mm) of the claddings #19 - #21 estimated by cladding diameter change. (Please note: sample numbers do not match the rod numbers).



Front side view

21 pressure valves

precise pressure control



Rear side view

21 capillary tubes to test bundle

21 pressure transducers

21 adjustable compensation volumes to setting of original volume value of 31.5 cm³

Figure 16 QUENCH-L4; Rod pressure control and measurement panel.

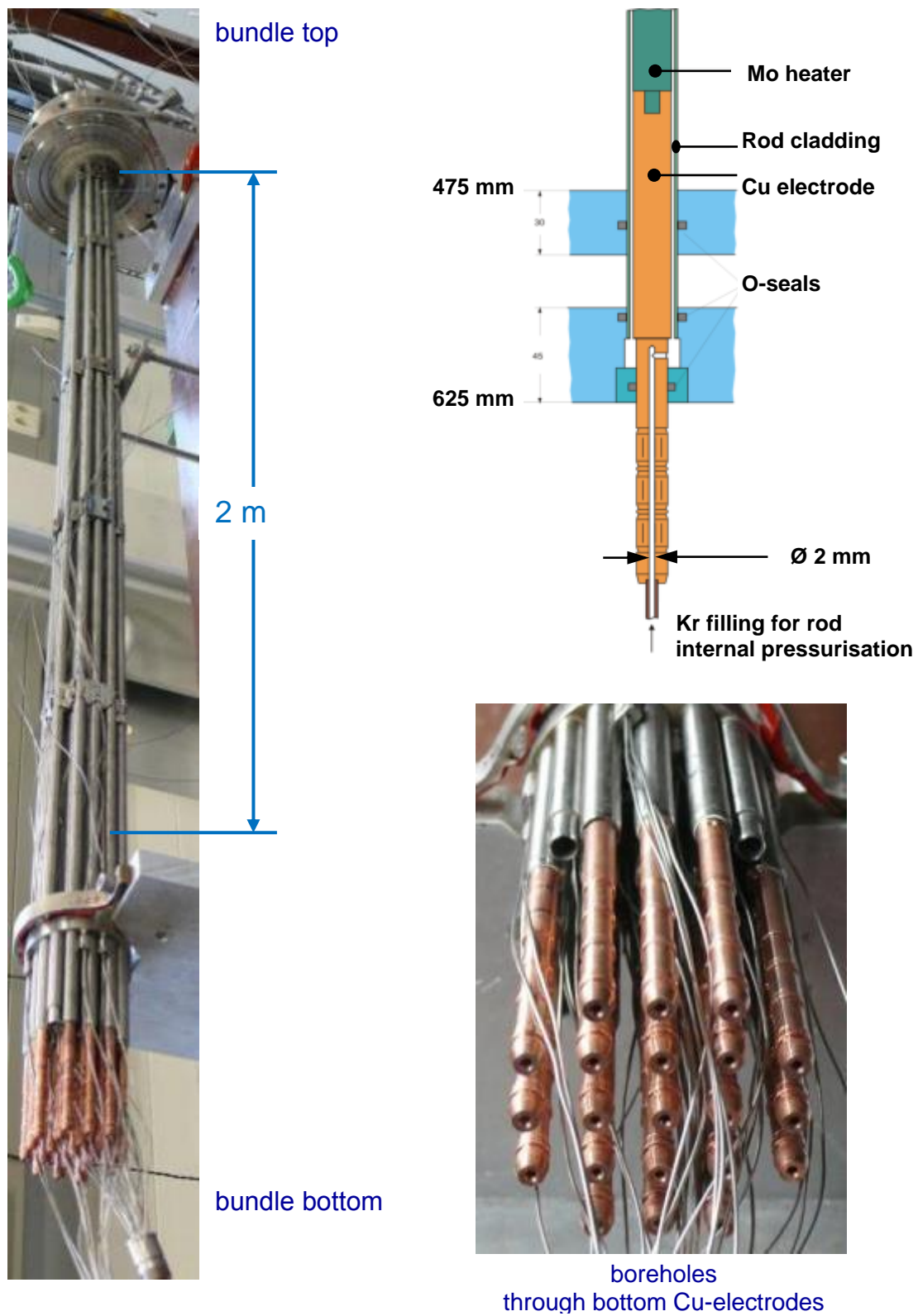


Figure 17 QUENCH-L4; Rod pressurization.

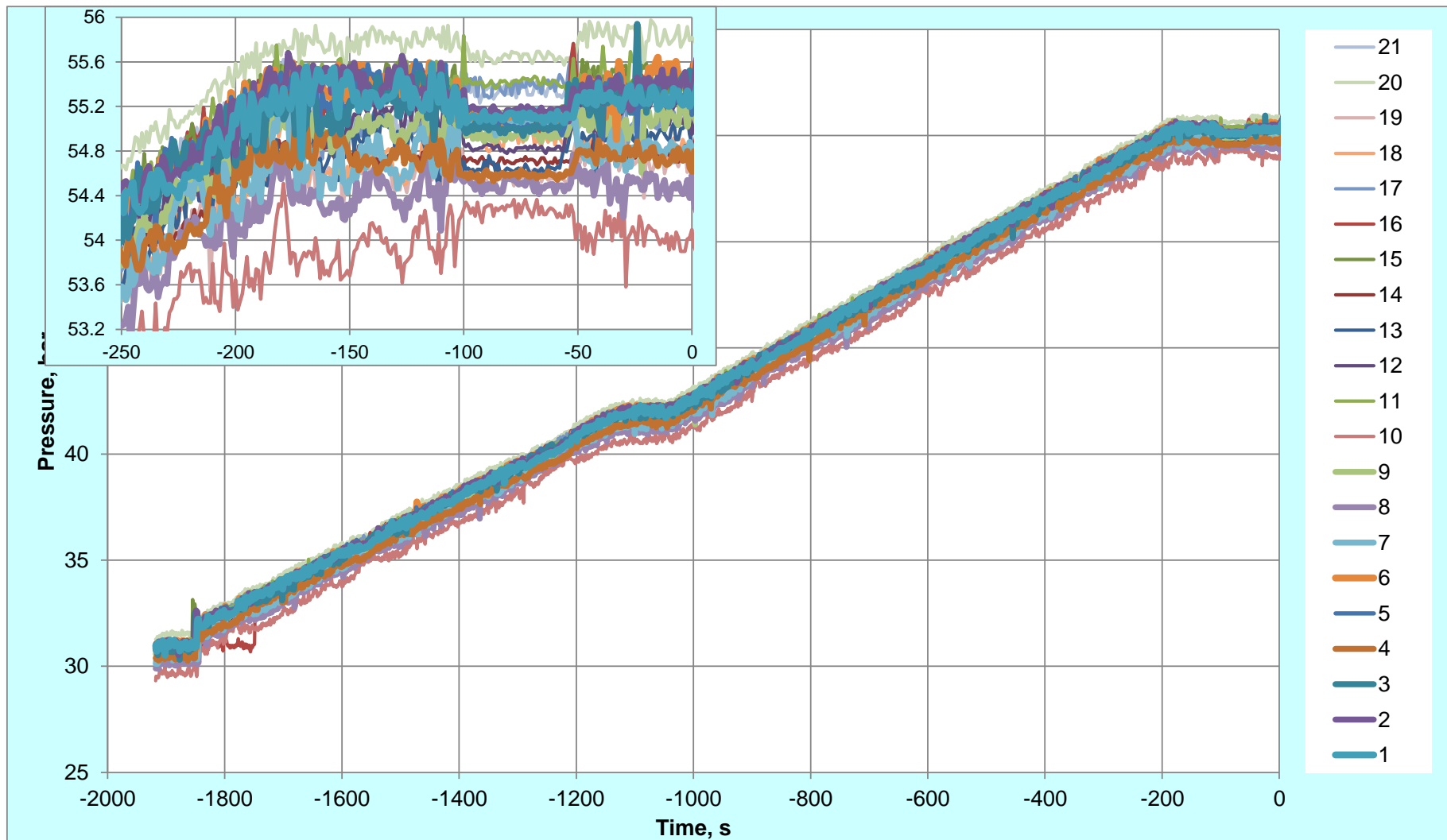


Figure 18 QUENCH-L4; Rod pressurization process at $T_{pct} = 550 \text{ }^{\circ}\text{C}$.

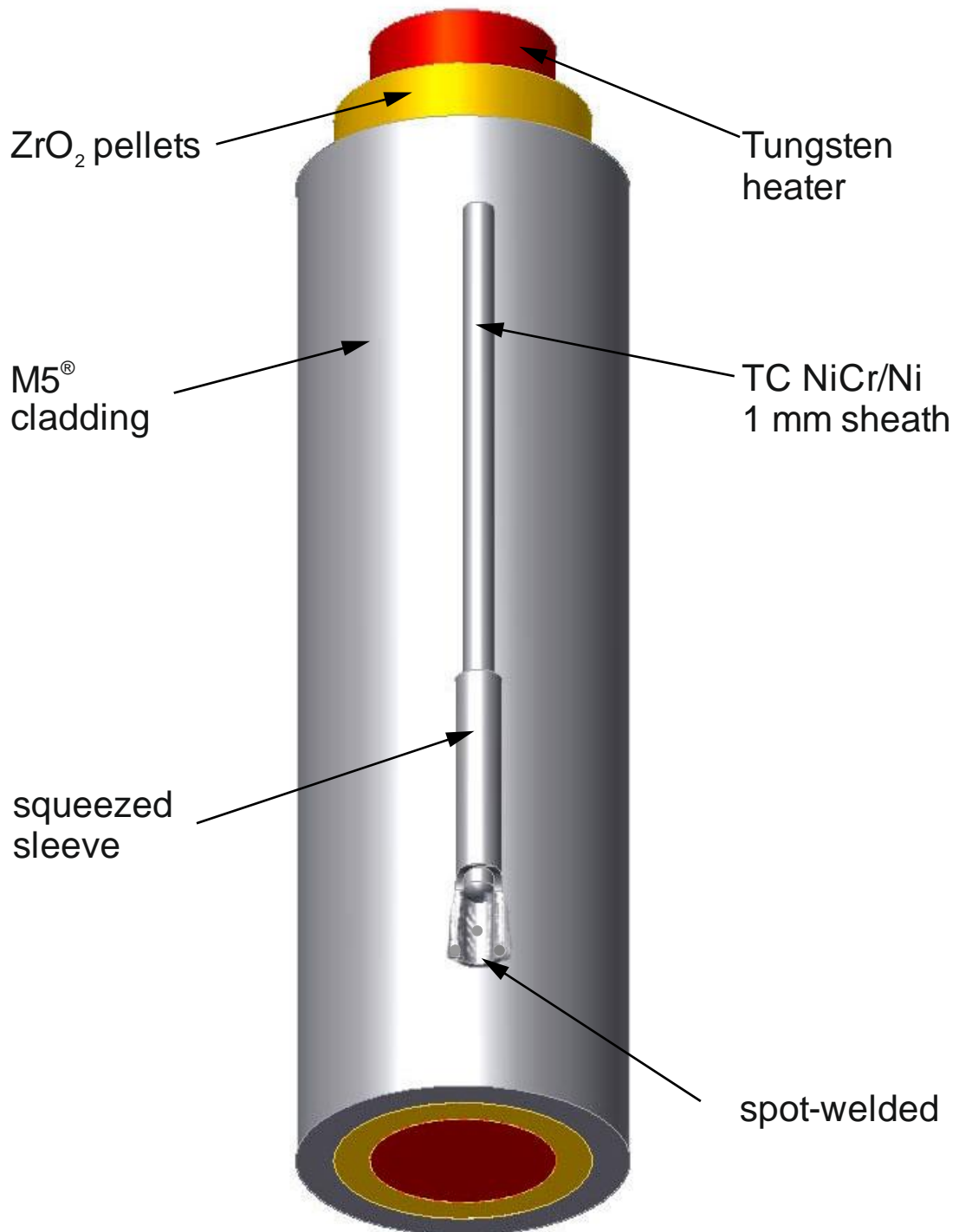


Figure 19 QUENCH-L4; Concept for TC fastening at the test rod.

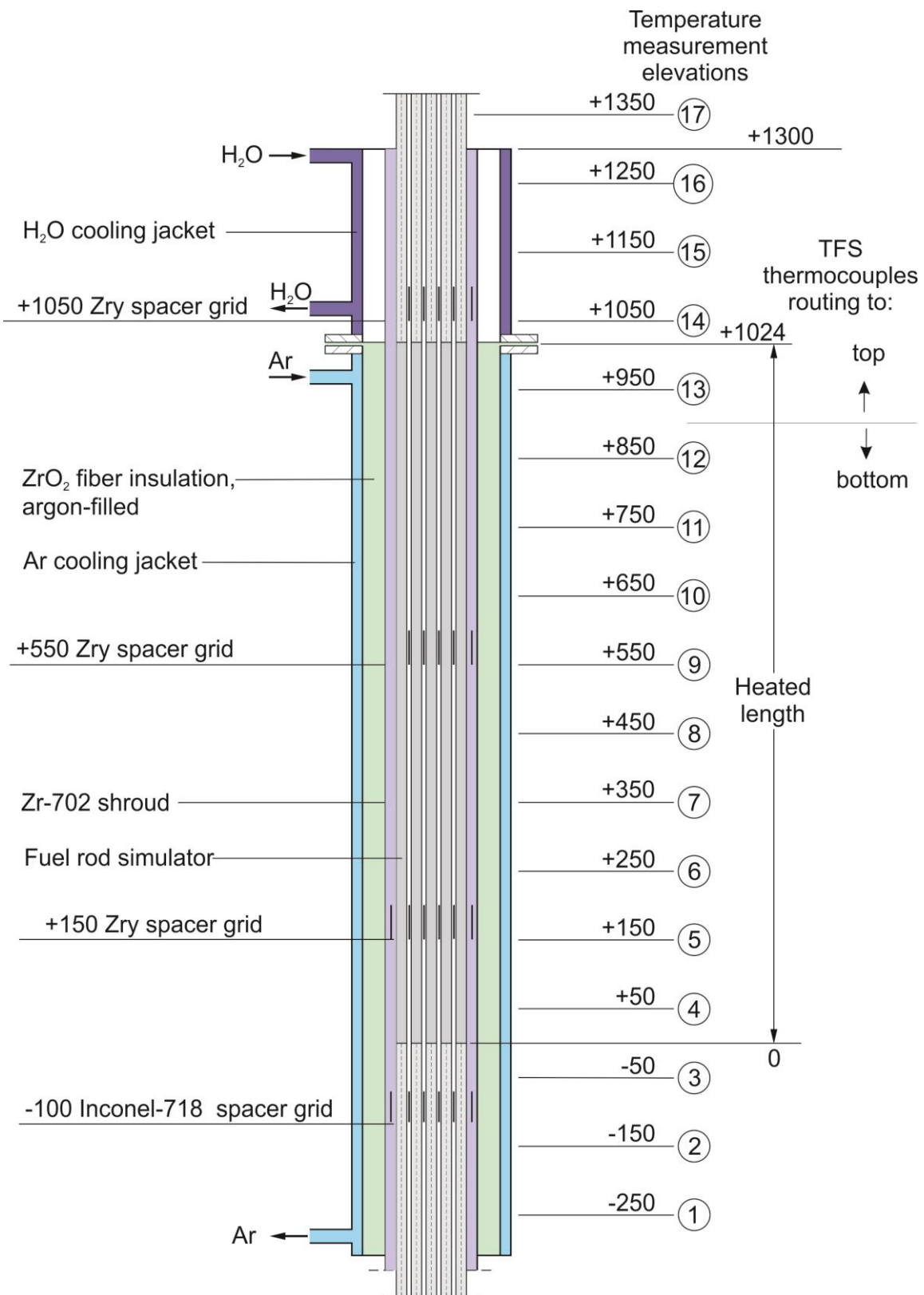


Figure 20 Axial temperature measurement locations in the QUENCH-L4 test section.

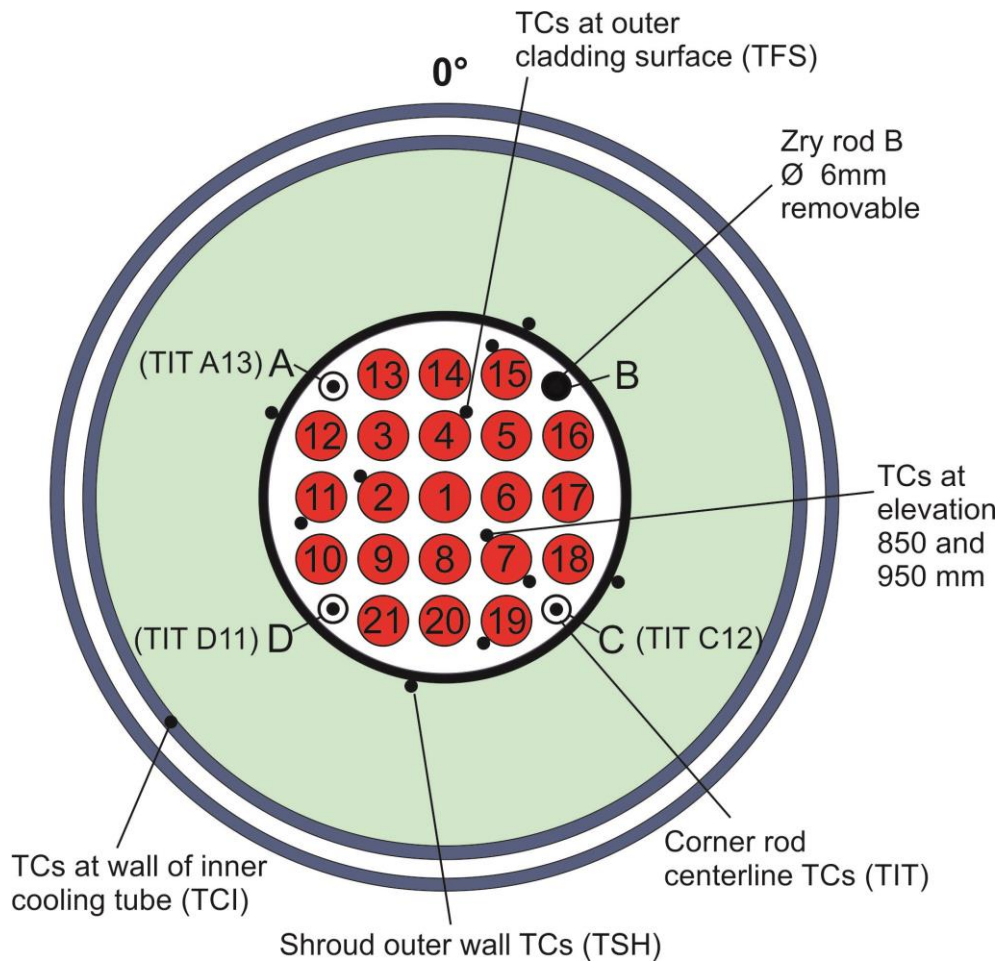
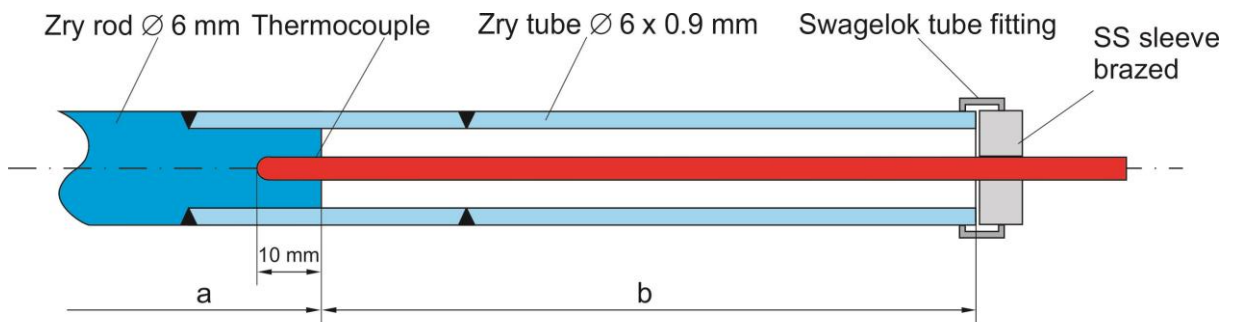


Figure 21 QUENCH-L4; Test bundle; TC instrumentation and rod design (top view).



Rod A: TIT A13 (950 mm), a = 360 mm, b = 2080 mm

Rod C: TIT C12 (850 mm), a = 460 mm, b = 1980 mm

Rod D: TIT D11 (750 mm), a = 560 mm, b = 1880 mm

Figure 22 QUENCH-L4; Arrangement of the thermocouples inside the corner rods.

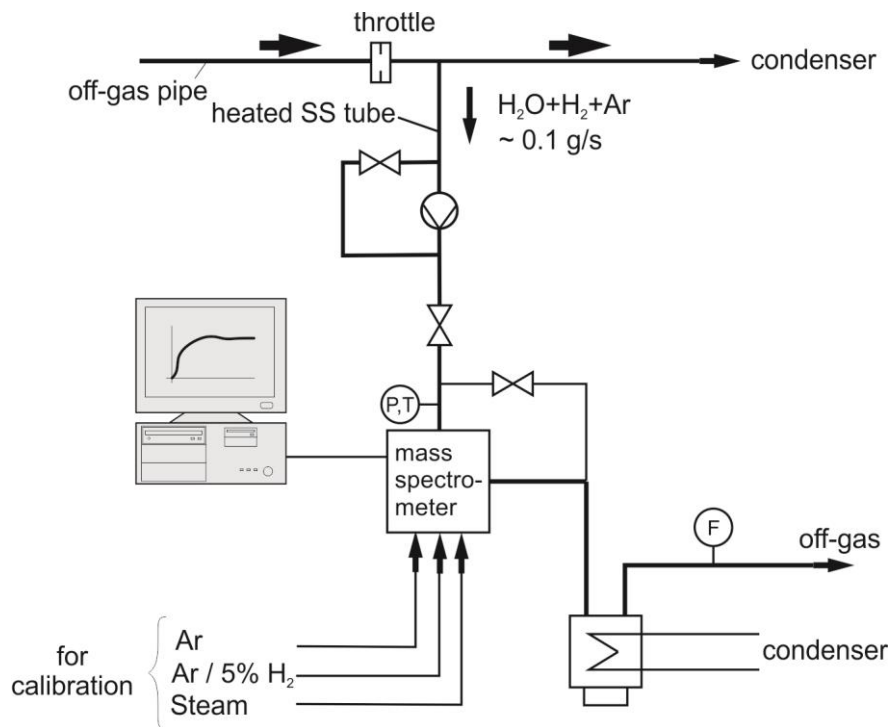


Figure 23 QUENCH Facility; H₂ measurement with the GAM 300 mass spectrometer.

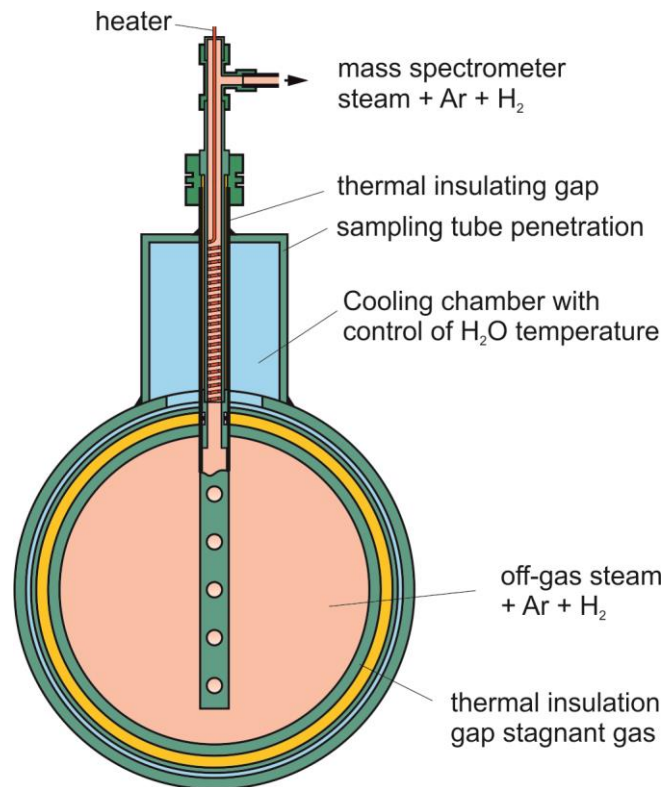


Figure 24 Mass spectrometer sampling position at the off-gas pipe of the QUENCH test facility.

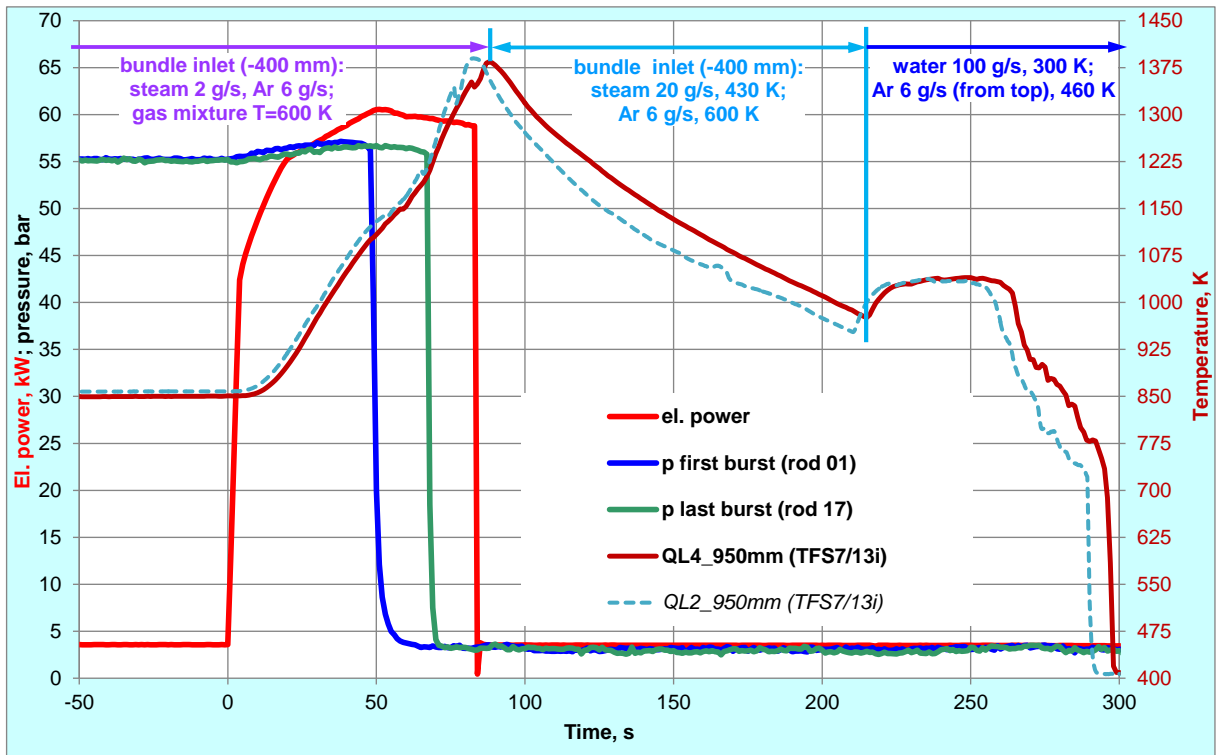


Figure 25 QUENCH-L4; Test progress, comparison with QUENCH-L2 temperature.

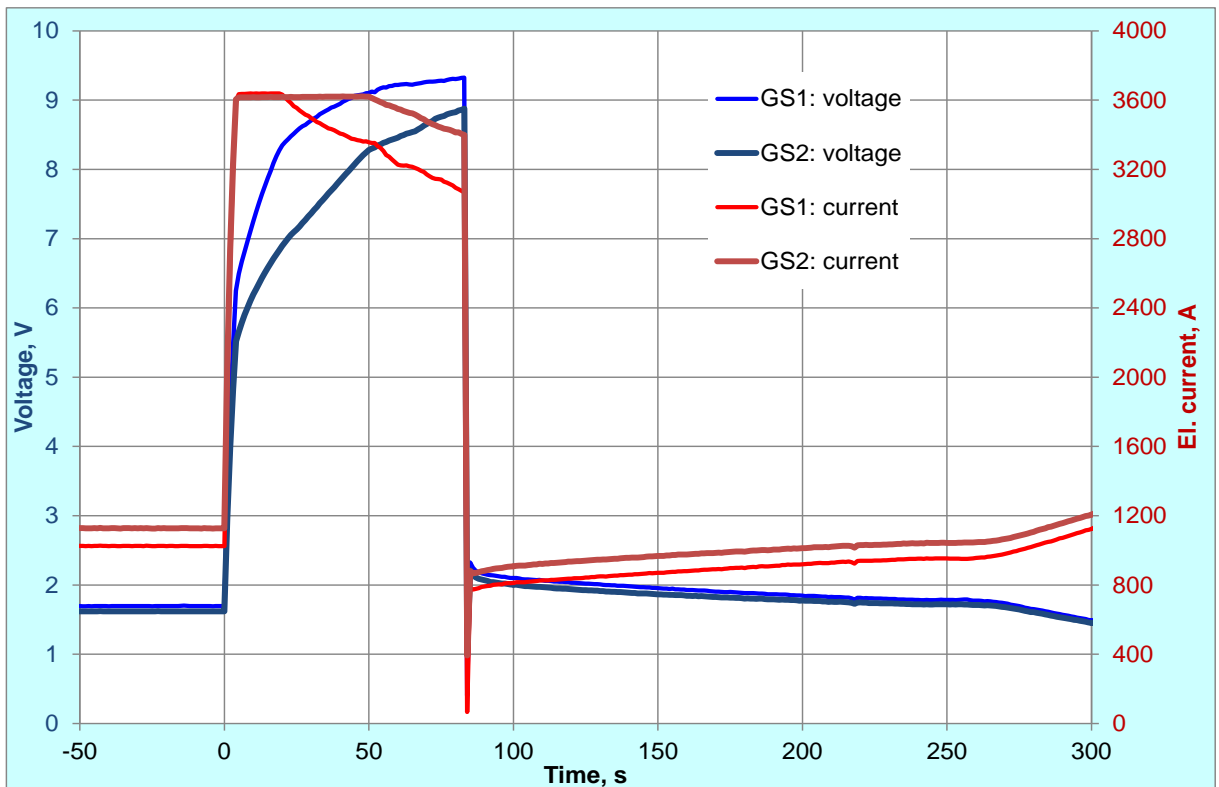


Figure 26 QUENCH-L4; Voltage and current of two DC-generators.

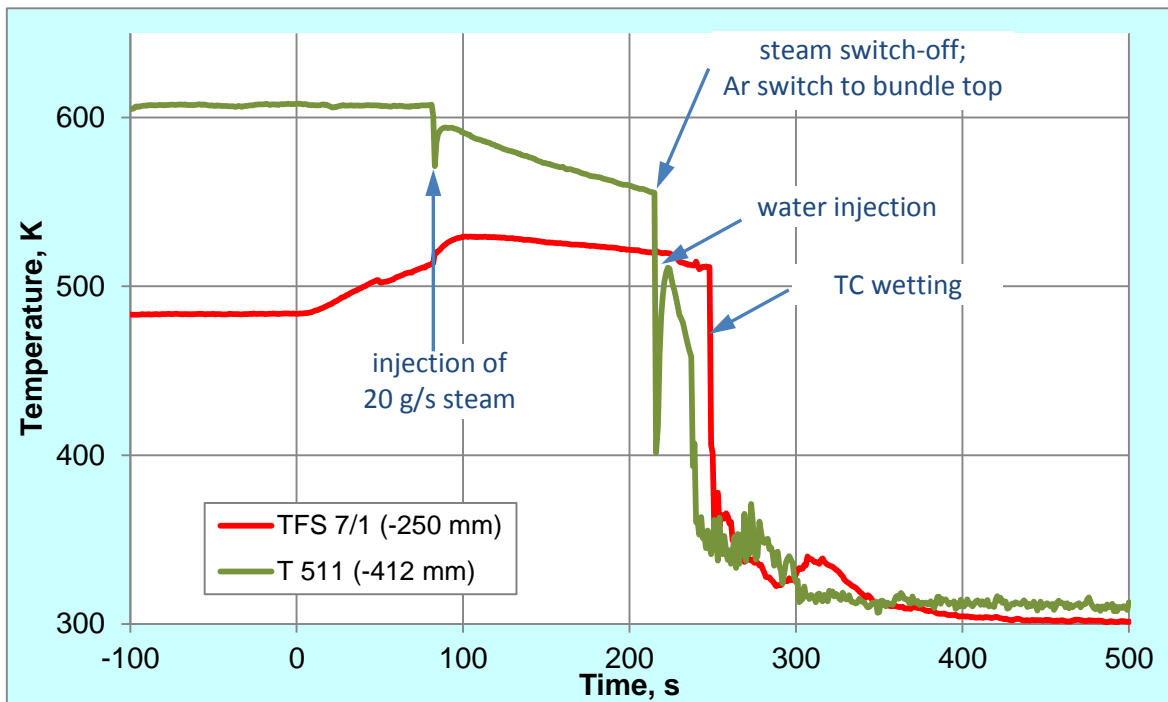


Figure 27 QUENCH-L4; Temperatures measured by gas inlet thermocouple (T 511) at -412 mm and rod cladding (TFS 7/1) thermocouple at -250 mm elevation.

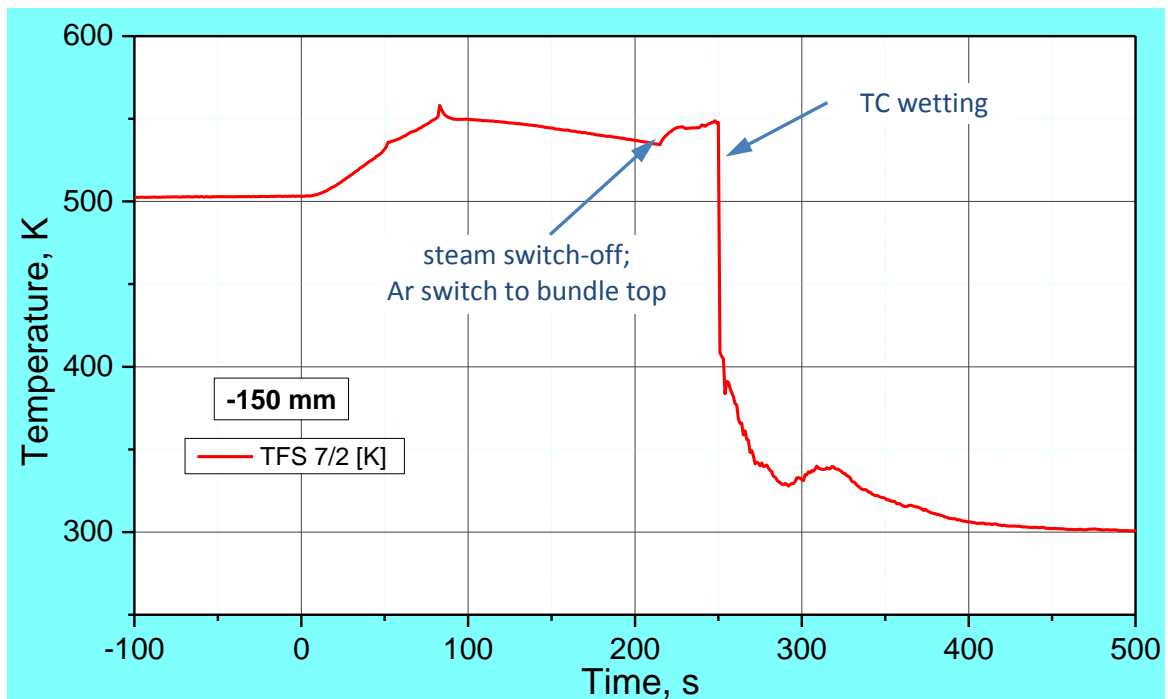


Figure 28 QUENCH-L4; Temperatures measured by rod cladding (TFS 7/2) thermocouple at -150 mm elevation.

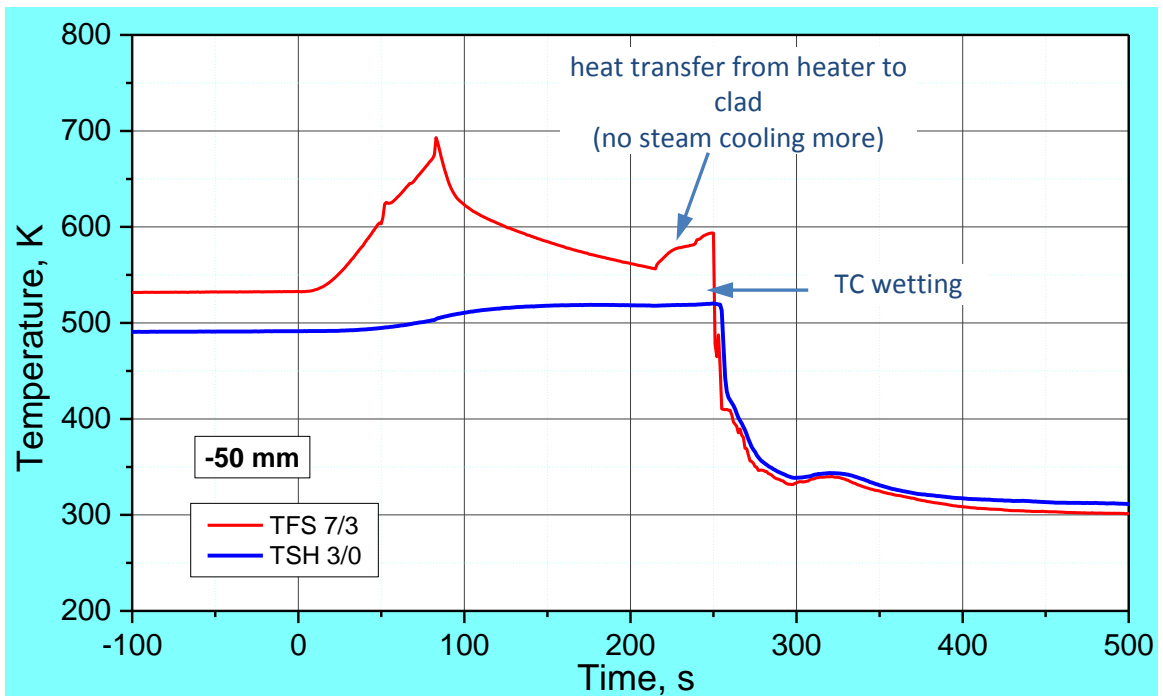


Figure 29 QUENCH-L4; Temperatures measured by rod cladding (TFS 7/3) and shroud (TSH 3/0) thermocouples at -50 mm elevation.

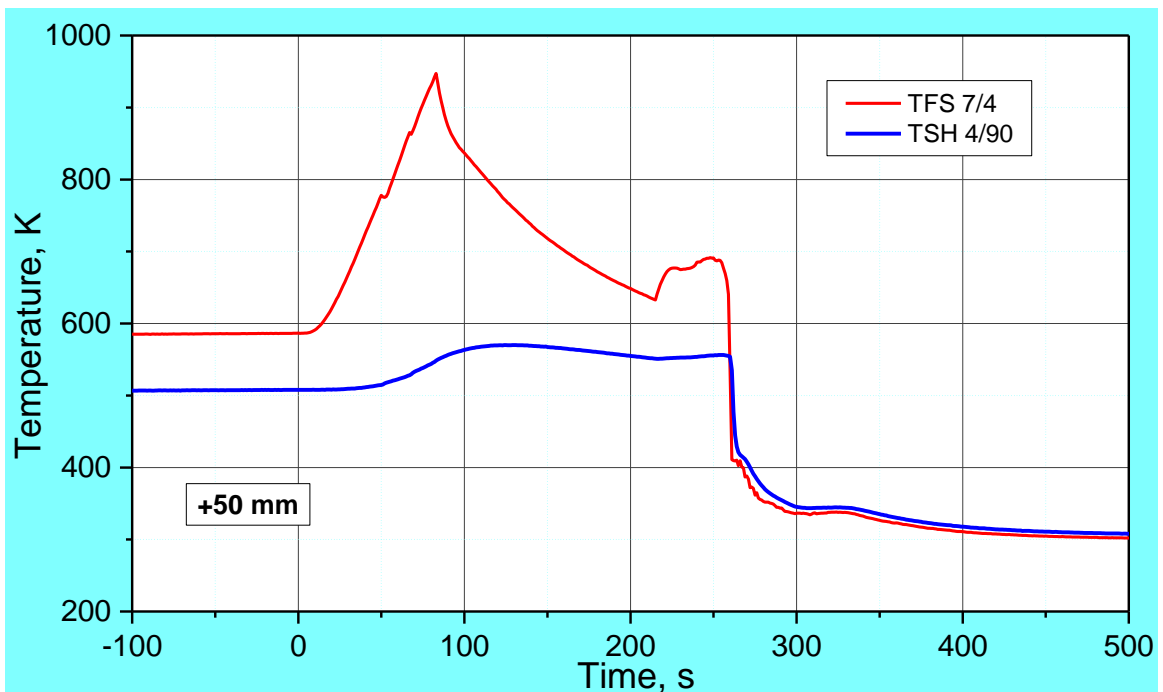


Figure 30 QUENCH-L4; Temperatures measured by rod cladding (TFS 7/4) and shroud (TSH 4/90) thermocouples at 50 mm elevation.

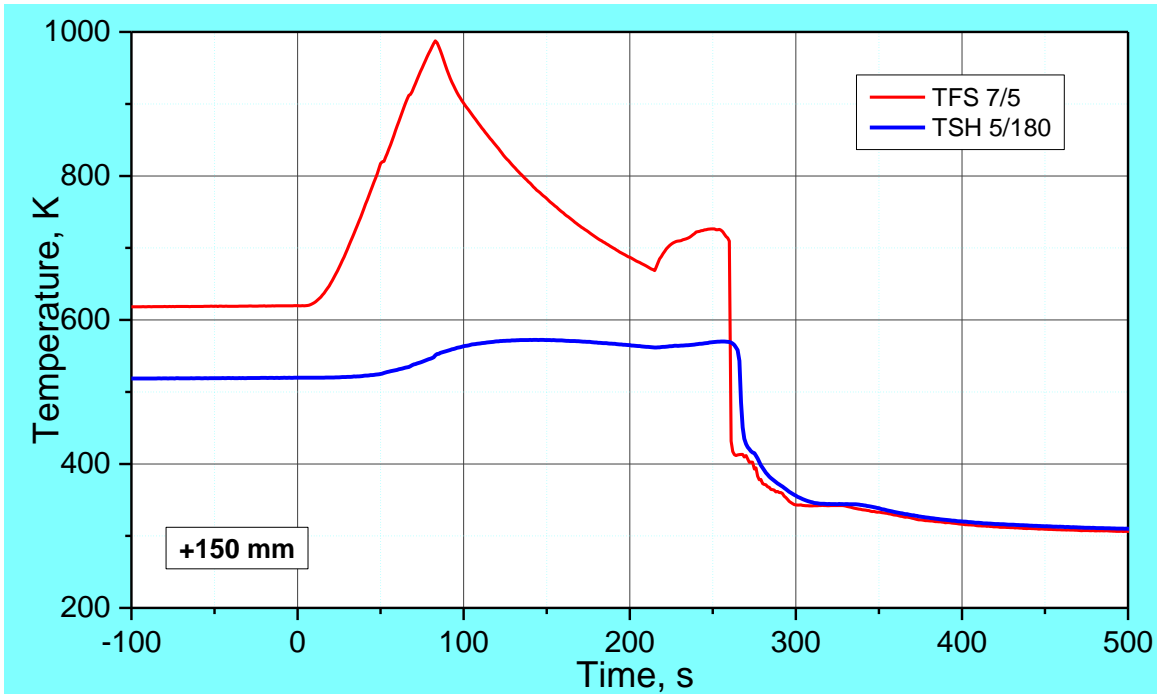


Figure 31 QUENCH-L4; Temperatures measured by rod cladding (TFS 7/5) and shroud (TSH 5/180) thermocouples at 150 mm elevation.

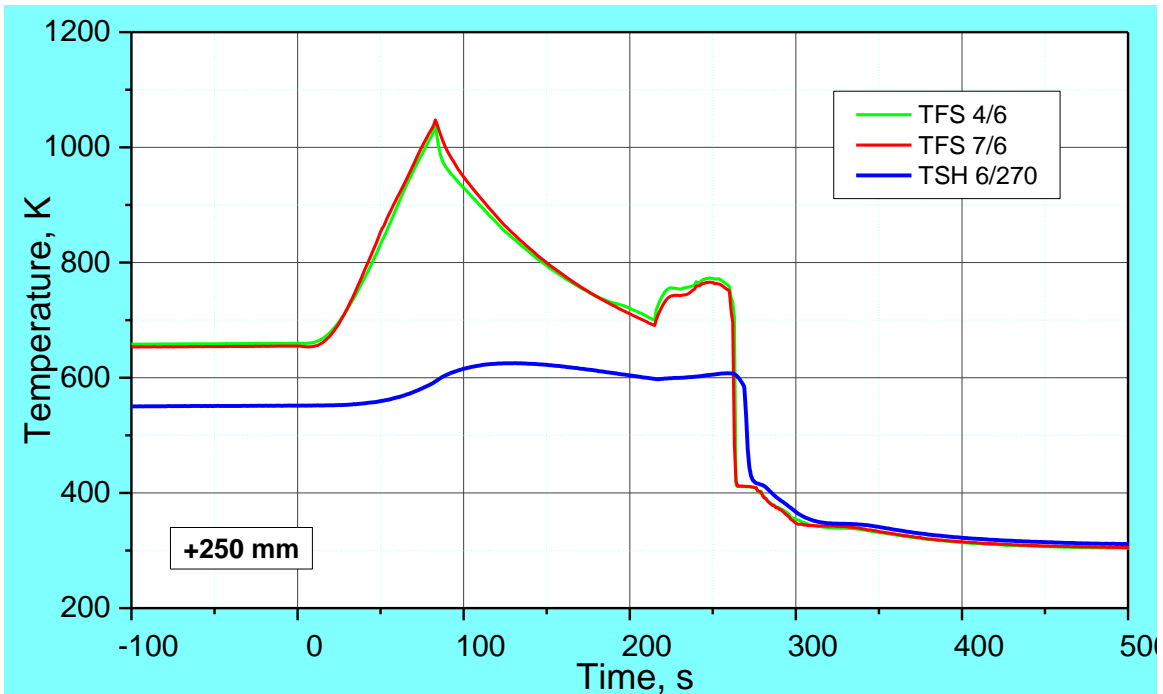


Figure 32 QUENCH-L4; Temperatures measured by rod cladding (TFS) and shroud (TSH 6/270) thermocouples at 250 mm elevation.

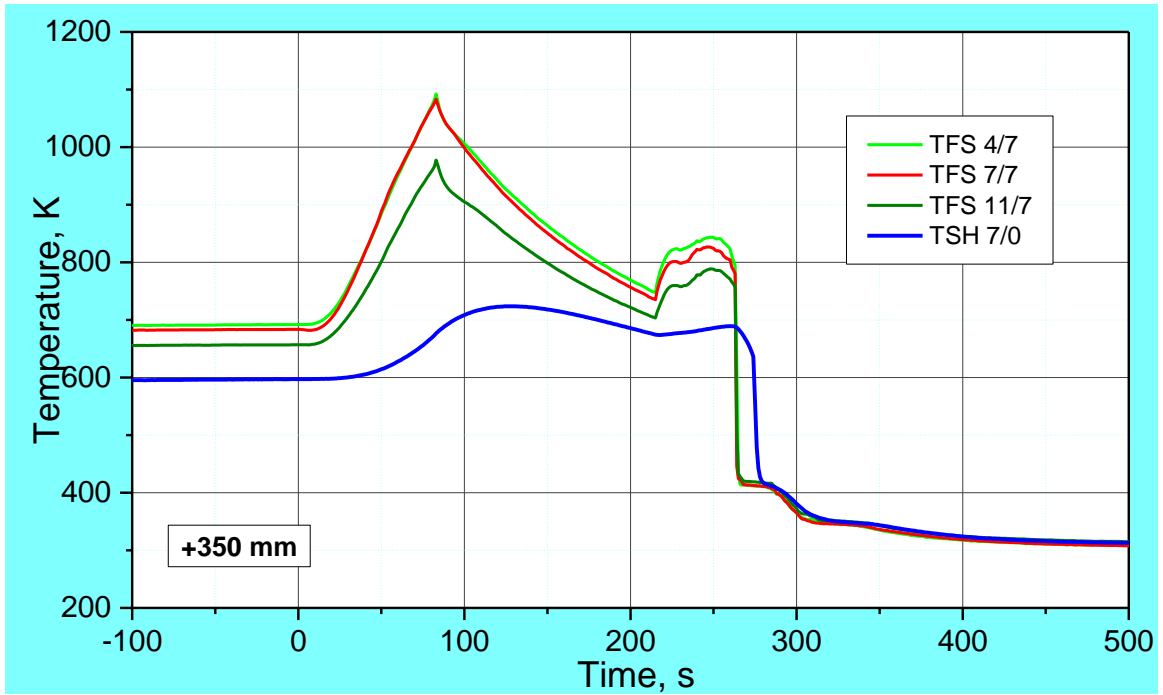


Figure 33 QUENCH-L4; Temperatures measured by rod cladding (TFS) and shroud (TSH 7/0) thermocouples at 350 mm elevation.

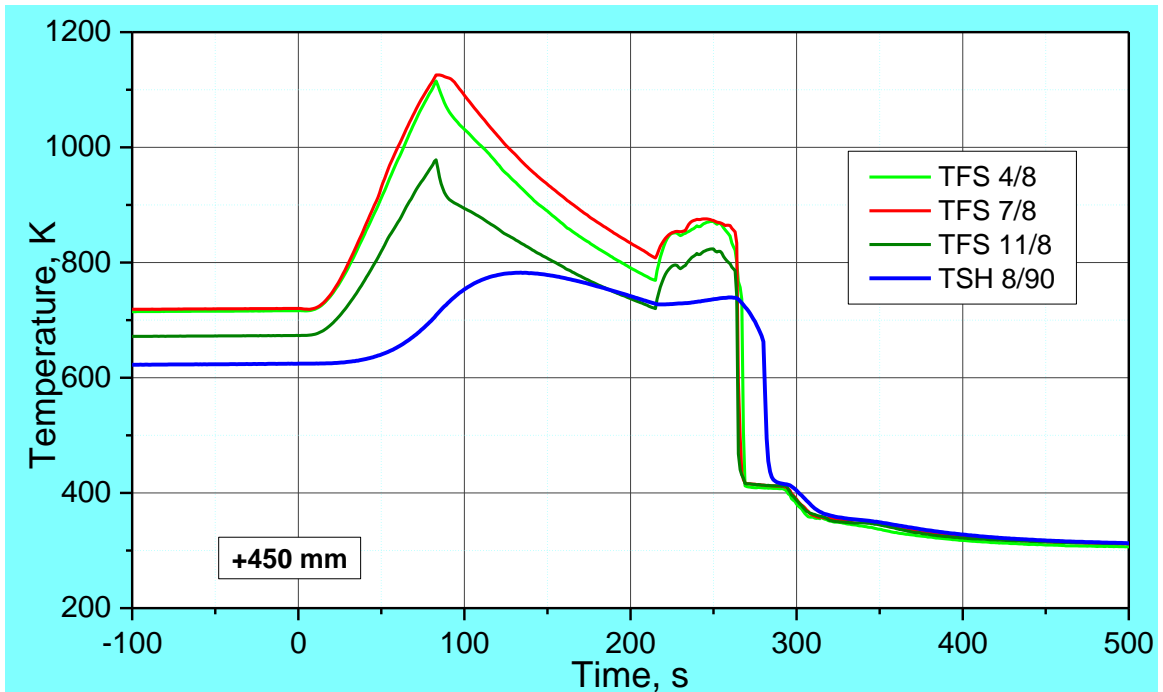


Figure 34 QUENCH-L4; Temperatures measured by rod cladding (TFS) and shroud (TSH 8/90) thermocouples at 450 mm elevation.

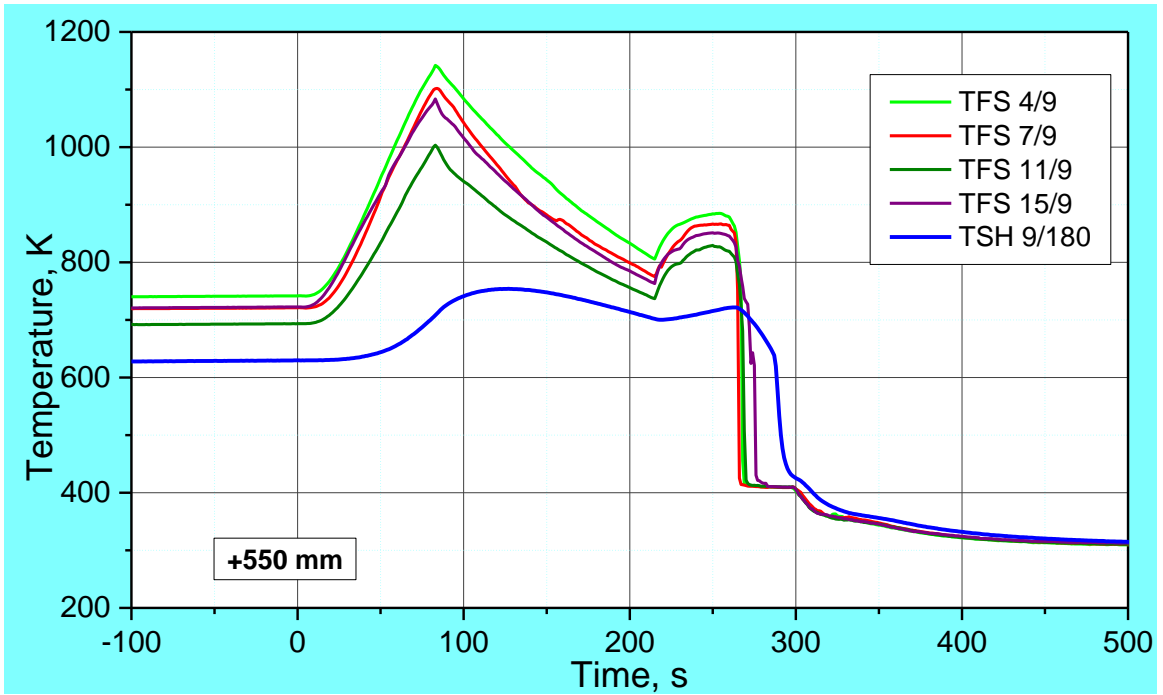


Figure 35 QUENCH-L4; Temperatures measured by rod cladding (TFS) and shroud (TSH 9/180) thermocouples at 550 mm elevation.

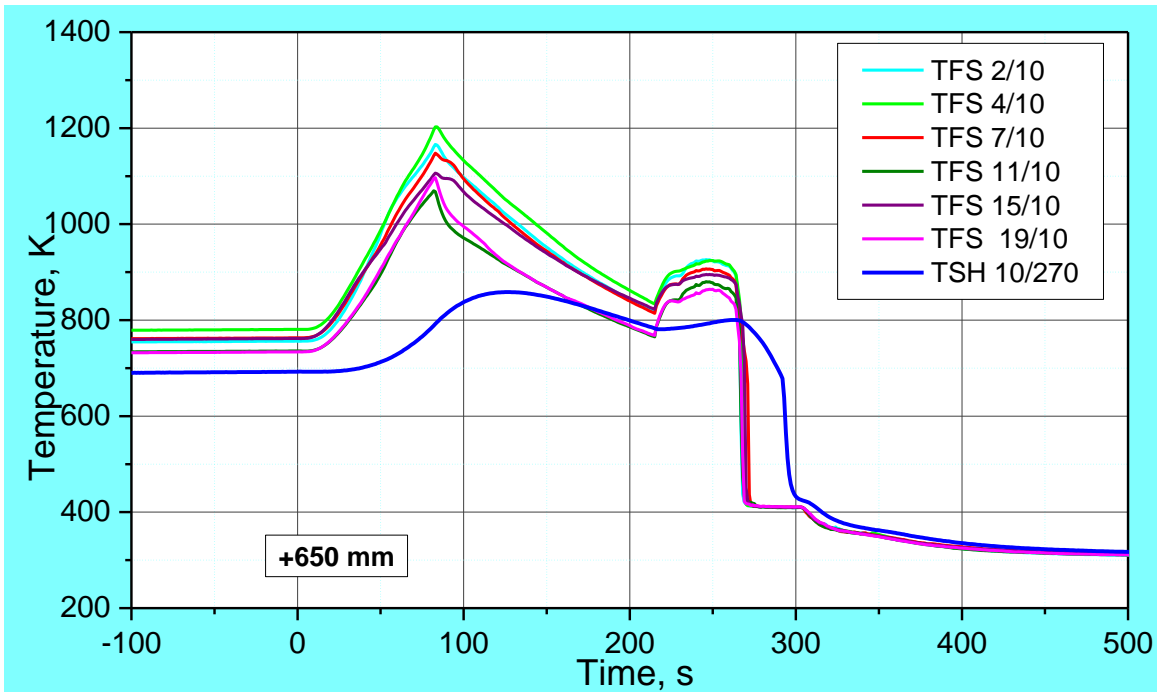


Figure 36 QUENCH-L4; Temperatures measured by rod cladding (TFS) and shroud (TSH 10/270) thermocouples at 650 mm elevation.

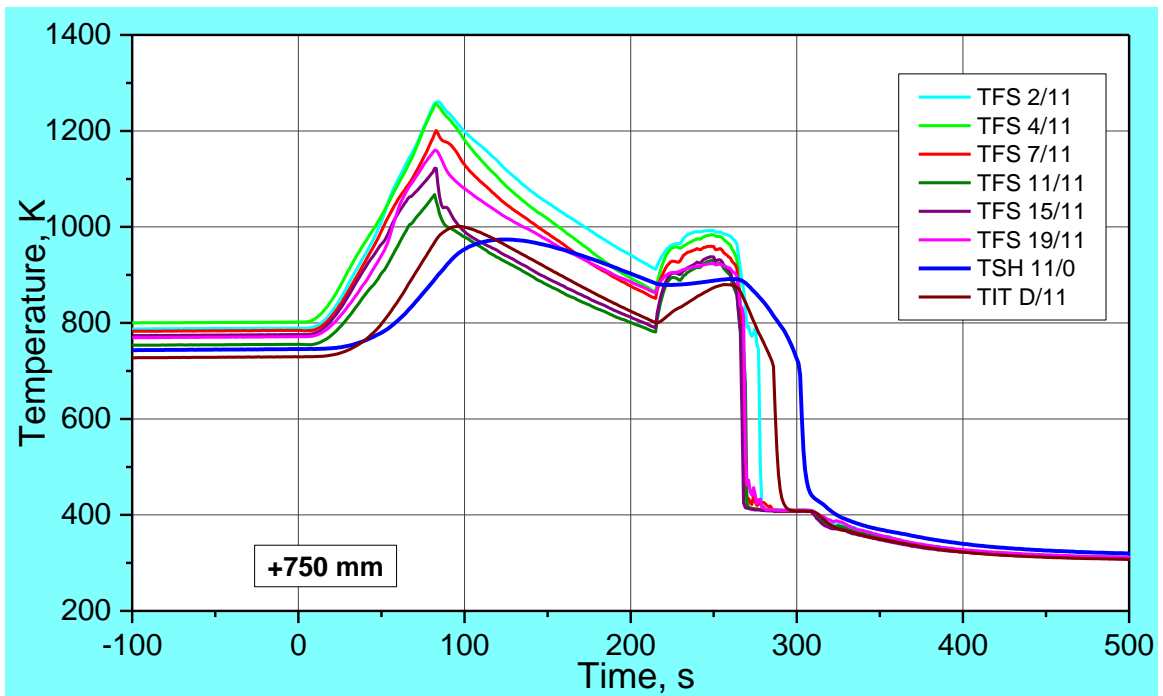


Figure 37 QUENCH-L4; Temperatures measured by rod cladding (TFS) and shroud (TSH 11/0), and corner rod internal (TIT D/11) thermocouples at 750 mm elevation.

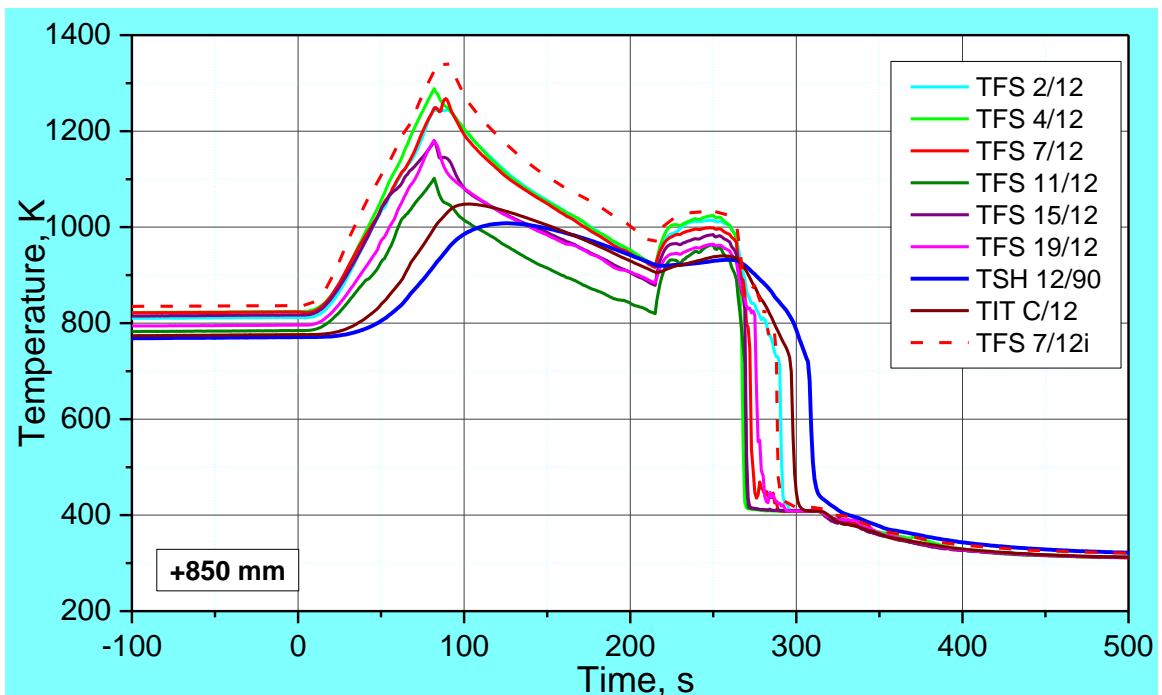


Figure 38 QUENCH-L4; Temperatures measured by rod cladding (TFS), shroud (TSH 12/90), and corner rod internal (TIT C/12) thermocouples at 850 mm elevation.

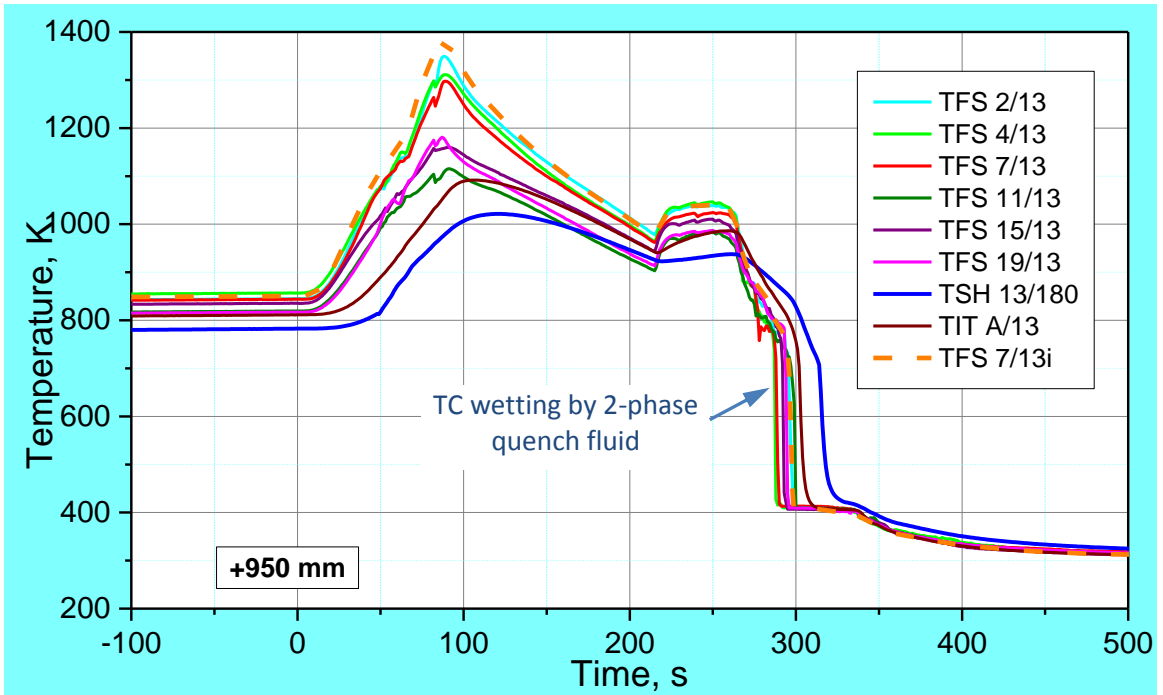


Figure 39 QUENCH-L4; Temperatures measured by rod cladding (TFS), shroud (TSH 13/180), and corner rod internal (TIT A/13) thermocouples at 950 mm elevation.

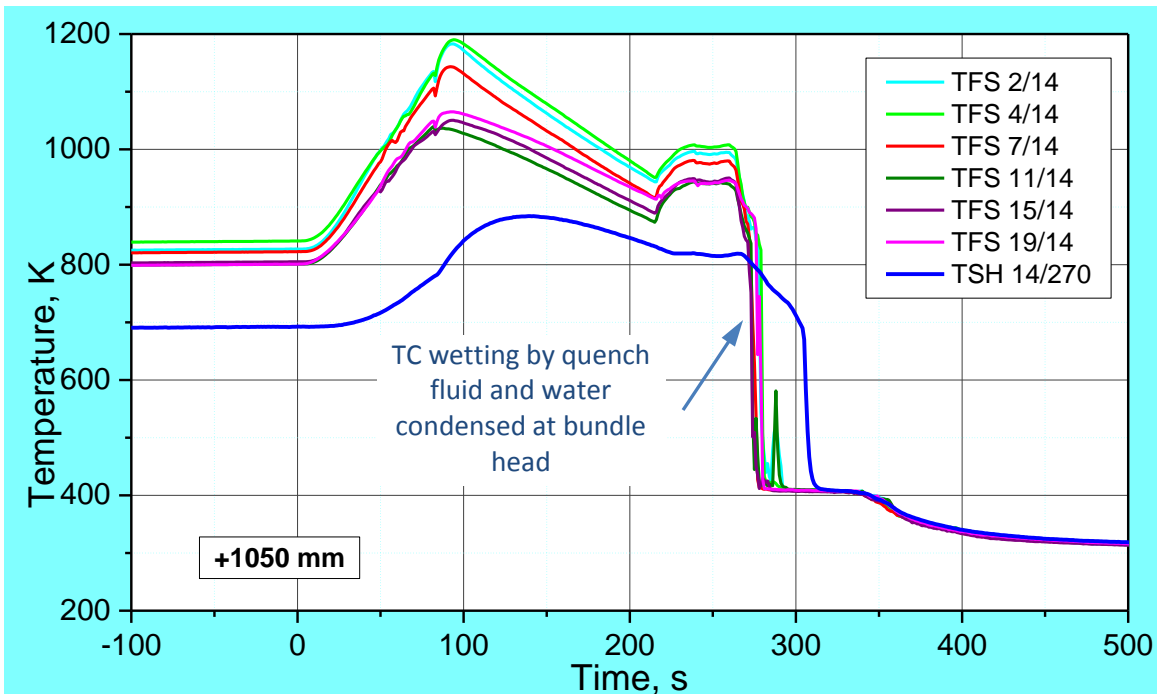


Figure 40 QUENCH-L4; Temperatures measured by rod cladding (TFS) and shroud (TSH 14/270) thermocouples at 1050 mm elevation.

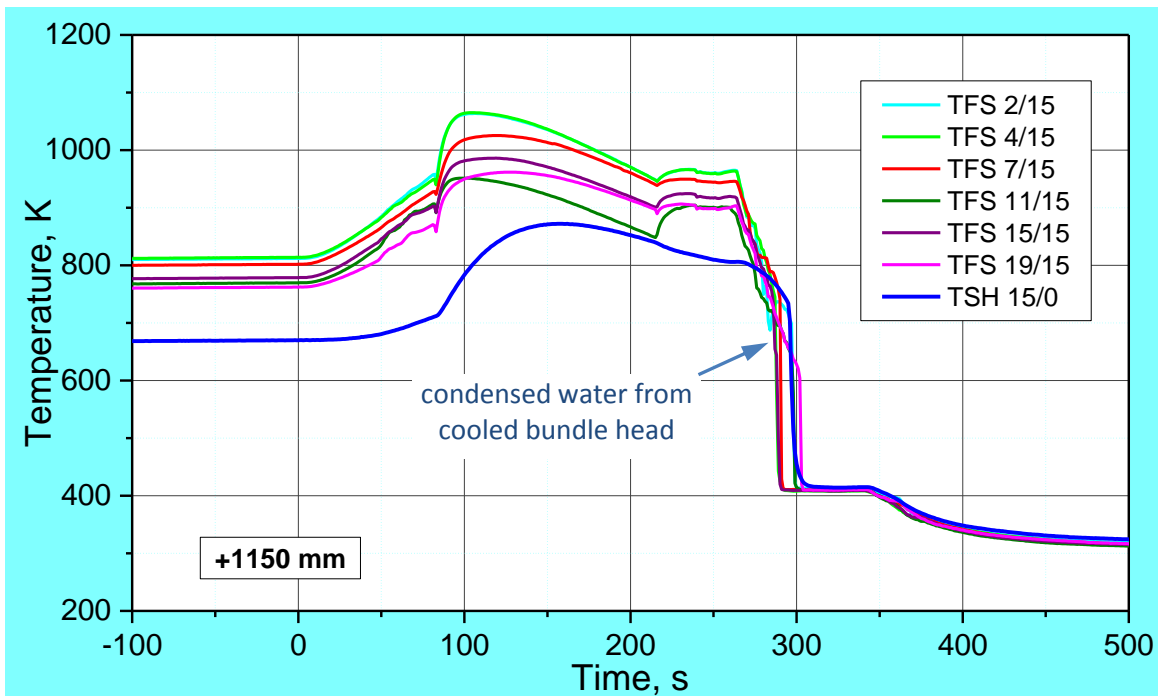


Figure 41 QUENCH-L4; Temperatures measured by rod cladding (TFS) and shroud (TSH 15/0) thermocouples at 1150 mm elevation.

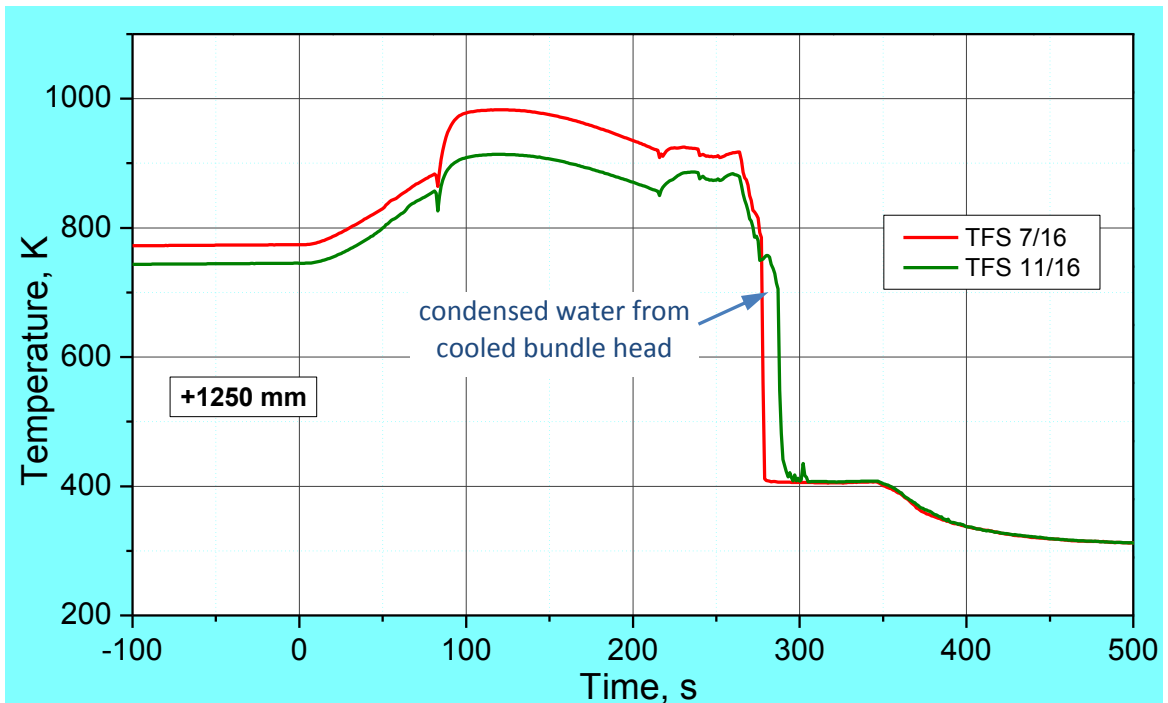


Figure 42 QUENCH-L4; Temperatures measured by rod cladding (TFS) thermocouples at 1250 mm elevation.

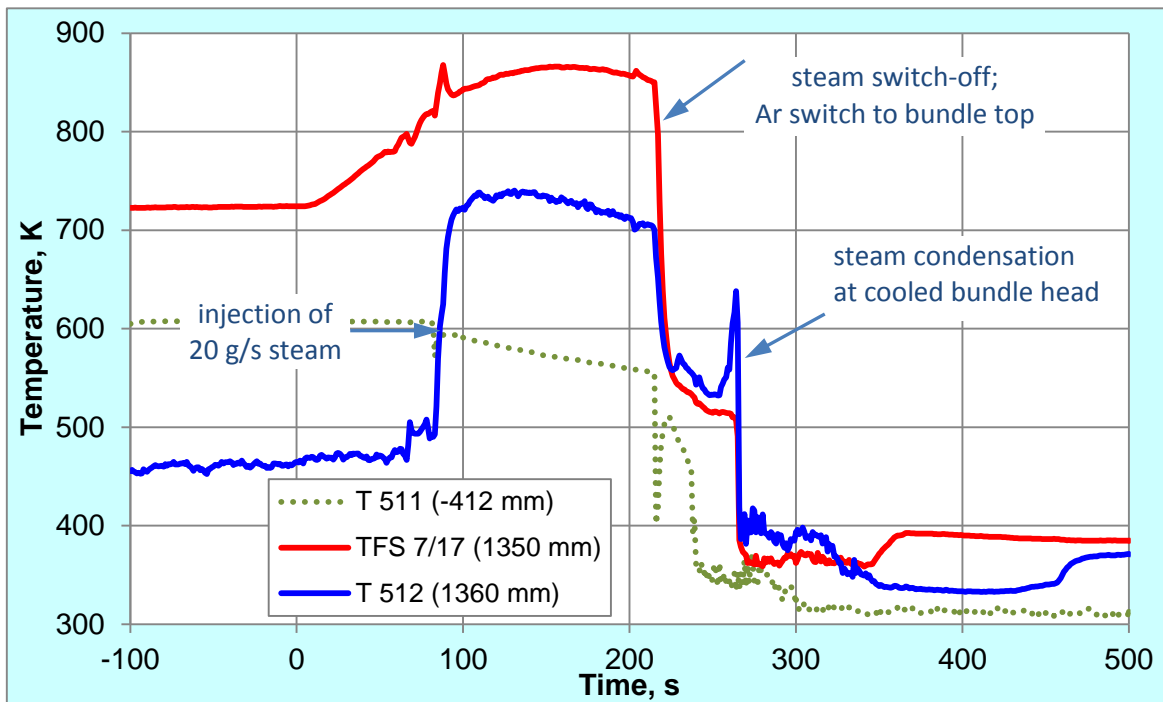


Figure 43 QUENCH-L4; Temperatures measured by rod cladding (TFS 7/17) thermocouple at 1350 mm elevation and gas temperature (T 512) at 1360 mm between shroud and rod #20; T511 depicts the gas temperature at the bundle inlet.

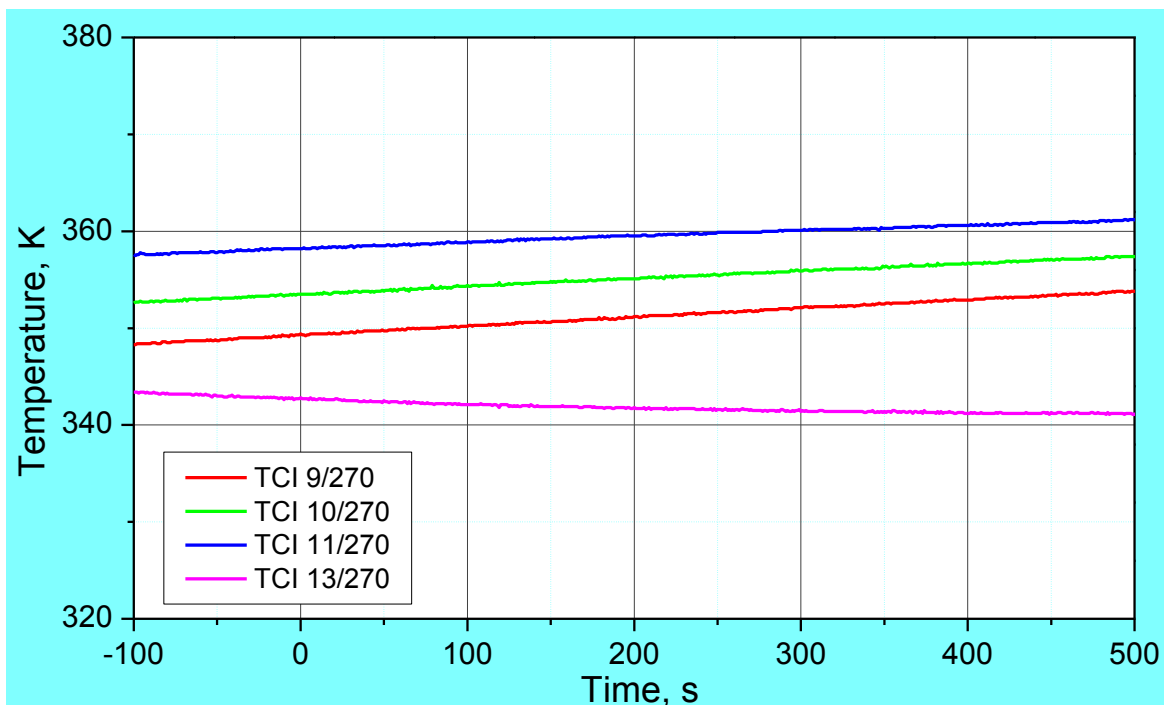


Figure 44 QUENCH-L4; Overview of the TCI (inner cooling jacket).

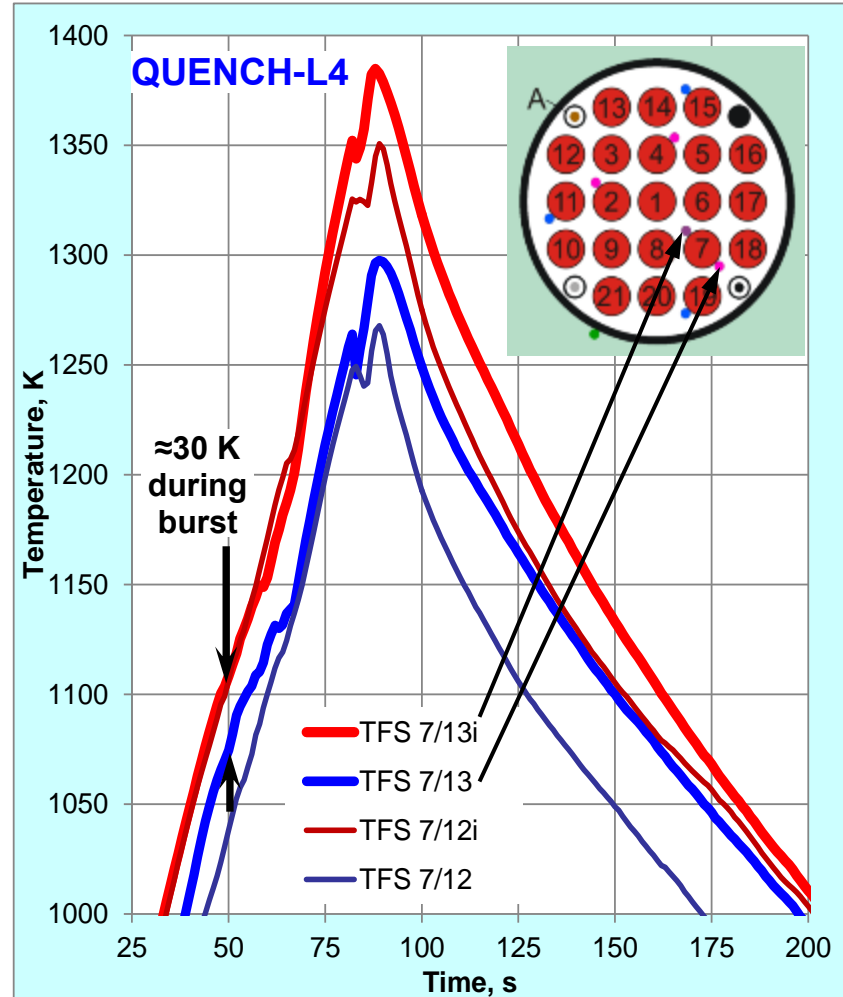
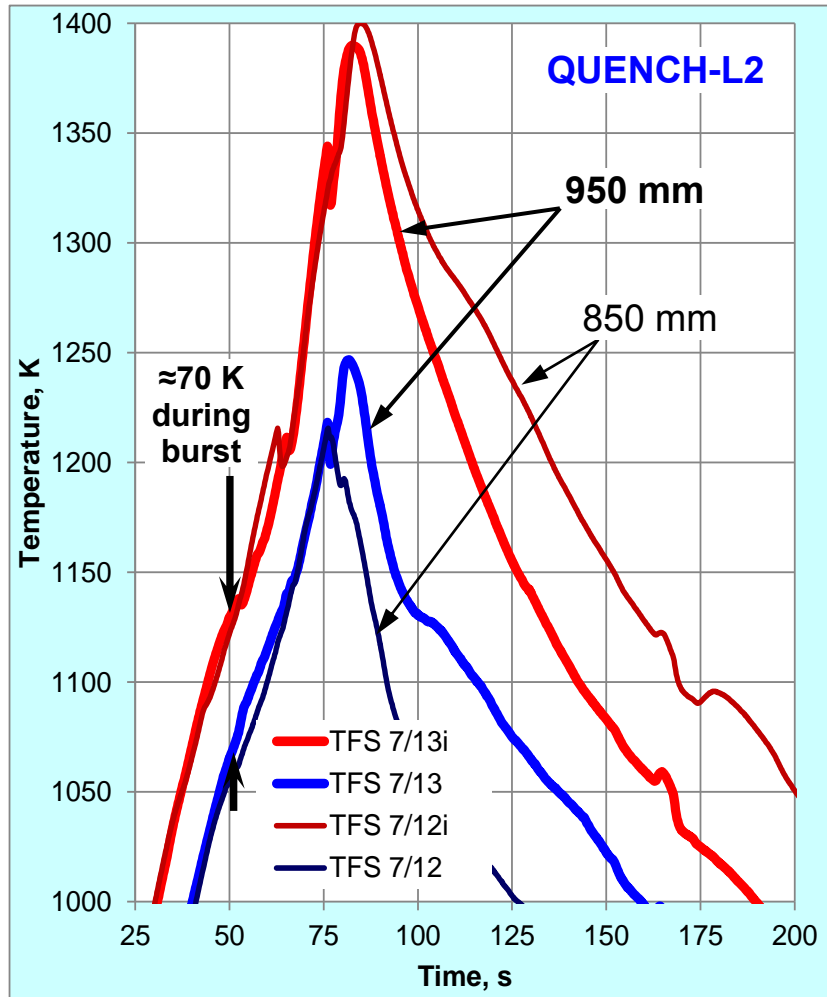


Figure 45 Comparison of radial temperature difference at rod #7 for bundles QUENCH-L2 and QUENCH-L4.

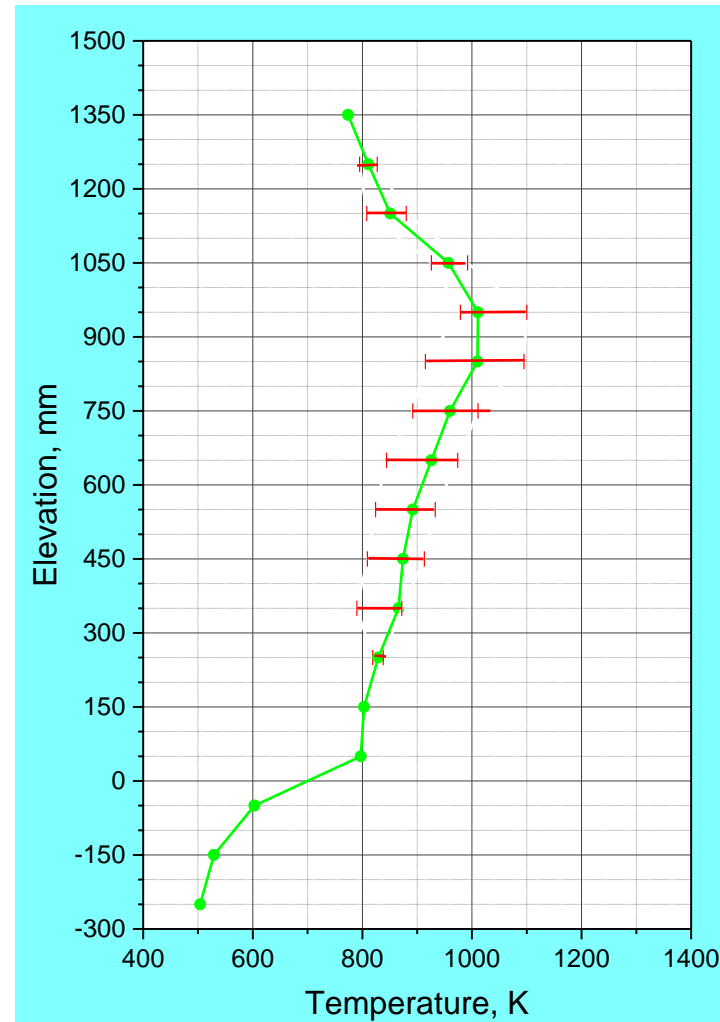
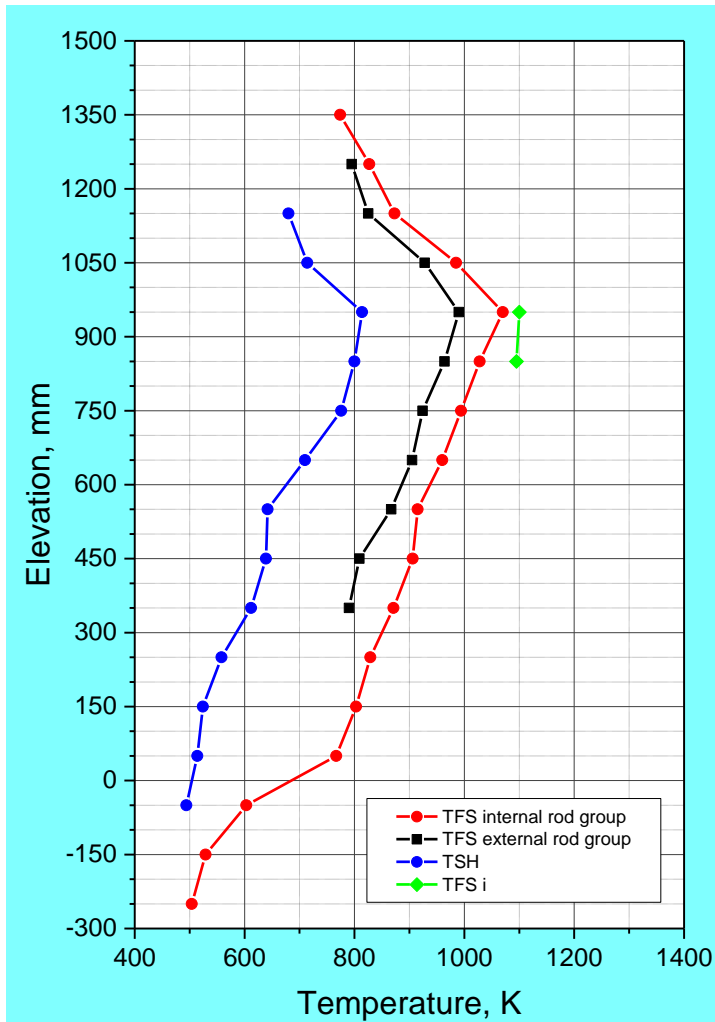


Figure 46 QUENCH-L4; Axial temperature profile TFS internal and external rod group together with TSH (left) and axial temperature profile of all TFS (right) at 48 s (first cladding burst).

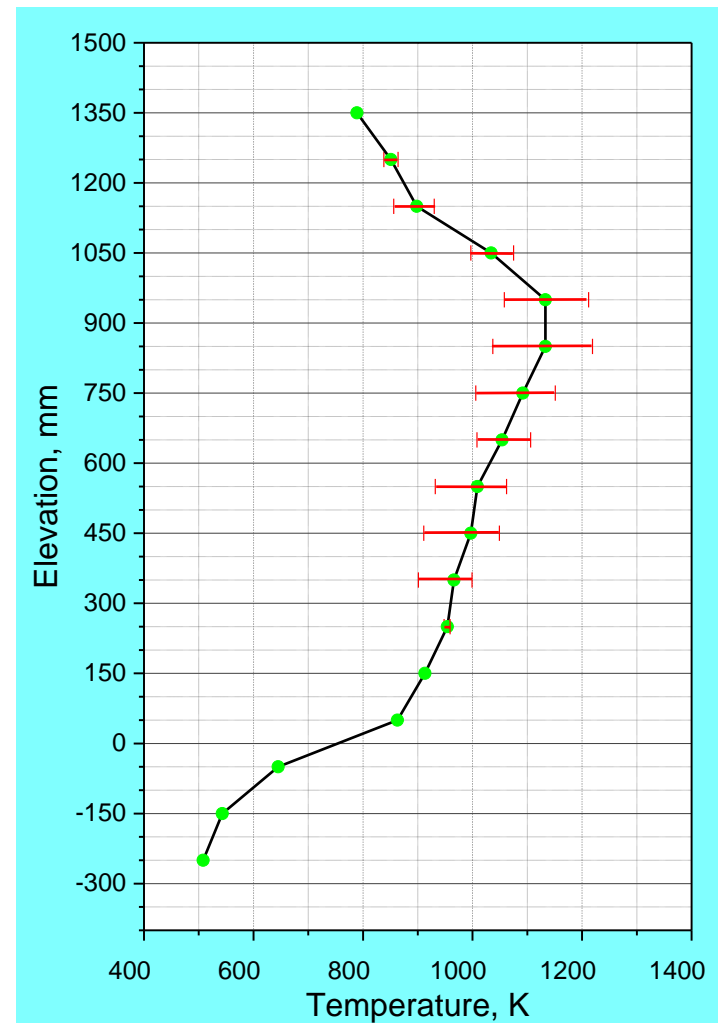
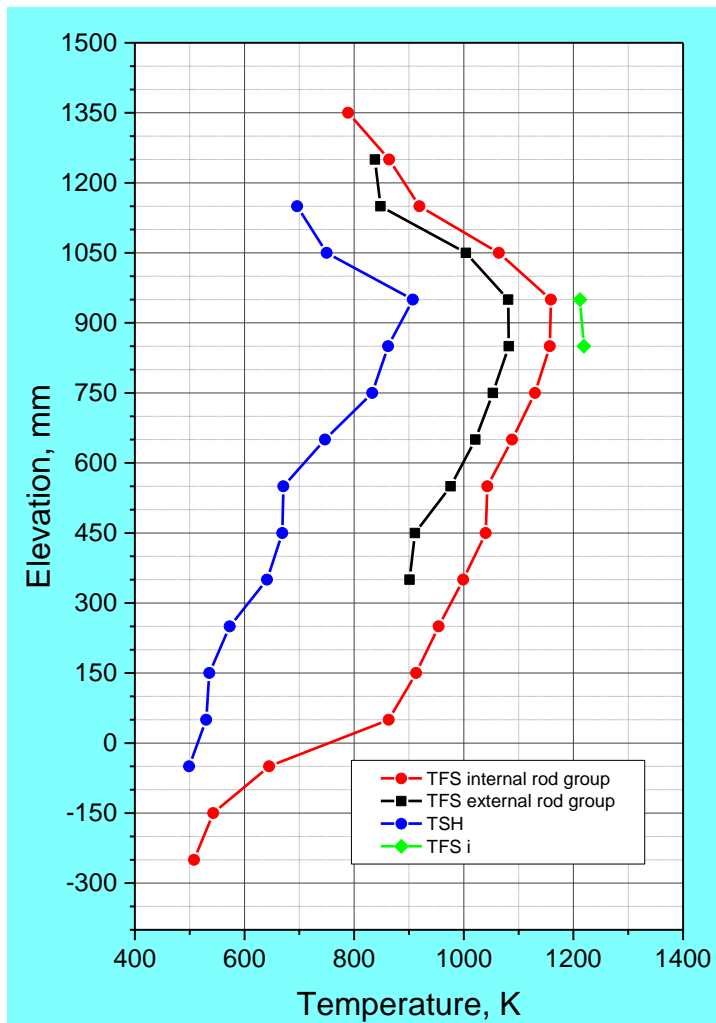


Figure 47 QUENCH-L4; Axial temperature profile TFS internal and external rod group together with TSH (left) and axial temperature profile of all TFS (right) at 68 s (last cladding burst).

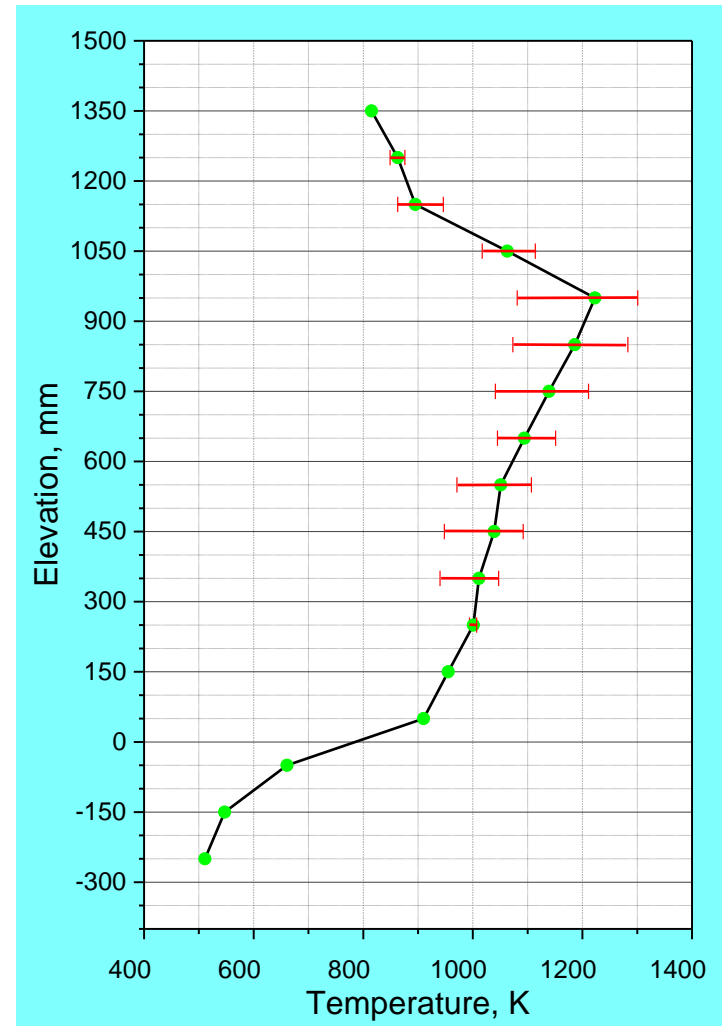
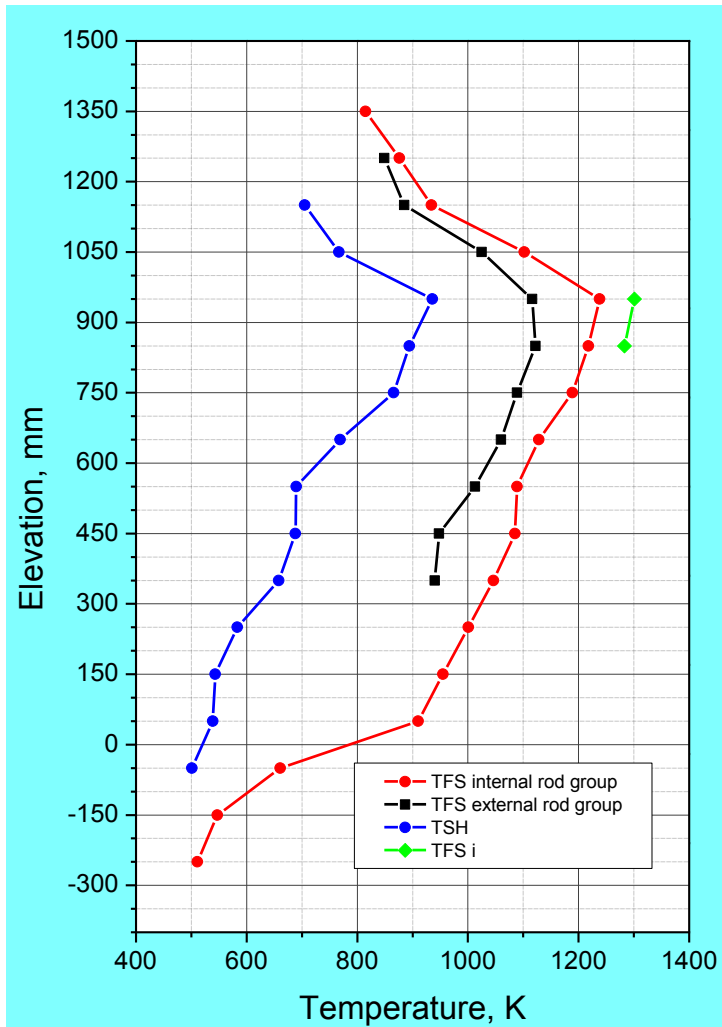


Figure 48 QUENCH-L4; Axial temperature profile TFS internal and external rod group together with TSH (left) and axial temperature profile of all TFS (right) at 76 s (end of transient).

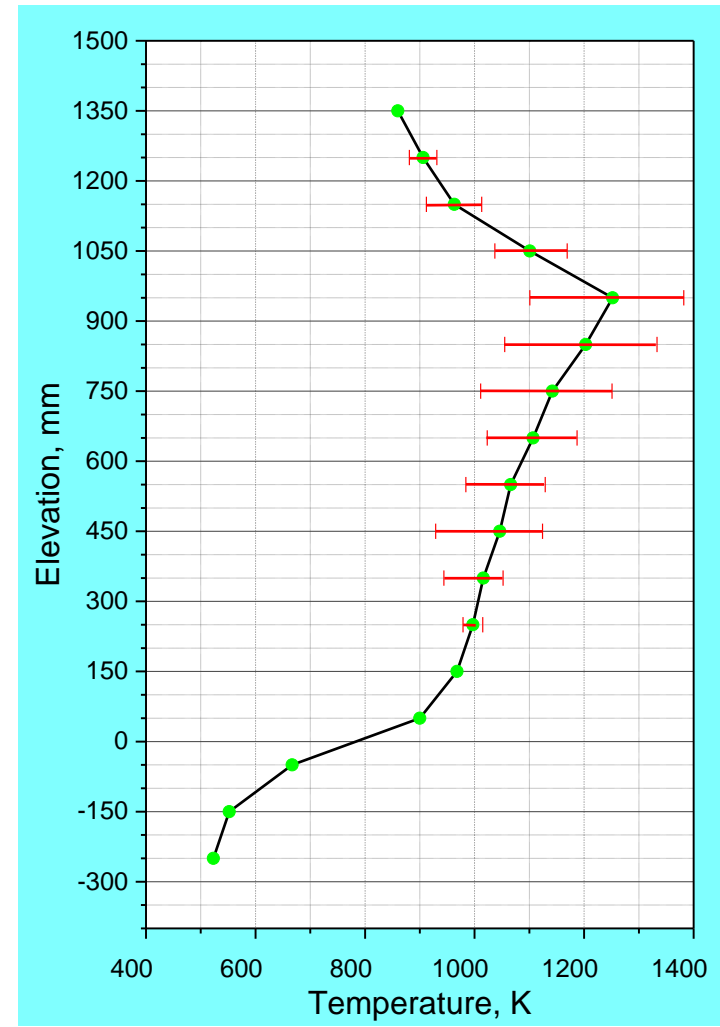
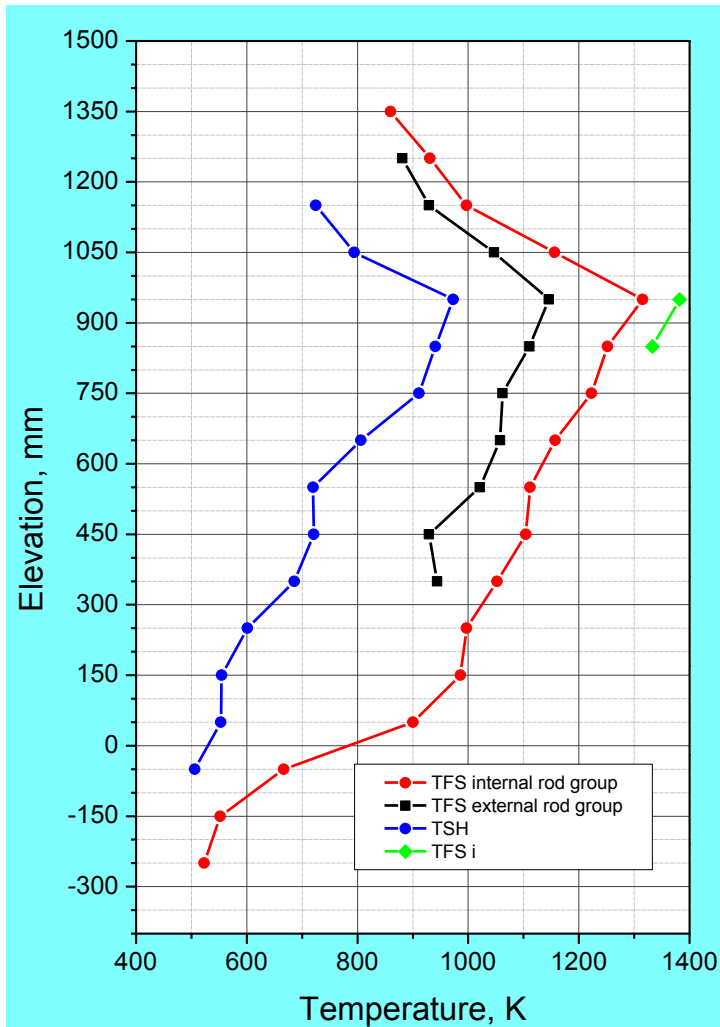


Figure 49 QUENCH-L4; Axial temperature profile TFS internal and external rod group together with TSH (left) and axial temperature profile of all TFS (right) at 87 s (max bundle temperature).

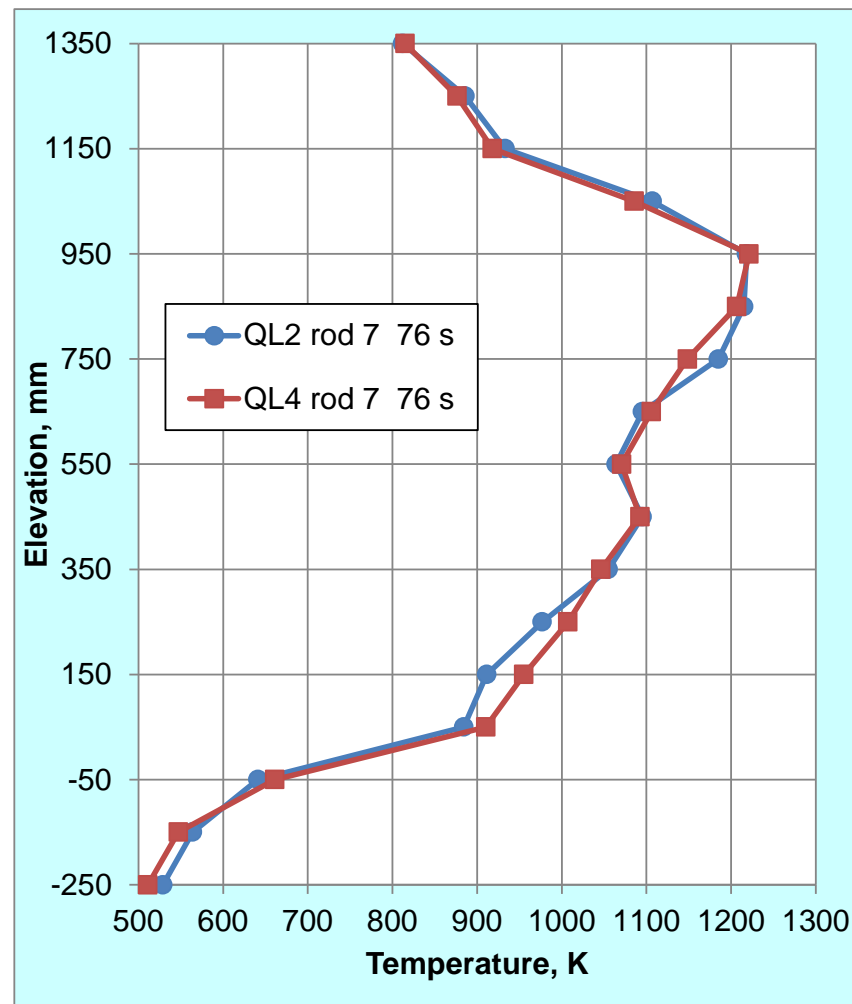
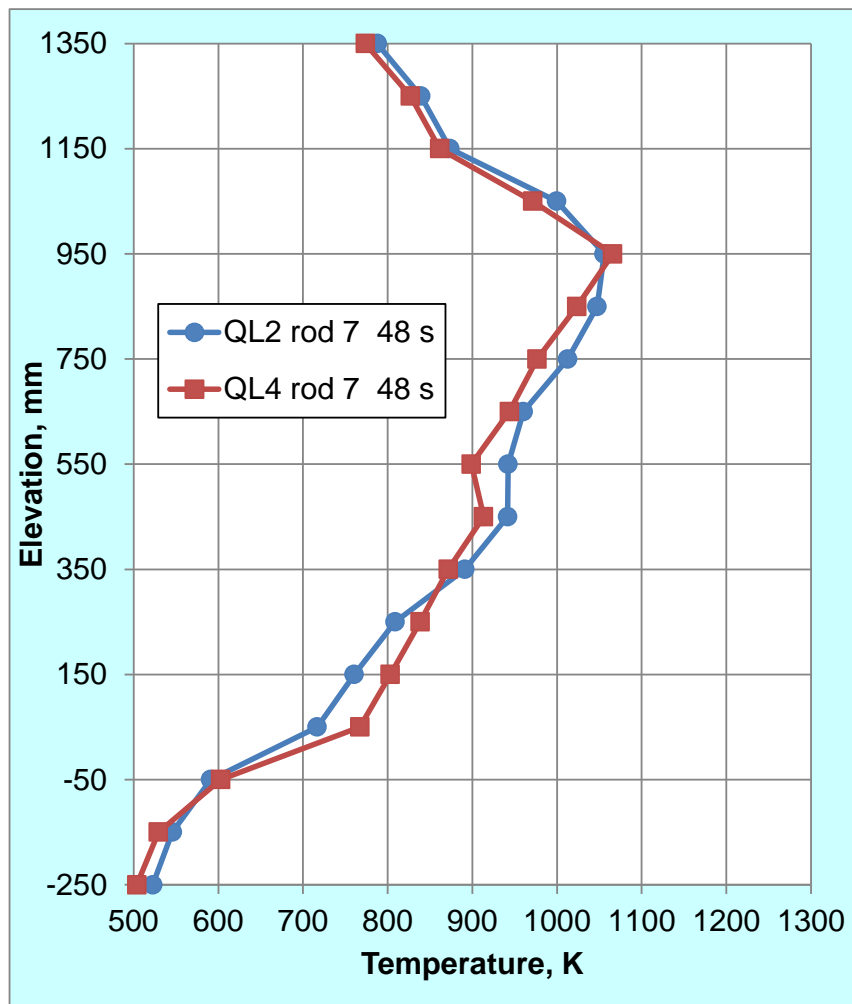


Figure 50 Similar axial temperature distribution for rod #7 for bundles QUENCH-L2 and QUENCH-L4 on the first cladding burst (48 s) and on the end of transition (76 s).

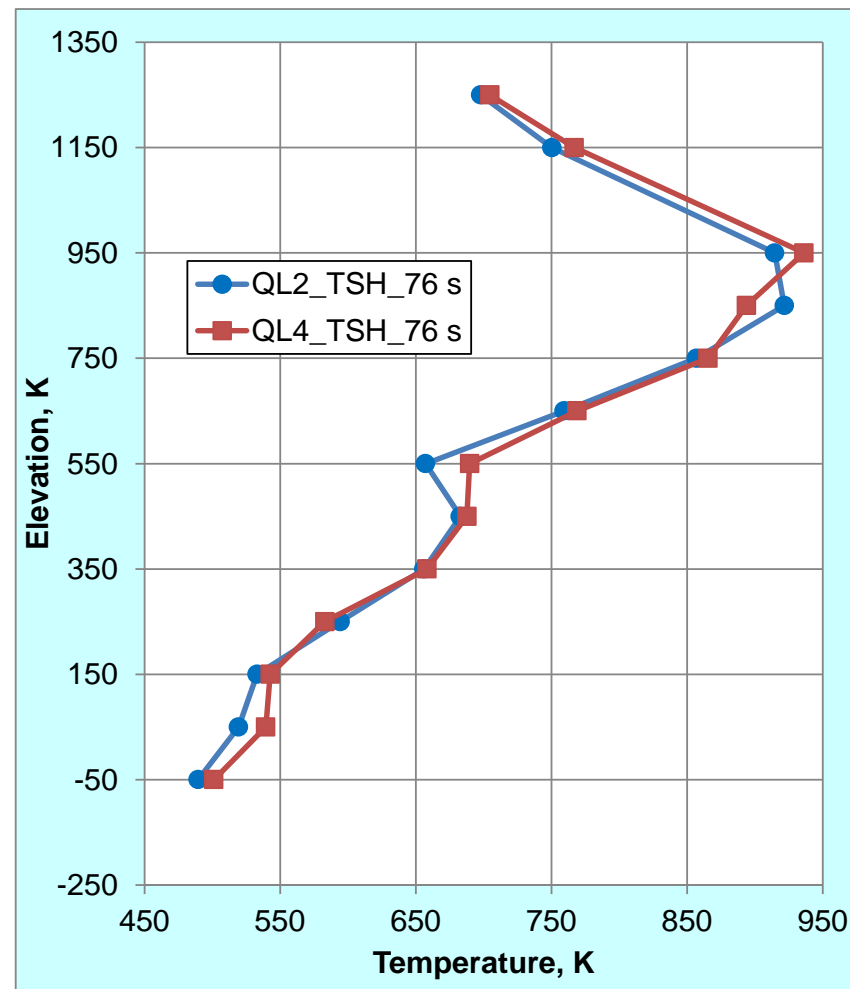
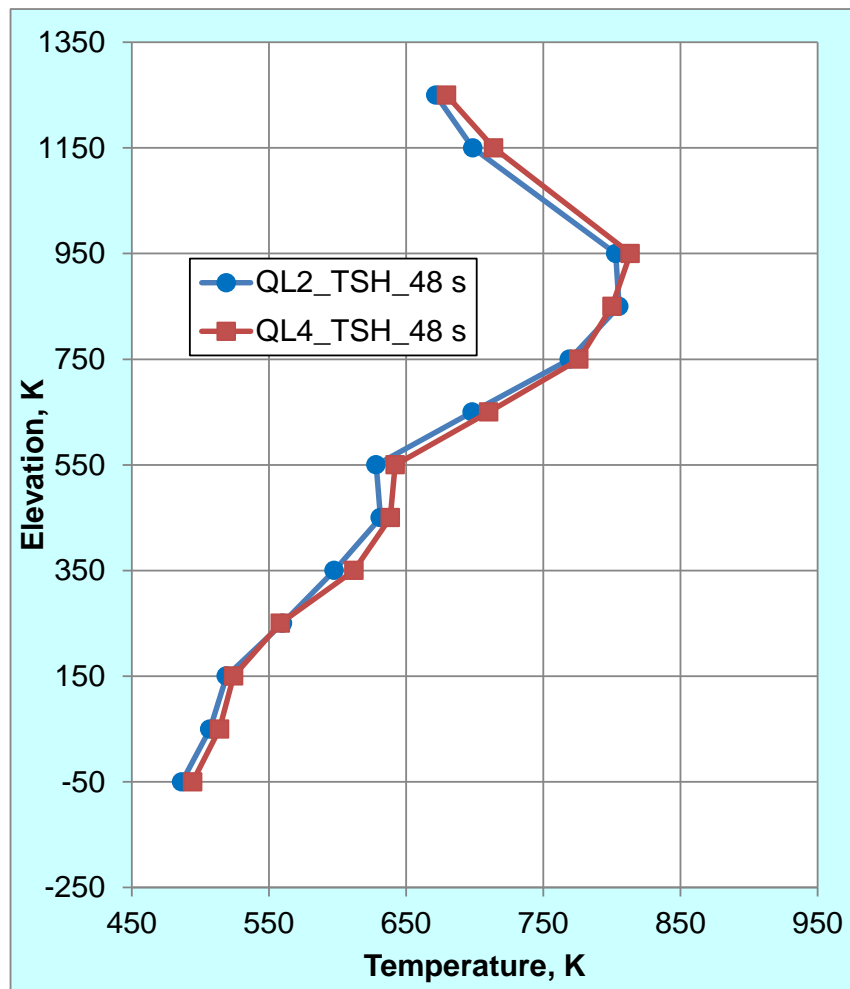


Figure 51 Similar axial temperature distribution for shroud of bundles QUENCH-L2 and QUENCH-L4 on the first cladding burst (48 s) and on the end of transition (76 s).

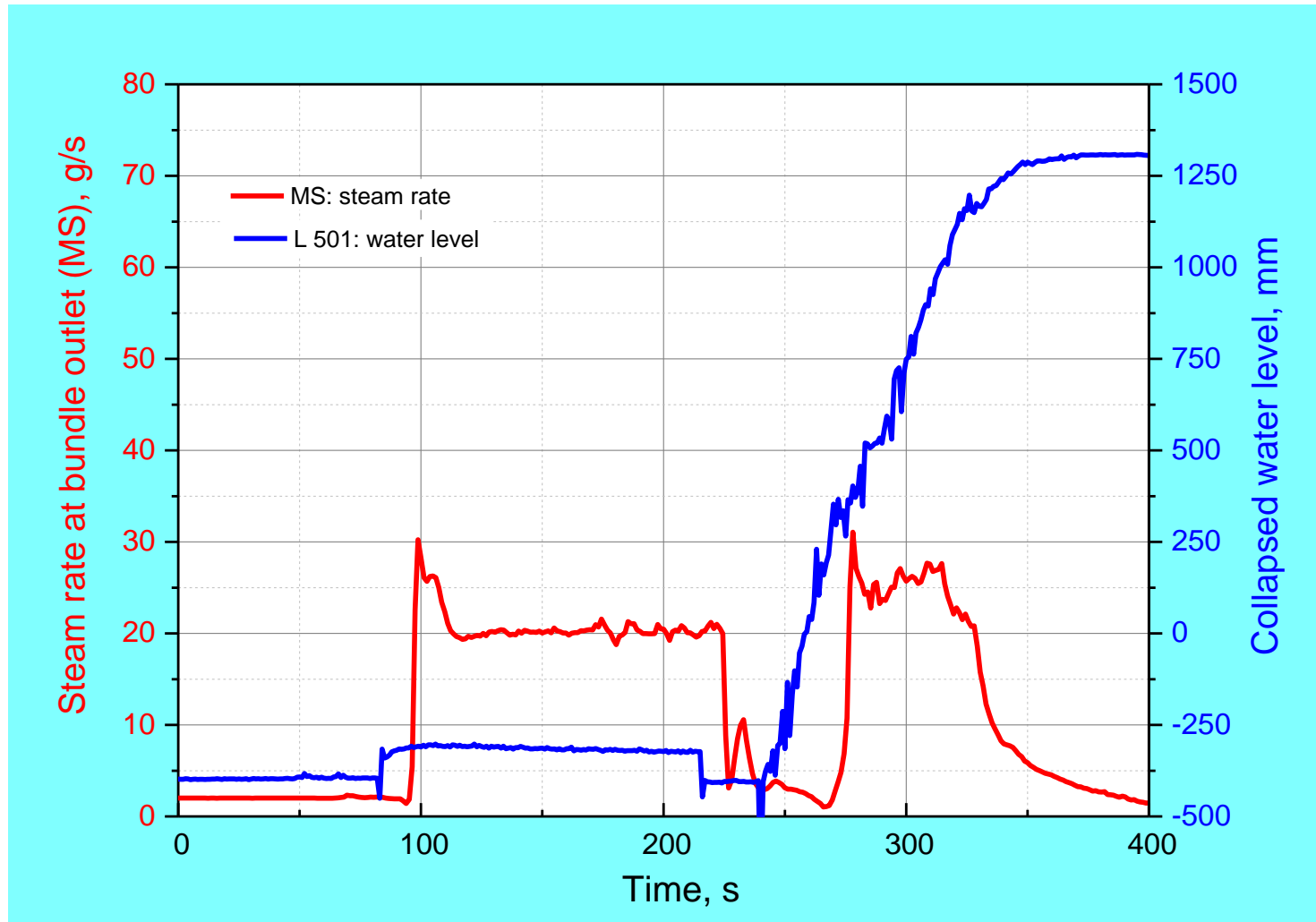


Figure 52 QUENCH-L4; Mass spectrometer measurements: steam during reflood.

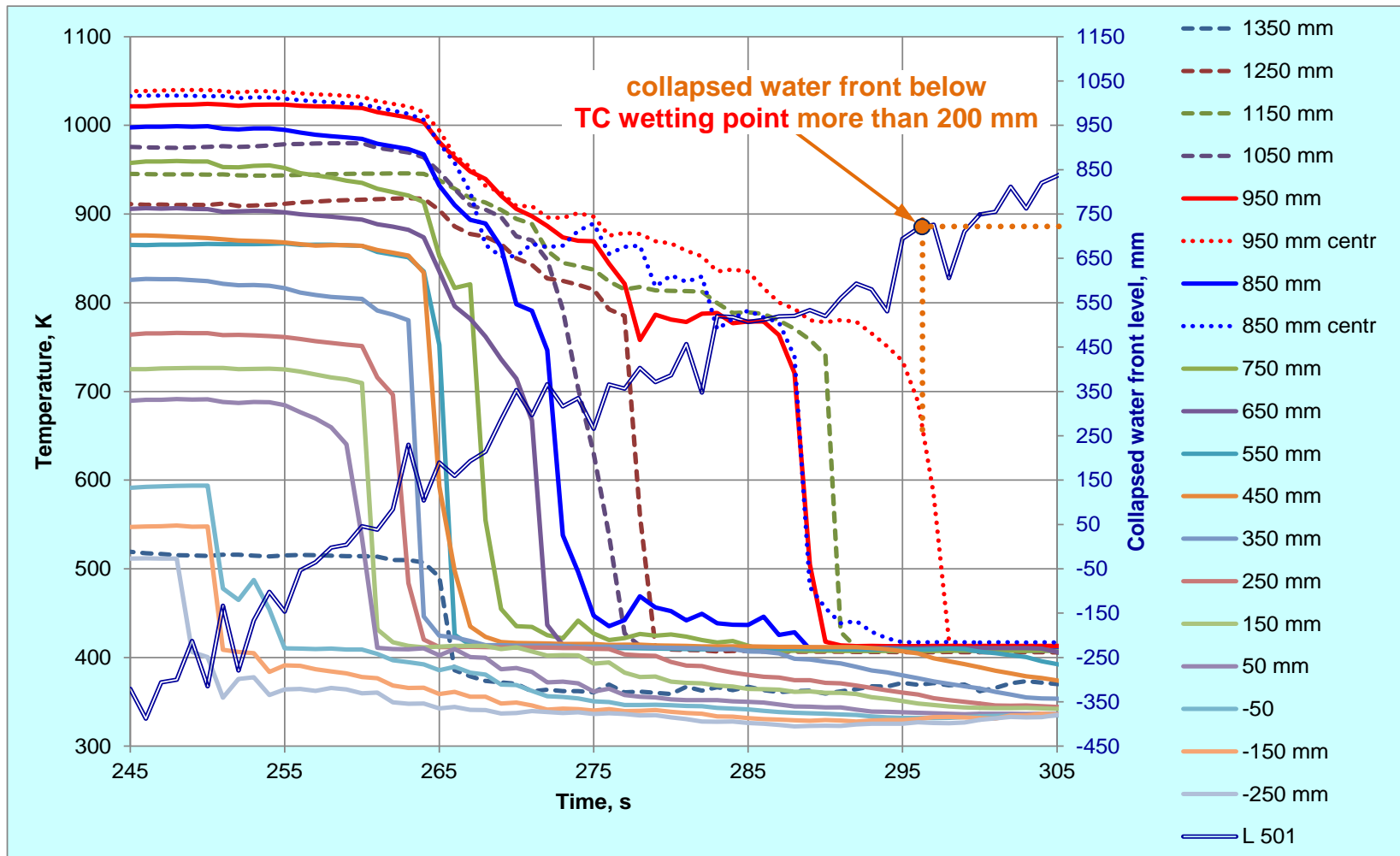


Figure 53 QUENCH-L4; Sequence of wetting of surface thermocouples for rod #7 by 2-phase fluid formed above collapsed water front (L 501).

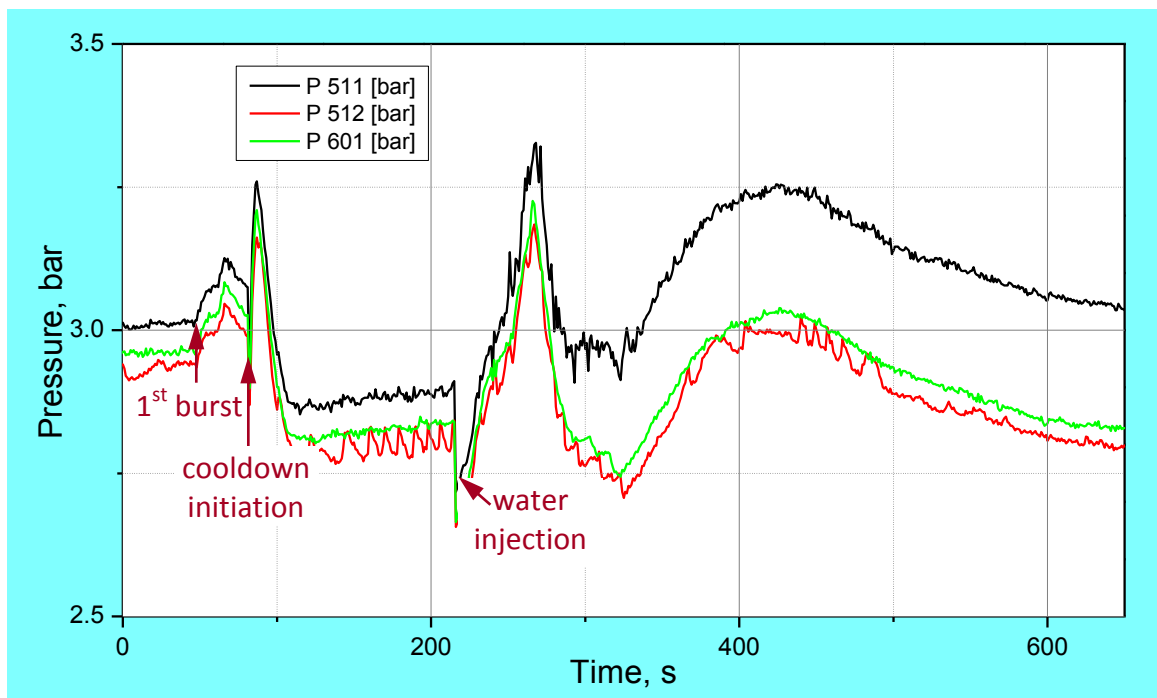


Figure 54 QUENCH-L4; System pressure measured at test section inlet P 511, at outlet P 512, and in the off-gas pipe P 601.

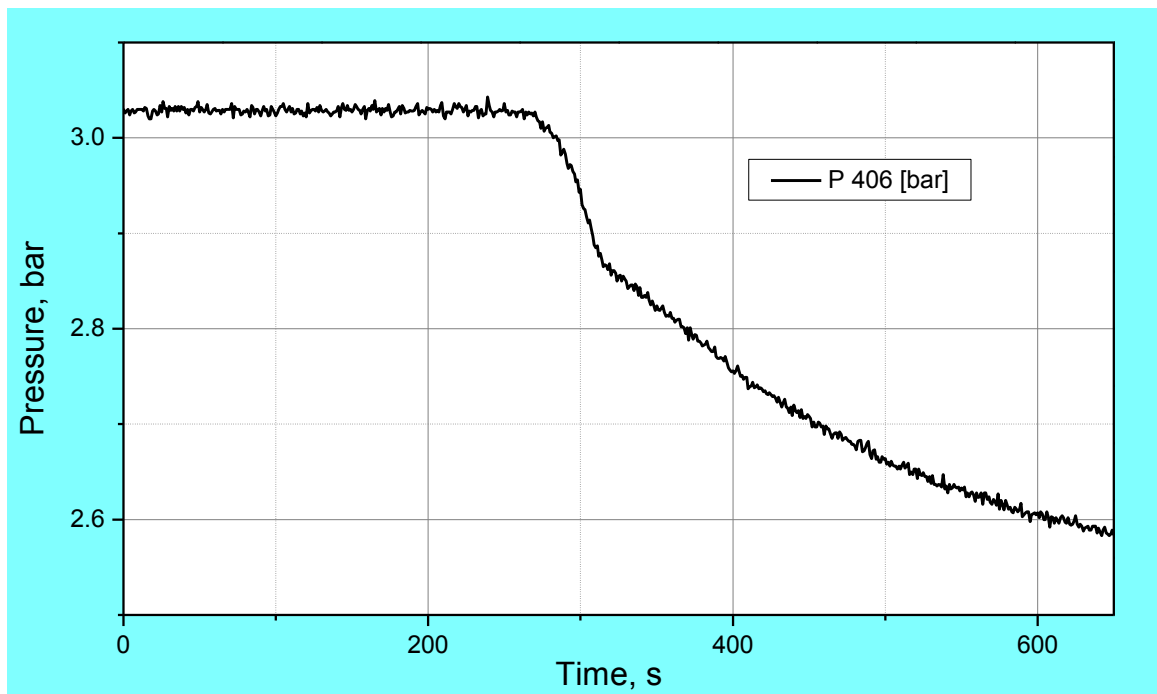


Figure 55 QUENCH-L4; Argon pressure between shroud and cooling jacket P 406 demonstrates tightness of the shroud (pressure change is independent from system pressure oscillations).

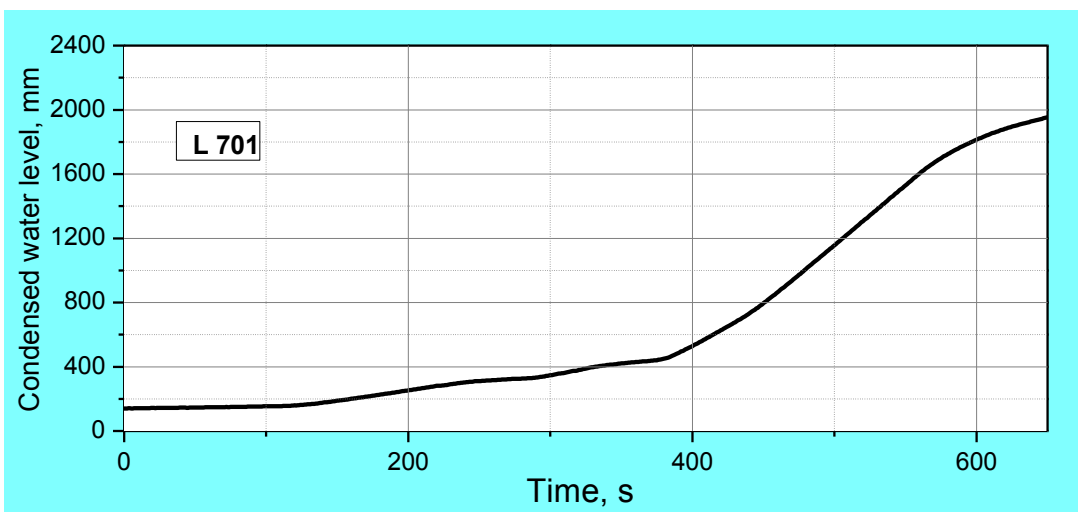
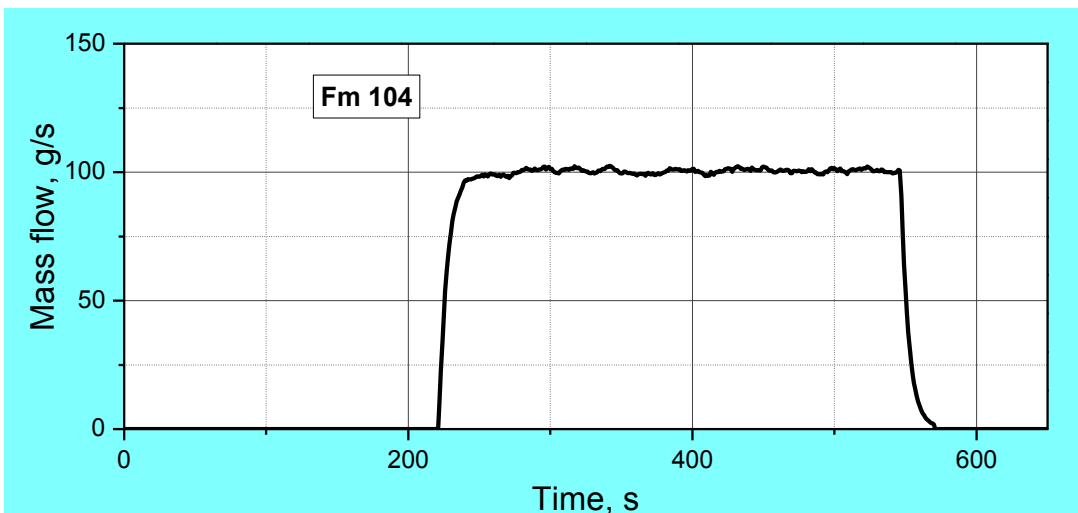
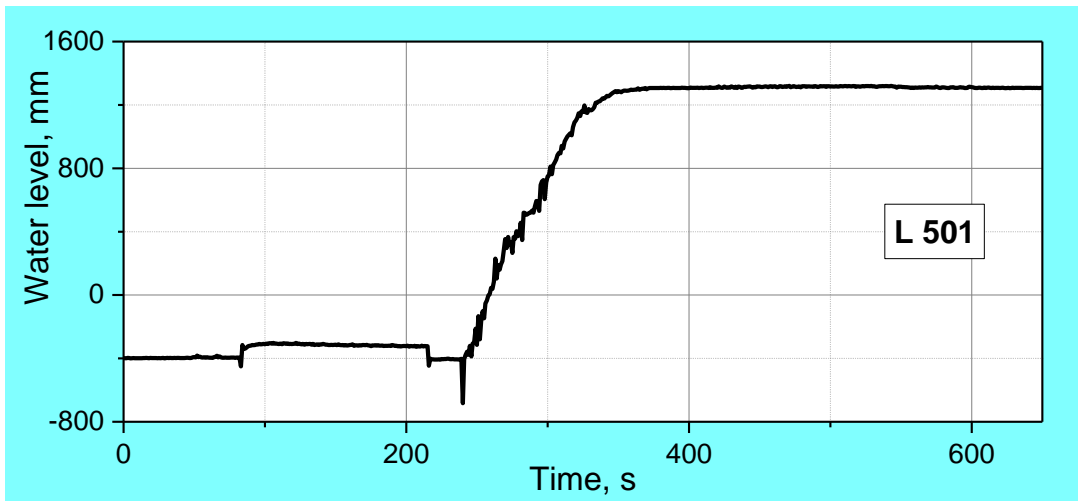


Figure 56 QUENCH-L4; Quench measurement of collapsed water level (L 501), top, water mass flow rate (Fm 104), center, condensed water (L 701), bottom.

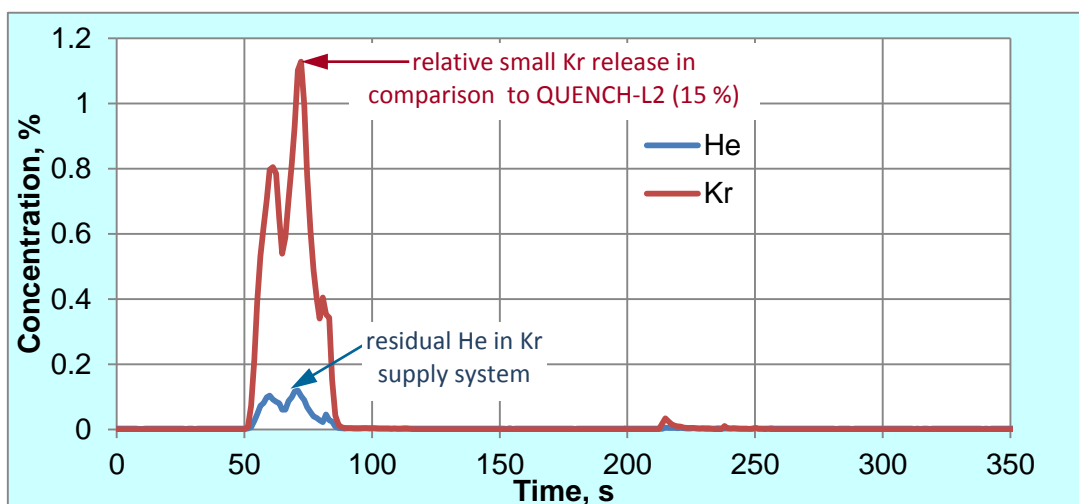
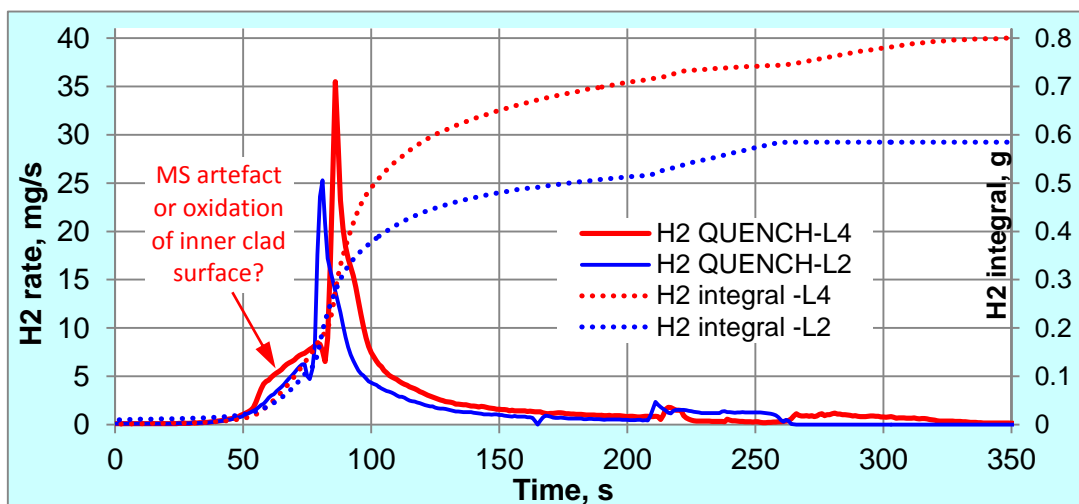
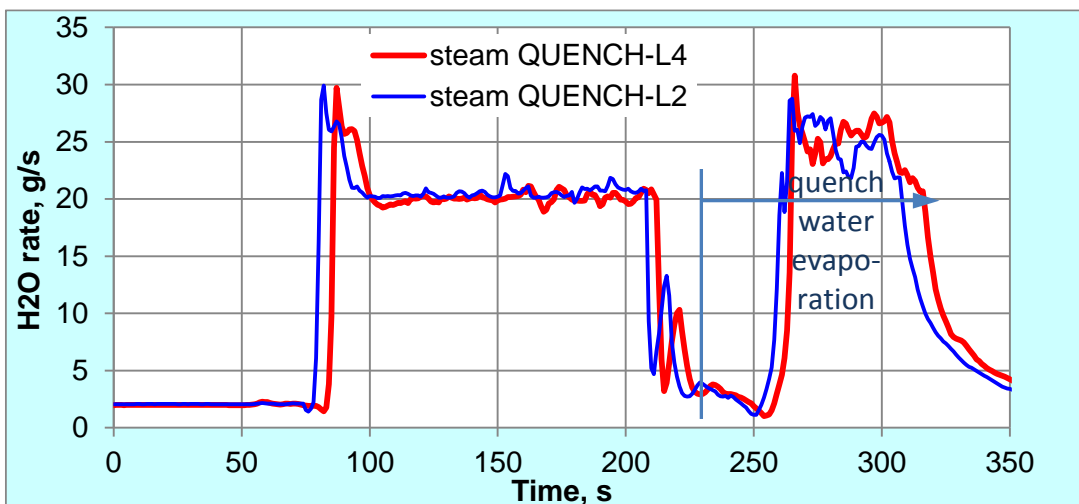


Figure 57 QUENCH-L4; Steam rate (top), hydrogen rate (center), krypton concentration (bottom) measured by mass spectrometry (MS).

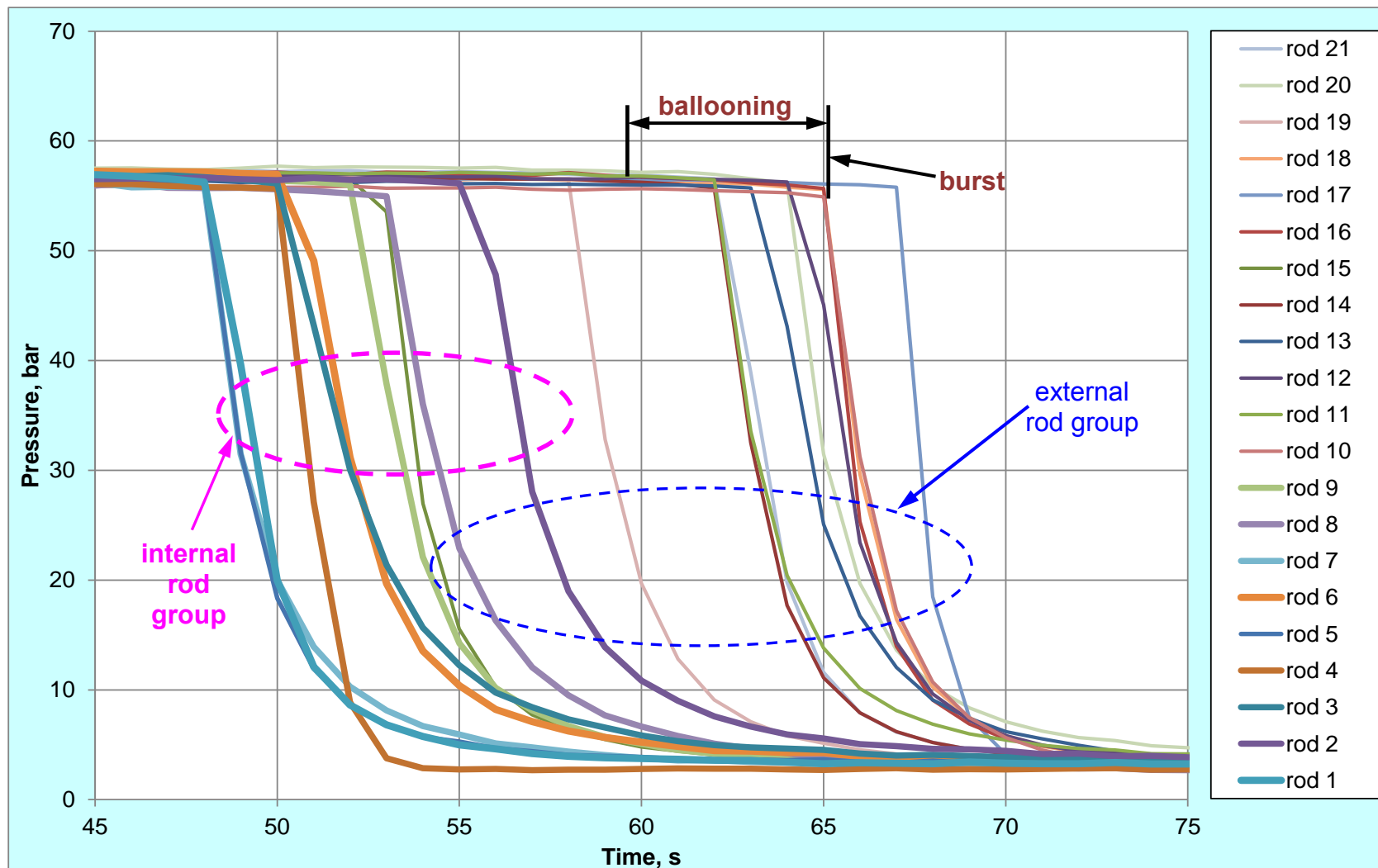


Figure 58 QUENCH-L4; Pressure change during the heating phase, cladding ballooning and burst.

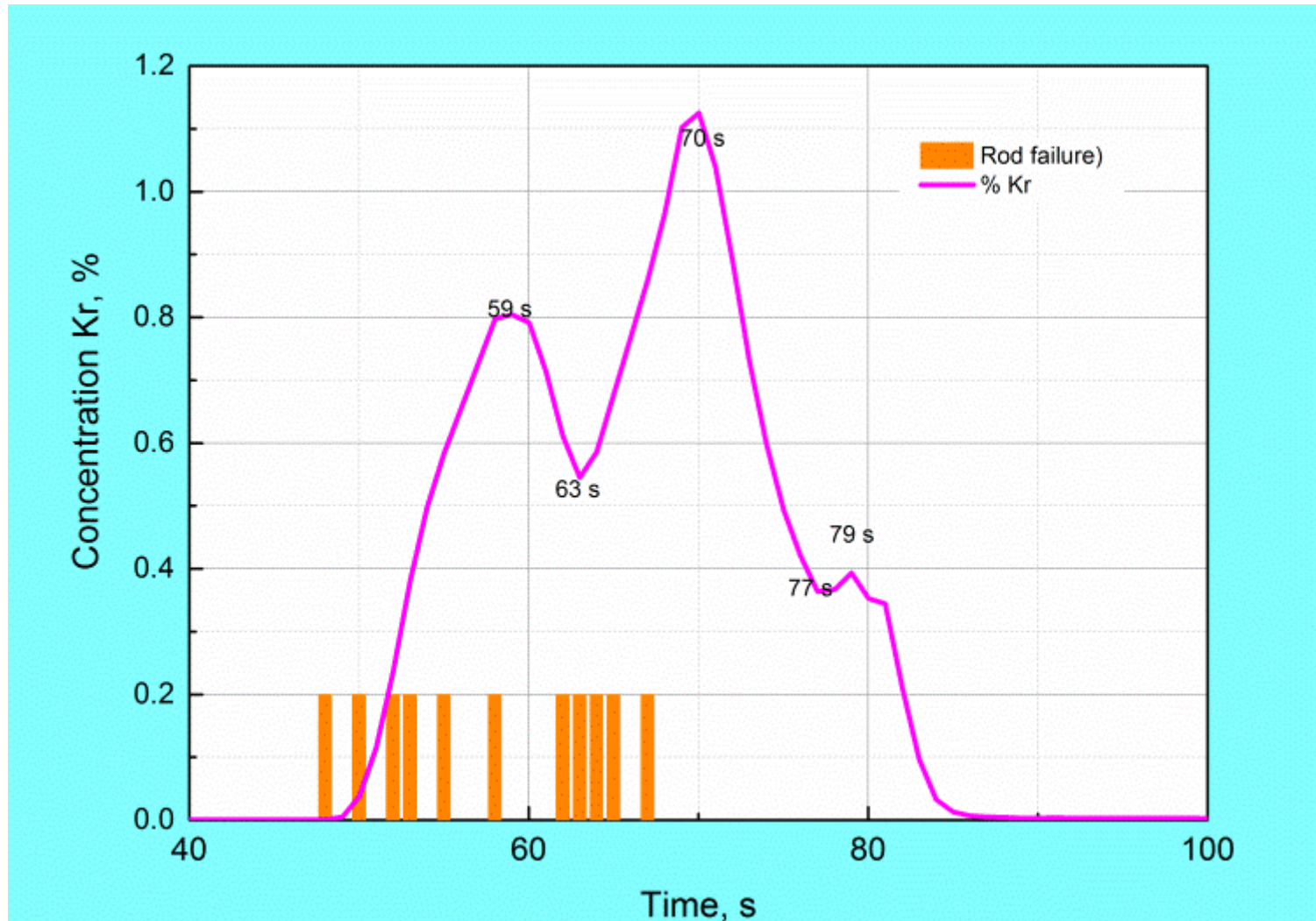


Figure 59 QUENCH-L4; Mass spectrometer measurements: krypton as burst indicator.

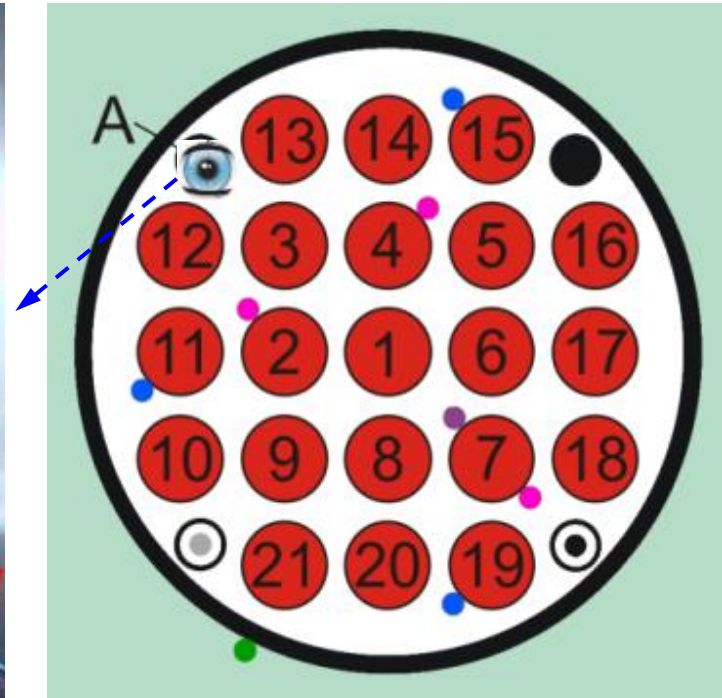
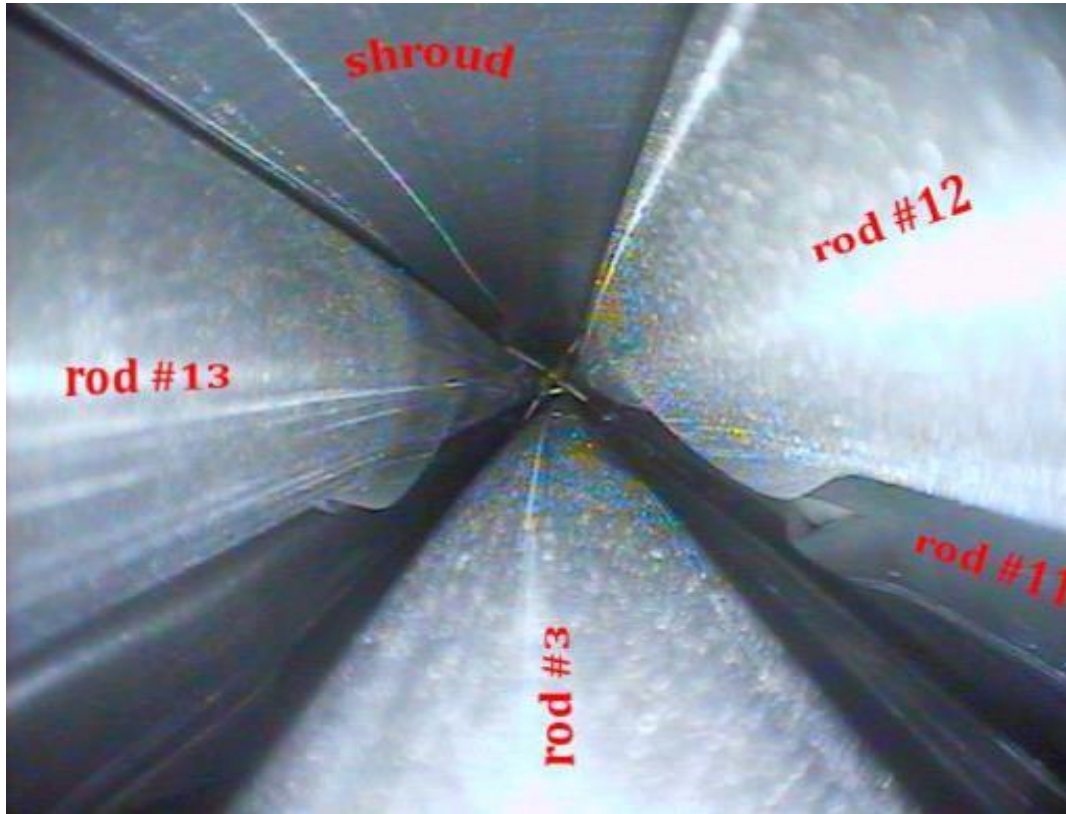


Figure 60 QUENCH-L4; Videoscope observations with camera inserted from the bundle bottom at position of corner rod A.

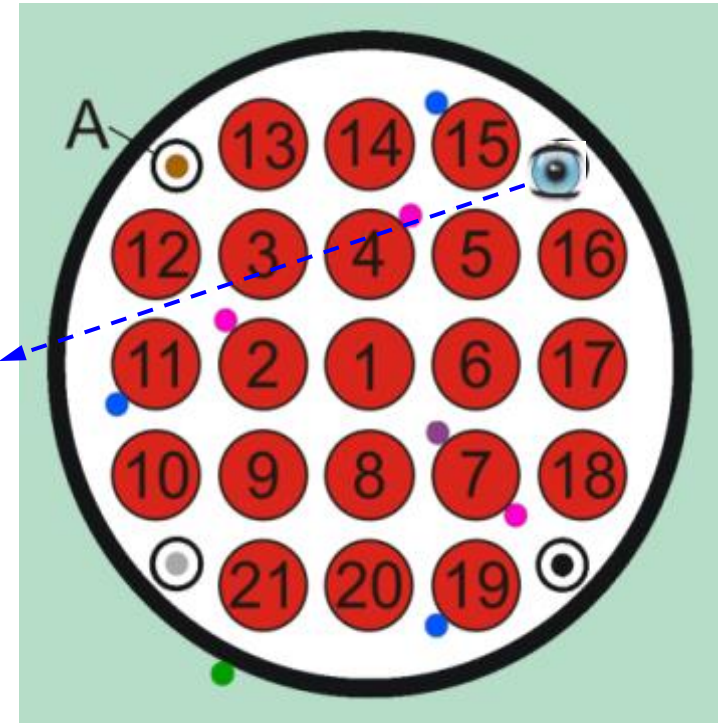
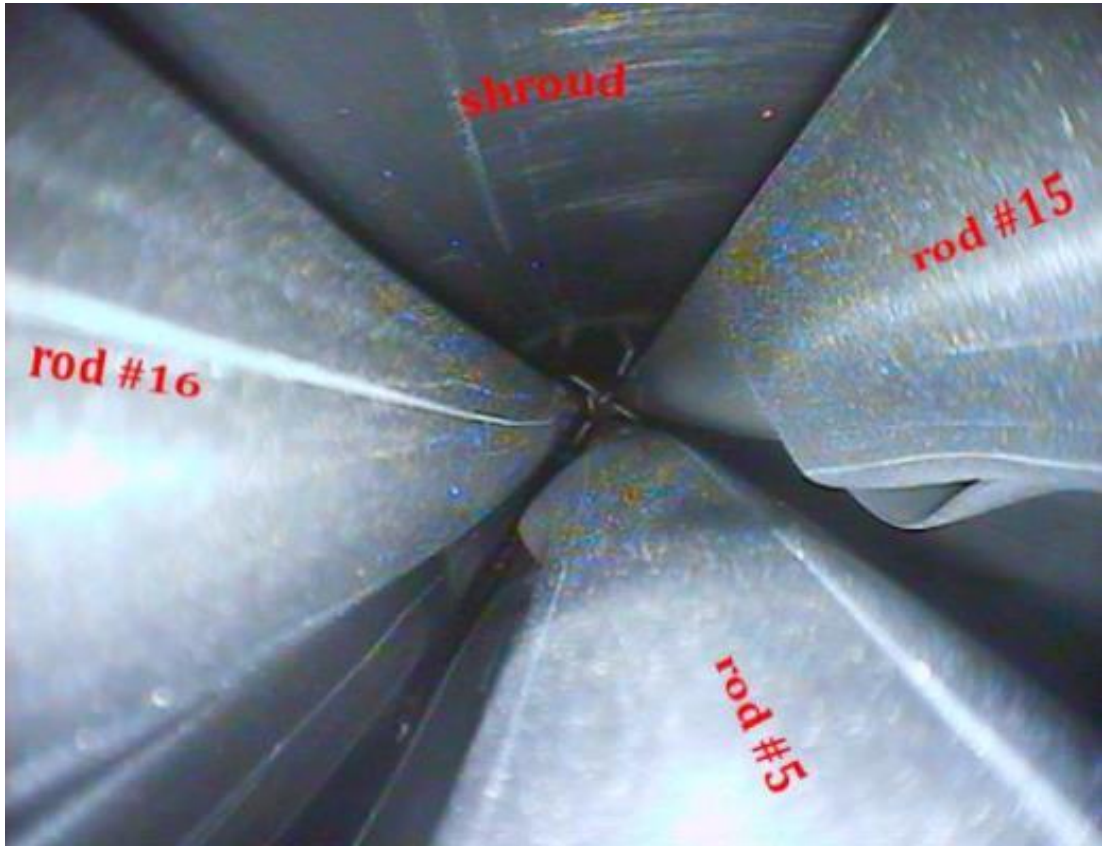


Figure 61 QUENCH-L4; Videoscope observations with camera inserted from the bundle bottom at position of corner rod B.

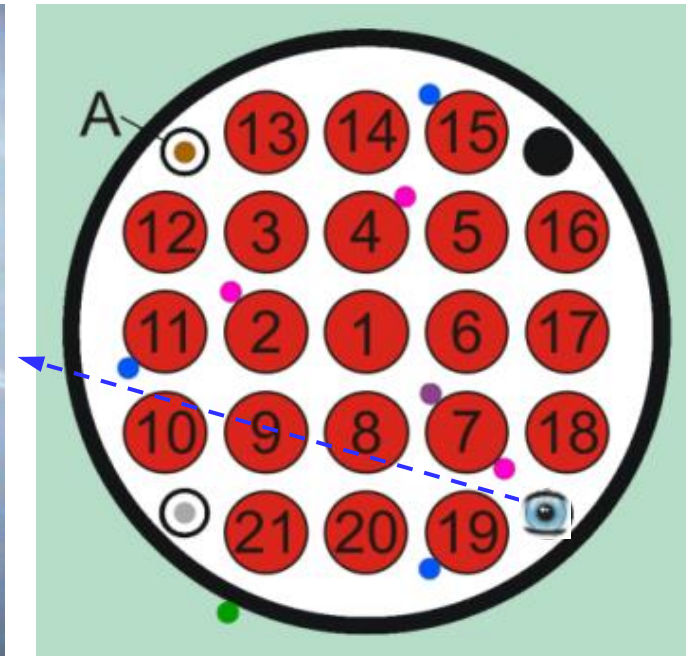
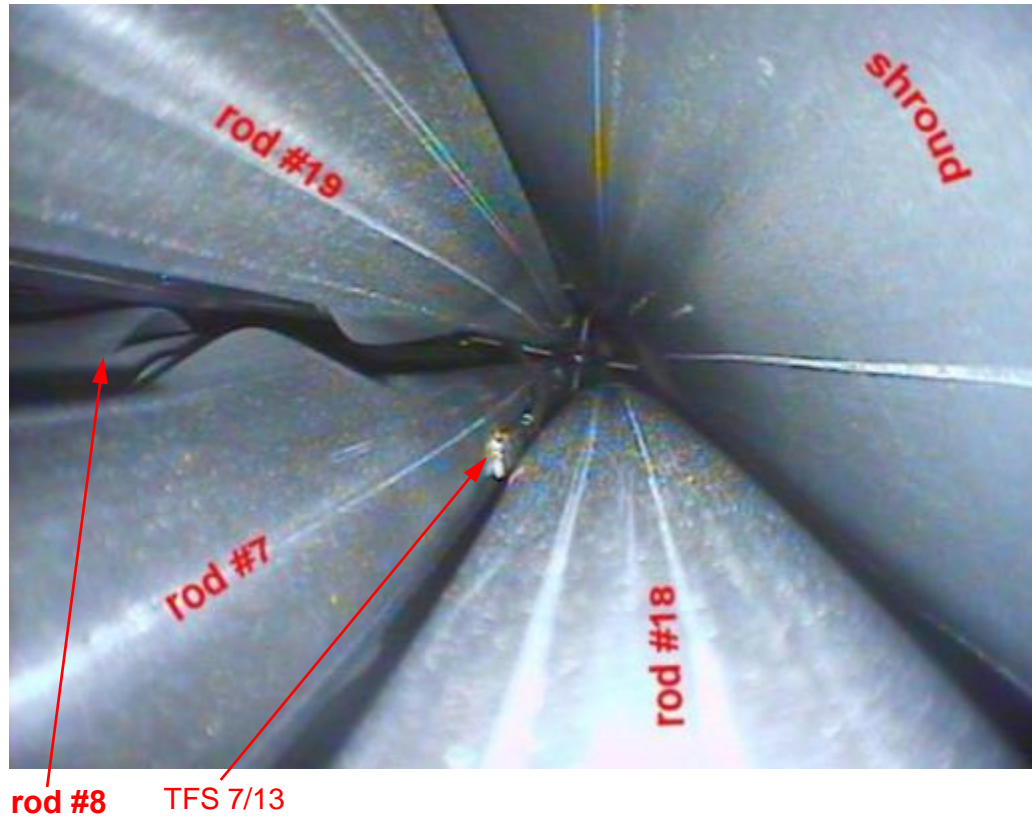


Figure 62 QUENCH-L4; Videoscope observations with camera inserted from the bundle bottom at position of corner rod C.

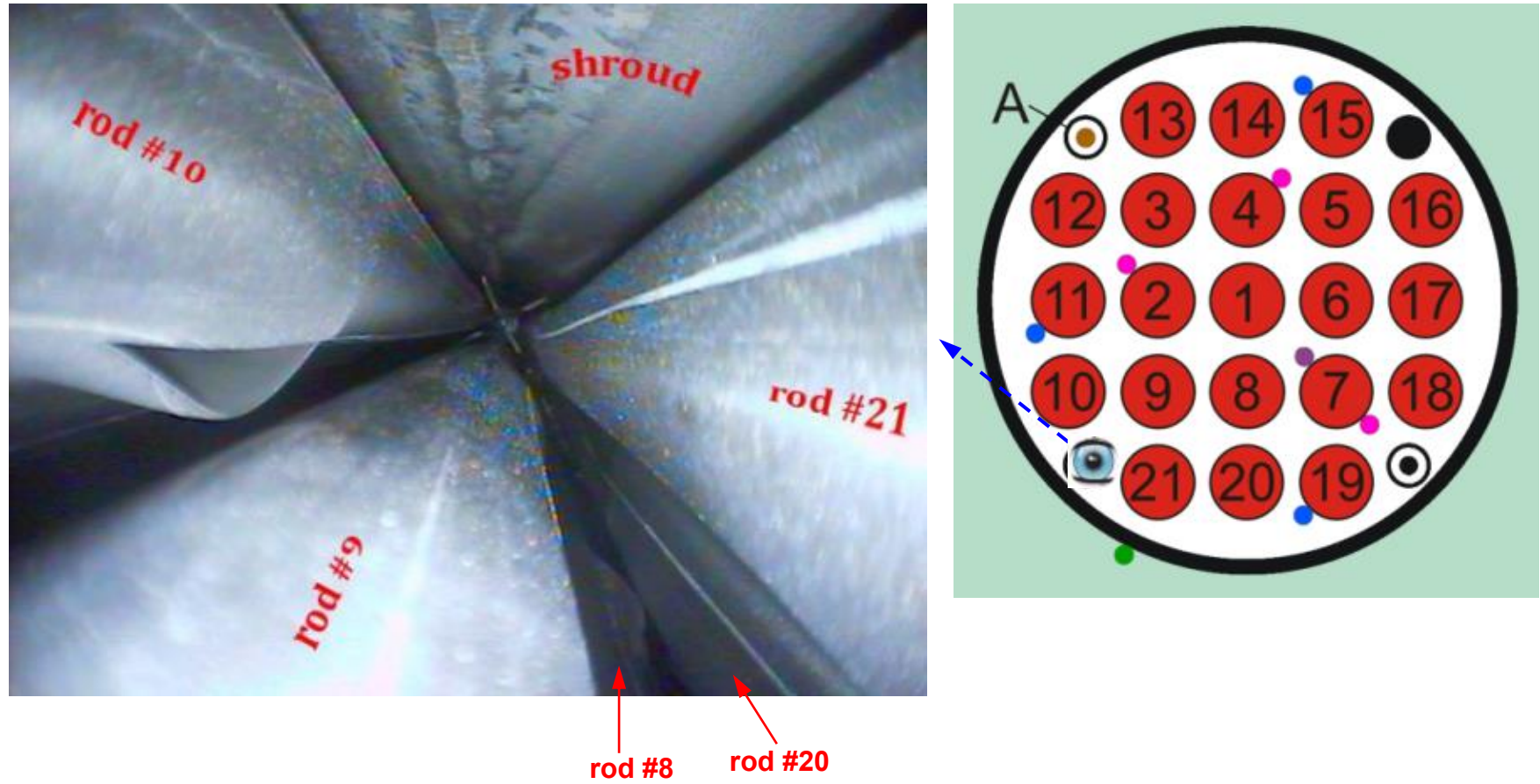
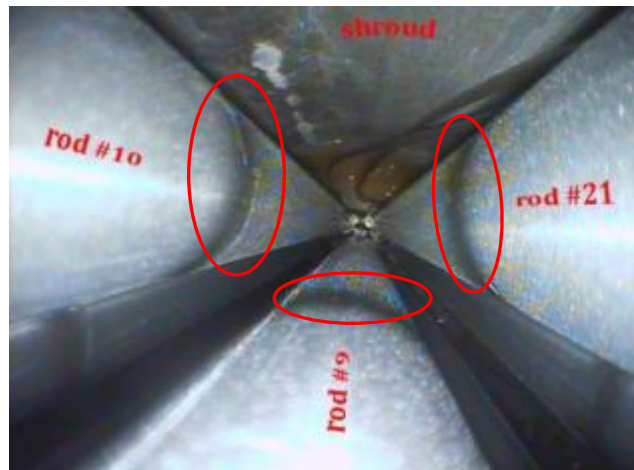
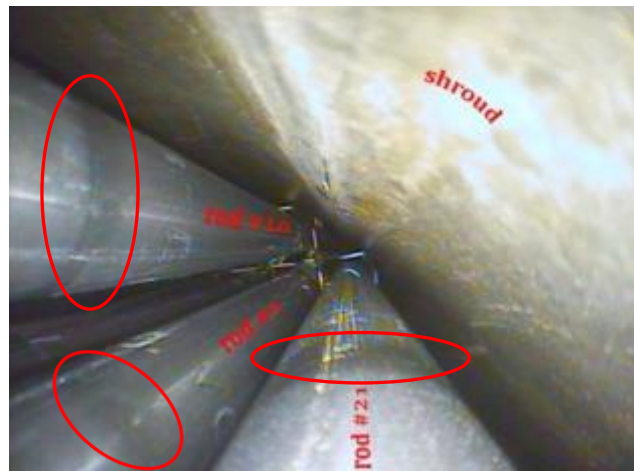


Figure 63 QUENCH-L4; Videoscope observations with camera inserted from the bundle bottom at position of corner rod D.



1250 mm



50 mm

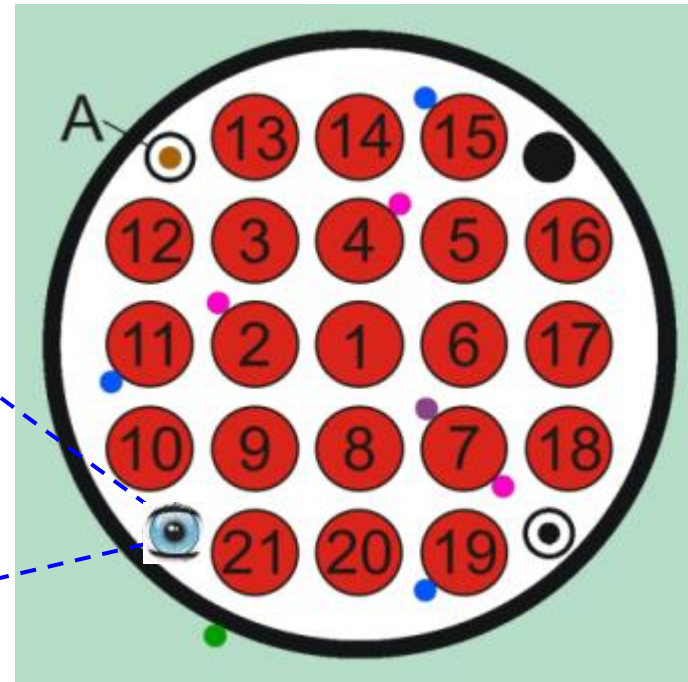


Figure 64 QUENCH-L4; Videoscope observations of weld seams at elevations 50 and 1250 mm at the position of corner rod D.

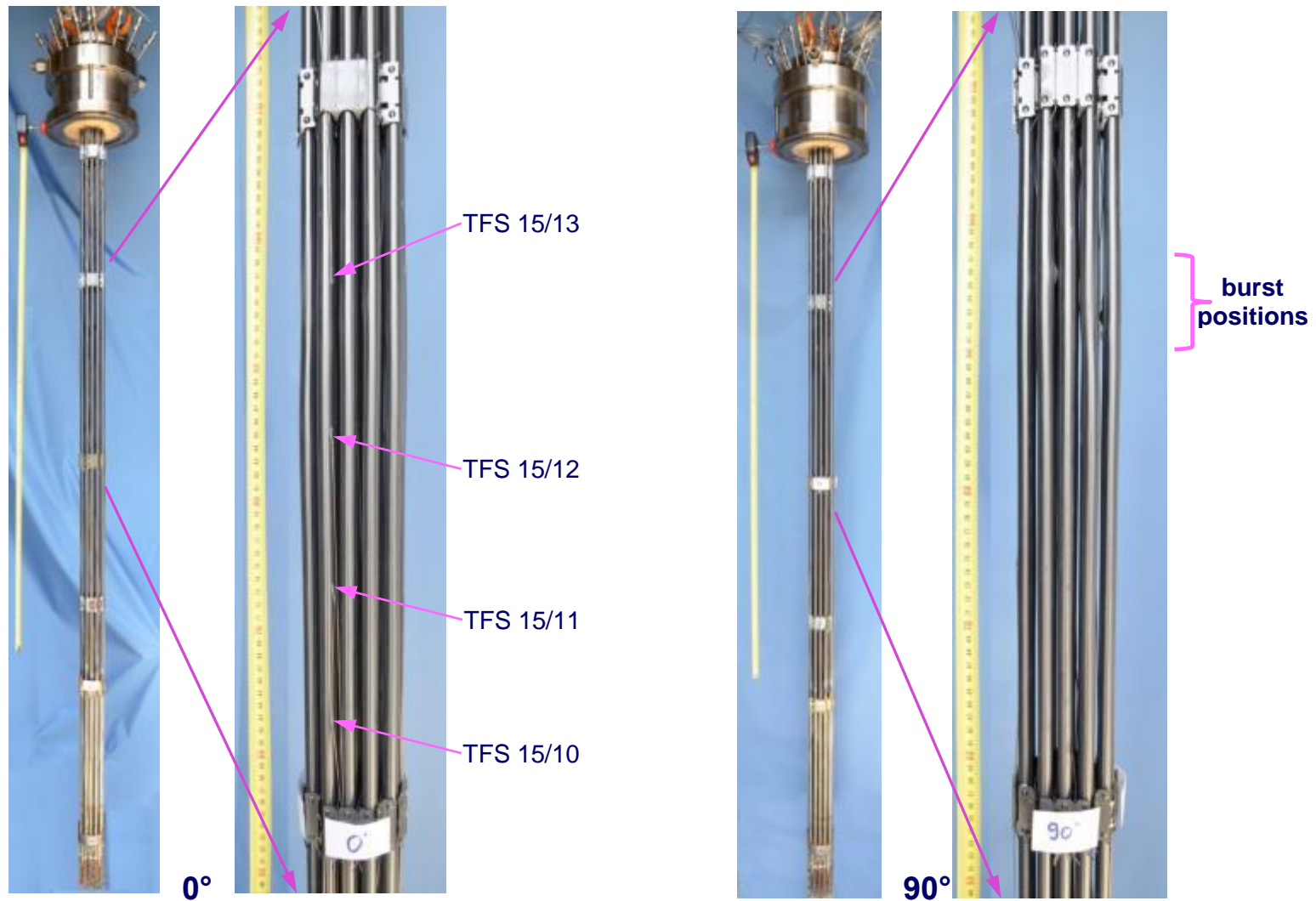


Figure 65 QUENCH-L4; Views of bundle at angle positions of 0° and 90°: negligible rod bending and intact thermocouples.

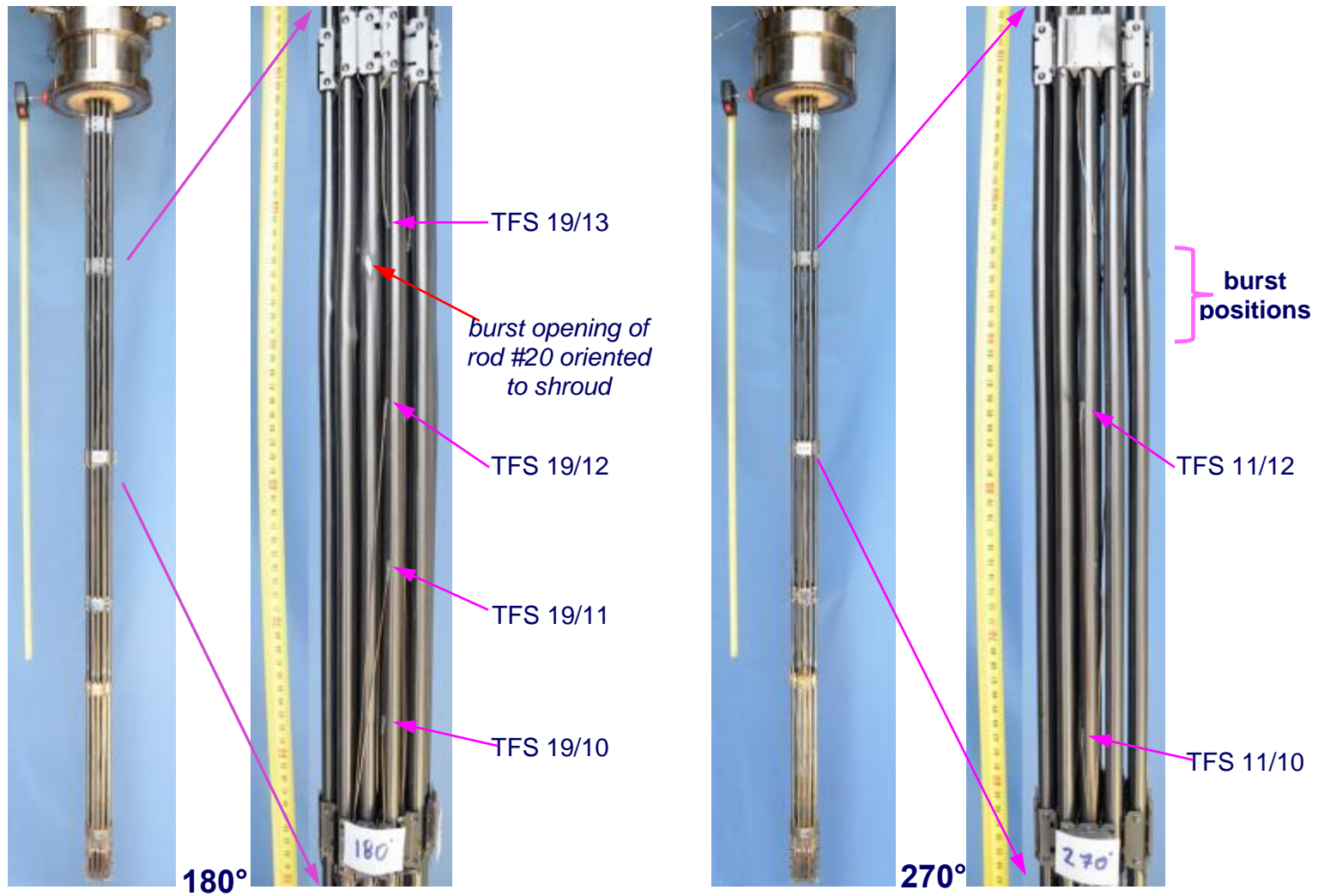


Figure 66 QUENCH-L4; Views of bundle at angle positions of 180° and 270°: negligible rod bending and intact thermocouples.

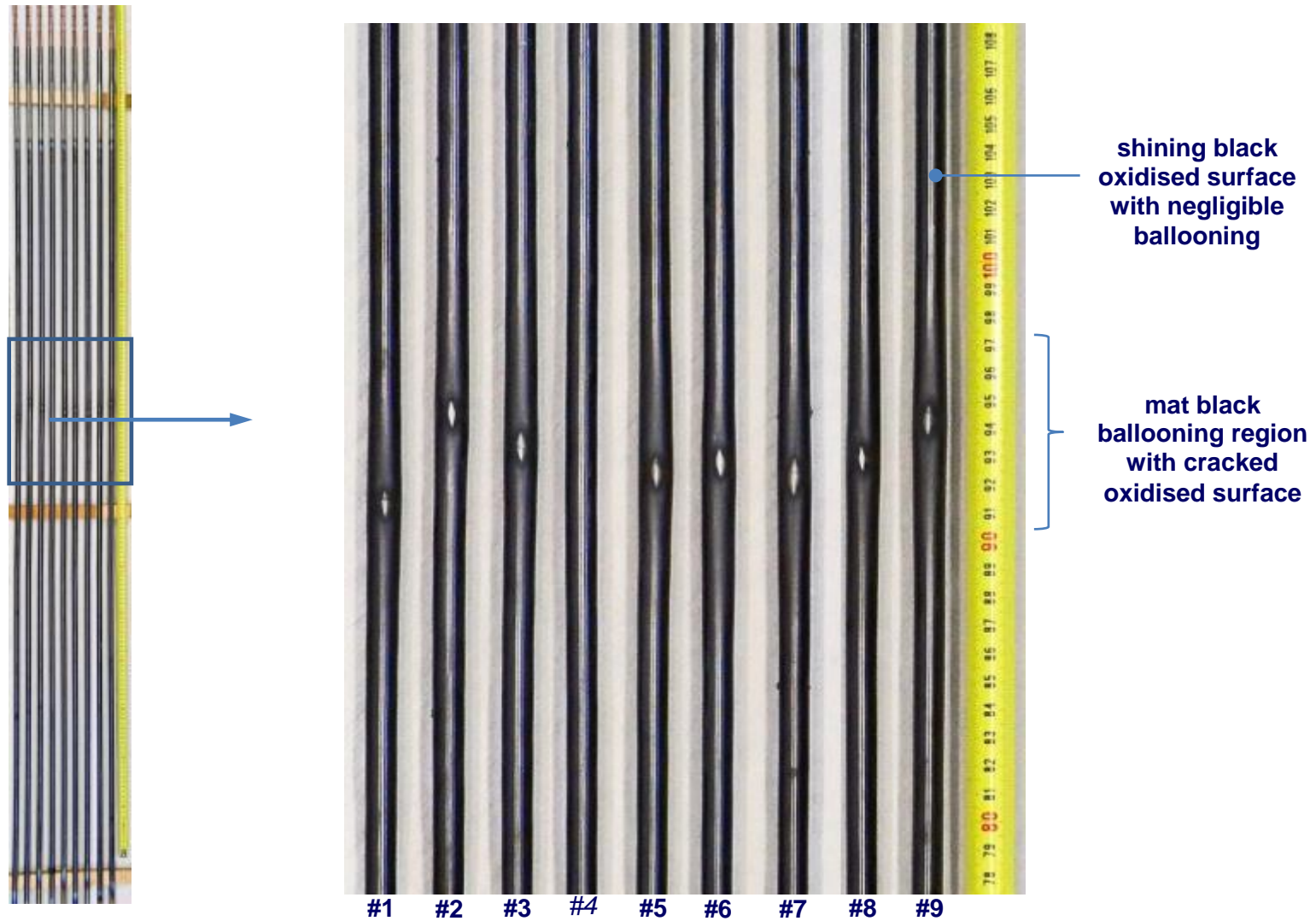


Figure 67 QUENCH-L4; Post-test overview of inner rods: no bending, localized ballooning region.

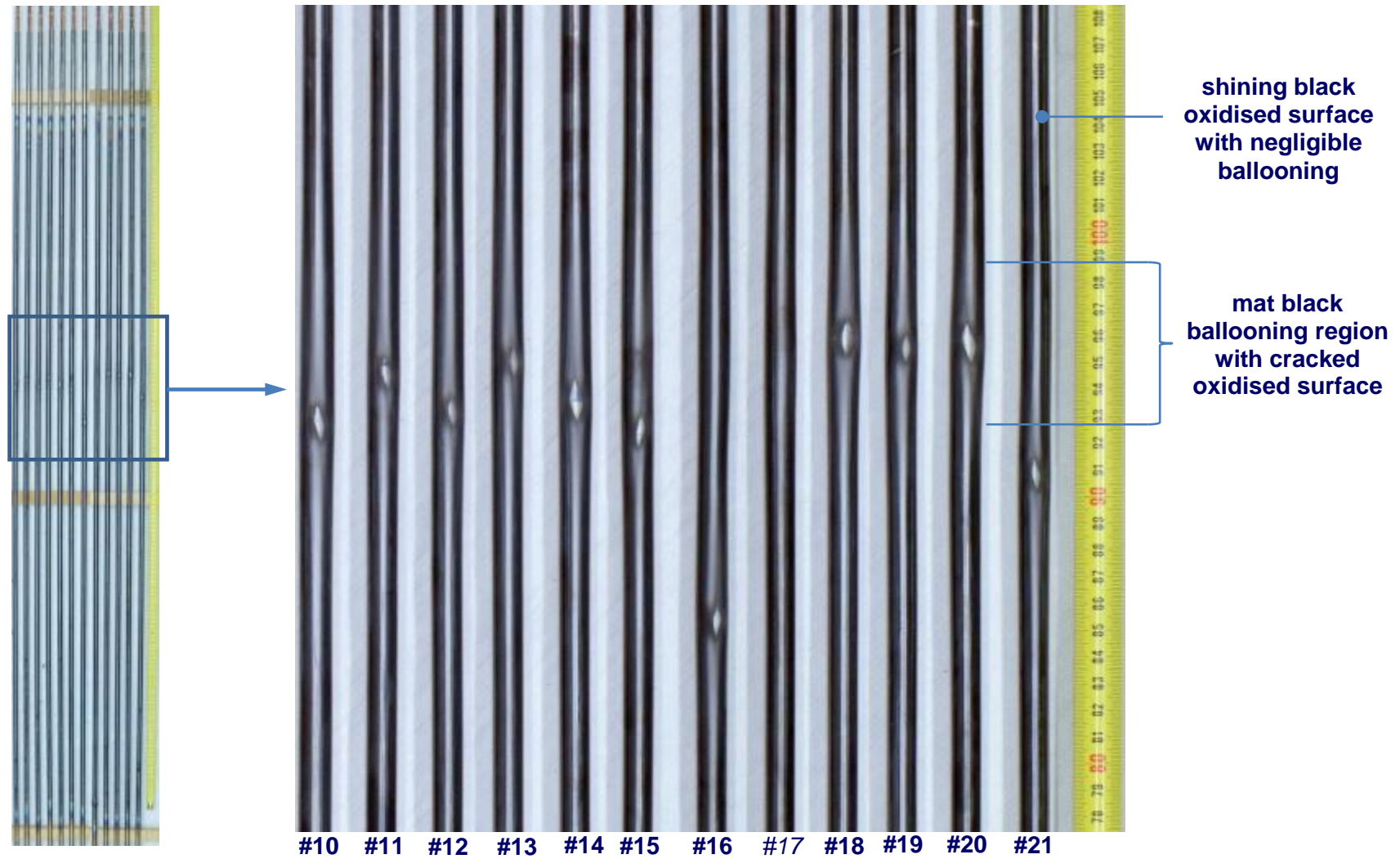
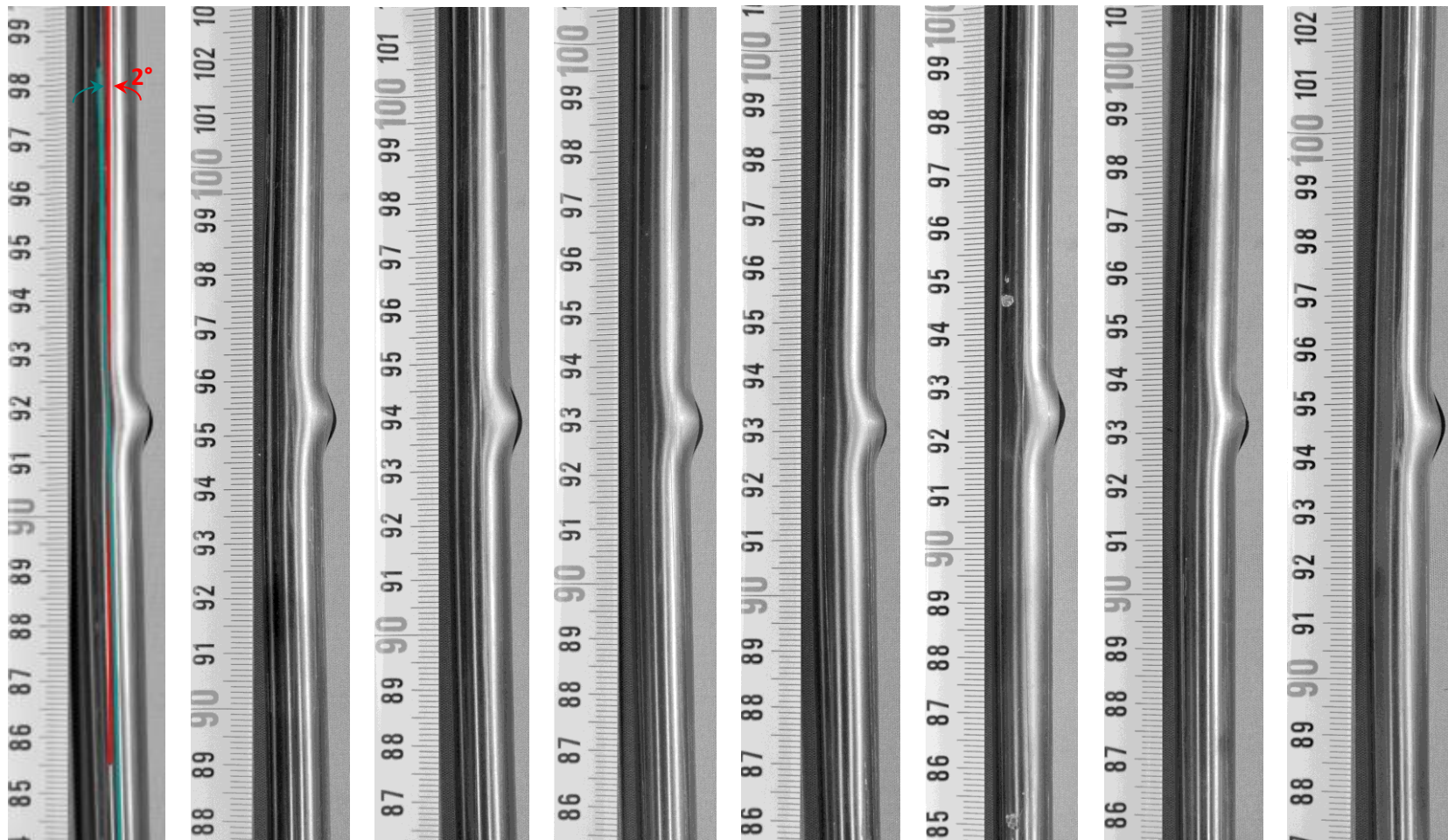


Figure 68 QUENCH-L4; Post-test overview of outer rods: no bending, localized ballooning region.



rod #1; center
lines: red for
upper part, cyan
for low part

rod #2

rod #3

rod #5

rod #6

rod #7

rod #8

rod #9

Figure 69 QUENCH-L4; Post-test inner rods (burst side view): bending about 2° , kink in burst region, burst opening always at concave side.

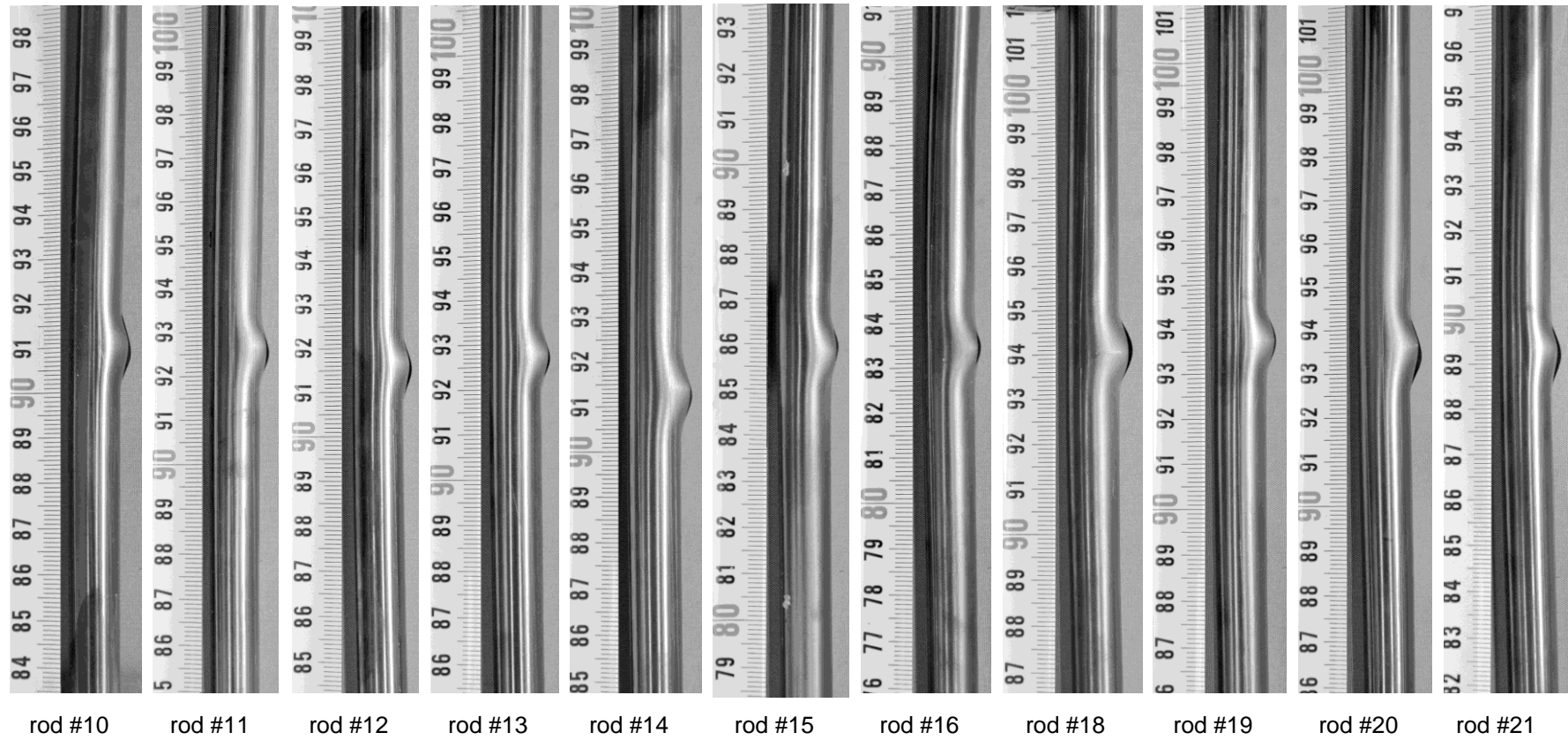


Figure 70 QUENCH-L4; Post-test outer rods (burst side view): bending about 2° , kink in burst region, burst opening always at concave side.

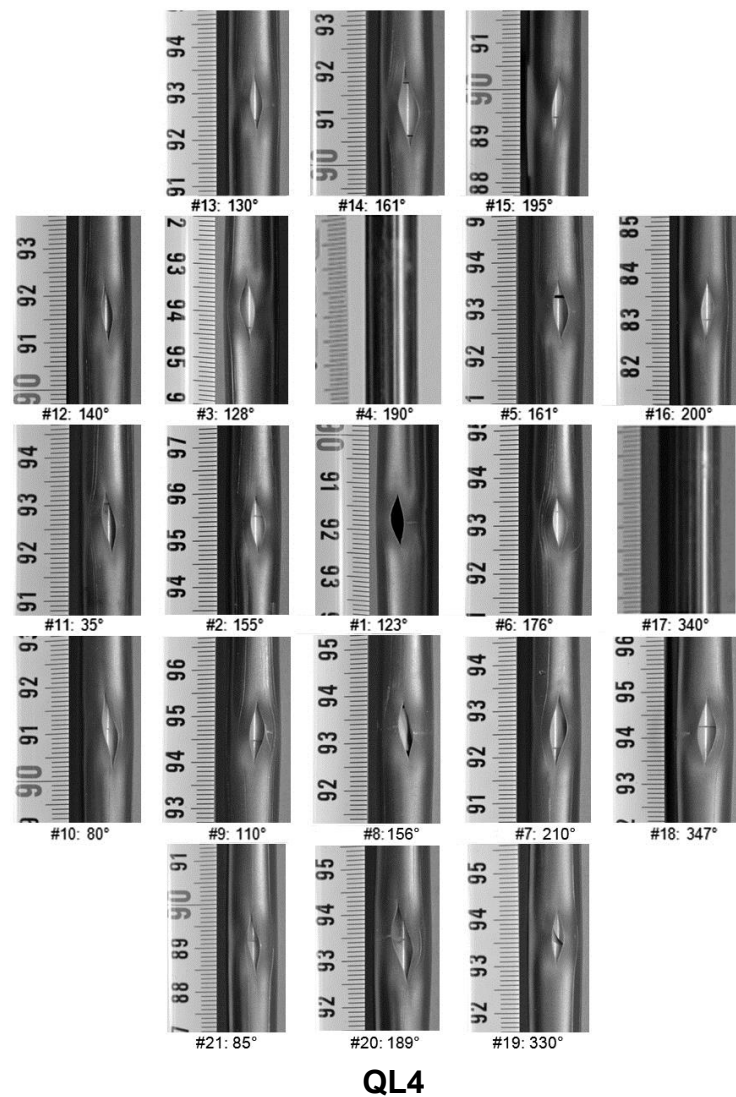
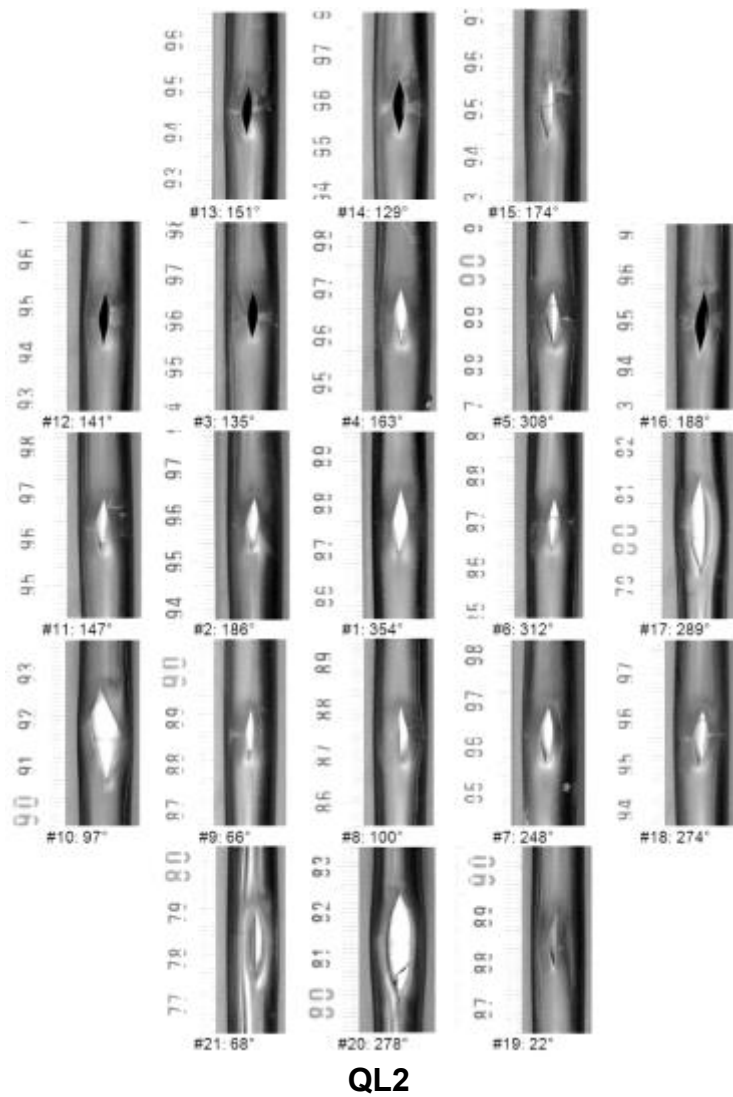


Figure 71 Burst openings of QUENCH-L2 and QUENCH-L4 bundles.

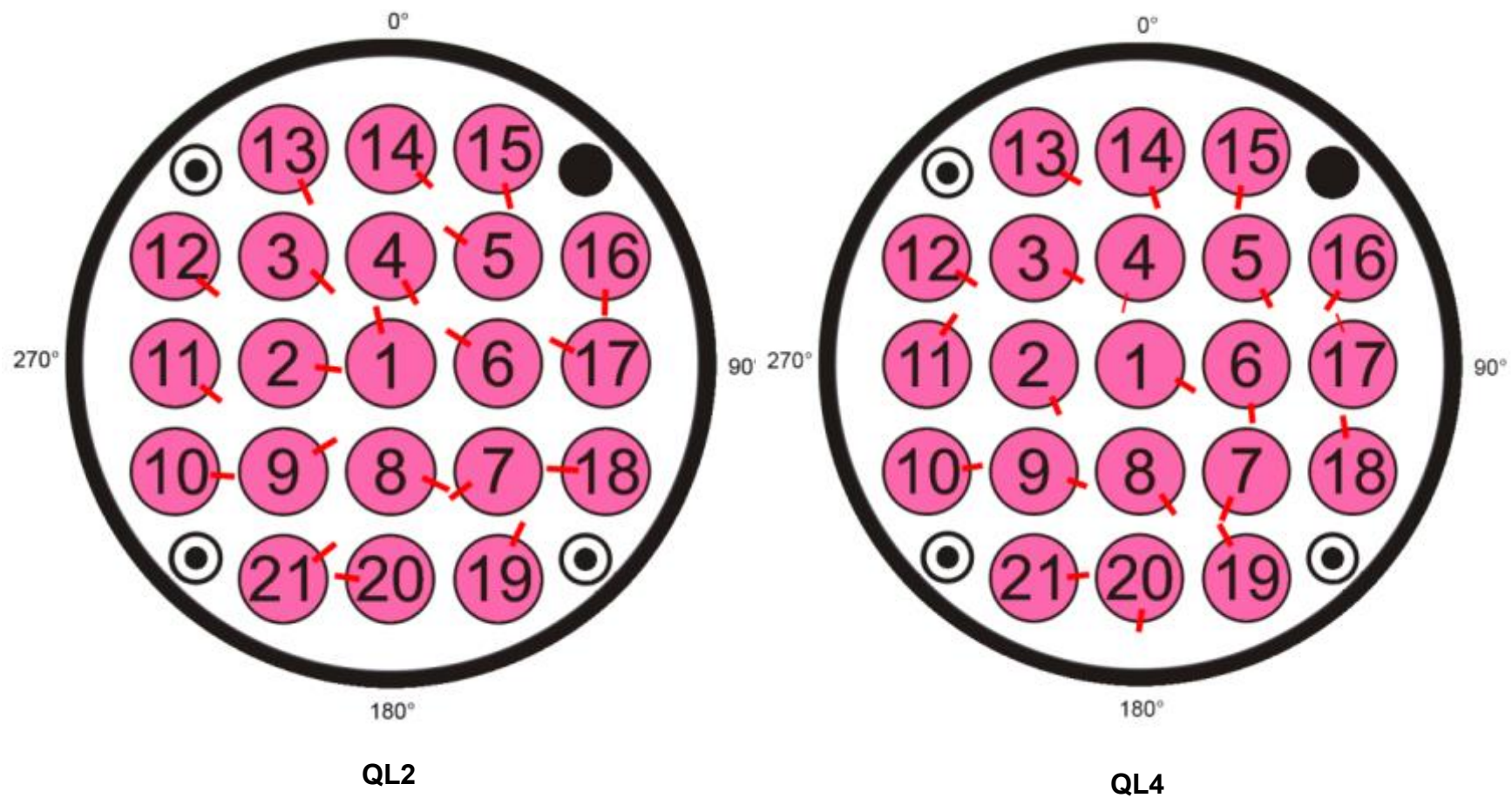
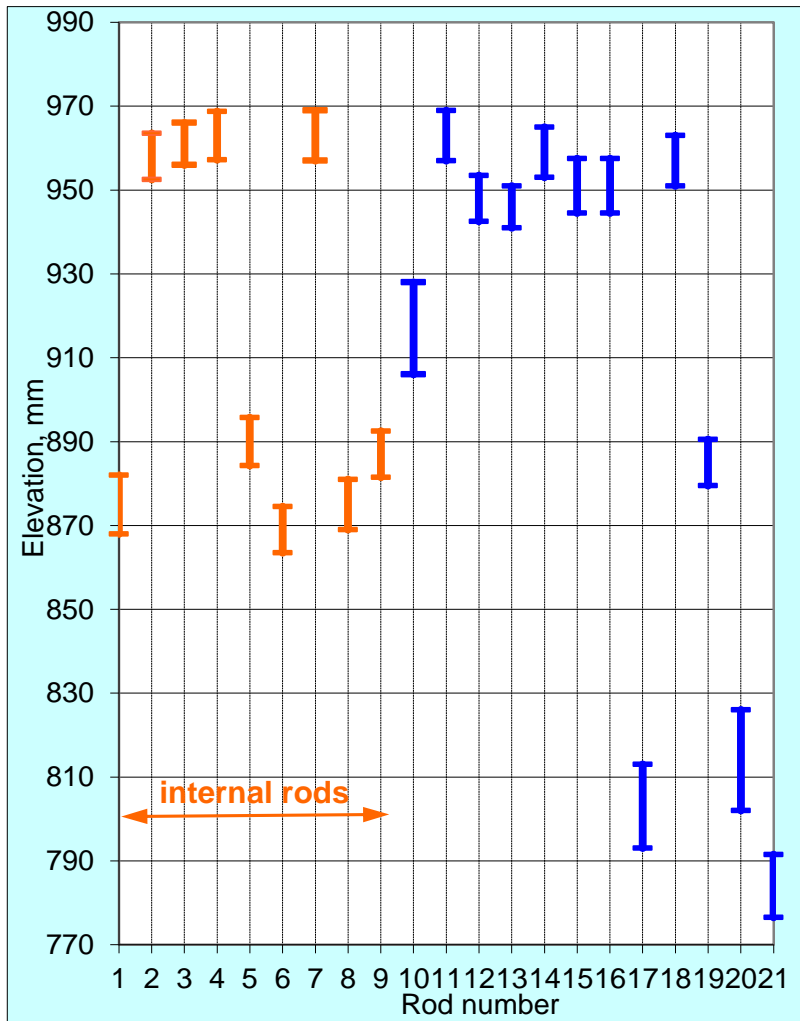
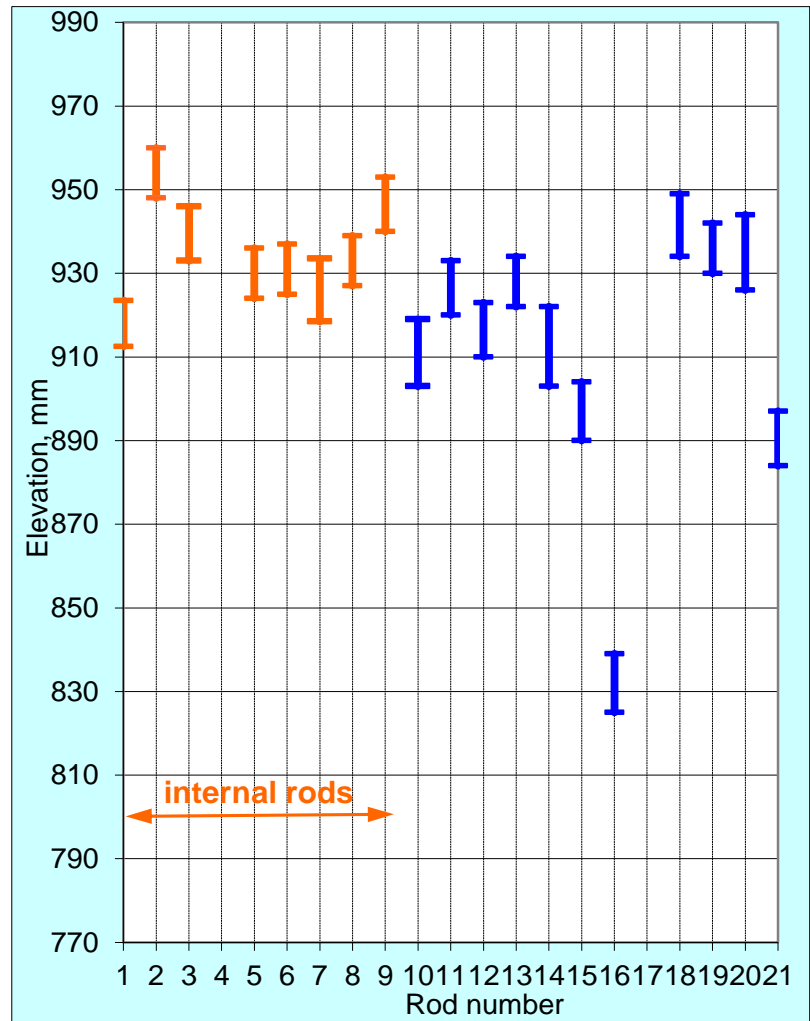


Figure 72 Burst opening orientations of QUENCH-L2 and QUENCH-L4 bundles.

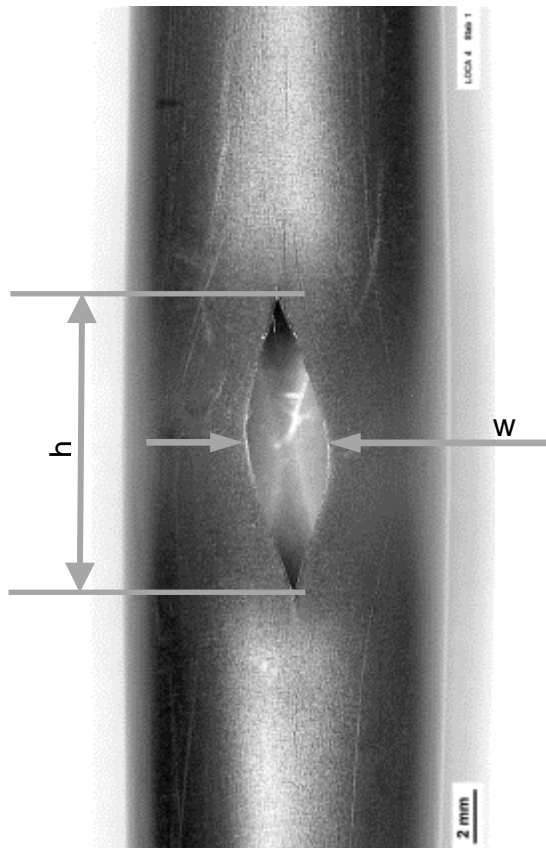


QL2

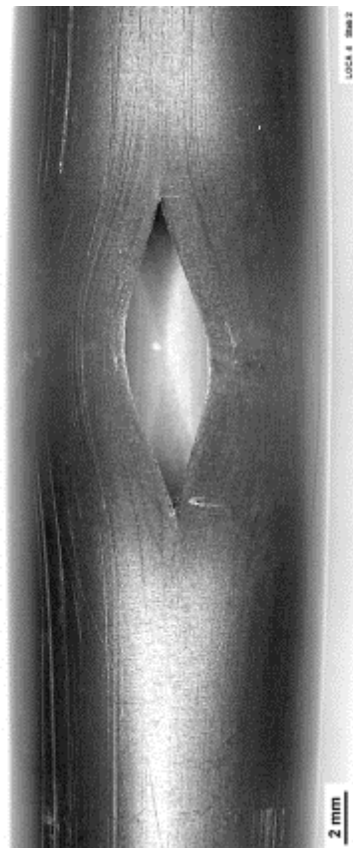


QL4

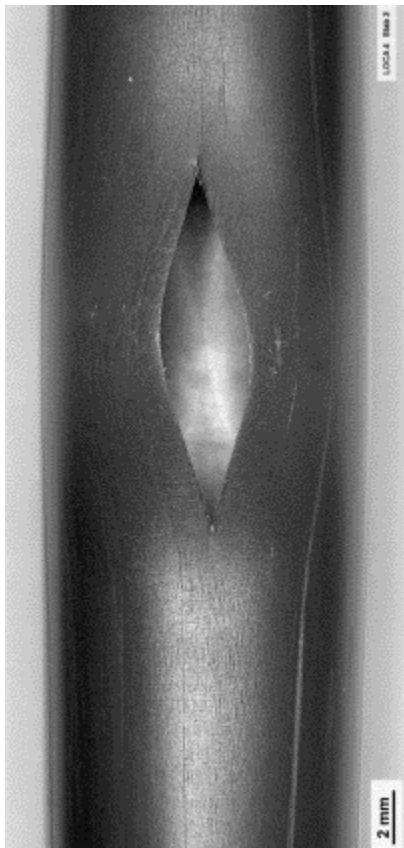
Figure 73 Vertical positions of burst openings for QUENCH-L2 and QUENCH-L4 bundles.



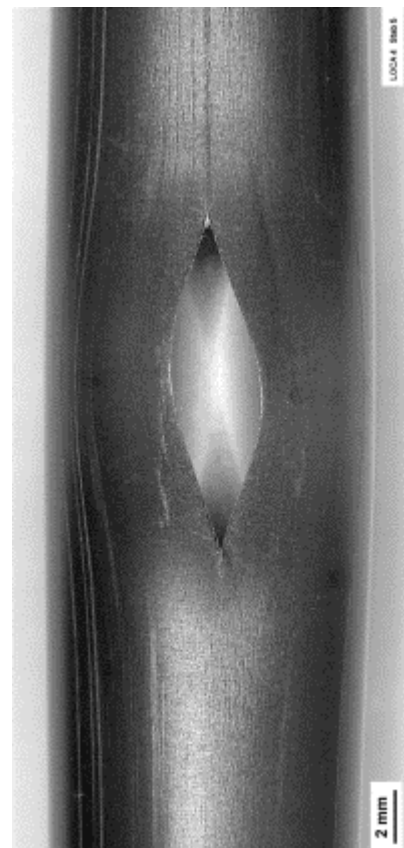
rod #1: burst at 123°; $A_{burst}=19.7 \text{ mm}^2$,
 $w=3.0 \text{ mm}$, $h=11.3 \text{ mm}$



rod #2: burst at 165°; $A_{burst}=20.8 \text{ mm}^2$,
 $w=3.1 \text{ mm}$, $h=11.8 \text{ mm}$

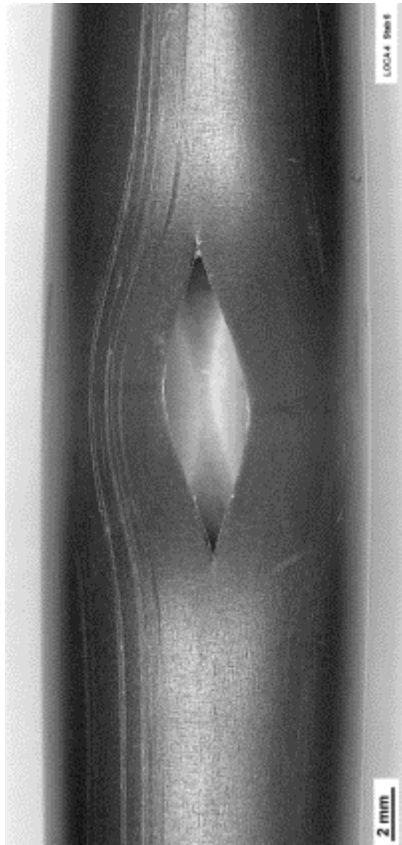


rod #3: burst at 125°; $A_{burst}=24.8 \text{ mm}^2$,
 $w=3.3 \text{ mm}$, $h=12.9 \text{ mm}$



rod #5: burst at 162°; $A_{burst}=24.4 \text{ mm}^2$,
 $w=3.3 \text{ mm}$, $h=12.4 \text{ mm}$

Figure 74 QUENCH-L4; Overview of burst structures of rods #1 - #3, #5.



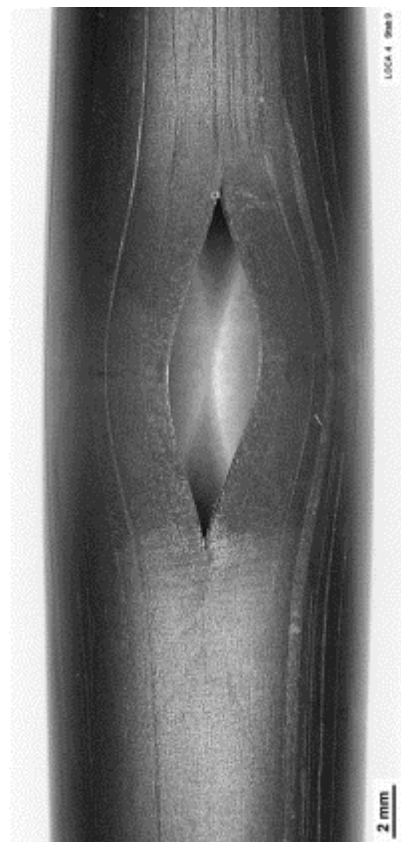
rod #6: burst at 178°; $A_{burst}=20.2 \text{ mm}^2$,
 $w=3.1 \text{ mm}$, $h=11.3 \text{ mm}$



rod #7: burst at 210°; $A_{burst}=33.6 \text{ mm}^2$,
 $w=4.0 \text{ mm}$, $h=15.6 \text{ mm}$



rod #8: burst at 156°; $A_{burst}=21.4 \text{ mm}^2$,
 $w=3.2 \text{ mm}$, $h=11.8 \text{ mm}$

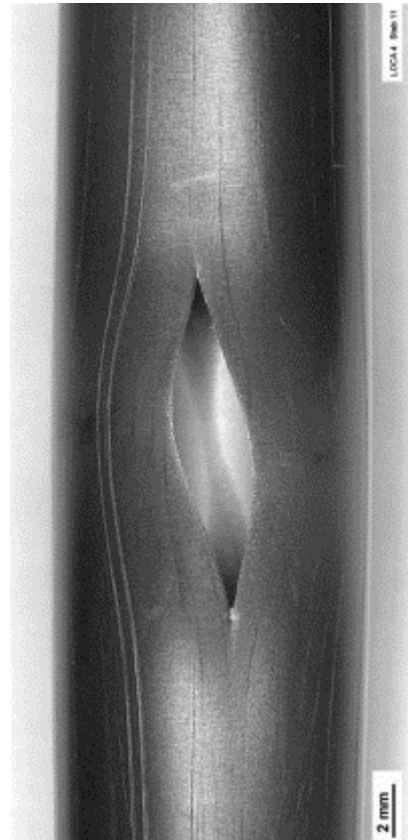


rod #9: burst at 117°; $A_{burst}=25.6 \text{ mm}^2$,
 $w=3.4 \text{ mm}$, $h=12.9 \text{ mm}$

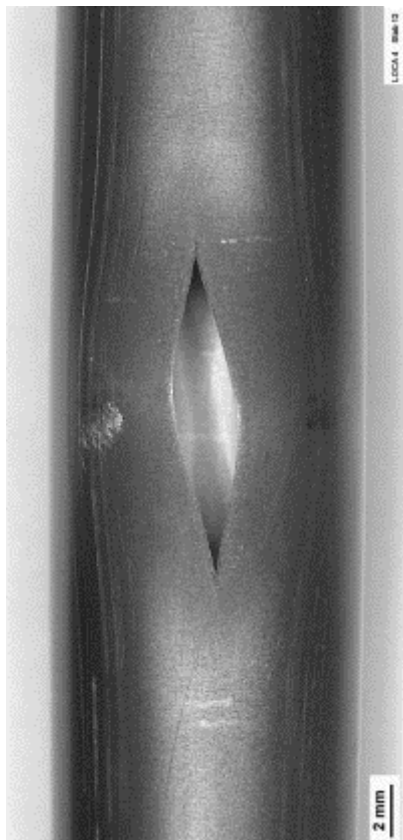
Figure 75 QUENCH-L4; overview of burst structures of rods #6 - #9.



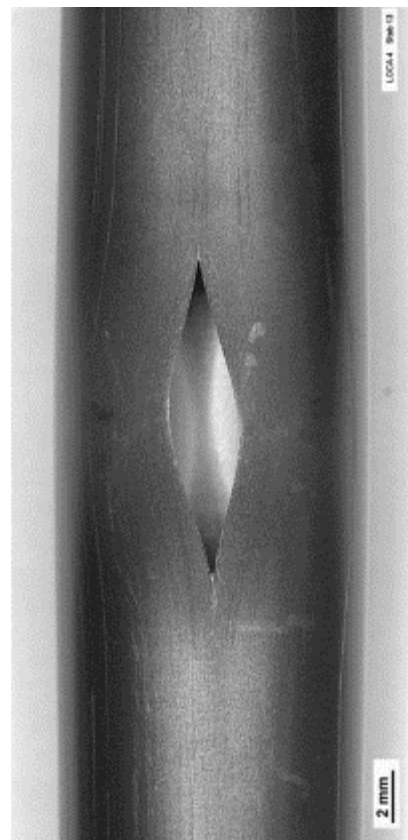
rod #10: burst at 90°; $A_{burst}=25.6 \text{ mm}^2$,
 $w=3.4 \text{ mm}$, $h=15.8 \text{ mm}$



rod #11: burst at 40°; $A_{burst}=19.8 \text{ mm}^2$,
 $w=3.0 \text{ mm}$, $h=12.4 \text{ mm}$

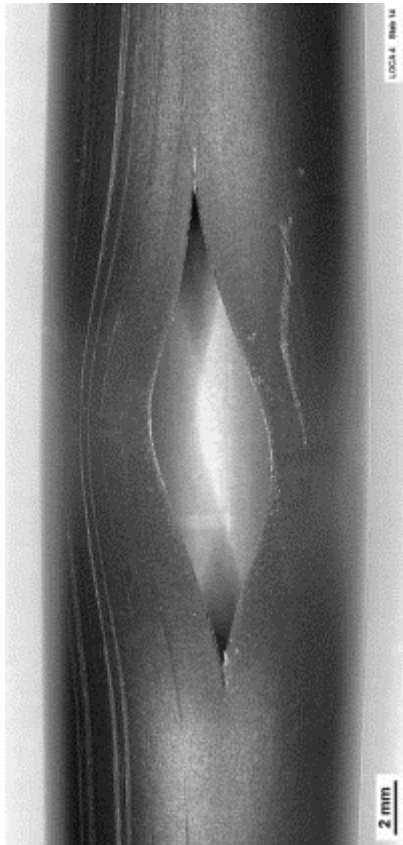


rod #12: burst at 134°; $A_{burst}=16.4 \text{ mm}^2$,
 $w=2.5 \text{ mm}$, $h=12.0 \text{ mm}$

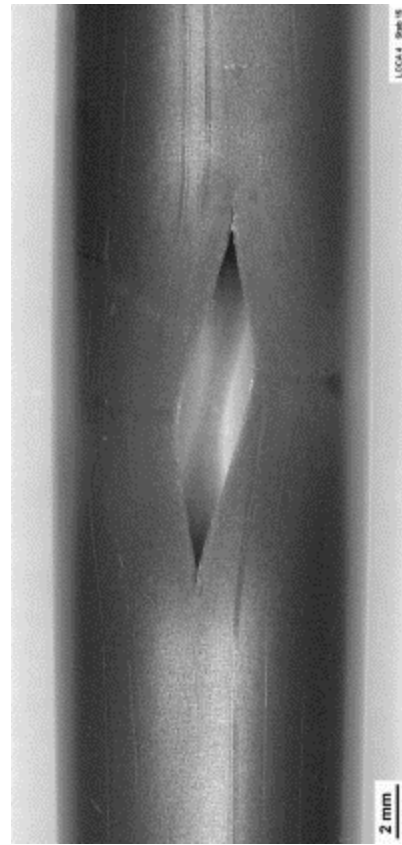


rod #13: burst at 130°; $A_{burst}=18.1 \text{ mm}^2$,
 $w=2.7 \text{ mm}$, $h=12.0 \text{ mm}$

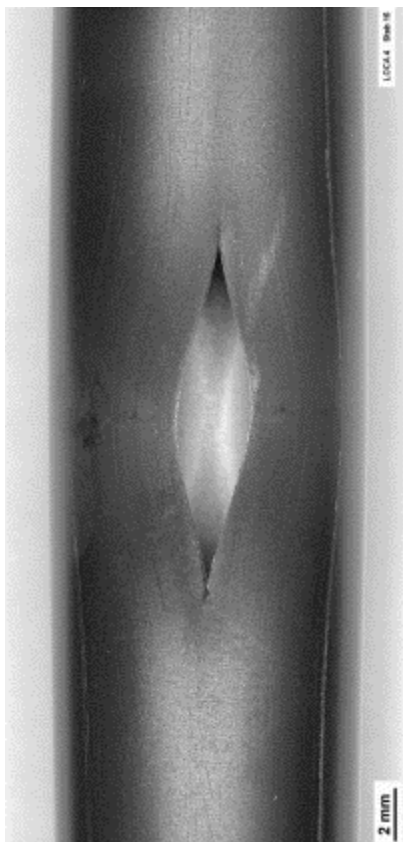
Figure 76 QUENCH-L4; Overview of burst structures of rods #10 - #13.



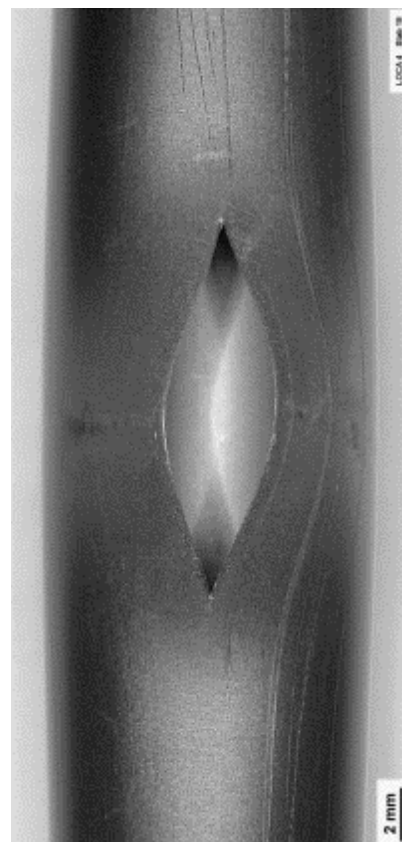
rod #14: burst at 163°; $A_{burst}=39.9 \text{ mm}^2$,
 $w=4.5 \text{ mm}$, $h=17.6 \text{ mm}$



rod #15: burst at 205°; $A_{burst}=18.4 \text{ mm}^2$,
 $w=2.8 \text{ mm}$, $h=12.7 \text{ mm}$

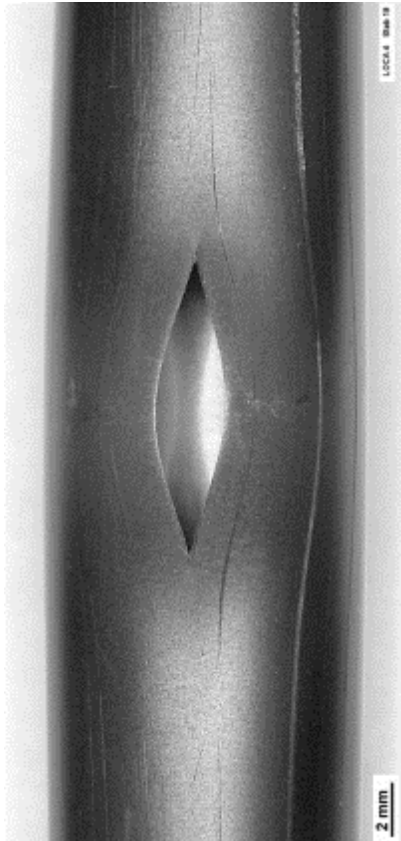


rod #16: burst at 195°; $A_{burst}=19.8 \text{ mm}^2$,
 $w=2.8 \text{ mm}$, $h=12.7 \text{ mm}$

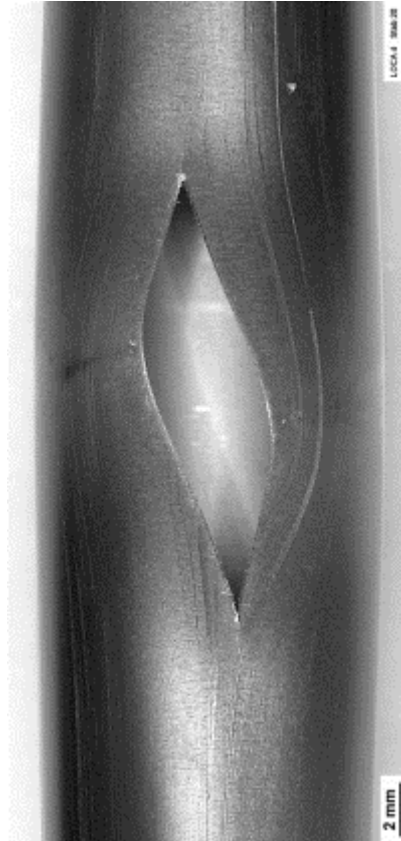


rod #18: burst at 353°; $A_{burst}=34.0 \text{ mm}^2$,
 $w=4.1 \text{ mm}$, $h=13.9 \text{ mm}$

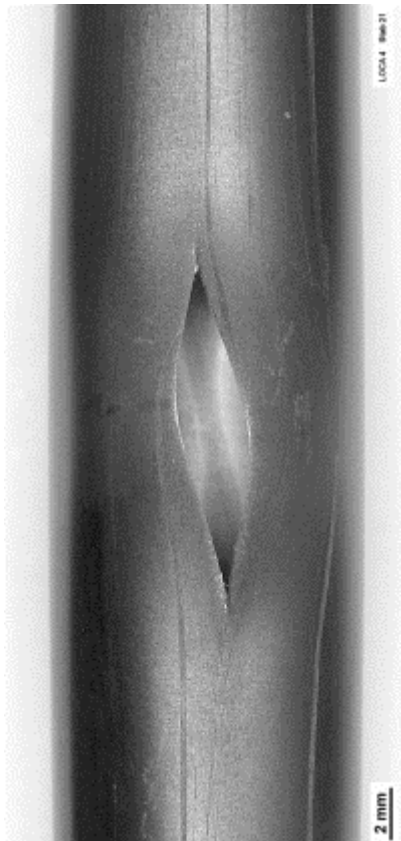
Figure 77 QUENCH-L4; Overview of burst structures of rods #14 - #16, #18.



rod #19: burst at 330°; $A_{burst}=17.1 \text{ mm}^2$,
 $w=2.6 \text{ mm}$, $h=11.0 \text{ mm}$



rod #20: burst at 189°; $A_{burst}=39.2 \text{ mm}^2$,
 $w=4.8 \text{ mm}$, $h=16.1 \text{ mm}$



rod #21: burst at 81°; $A_{burst}=18.7 \text{ mm}^2$,
 $w=2.7 \text{ mm}$, $h=12.4 \text{ mm}$

Figure 78 QUENCH-L4; Overview of burst structures of rods #19 - #21.

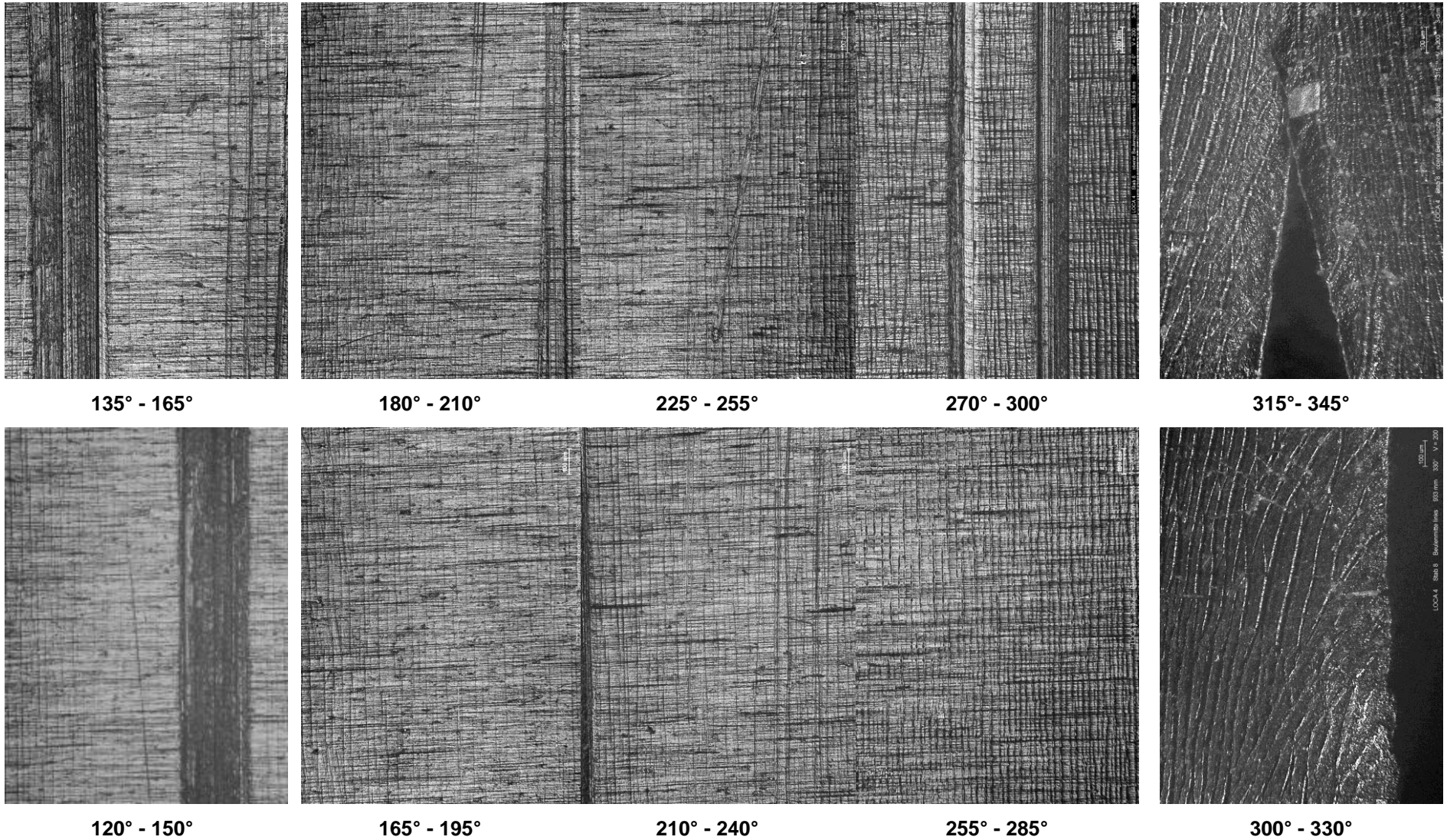


Figure 79 QUENCH-L4; Cladding surface structure (“tree bark”) at elevations 938 mm (top) and 933 mm (bottom) of rod #8: formation of longitudinal surface cracks in oxide during ballooning.

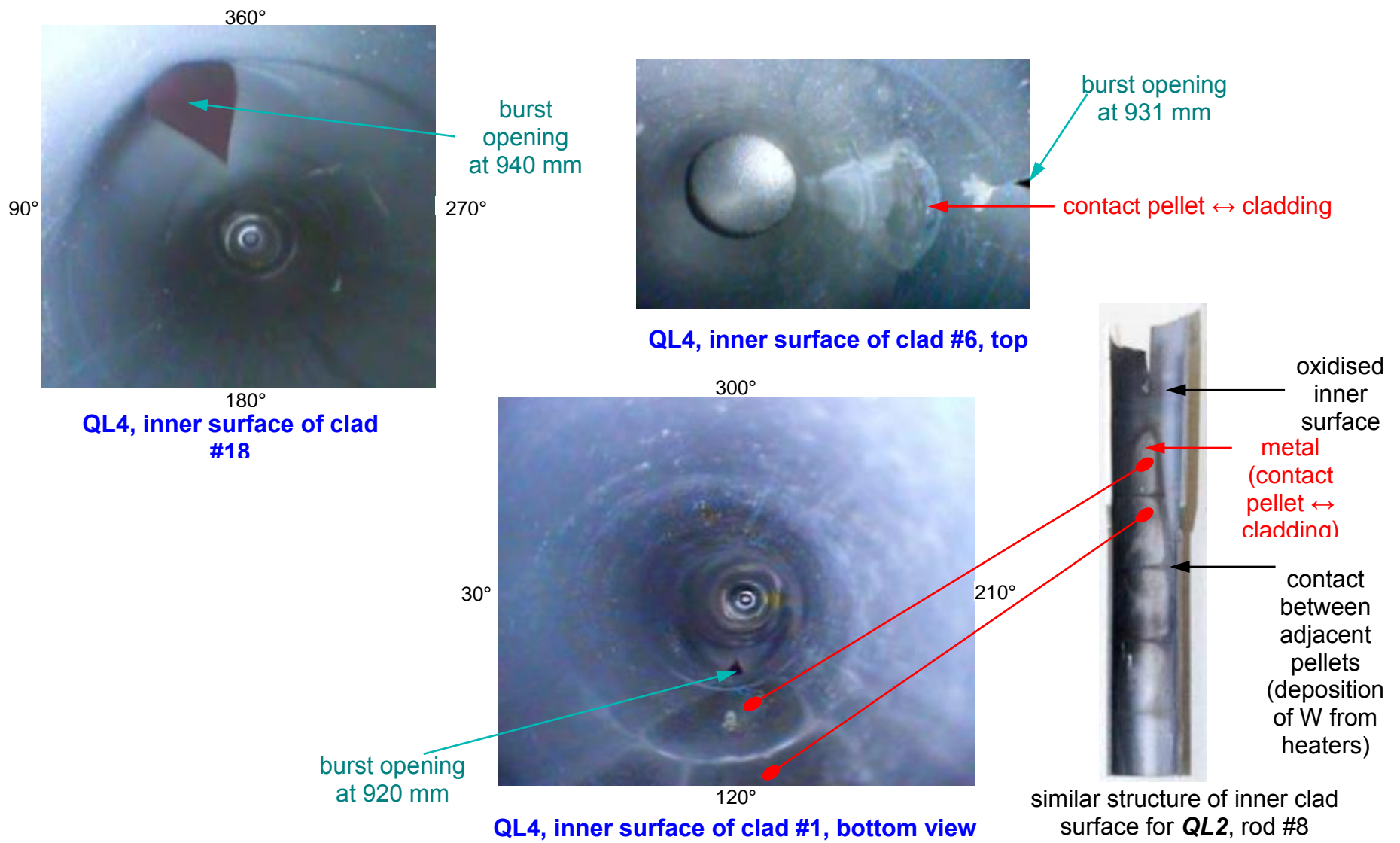
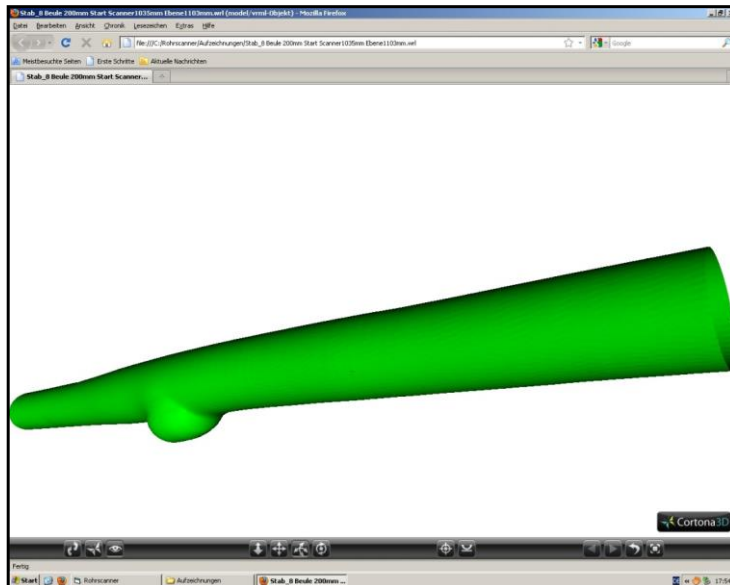


Figure 80 QUENCH-L4; Videoscope observations of cladding inner surface.



scanner facility



reconstructed scanned surface of rod #8:
angle step 1°; axial step 0.5 mm; scanned length 200 mm

Figure 81 QUENCH-L4; Tube scanner laser profilometry.

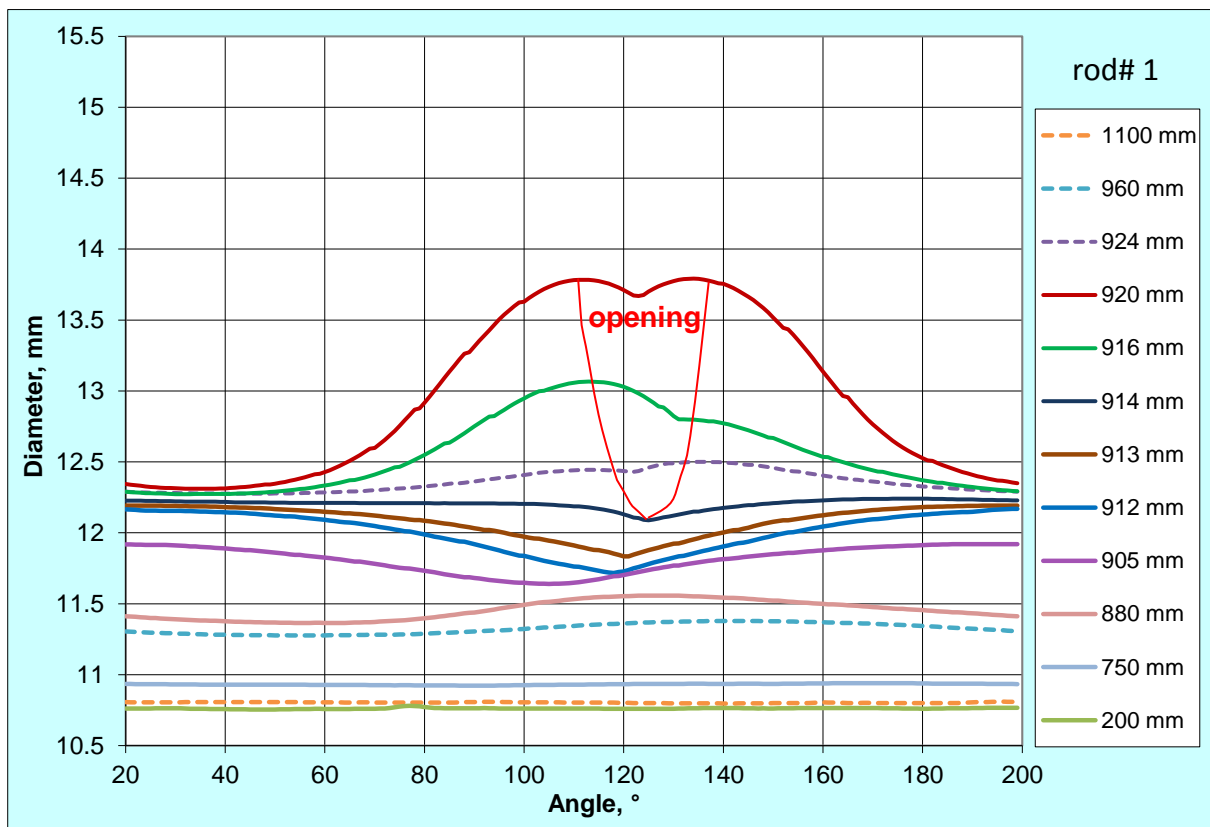
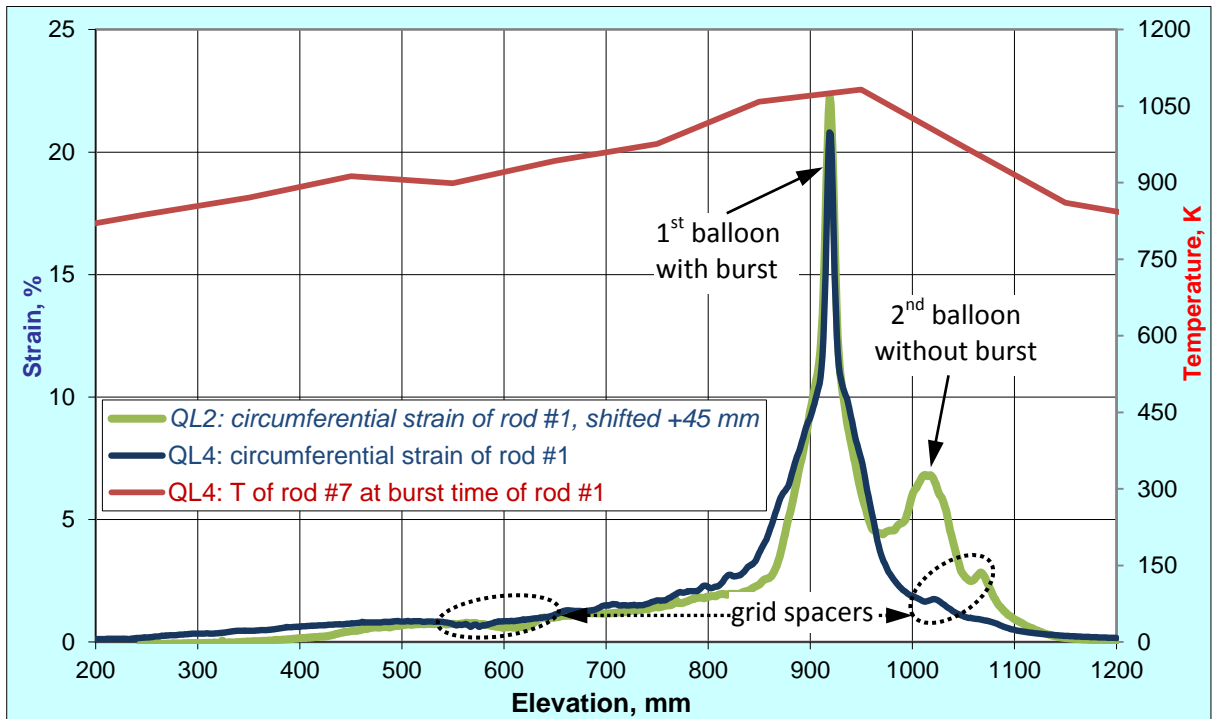


Figure 82 QUENCH-L4, Rod #1; longitudinal changing of circumferential strain (top): QL4 main balloon region is longer than QL2 one; azimuthal diameter downwards from burst (bottom).

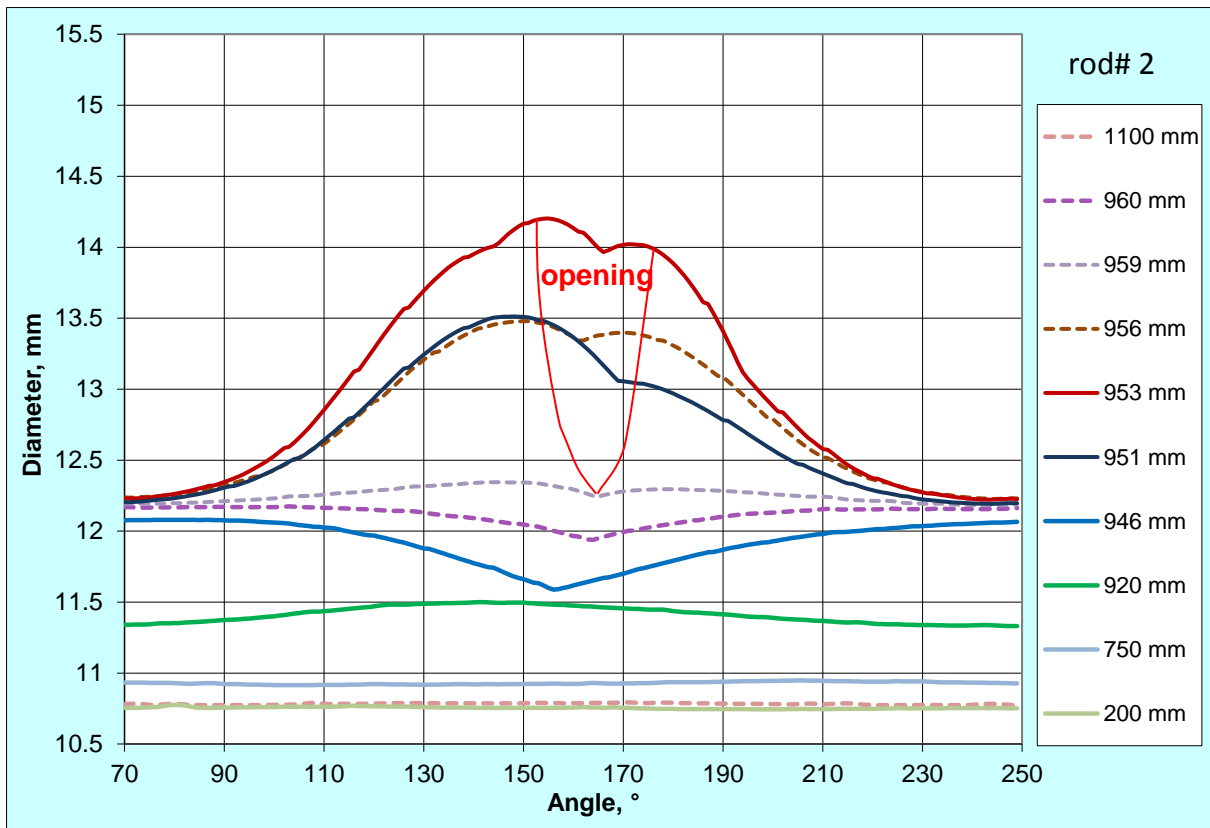
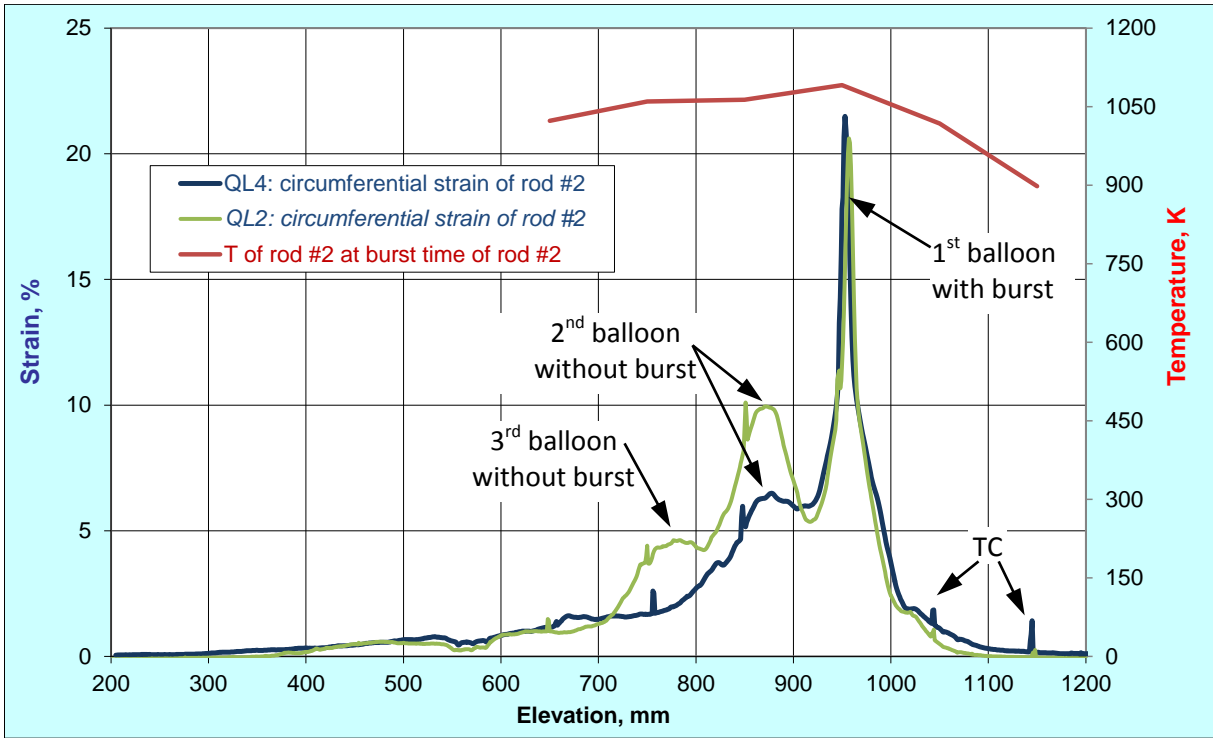


Figure 83 QUENCH-L4, Rod #2; longitudinal changing of circumferential strain (top): QL4 main balloon region is longer than QL2 one; azimuthal diameter downwards from burst (bottom).

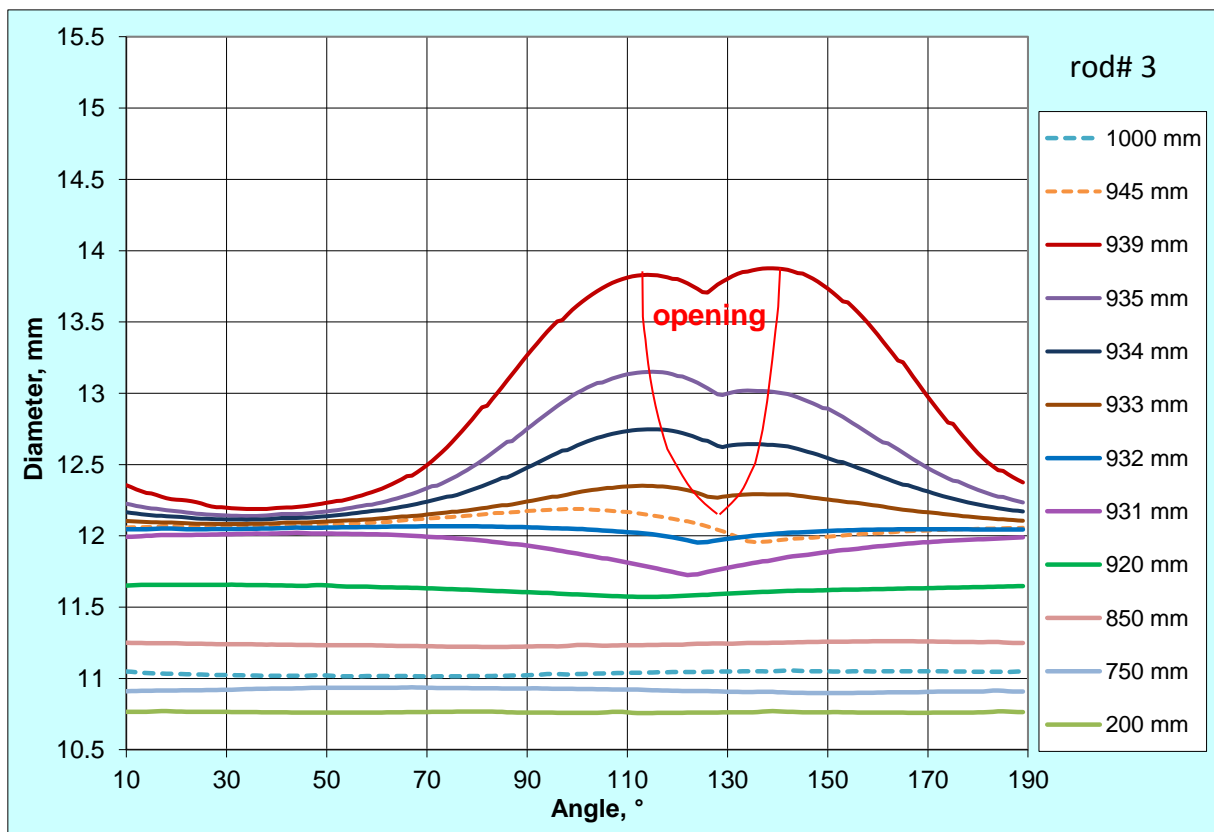
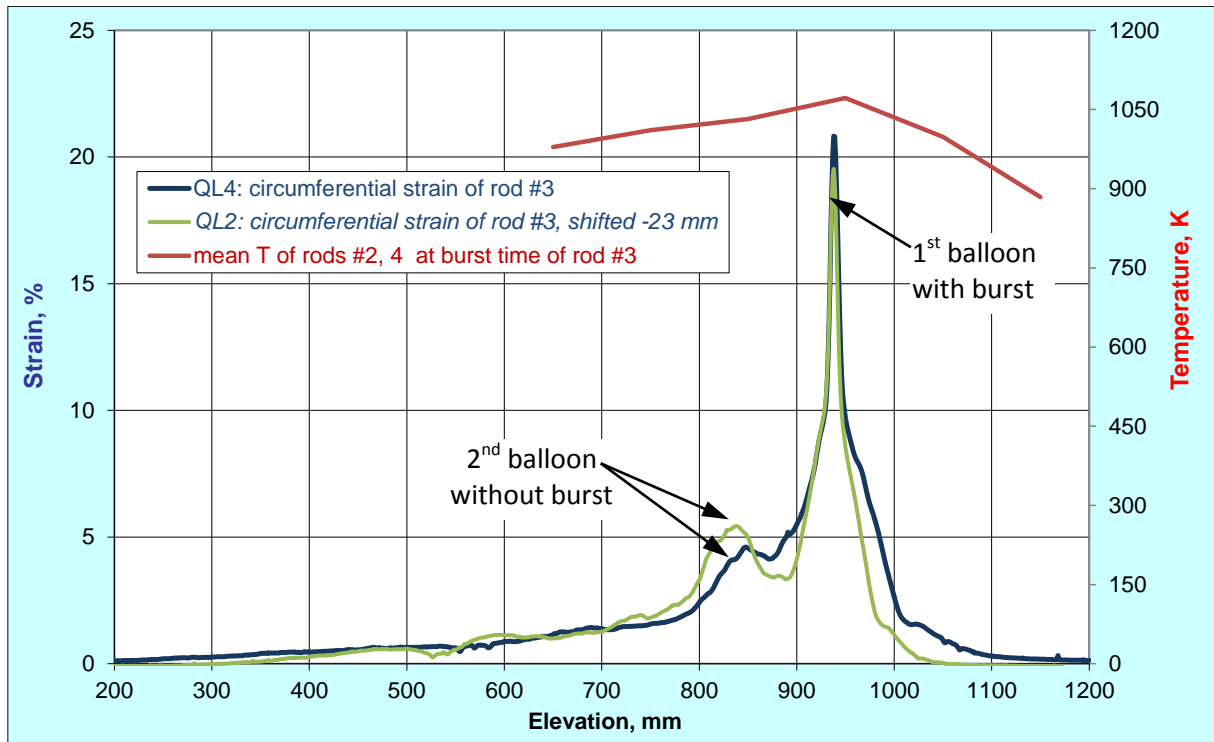


Figure 84 QUENCH-L4, Rod #3; longitudinal changing of circumferential strain (top): QL4 main balloon region is longer than QL2 one; azimuthal diameter downwards from burst (bottom).

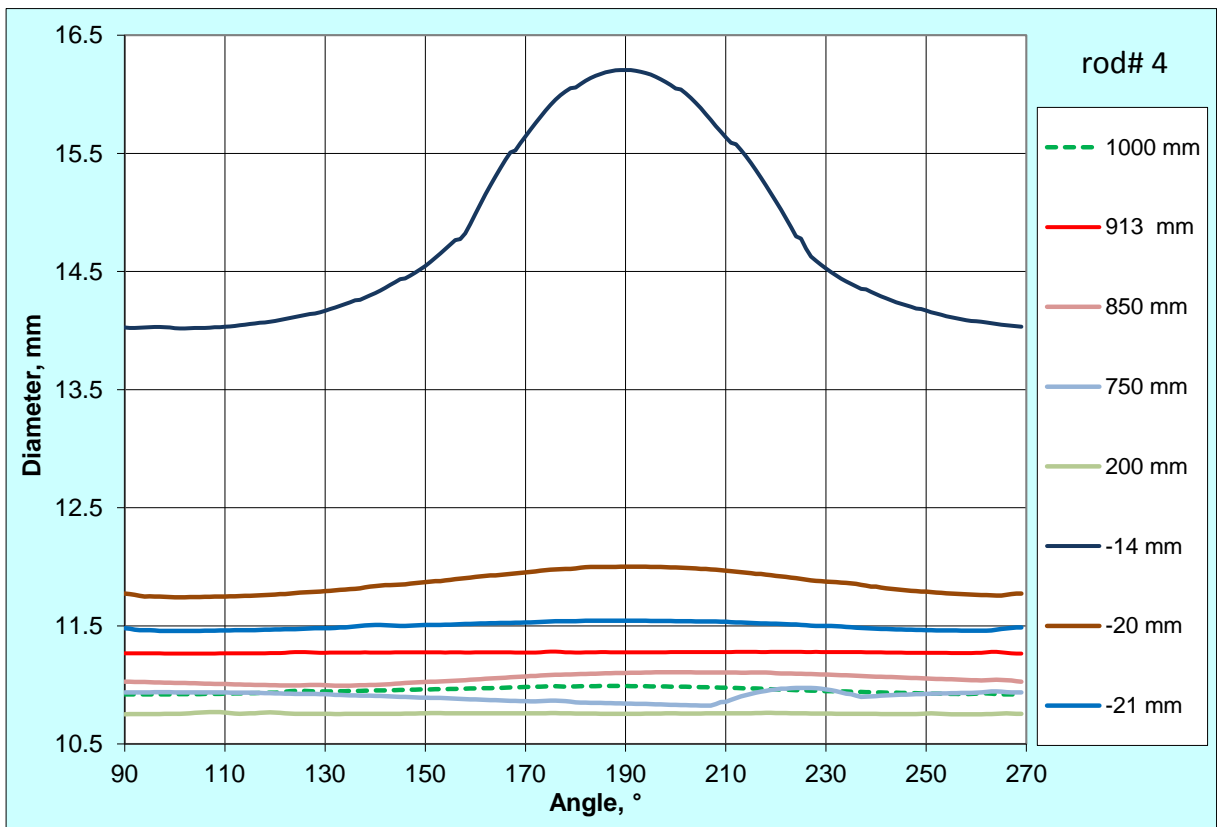
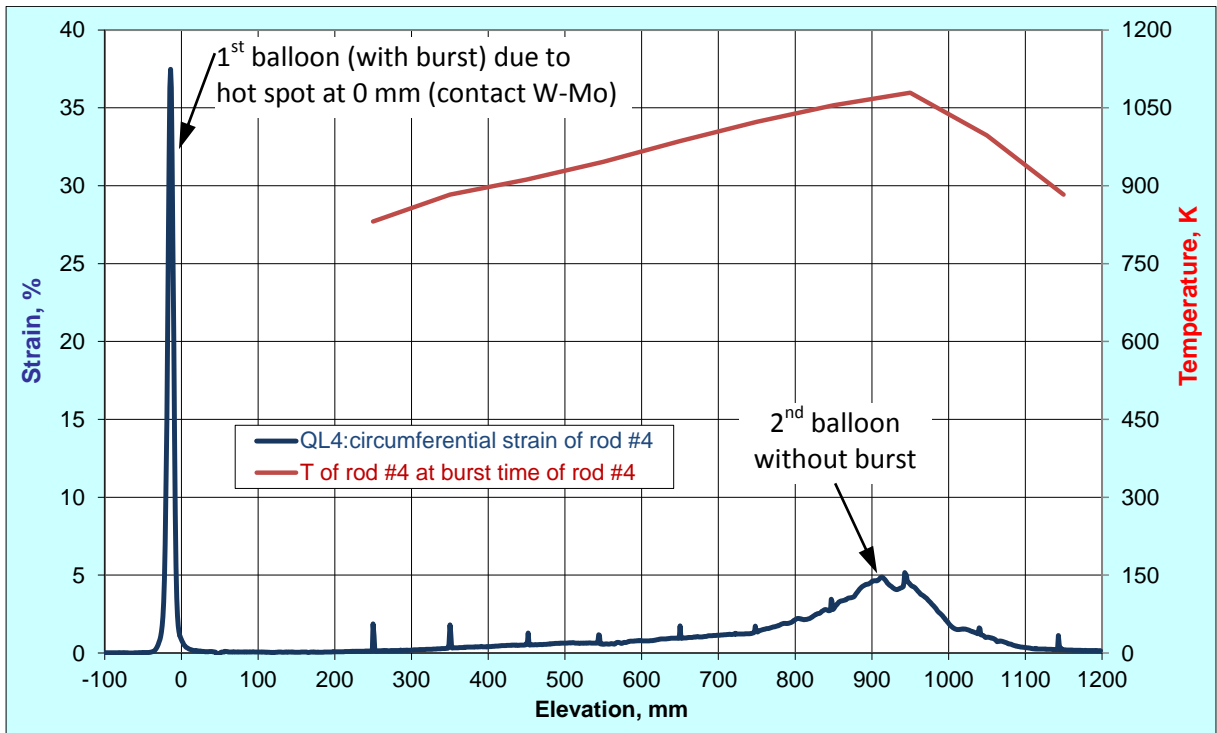


Figure 85 QUENCH-L4, Rod #4; longitudinal changing of circumferential strain (top); azimuthal diameter downwards from burst (bottom). Spikes: thermocouple.

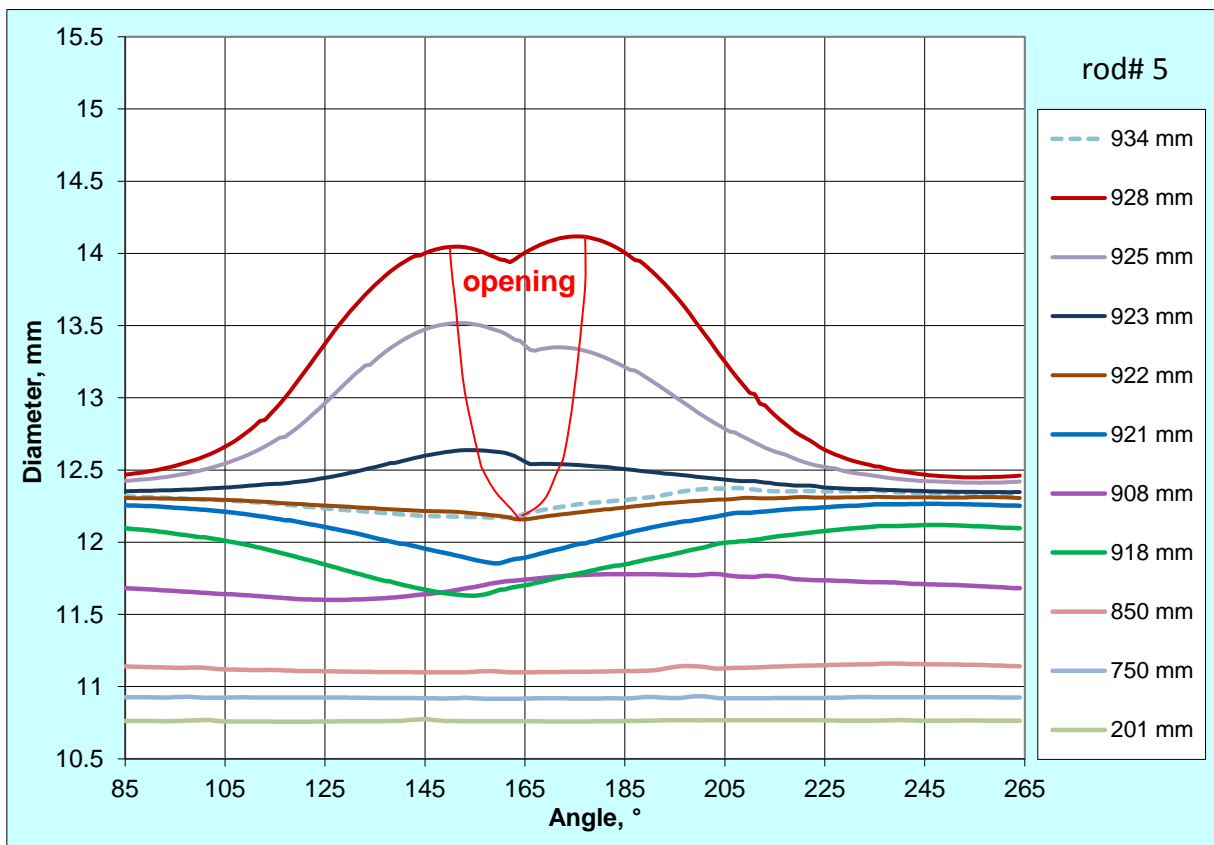
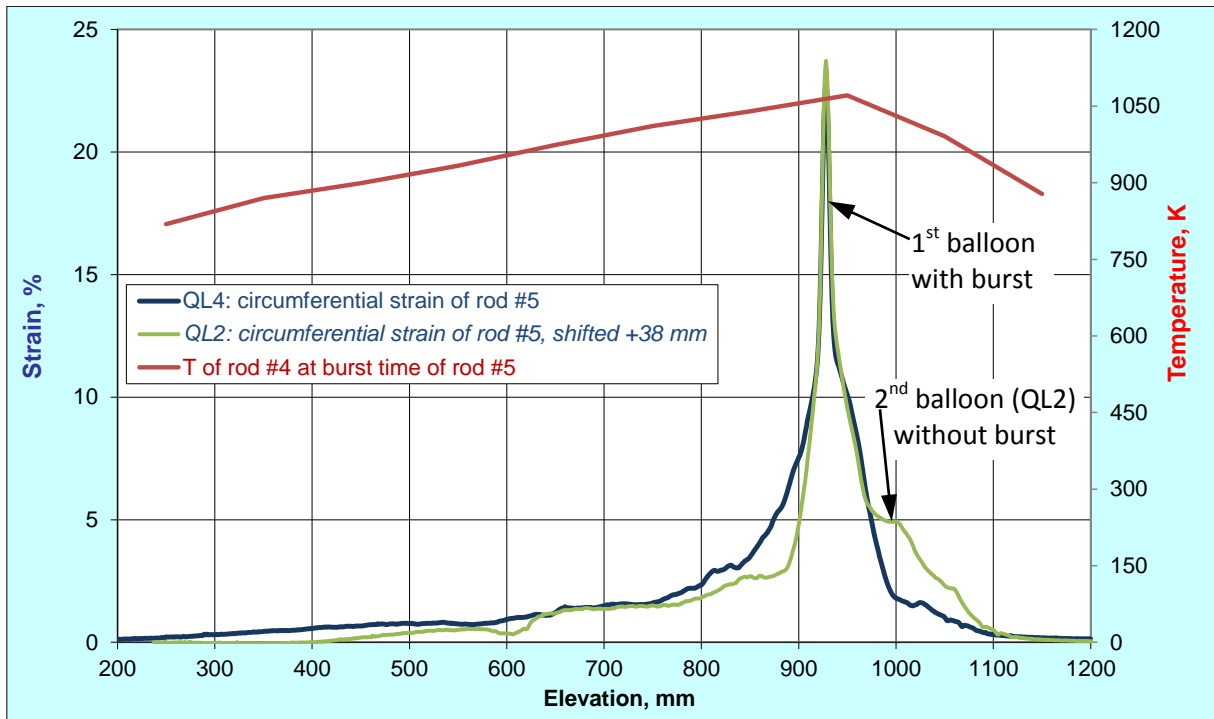


Figure 86 QUENCH-L4, Rod #5; longitudinal changing of circumferential strain (top): QL4 main balloon region is longer than QL2 one; azimuthal diameter downwards from burst (bottom).

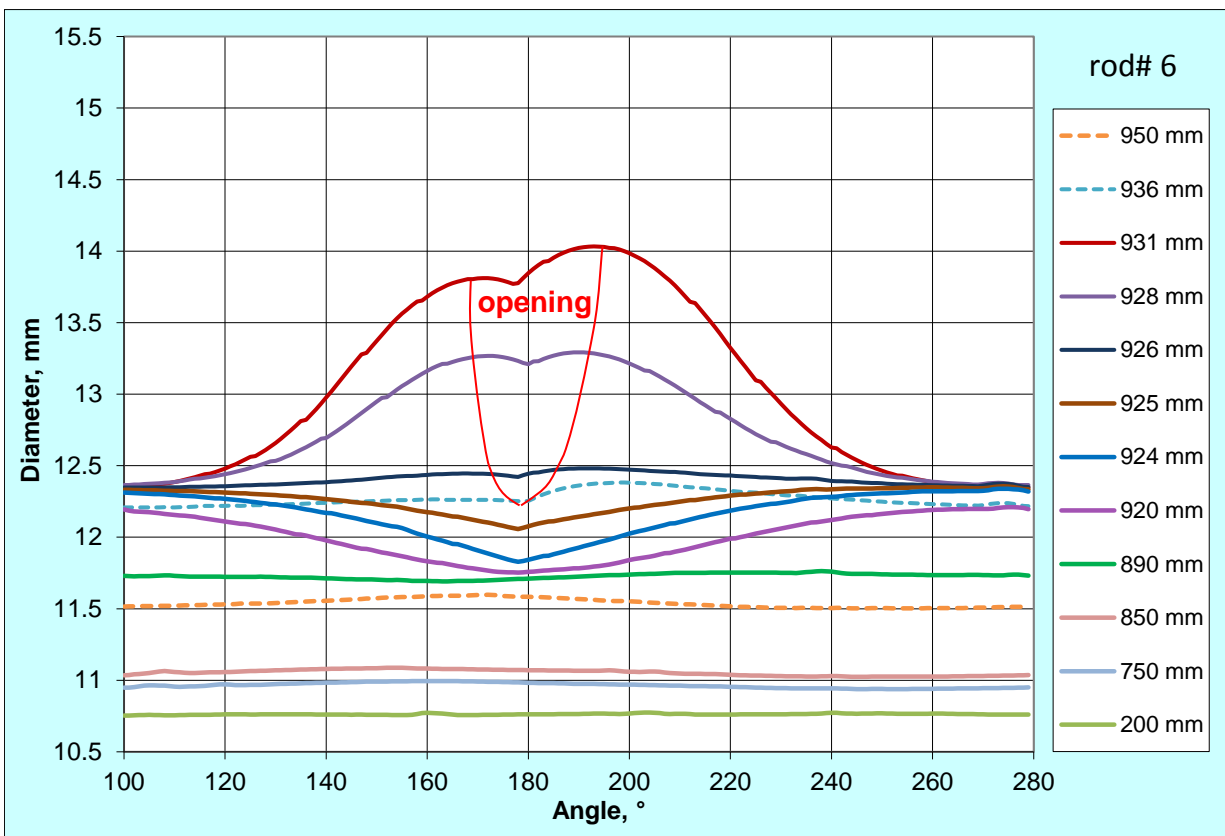
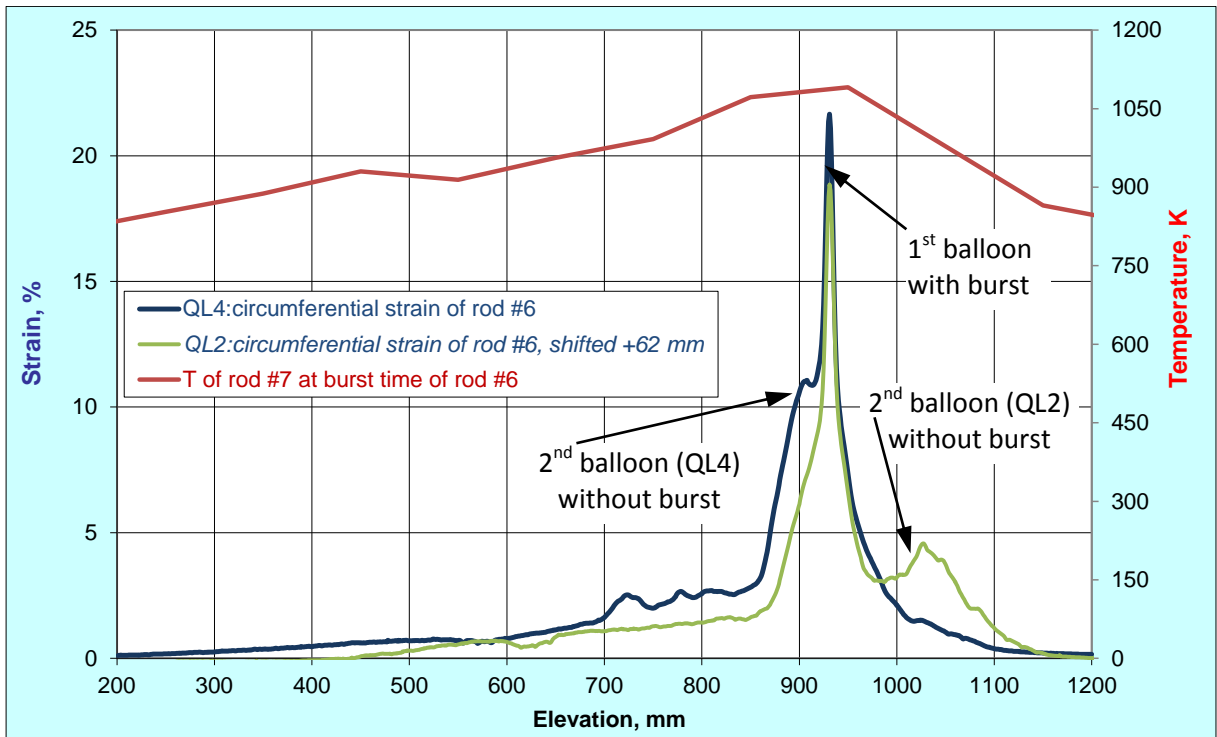


Figure 87 QUENCH-L4, Rod #6; longitudinal changing of circumferential strain (top): QL4 main balloon region is longer than QL2 one; azimuthal diameter downwards from burst (bottom).

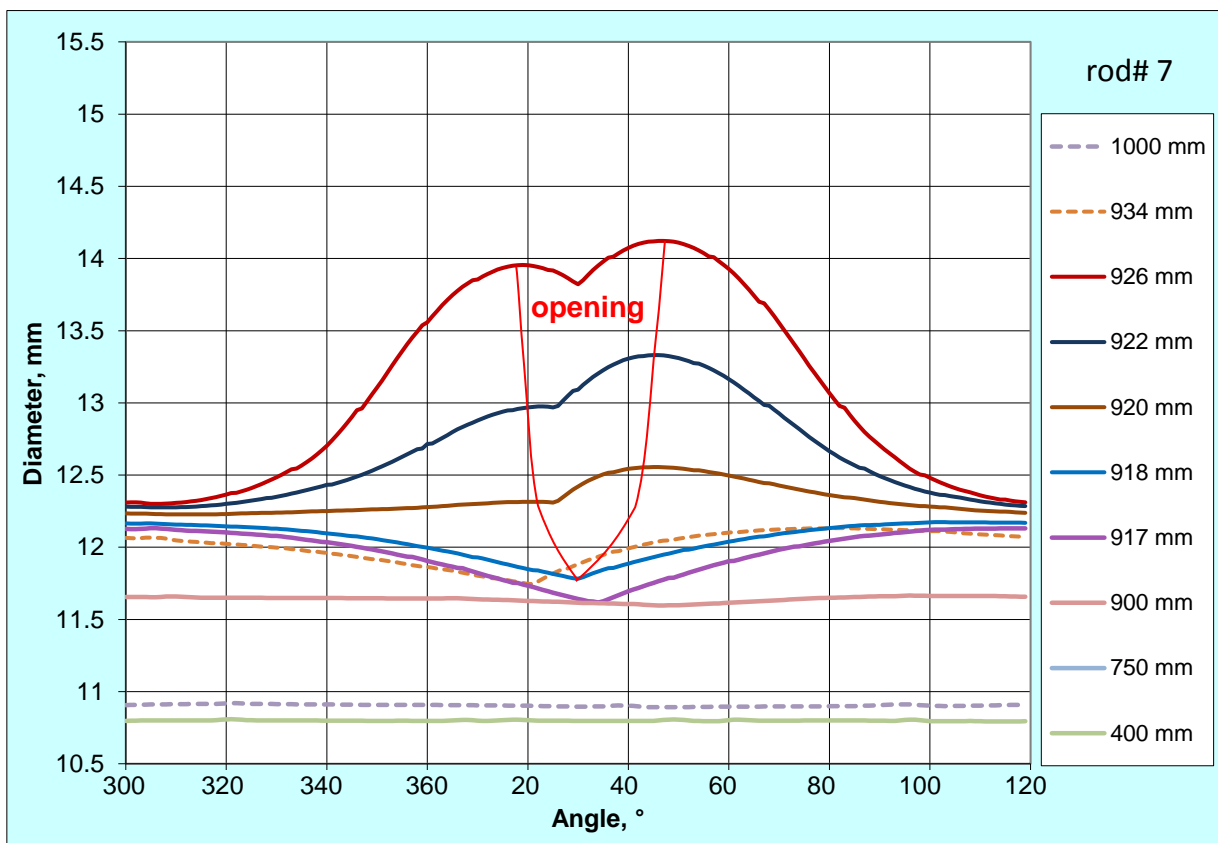
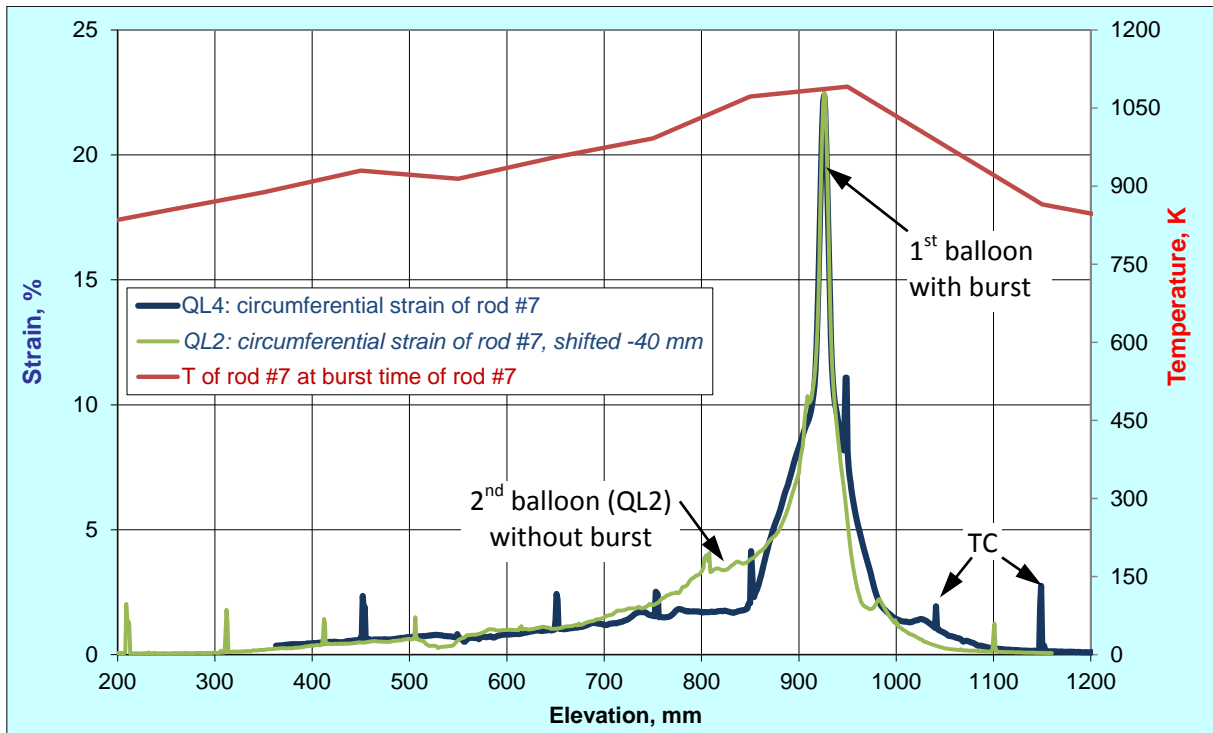


Figure 88 QUENCH-L4, Rod #7; longitudinal changing of circumferential strain (top): QL4 main balloon region is longer than QL2 one; azimuthal diameter downwards from burst (bottom).

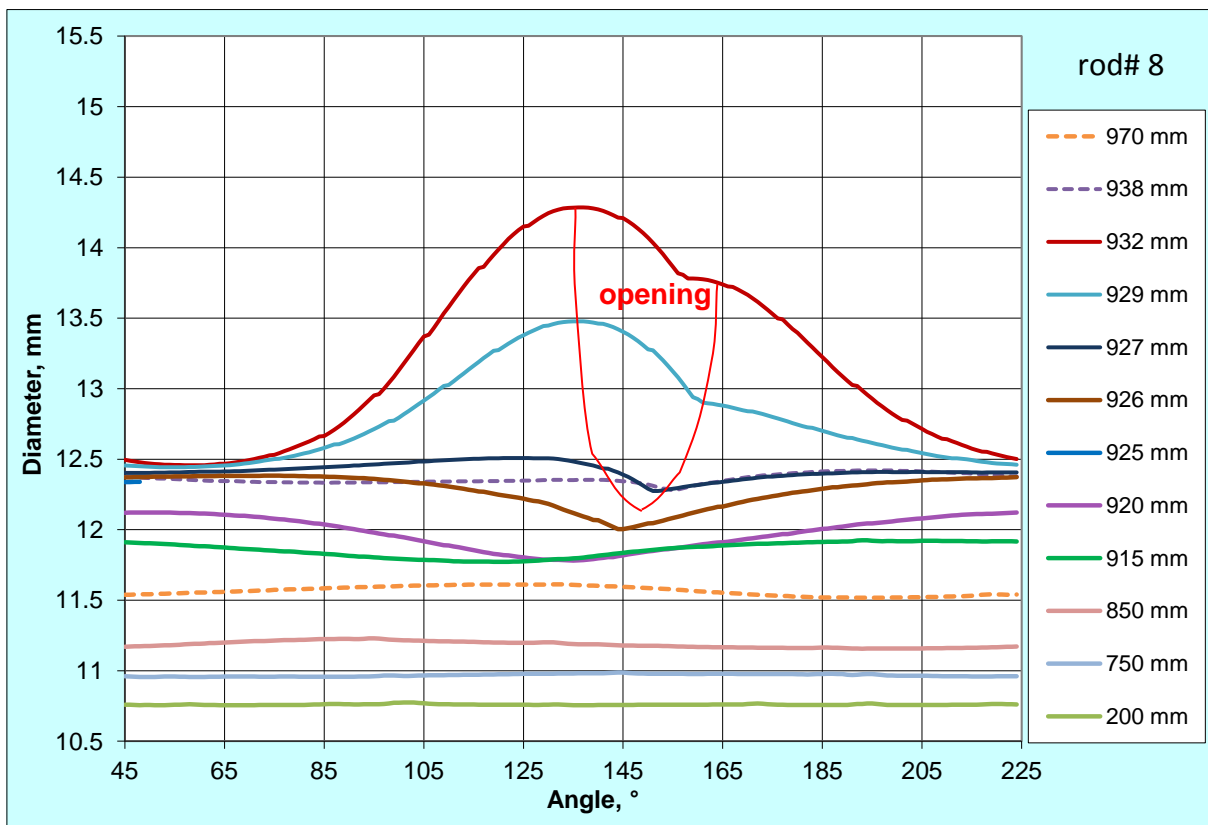
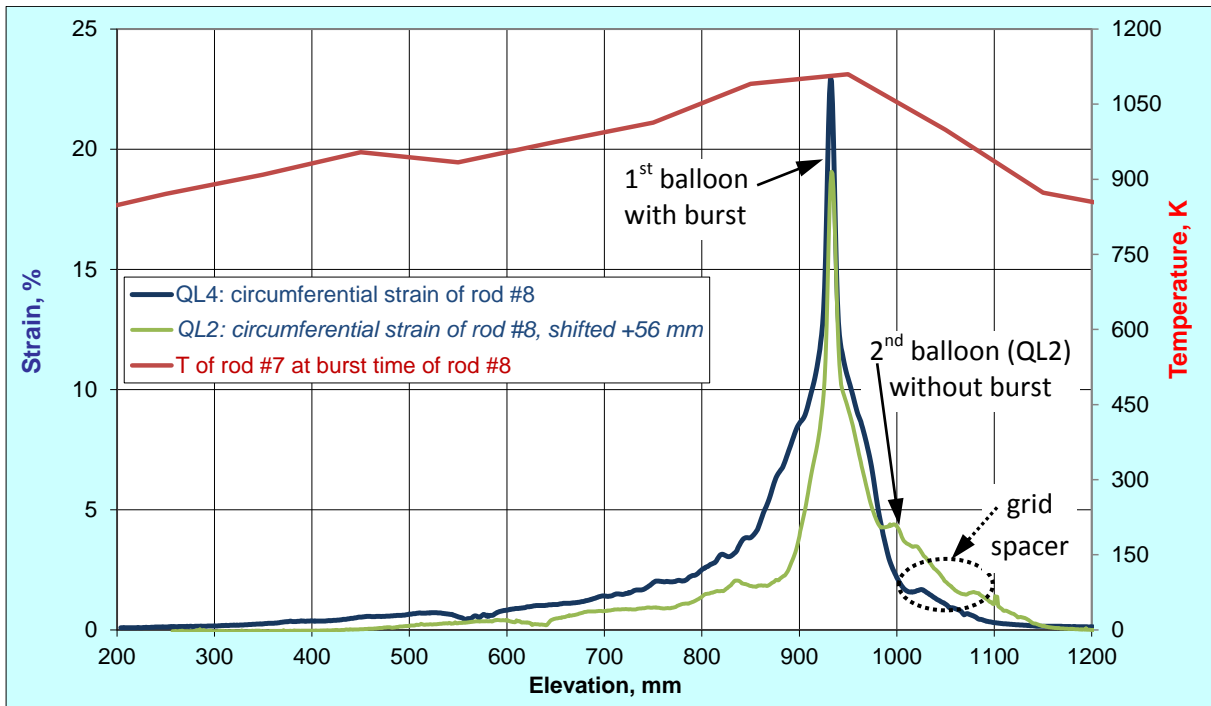


Figure 89 QUENCH-L4, Rod #8; longitudinal changing of circumferential strain (top): QL4 main balloon region is longer than QL2 one; azimuthal diameter downwards from burst (bottom).

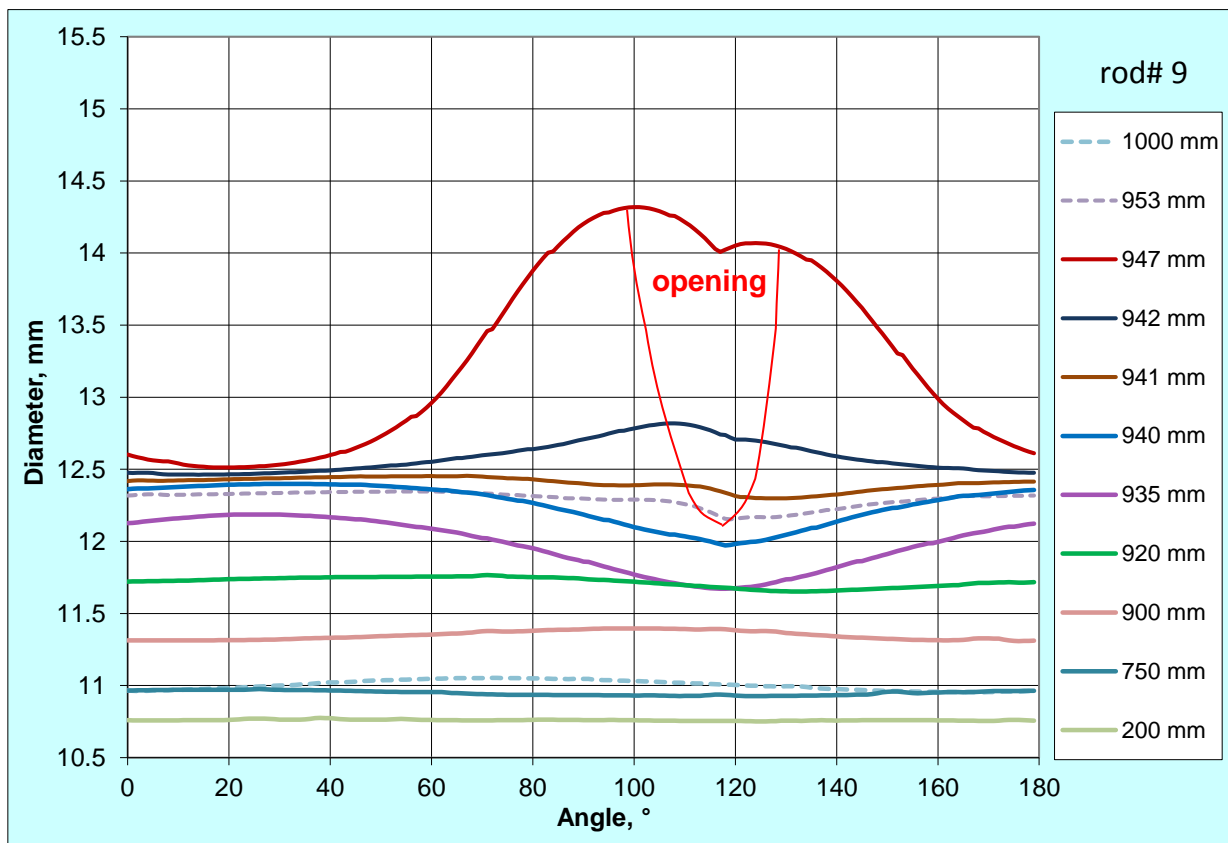
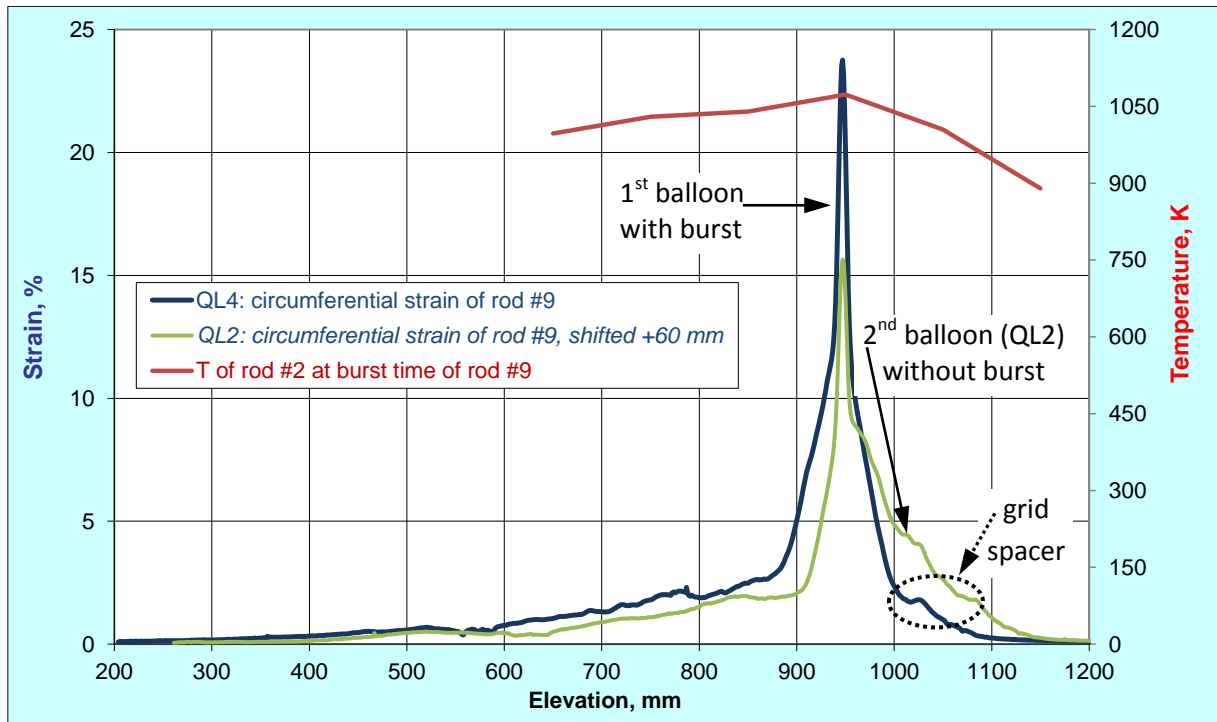


Figure 90 QUENCH-L4, Rod #9; longitudinal changing of circumferential strain (top); azimuthal diameter downwards from burst (bottom).

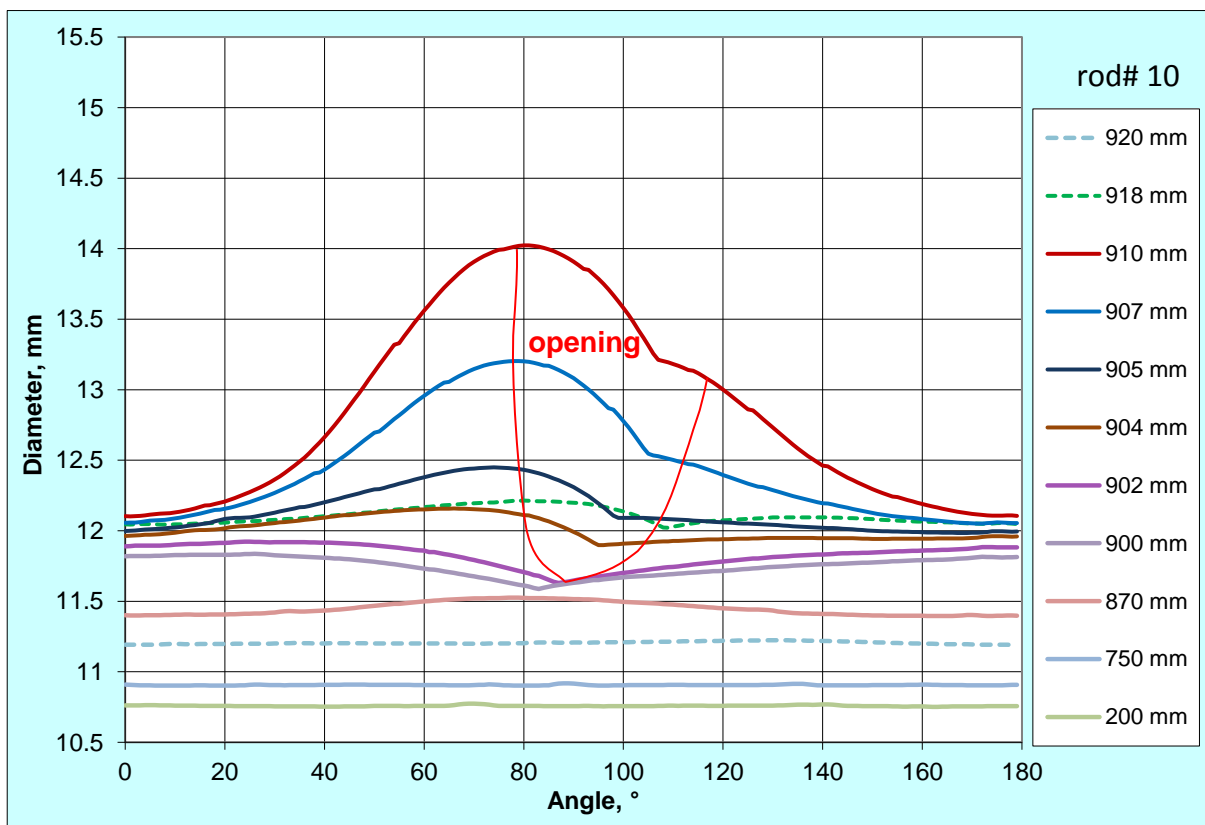
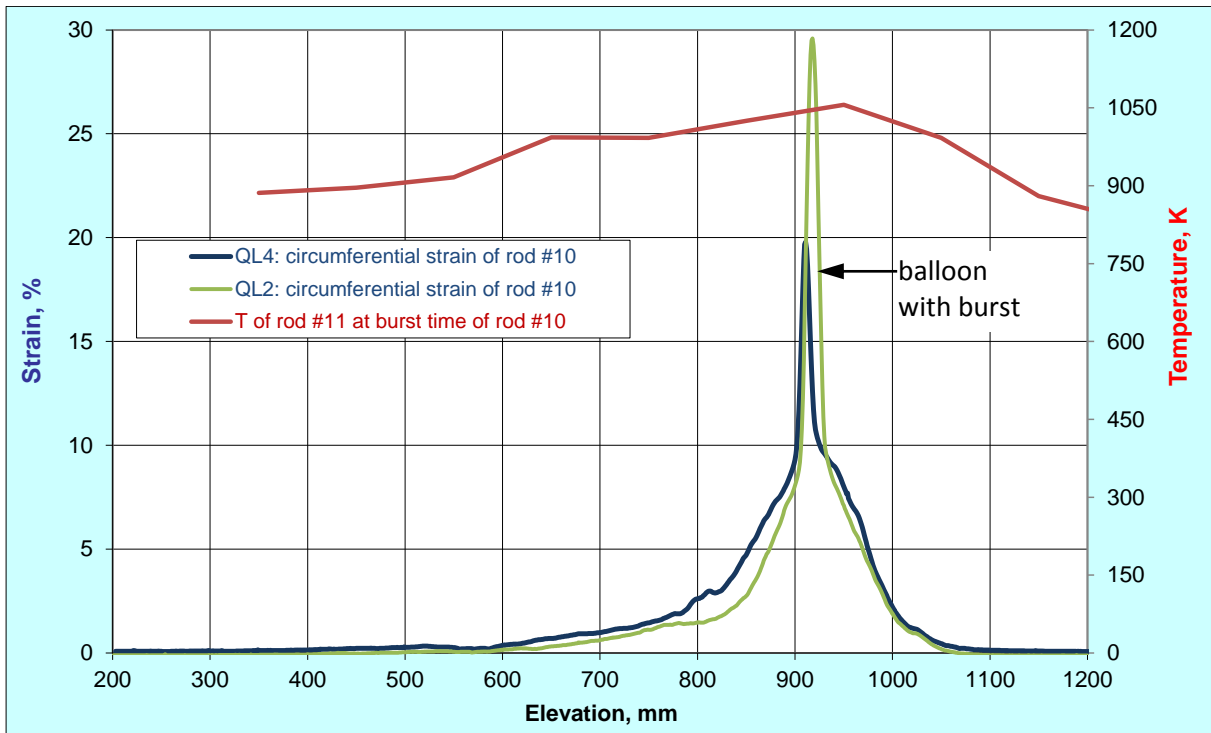


Figure 91 QUENCH-L4, Rod #10; longitudinal changing of circumferential strain (top): QL4 main balloon region is longer than QL2 one; azimuthal diameter downwards from burst (bottom).

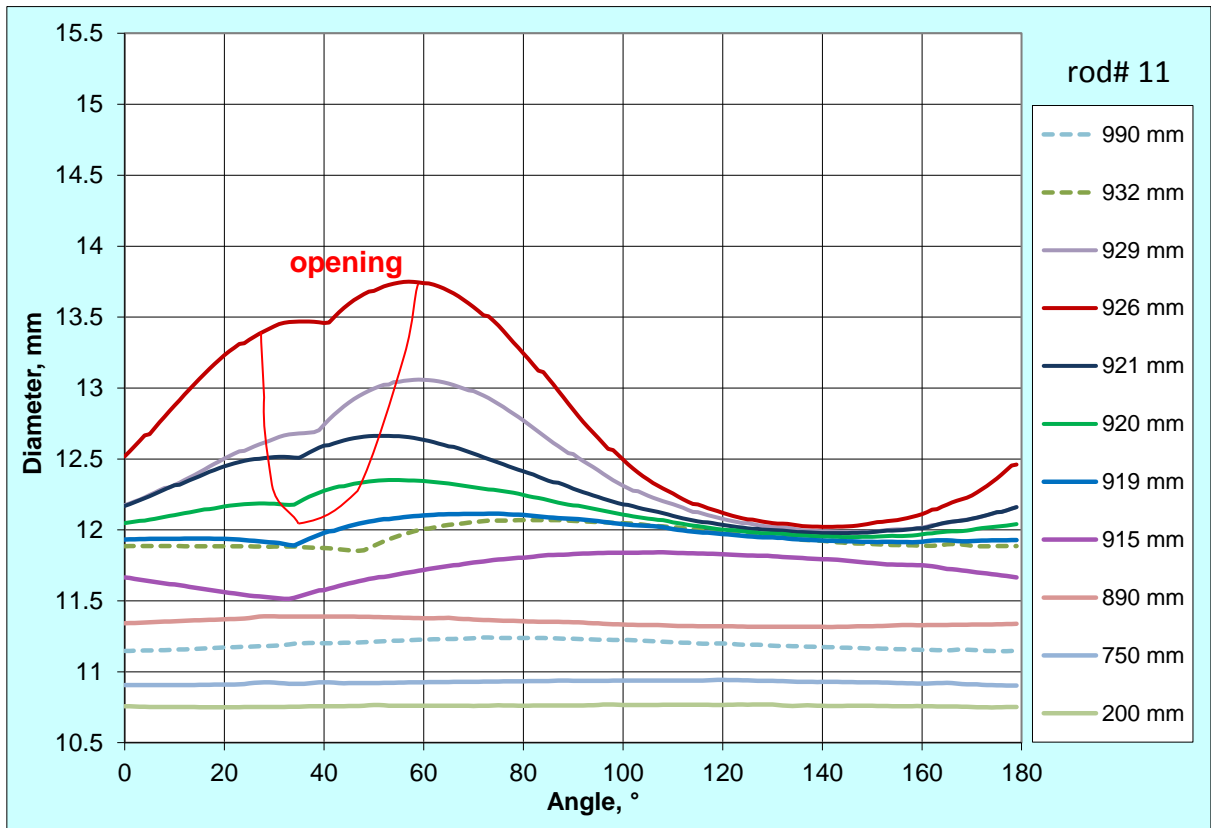
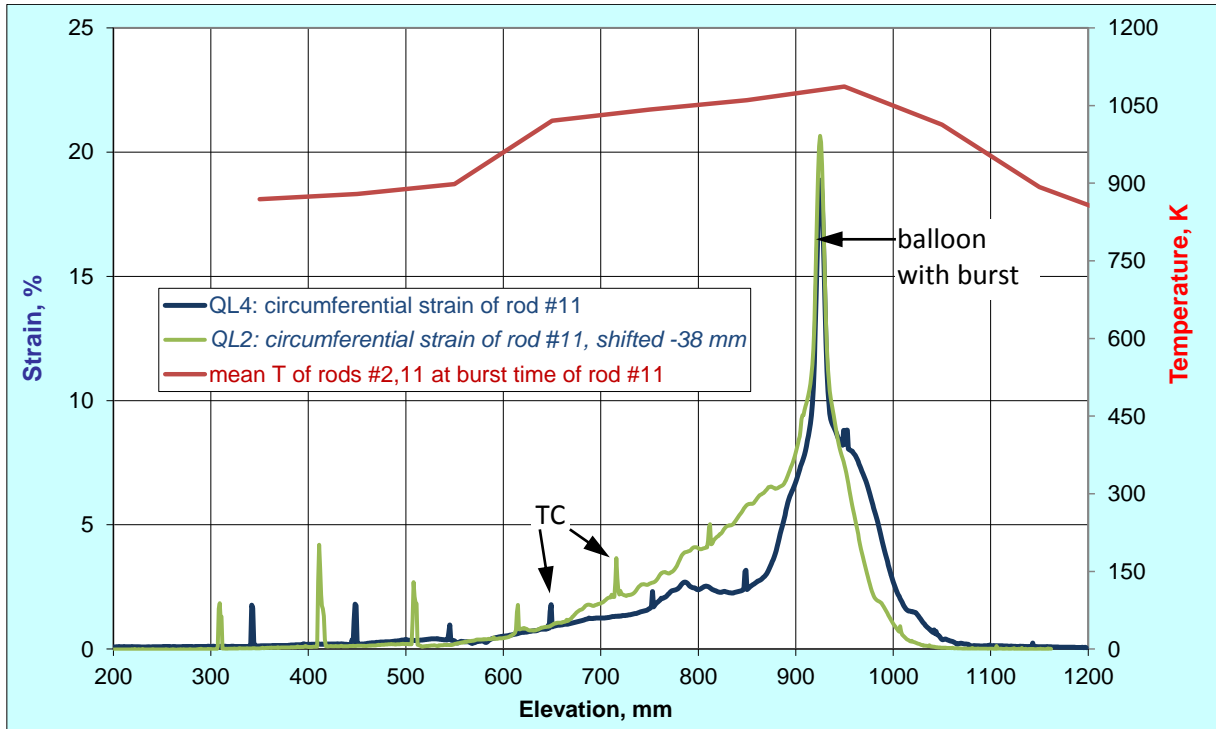


Figure 92 QUENCH-L4, Rod #11; longitudinal changing of circumferential strain (top); azimuthal diameter downwards from burst (bottom).

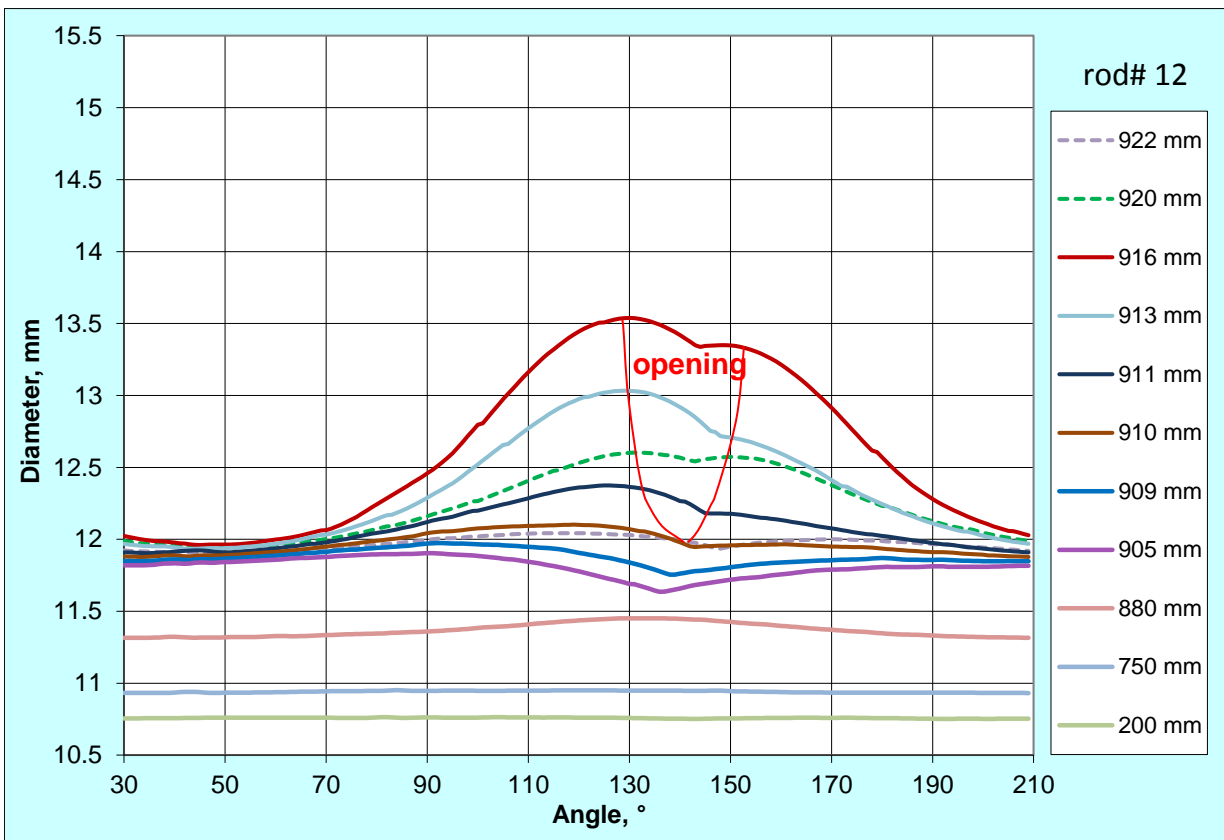
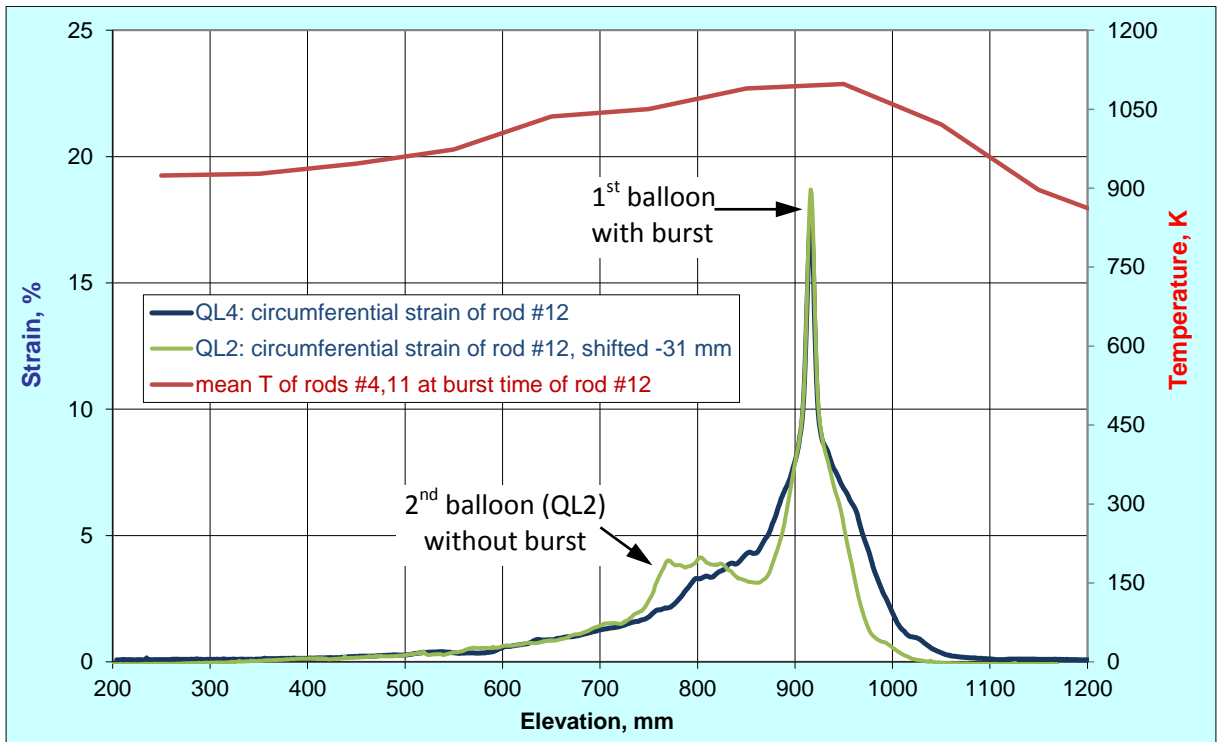


Figure 93 QUENCH-L4, Rod #12; longitudinal changing of circumferential strain (top): QL4 main balloon region is longer than QL2 one; azimuthal diameter downwards from burst (bottom).

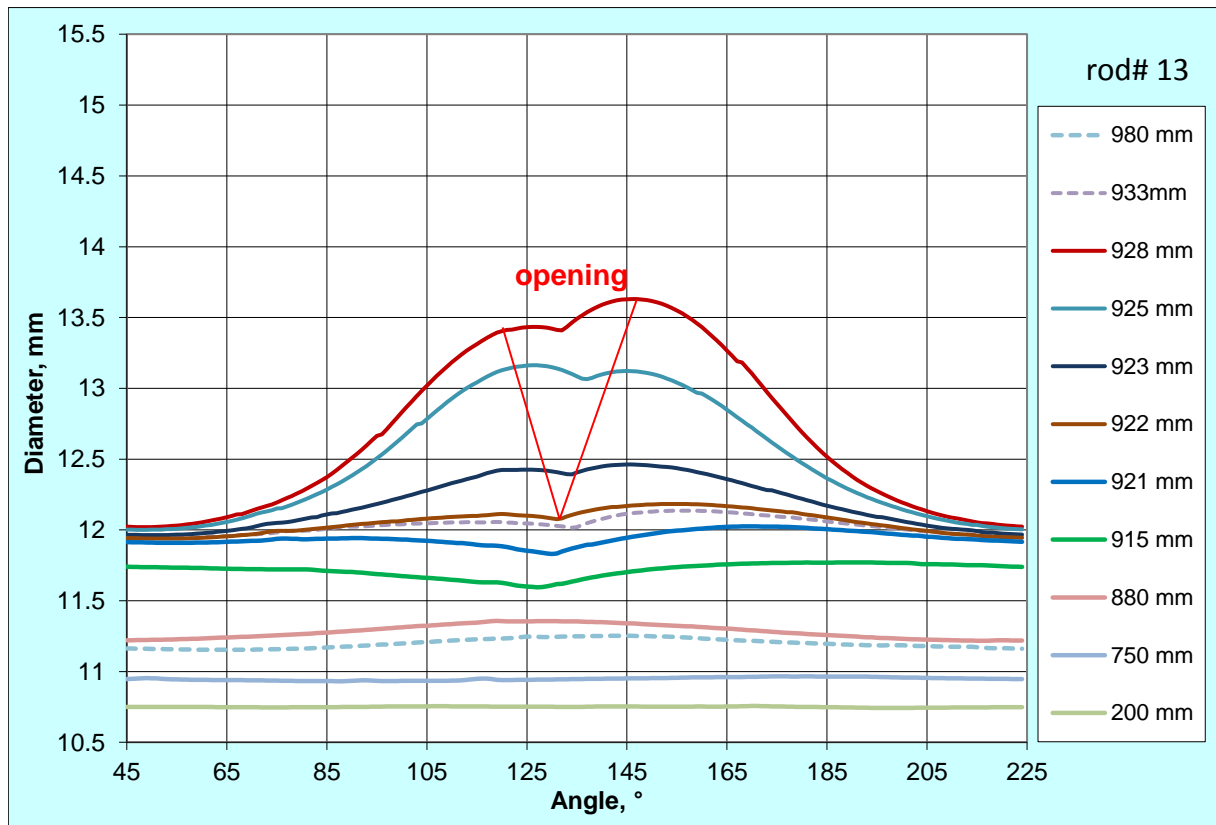
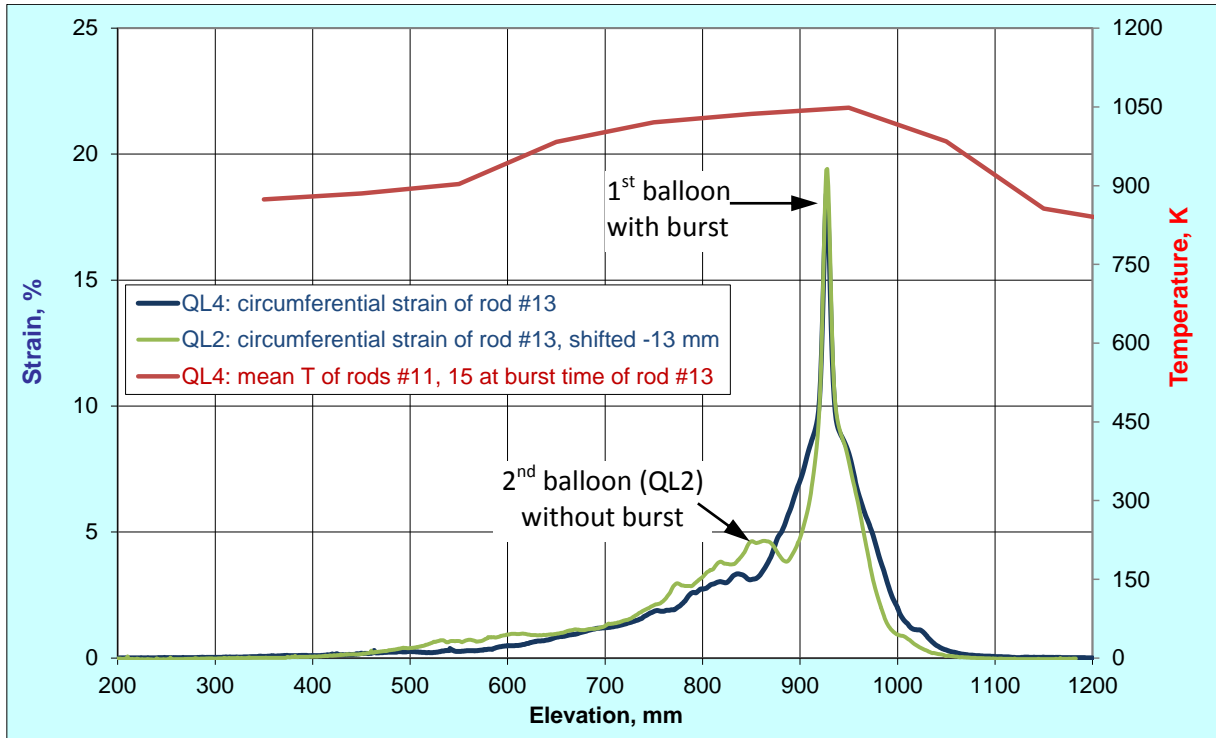


Figure 94 QUENCH-L4, Rod #13; longitudinal changing of circumferential strain (top); azimuthal diameter downwards from burst (bottom).

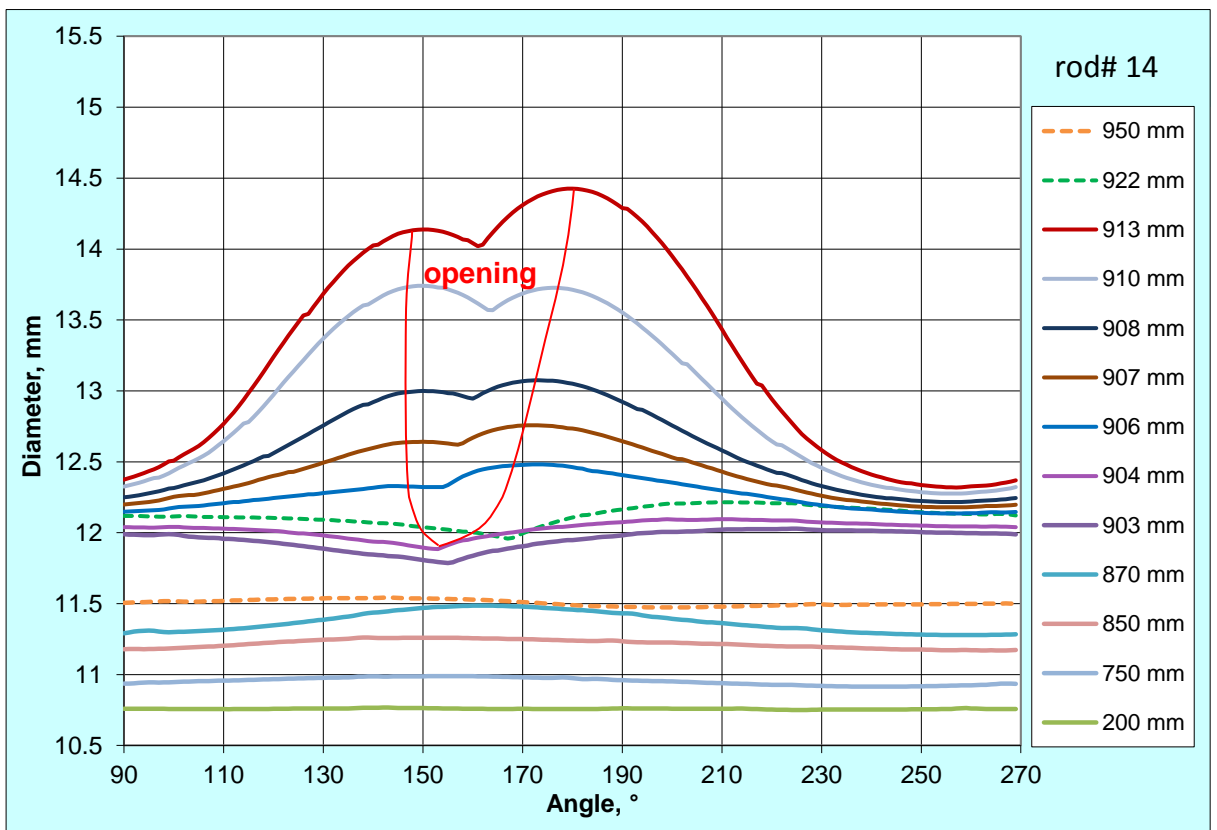
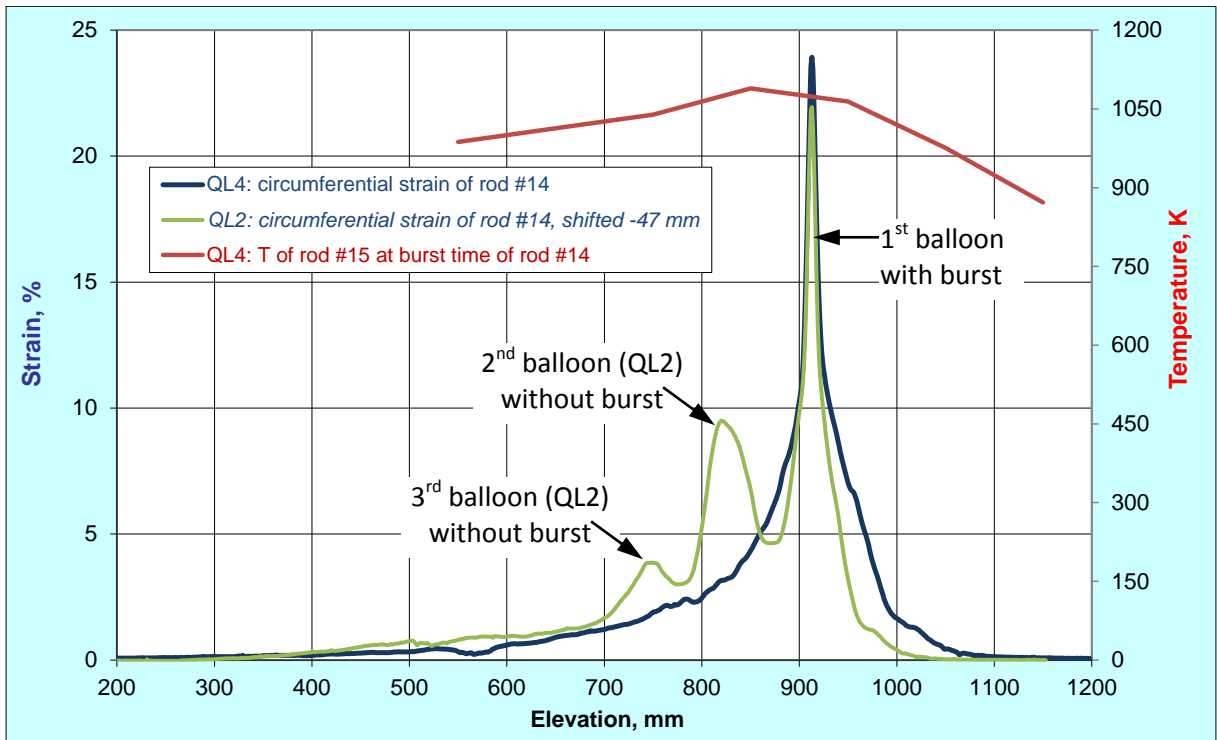


Figure 95 QUENCH-L4, Rod #14; longitudinal changing of circumferential strain (top): QL4 main balloon region is longer than QL2 one; azimuthal diameter downwards from burst (bottom).

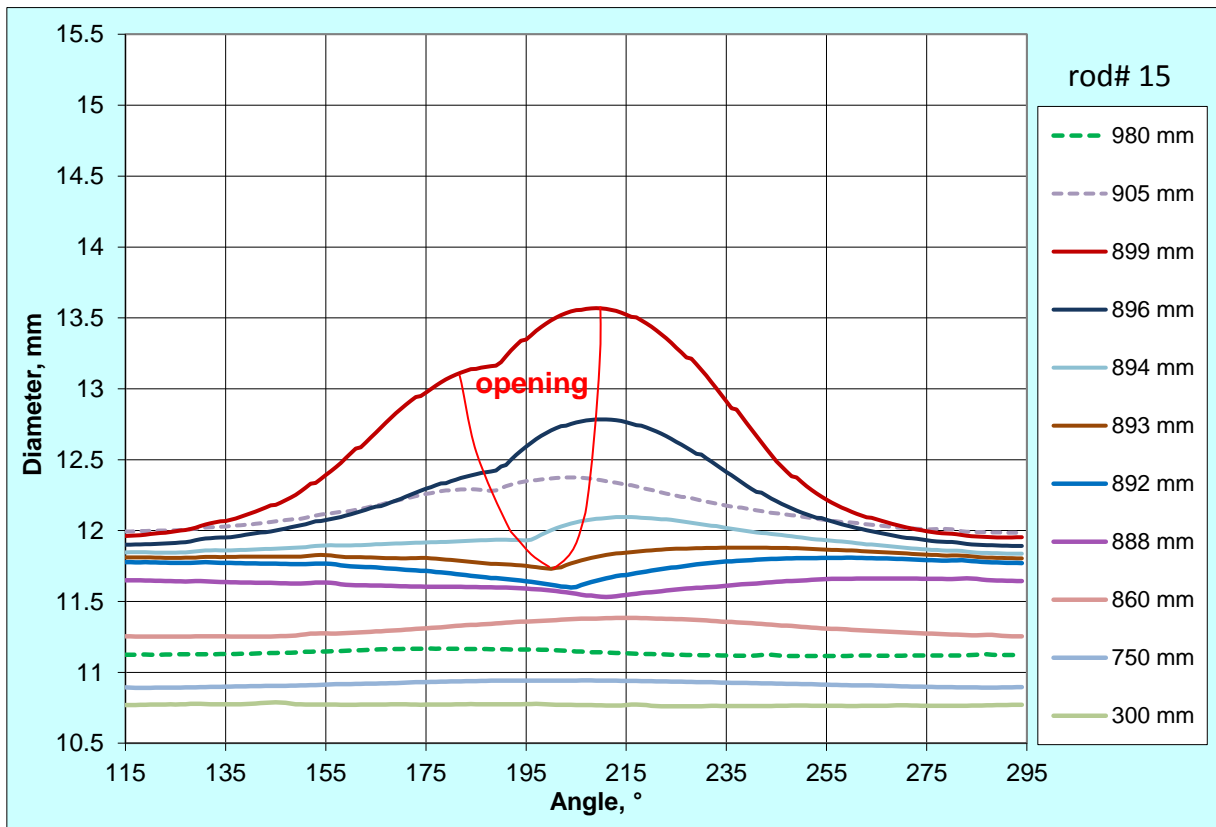
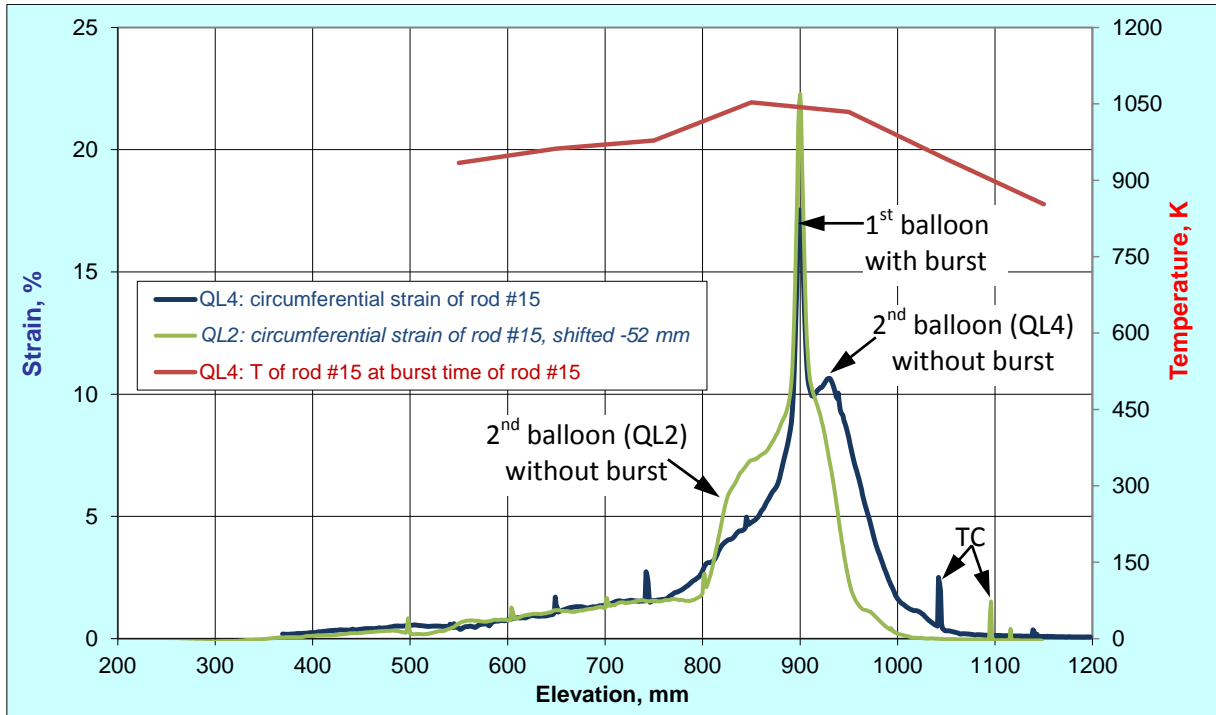


Figure 96 QUENCH-L4, Rod #15; longitudinal changing of circumferential strain (top); azimuthal diameter downwards from burst (bottom). Spikes: thermocouple.

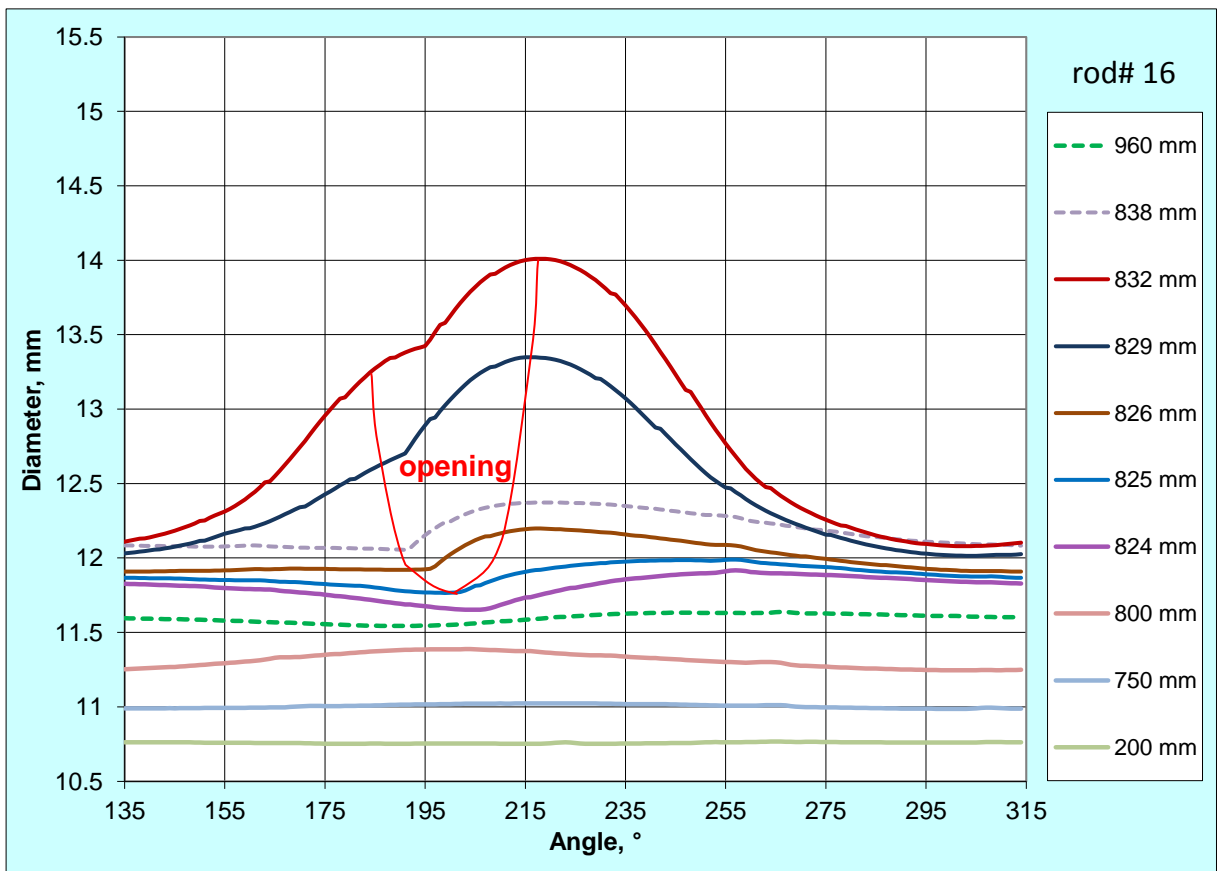
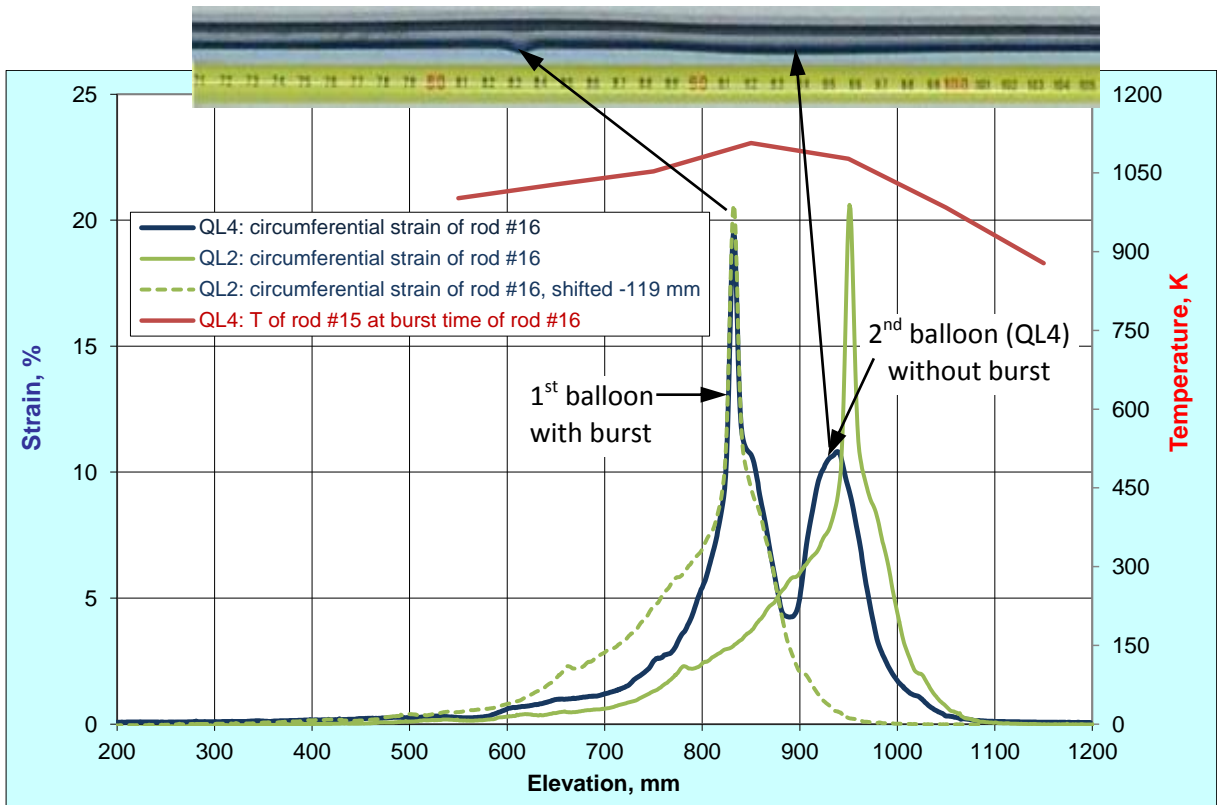


Figure 97 QUENCH-L4, Rod #16; longitudinal changing of circumferential strain in comparison to corresponding rod of QL2 and side view of the QL4-#16 rod (top); azimuthal diameter downwards from burst (bottom).

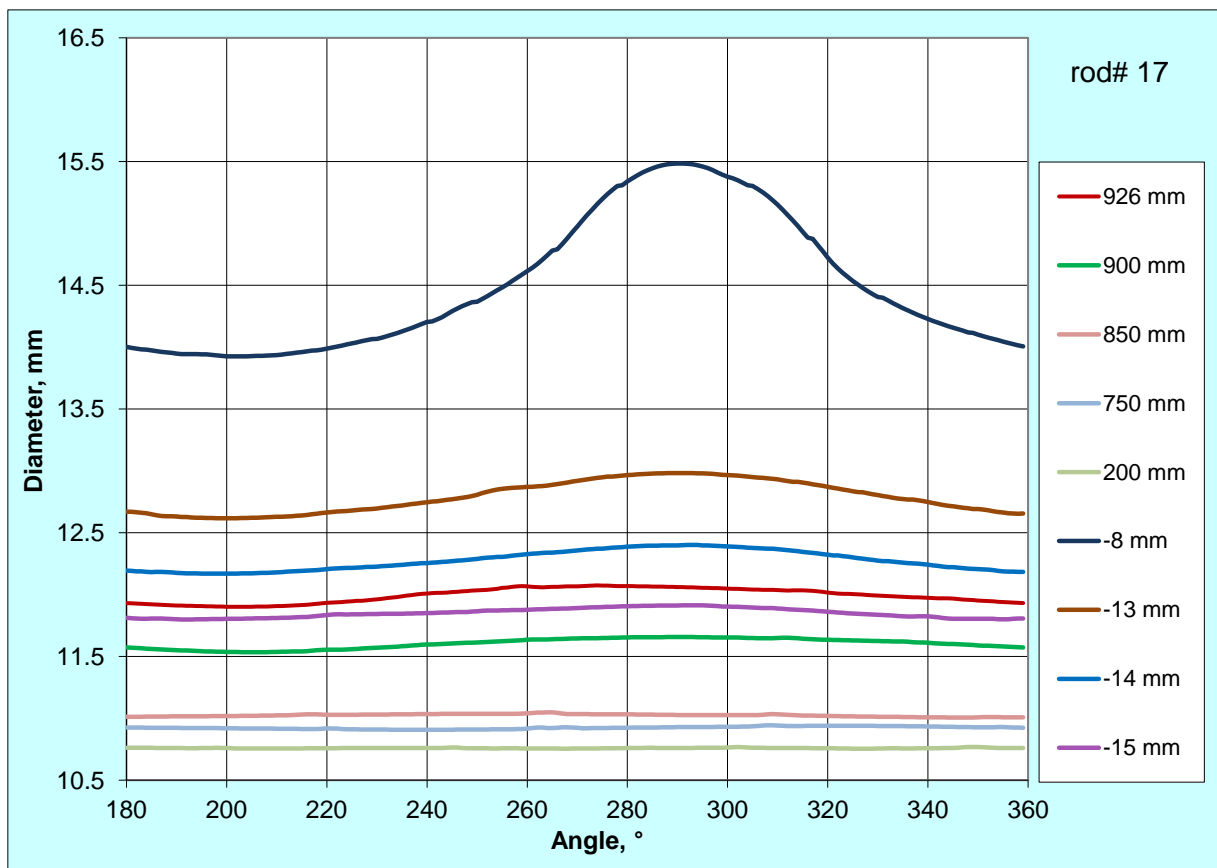
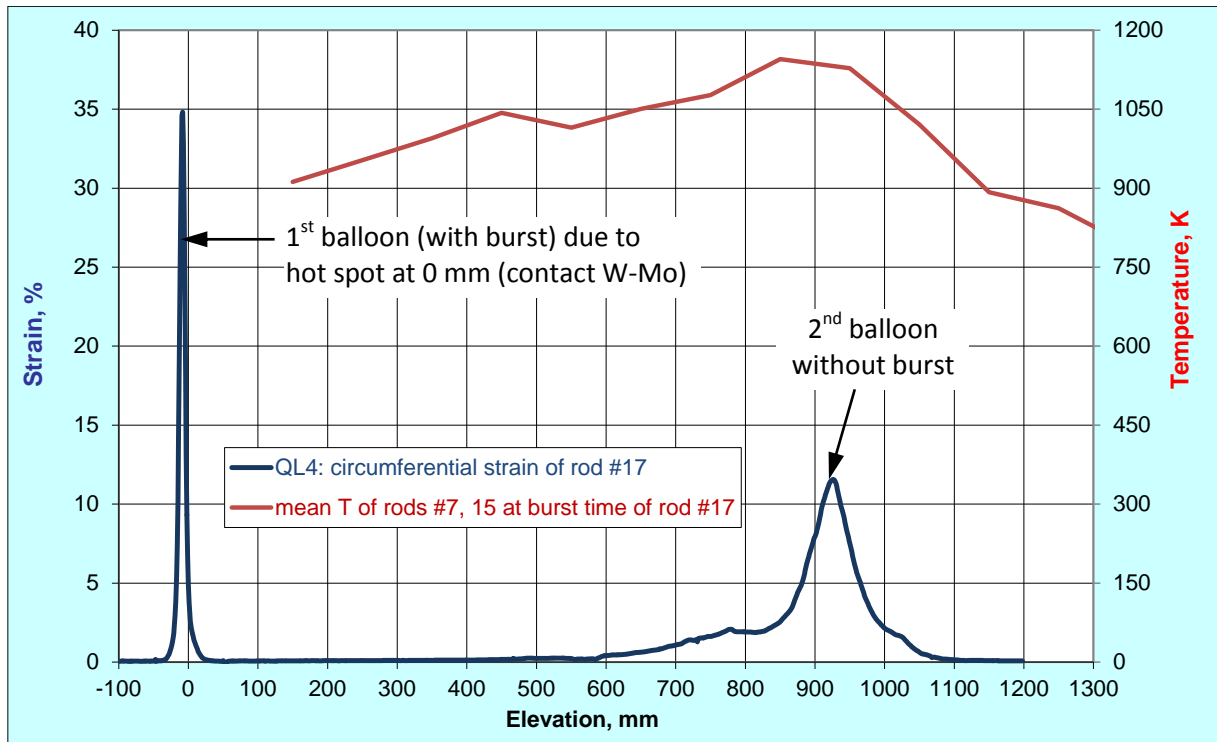


Figure 98 QUENCH-L4, Rod #17; longitudinal changing of circumferential strain (top); azimuthal diameter downwards from burst (bottom).

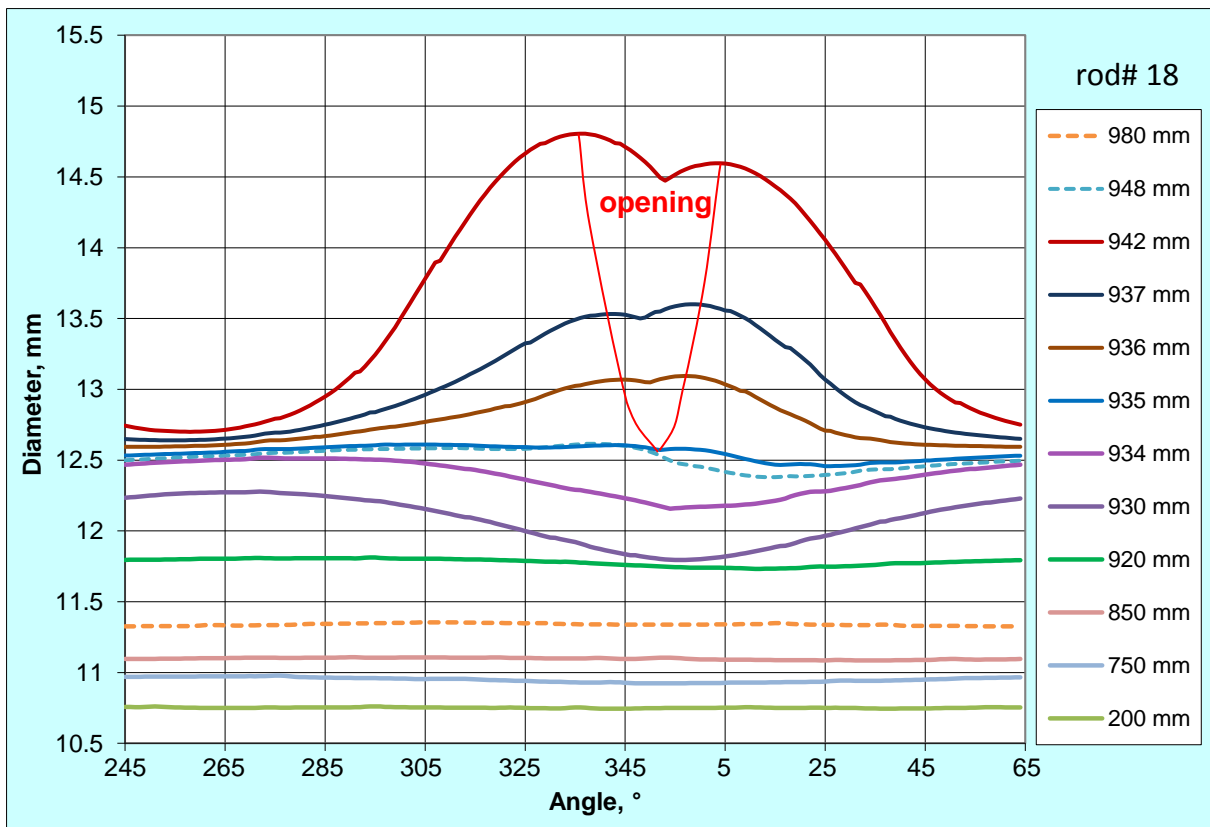
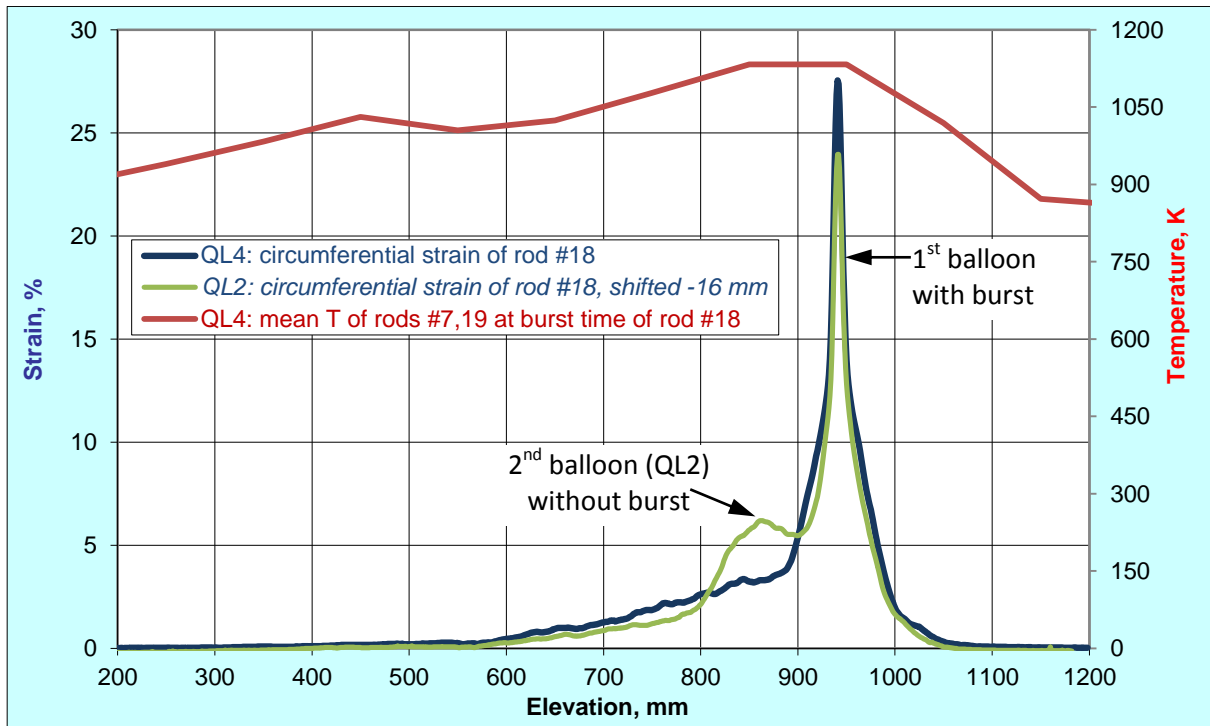


Figure 99 QUENCH-L4, Rod #18; longitudinal changing of circumferential strain (top): QL4 main balloon region is longer than QL2 one; azimuthal diameter downwards from burst (bottom).

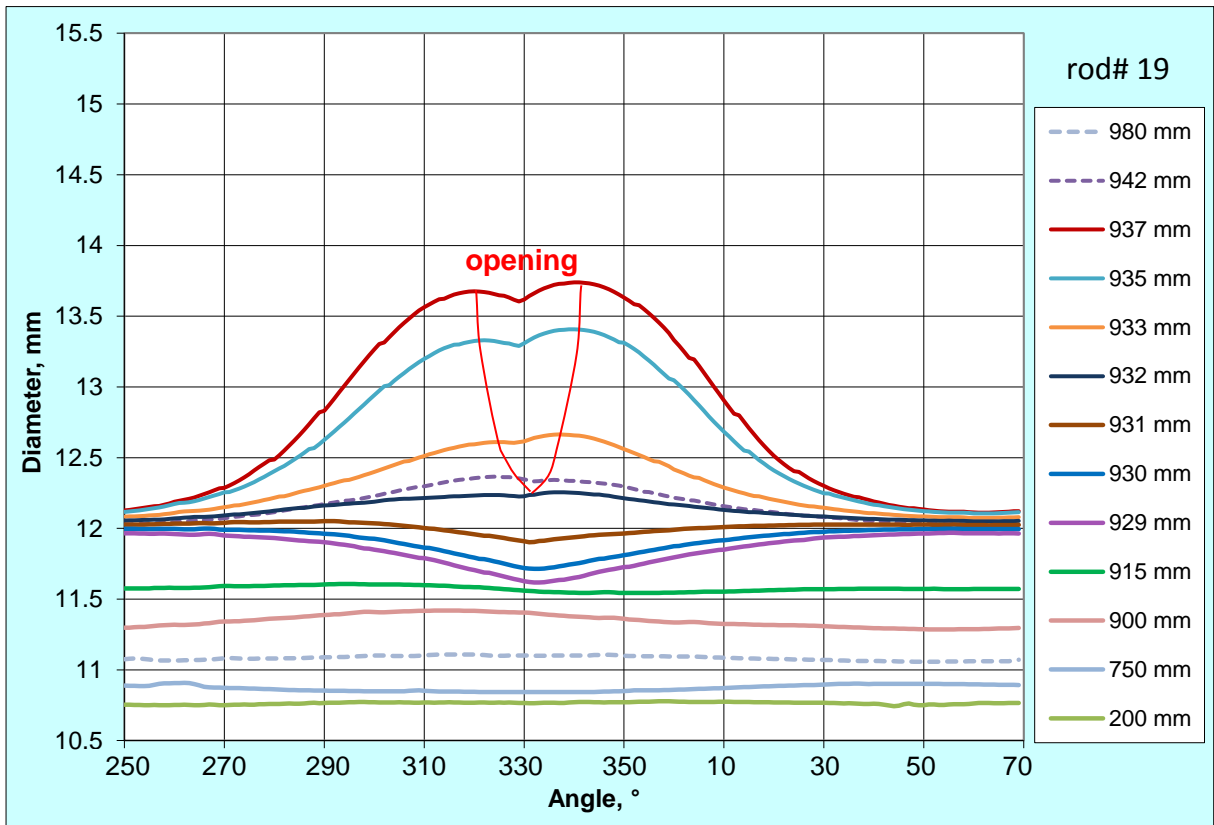
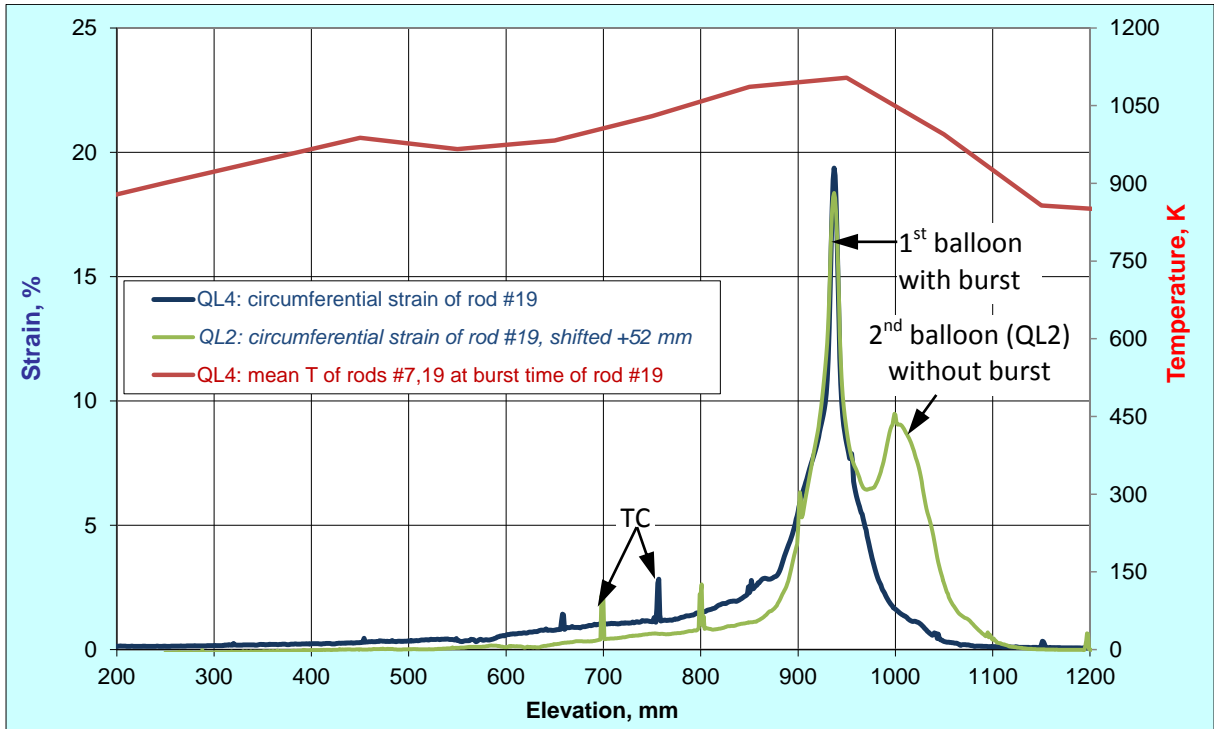


Figure 100 QUENCH-L4, Rod #19; longitudinal changing of circumferential strain (top); azimuthal diameter downwards from burst (bottom). Spikes: thermocouples.

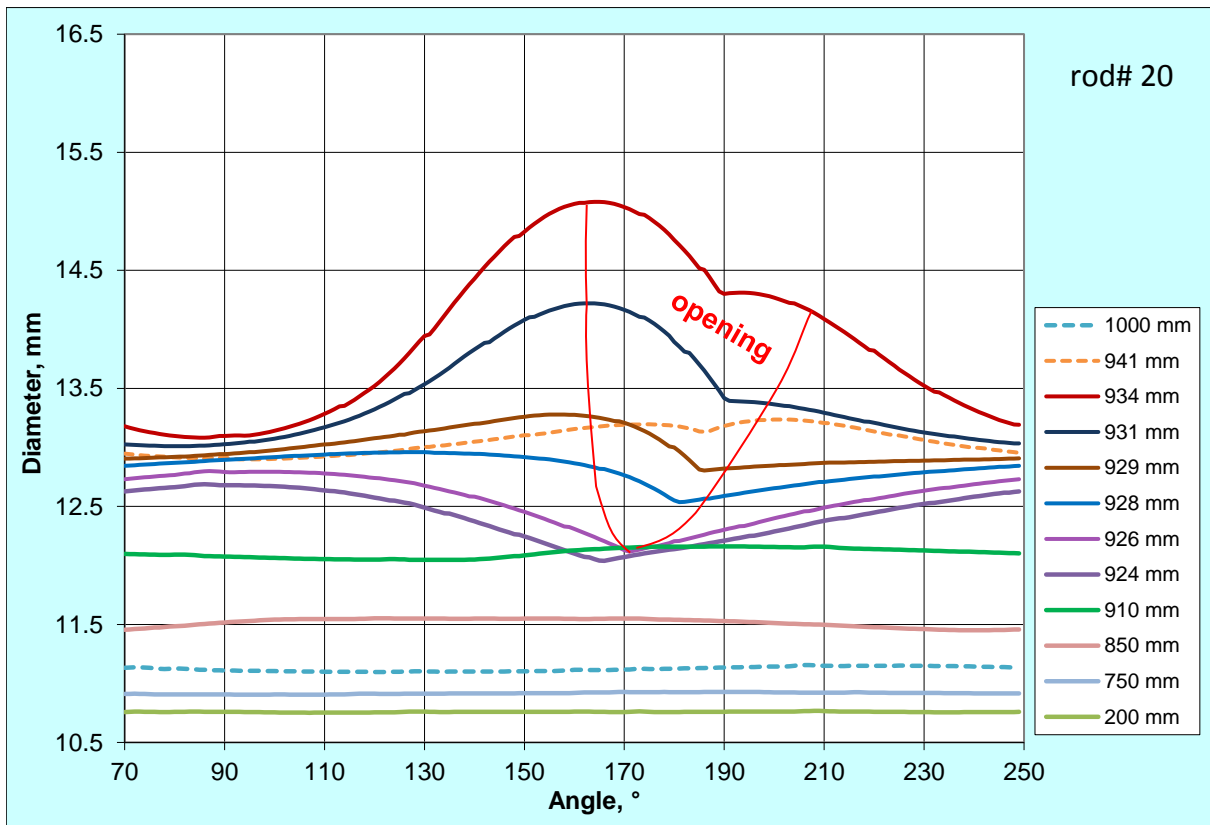
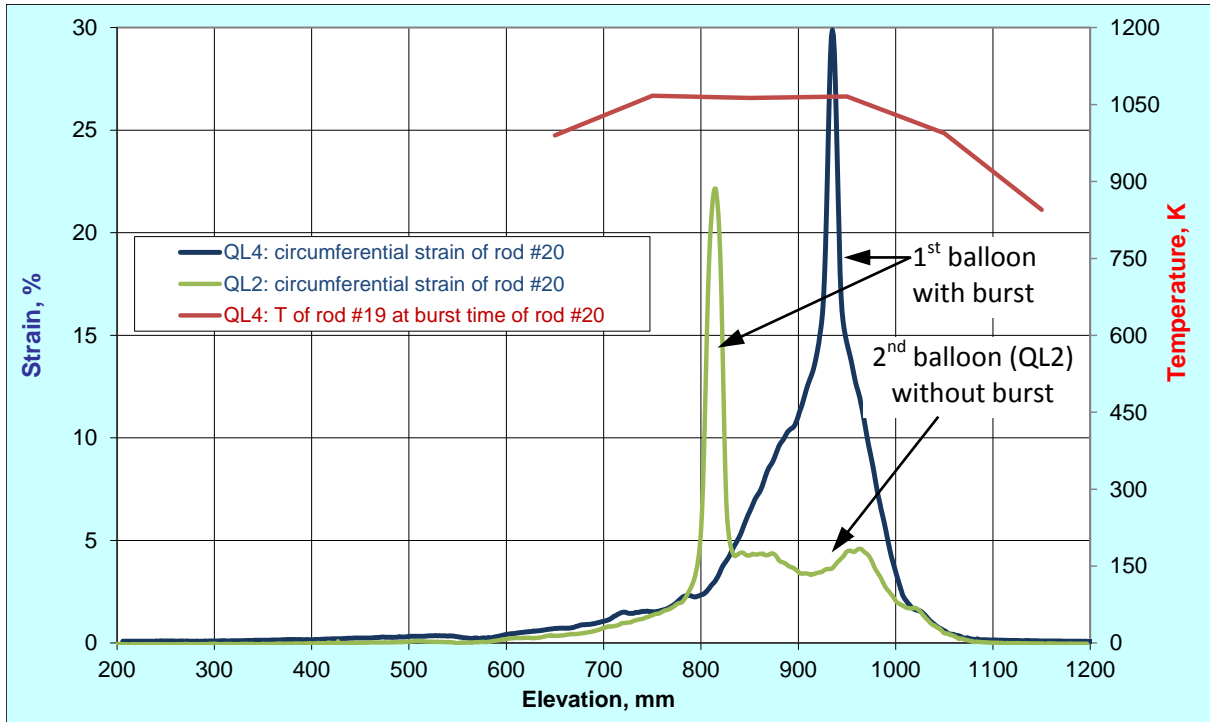


Figure 101 QUENCH-L4, Rod #20; longitudinal changing of circumferential strain (top); azimuthal diameter downwards from burst (bottom).

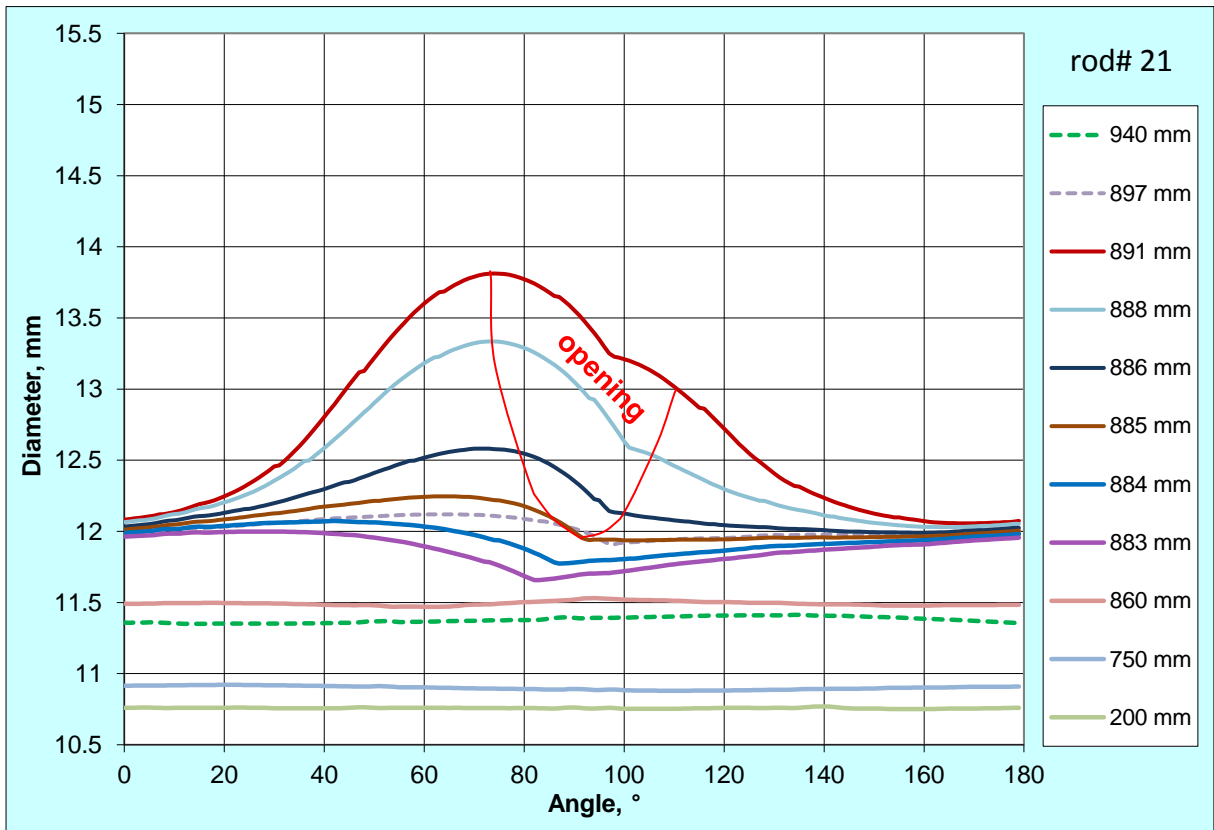
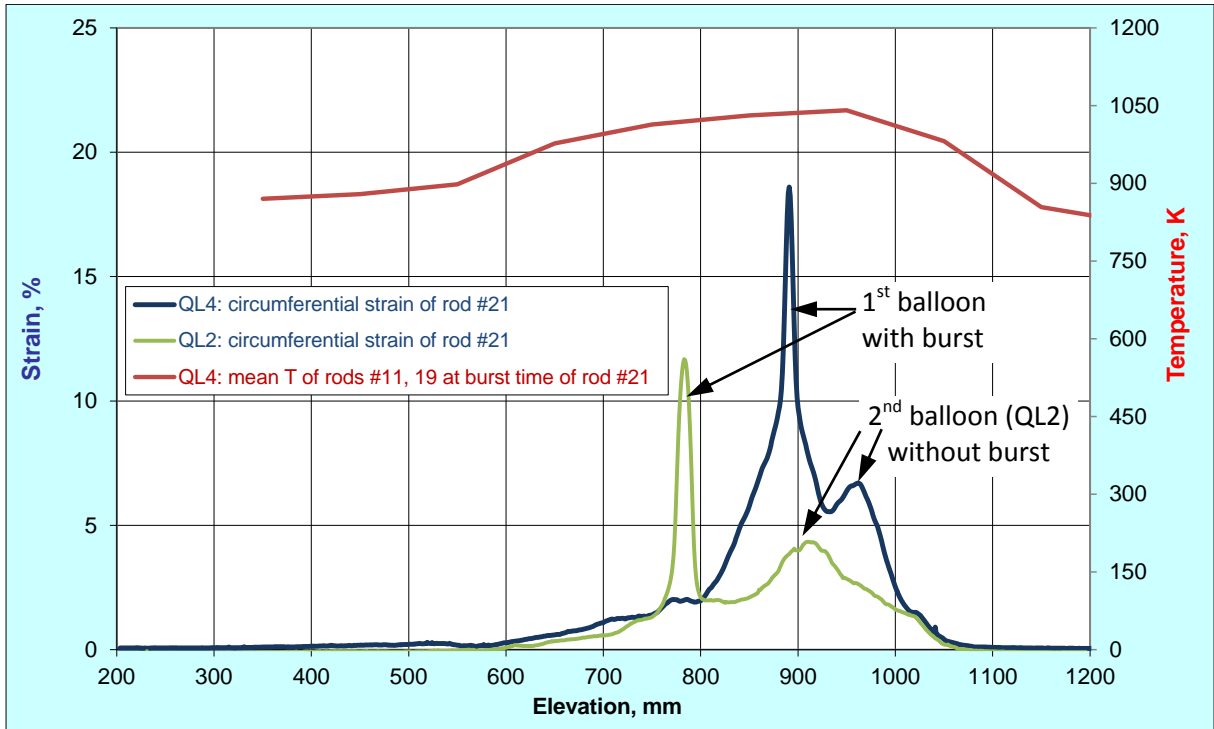


Figure 102 QUENCH-L4, Rod #21; longitudinal changing of circumferential strain (top); azimuthal diameter downwards from burst (bottom).

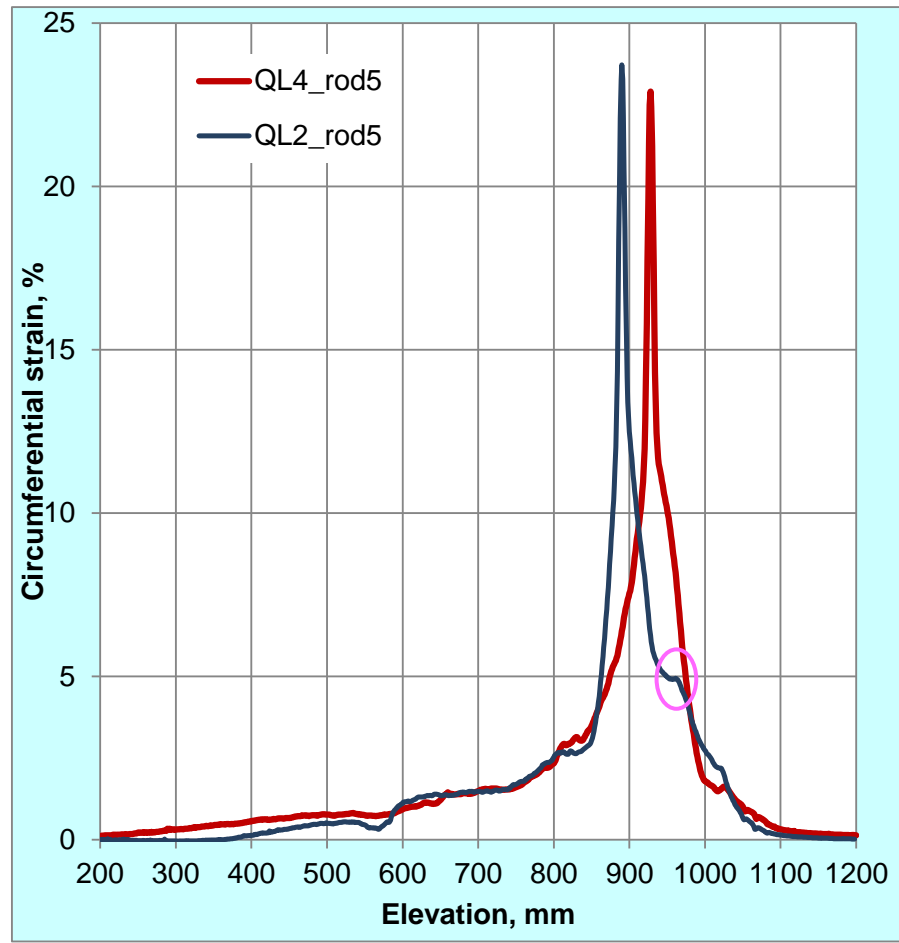
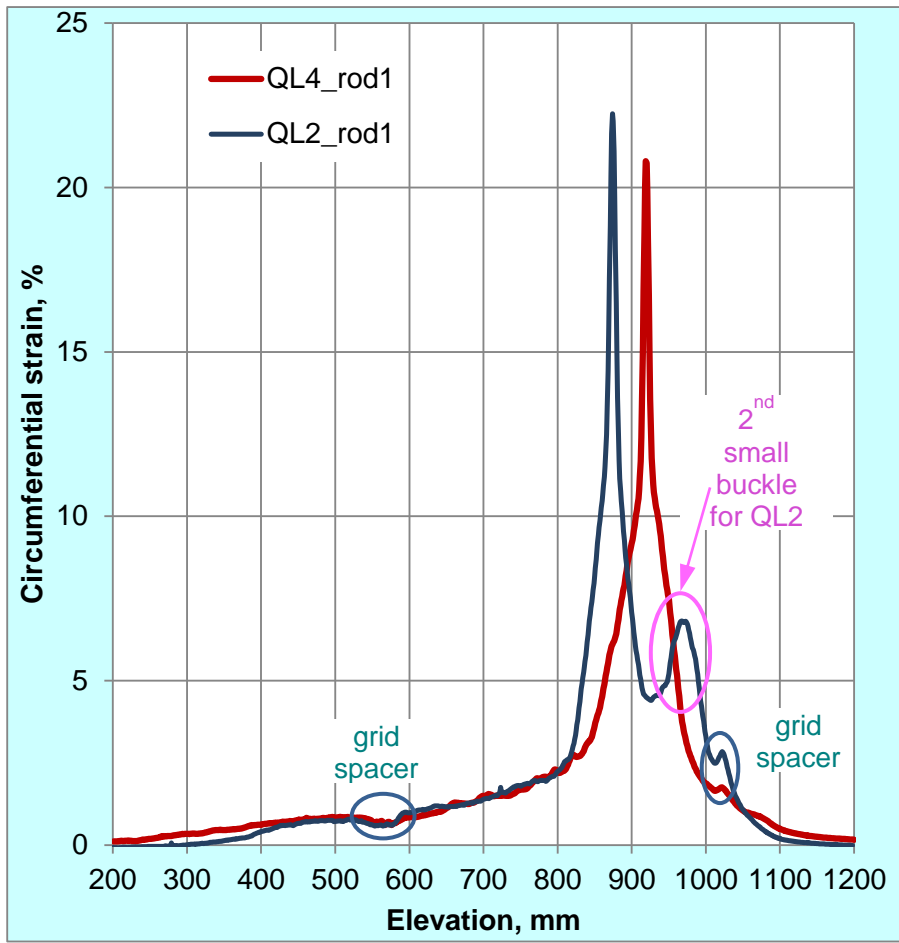


Figure 103 Comparison of circumferential strain between two rods of bundles QUENCH-L2 and QUENCH-L4.

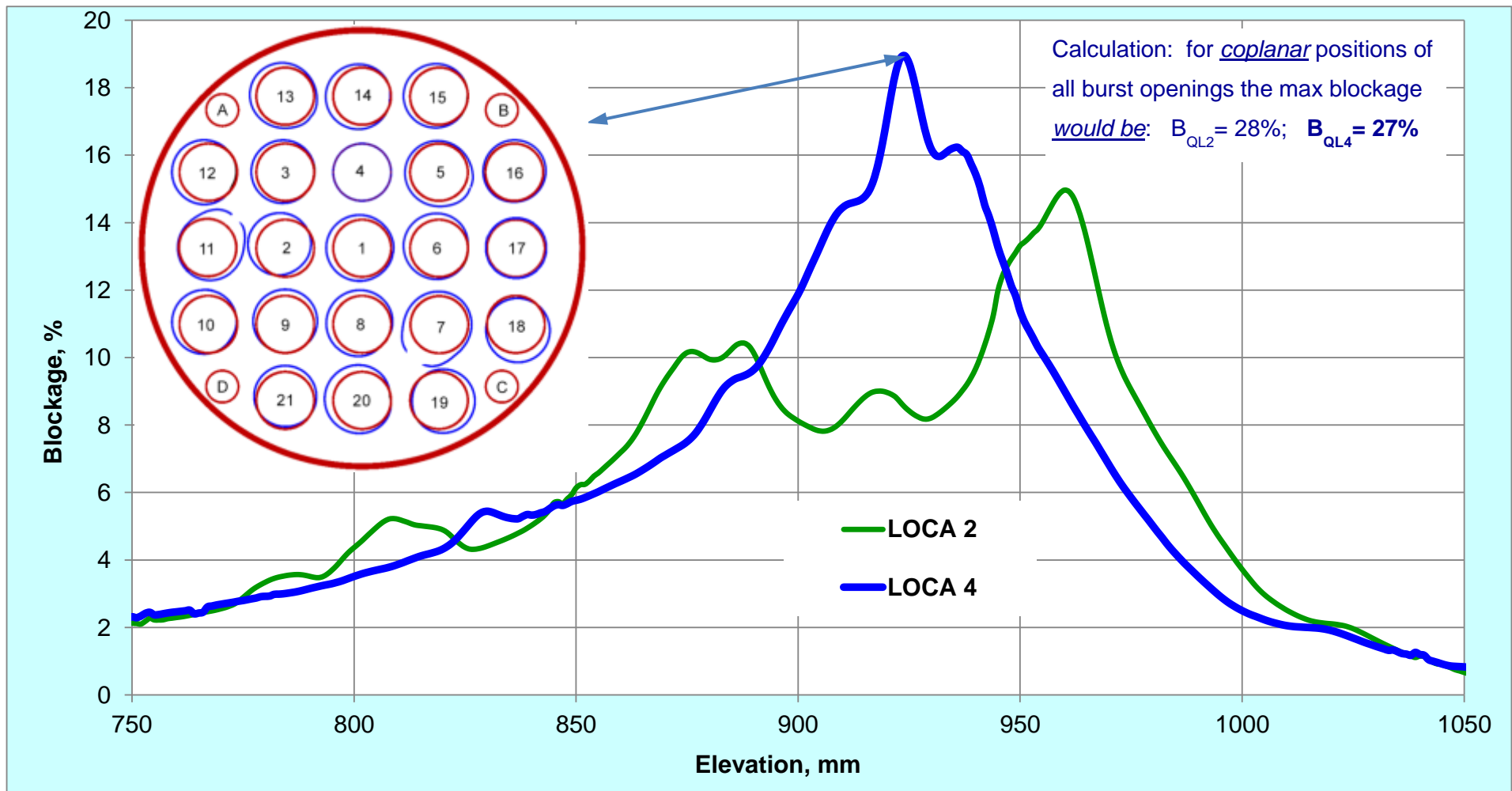


Figure 104 Axial distribution of coolant channel blockage for QUENCH-L2 and -L4 bundles. Cross section of QUENCH-L4 bundle corresponds to the bundle elevation 924 mm with a maximal blockage of 19% (blue lines - ballooned claddings; red lines - original claddings)

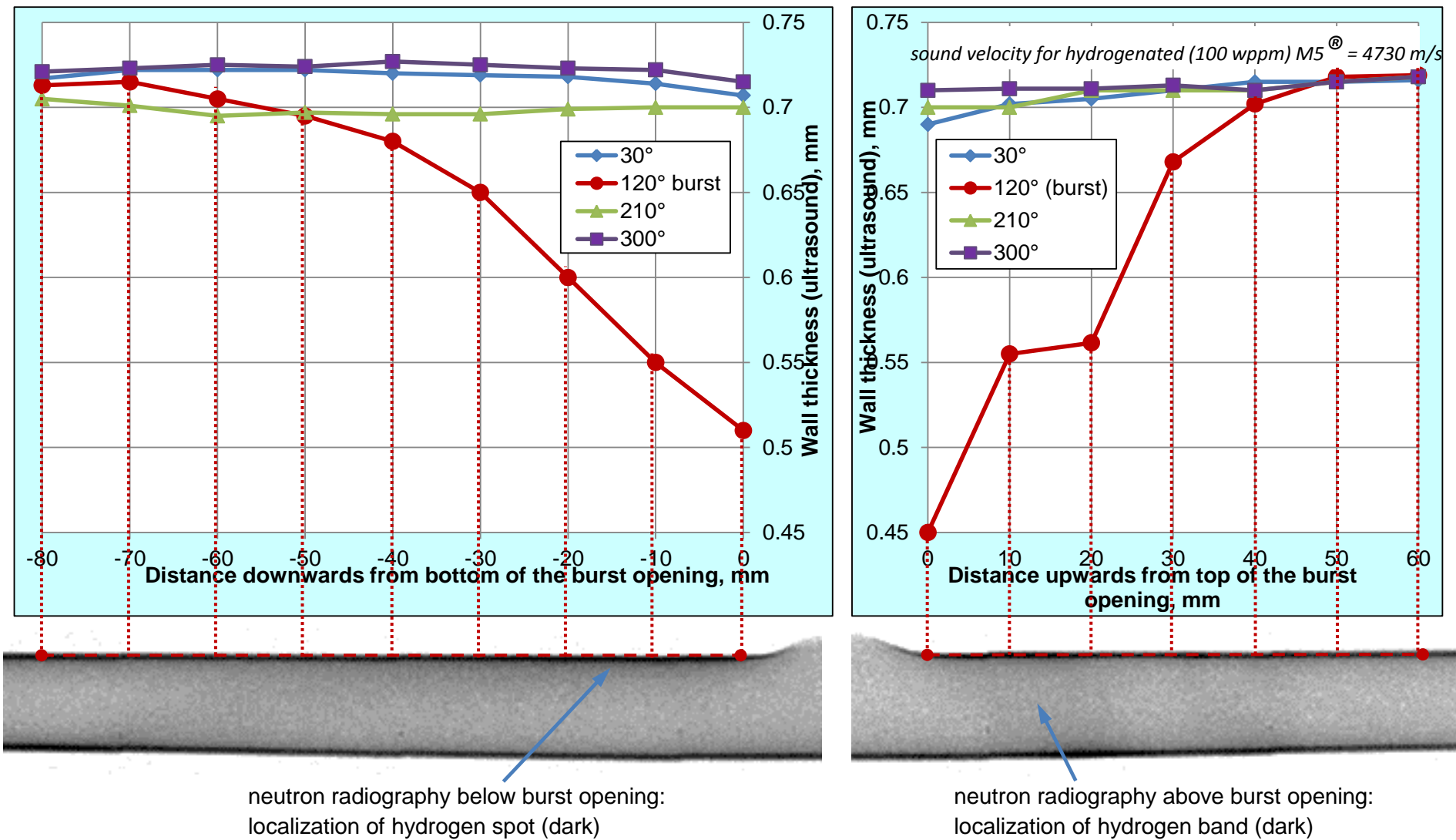


Figure 105 QUENCH-L4; Ultrasound measurement of wall thickness for rod #1 below and above the burst opening.

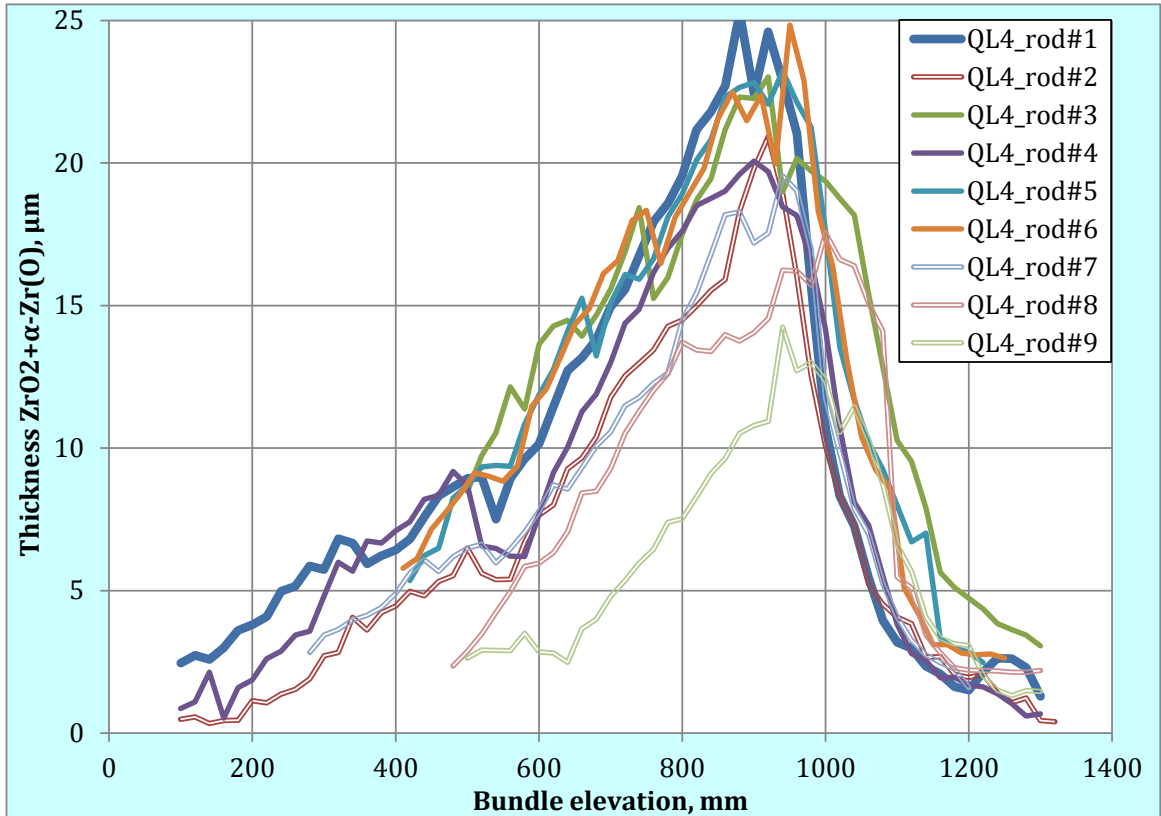


Figure 106 QUENCH-L4: results of eddy-current measurements of axial layer thickness distribution for inner rods

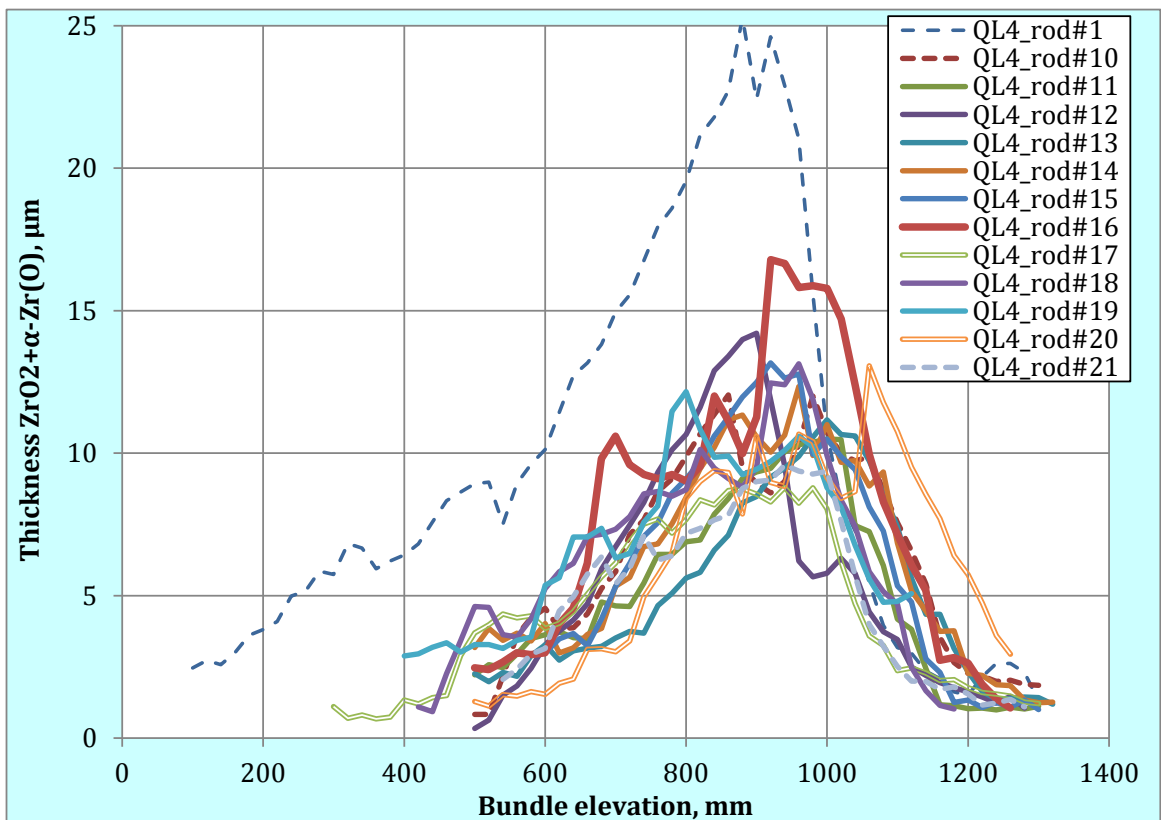


Figure 107 QUENCH-L4; Results of eddy-current measurements of axial layer thickness distribution for outer rods (and rod #1 for comparison).

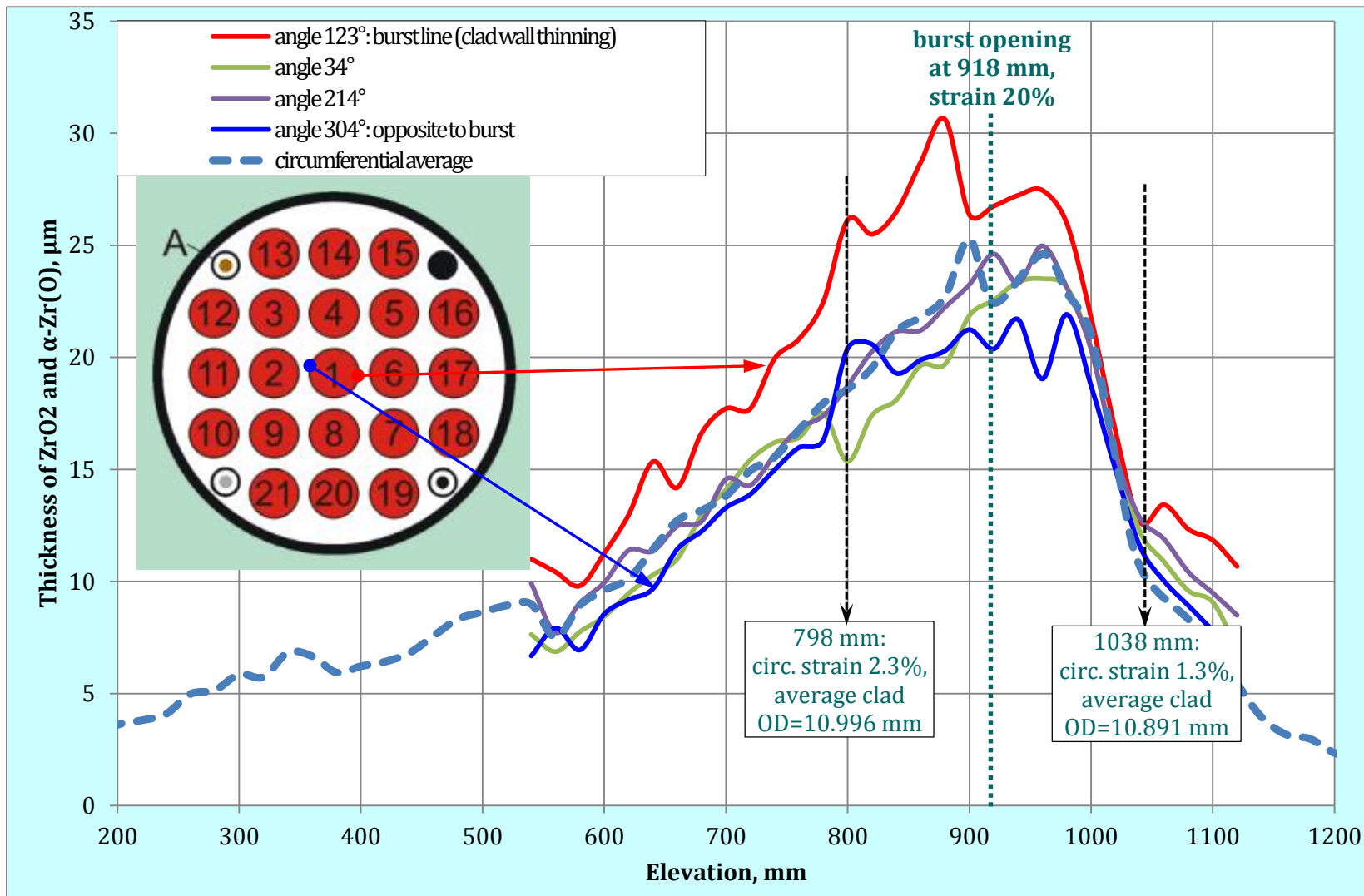


Figure 108 QUENCH-L4; Results of eddy-current measurements for different circumferential positions of rod #1.

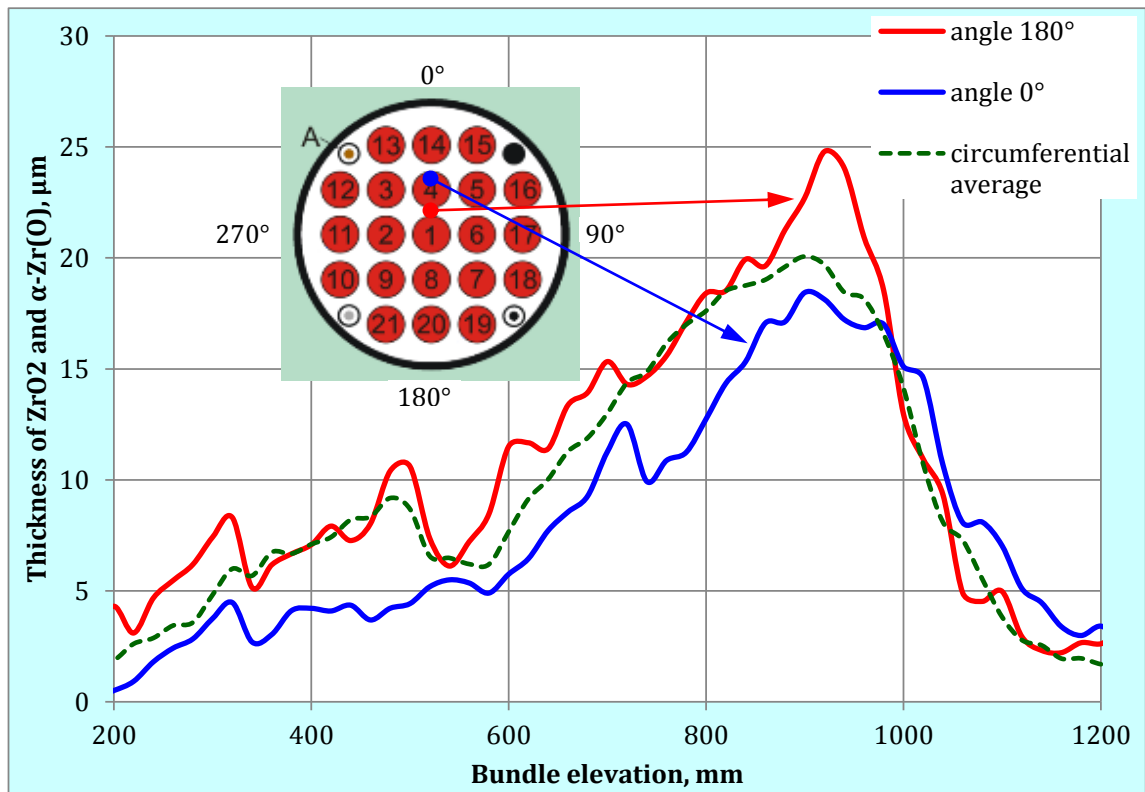


Figure 109 QUENCH-L4: results of eddy-current measurements for hottest and coolest sides of rod #4.

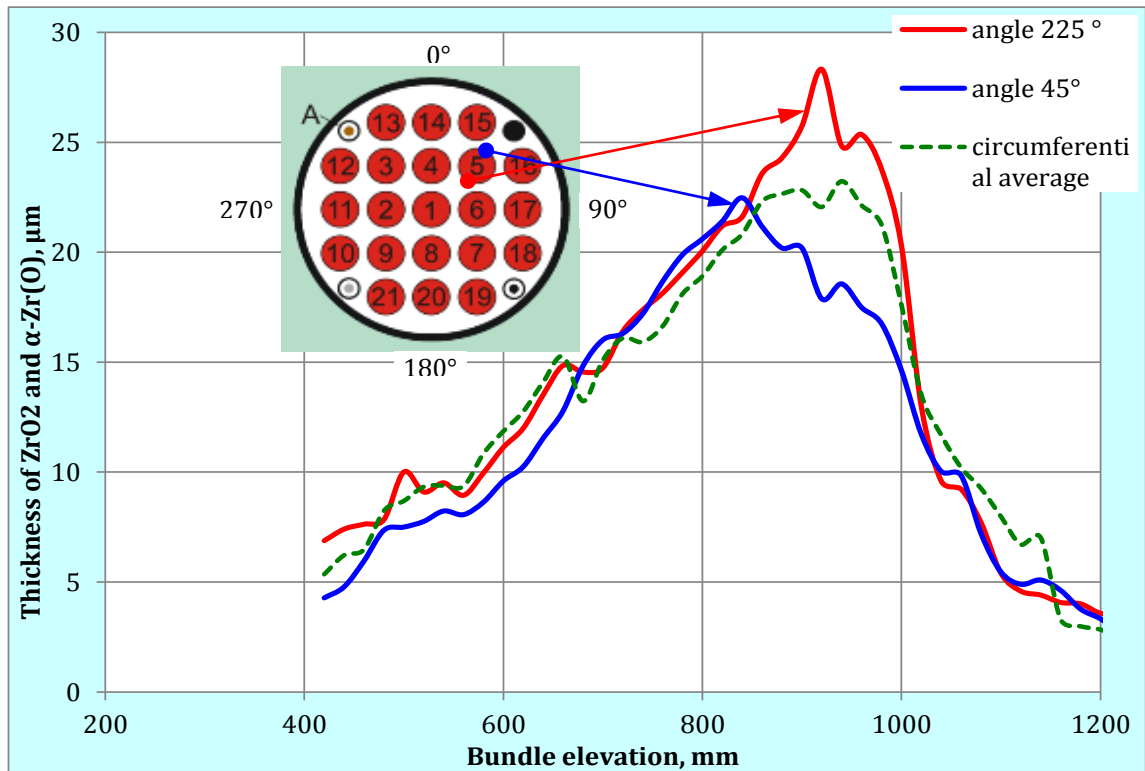


Figure 110 QUENCH-L4; Results of eddy-current measurements for hottest and coolest sides of rod #5

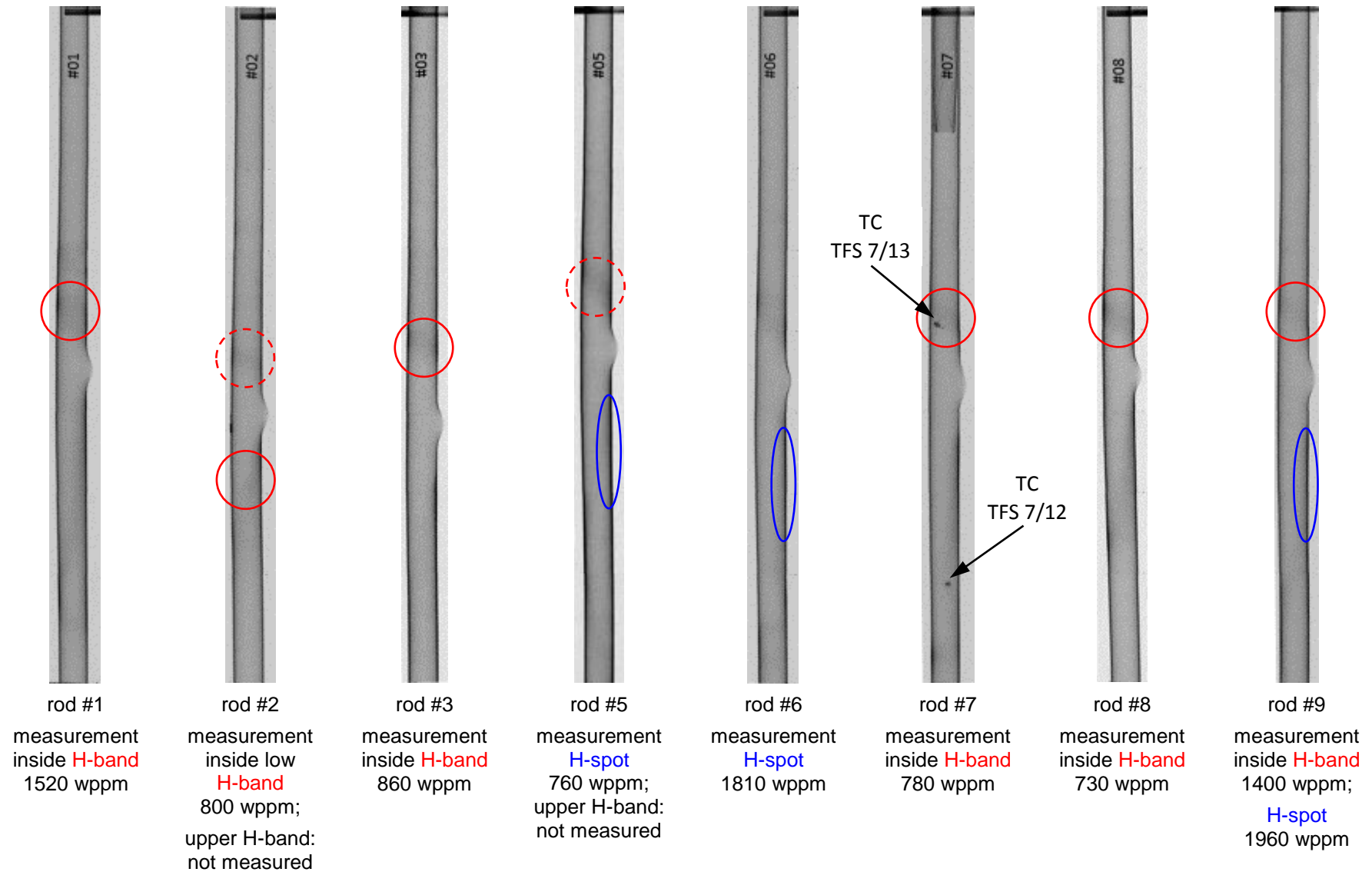


Figure 111 QUENCH-L4; Hydrogen bands on neutron radiographs of inner rods and maximum hydrogen content measured by neutron tomography.

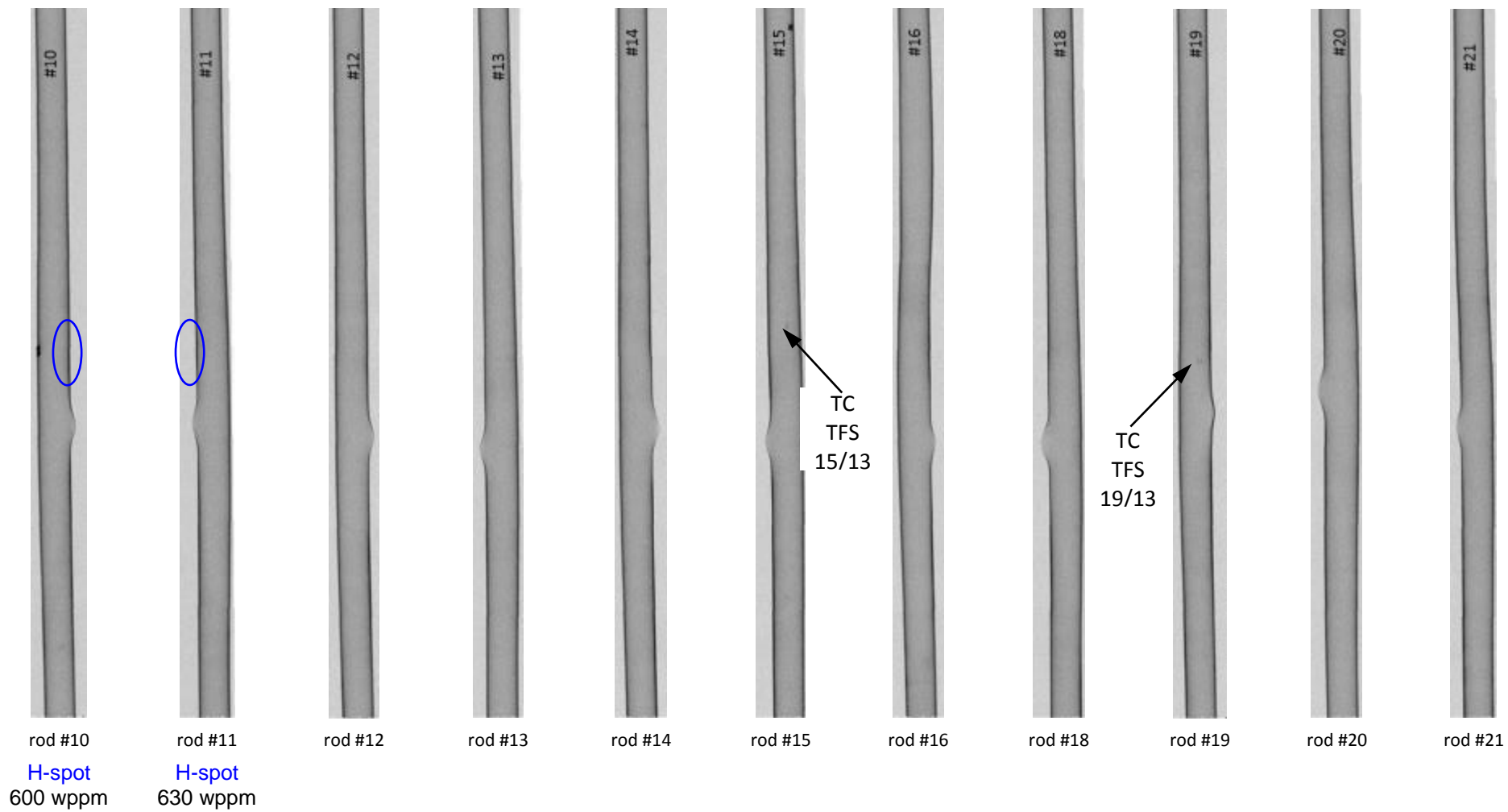


Figure 112 QUENCH-L4; Neutron radiographs of outer rods and maximum hydrogen content measured by neutron tomography.

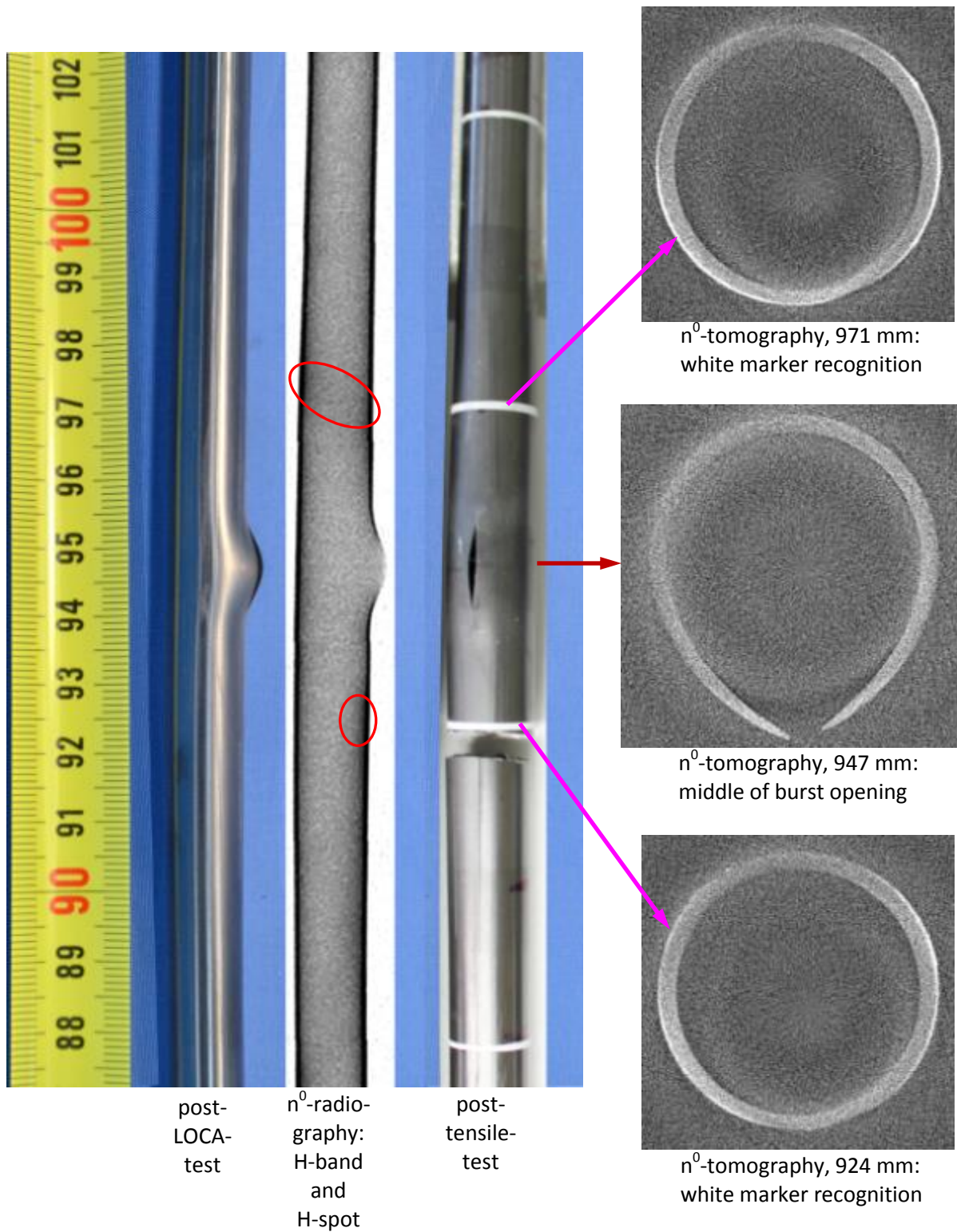


Figure 113 QUENCH-L4, Rod #9; results of n^0 -radio- and tomography.



rod #1; H-band (sample top): 1720 wppm,
H-spot (sample bottom): 1740 wppm



rod #6; H-spot (sample bottom): 1750 wppm



rod #9; H-band (sample top): 1490 wppm; H-spot (sample bottom): 1740 wppm

Figure 114 QUENCH-L4; Results of neutron tomography for internal rods fractured during the tensile tests at lower hydrogen spot. Dark blue points correspond to hydrogen bearing material. Rings are colouring markers dished up before tensile tests. The values are local maximal hydrogen concentrations.

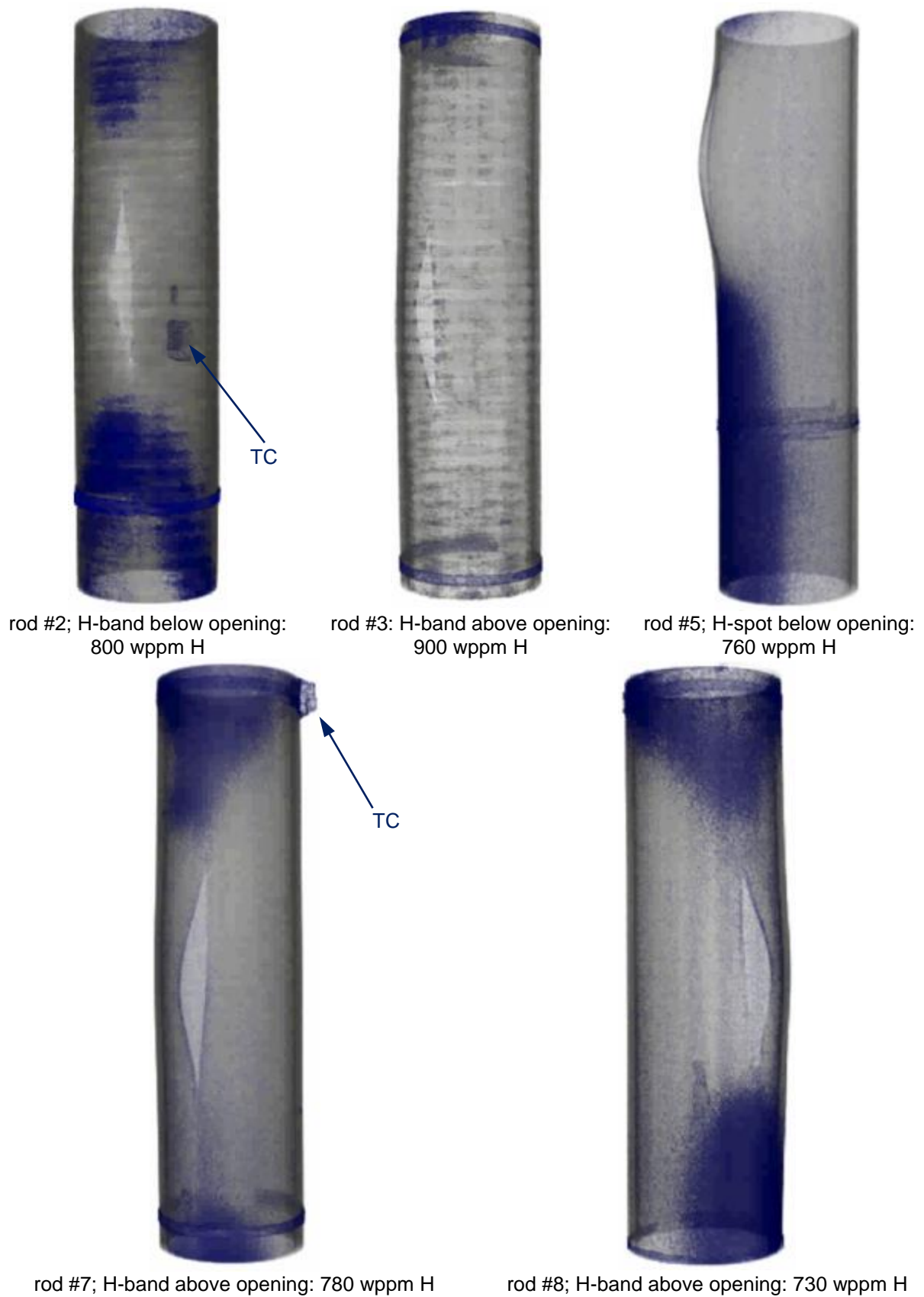


Figure 115 QUENCH-L4; Results of neutron tomography for internal rods fractured during the tensile tests by necking. Dark blue points correspond to hydrogen bearing material. Rings are colouring markers dished up before tensile tests. The values are local maximal hydrogen concentrations.

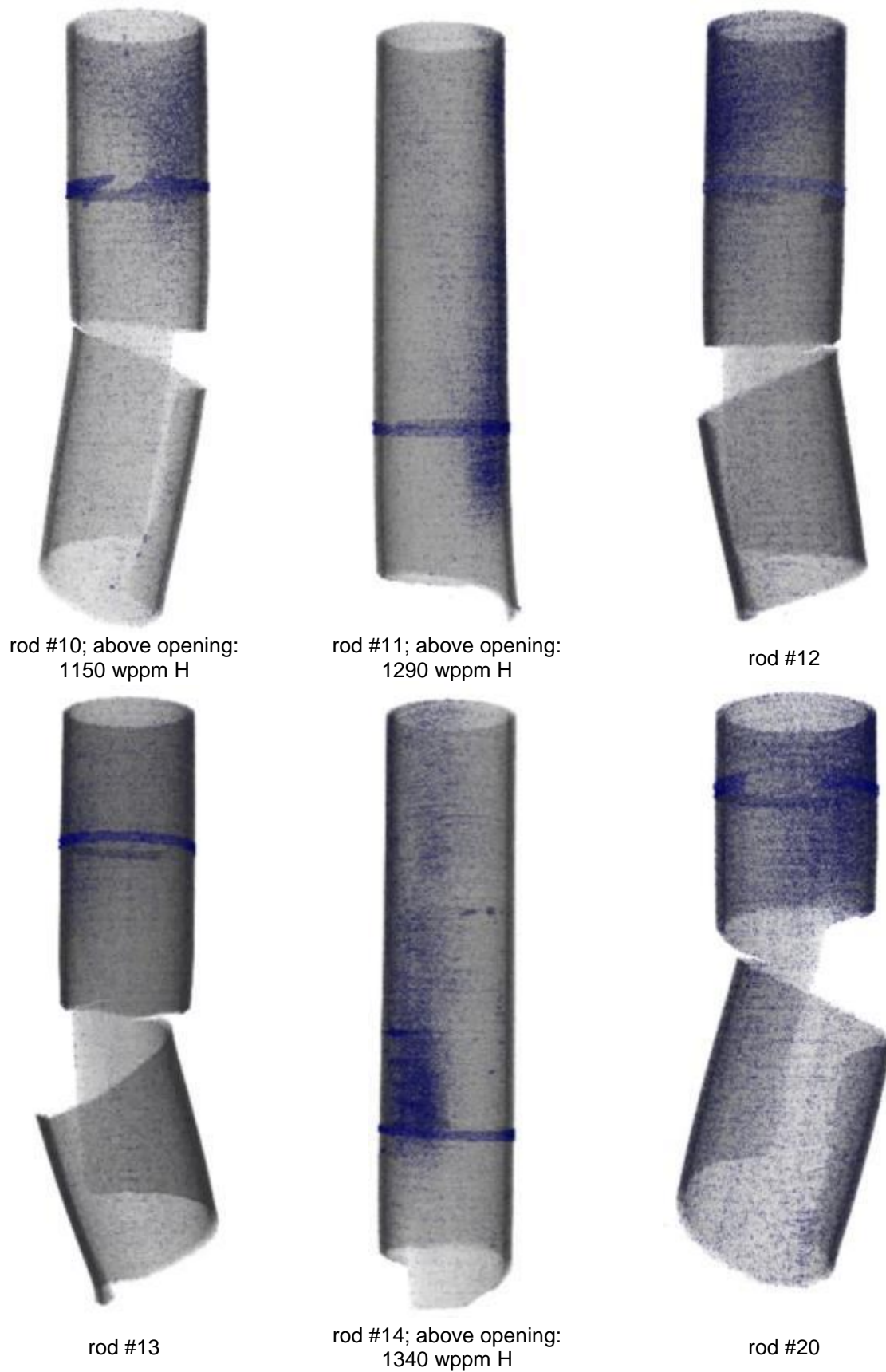


Figure 116 QUENCH-L4; Results of neutron tomography for some outer rods double fractured during the tensile tests at burst opening tips. Dark blue points correspond to hydrogen bearing material. Rings are colouring markers dished up before tensile tests. The values are local maximal hydrogen concentrations.

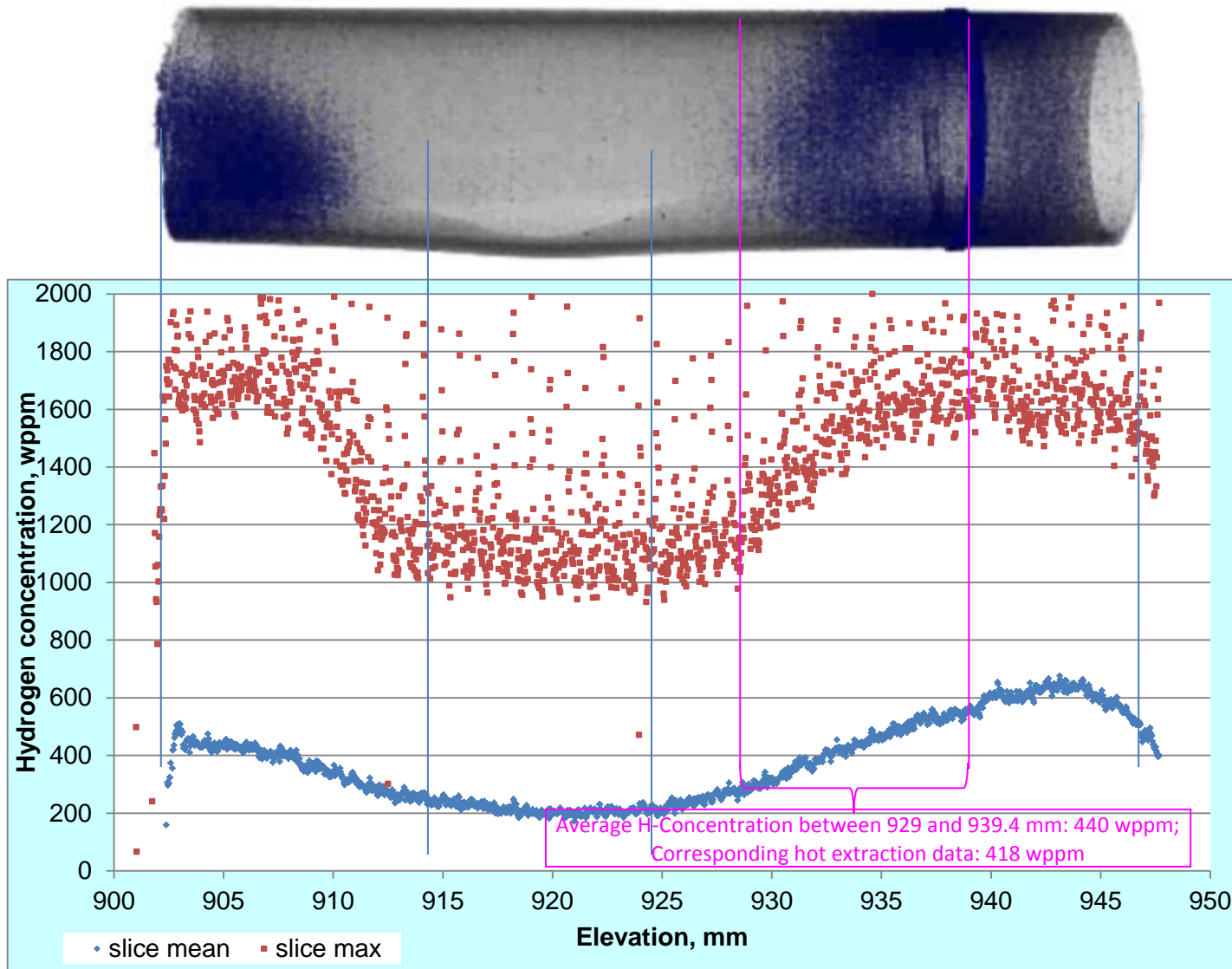


Figure 117 QUENCH-L4; correspondence between reconstruction of tomography image and plots of mean and maximal hydrogen concentrations (calculated for each cross section slice of 25.6 μm width) in rod #1: hydrogen band above and hydrogen spot below burst opening.

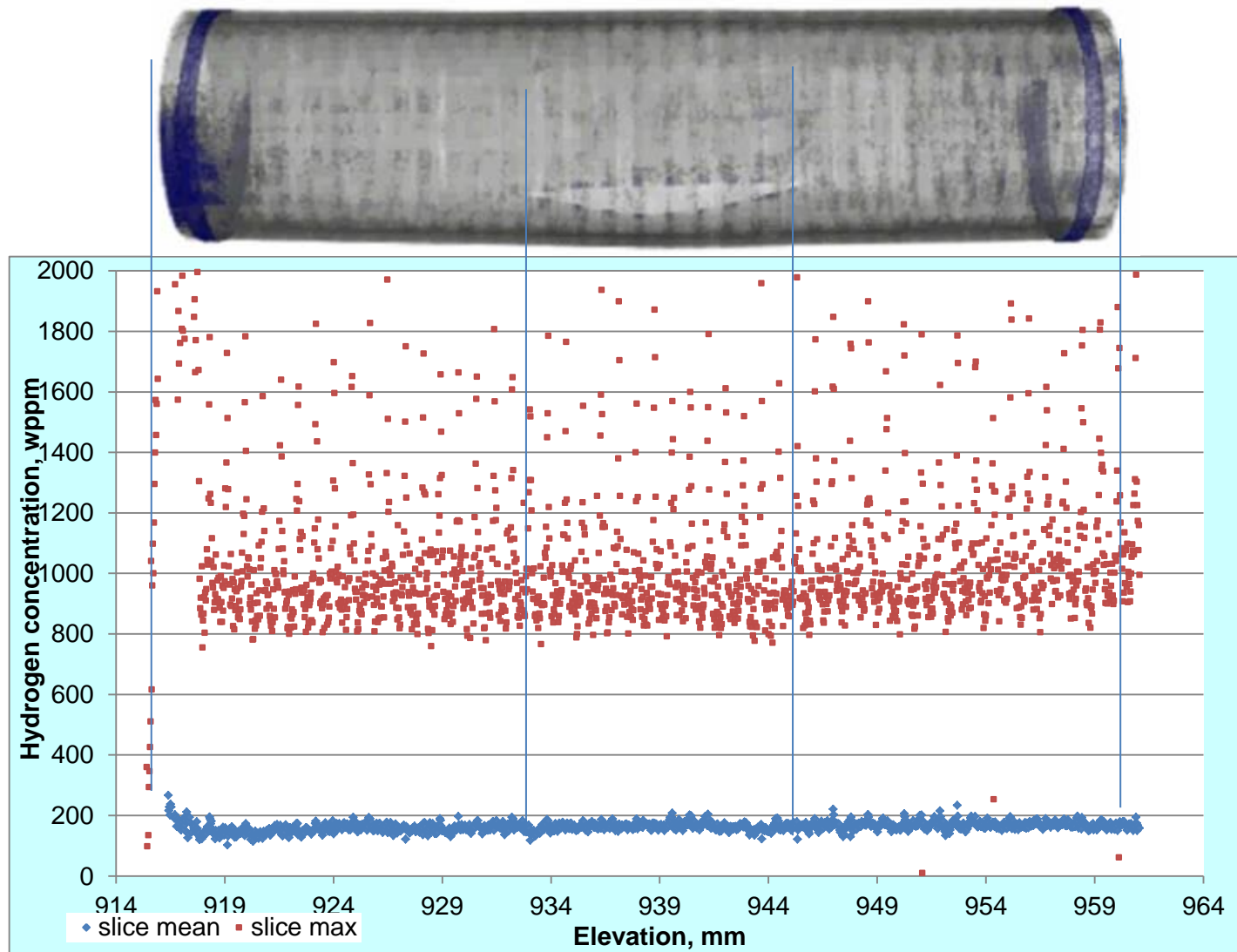


Figure 118 QUENCH-L4; correspondence between reconstruction of tomography image and plots of mean and maximal hydrogen concentrations (calculated for each cross section slice of 25.6 μm width) in rod #3: absence of hydrogen bands and spots.

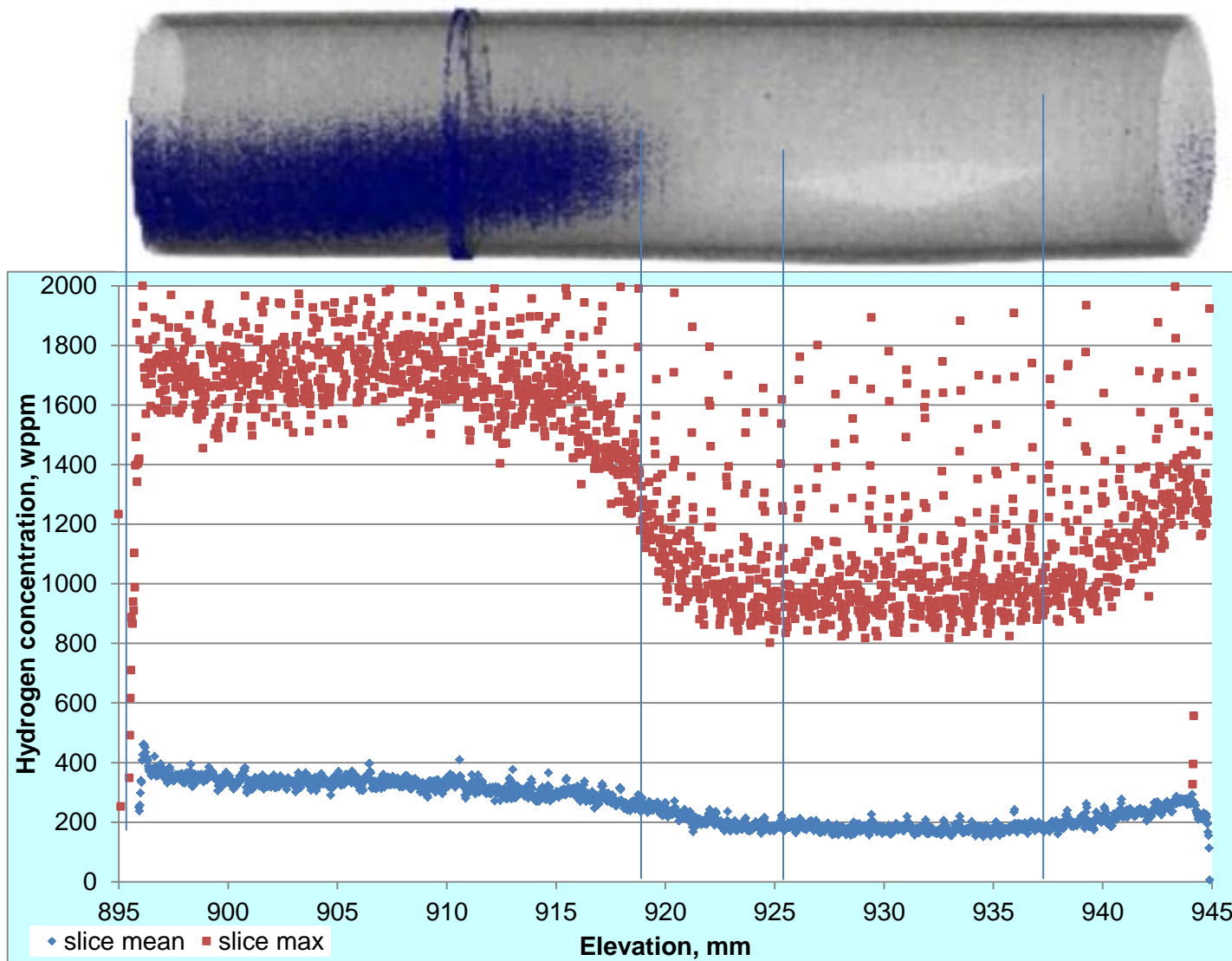


Figure 119 QUENCH-L4; correspondence between reconstruction of tomography image and plots of mean and maximal hydrogen concentrations (calculated for each cross section slice of 25.6 μm width) in rod #6: hydrogen spot below burst opening.

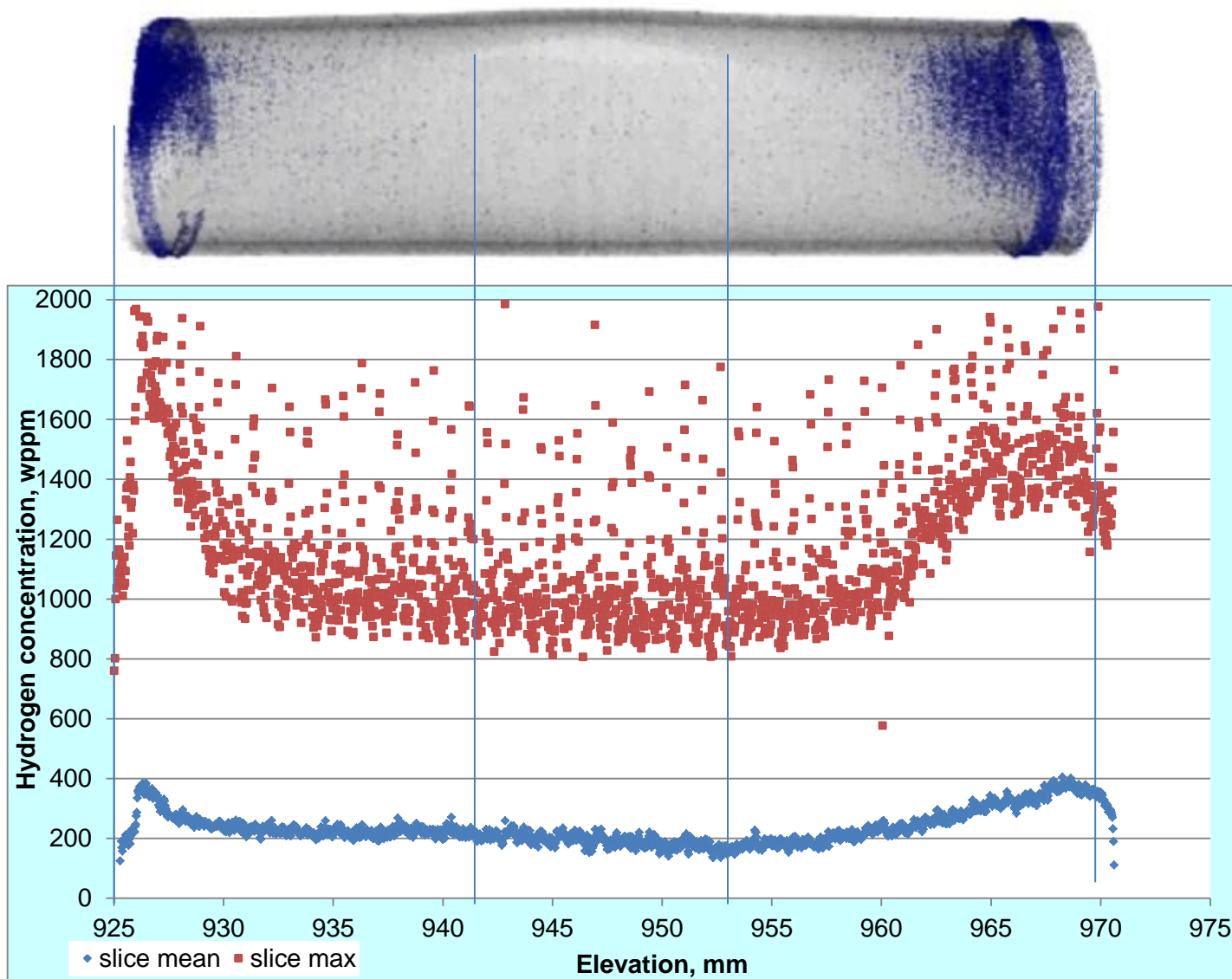


Figure 120 QUENCH-L4; correspondence between reconstruction of tomography image and plots of mean and maximal hydrogen concentrations (calculated for each cross section slice of 25.6 μm width) in rod #9: hydrogen band above and hydrogen spot below burst opening.

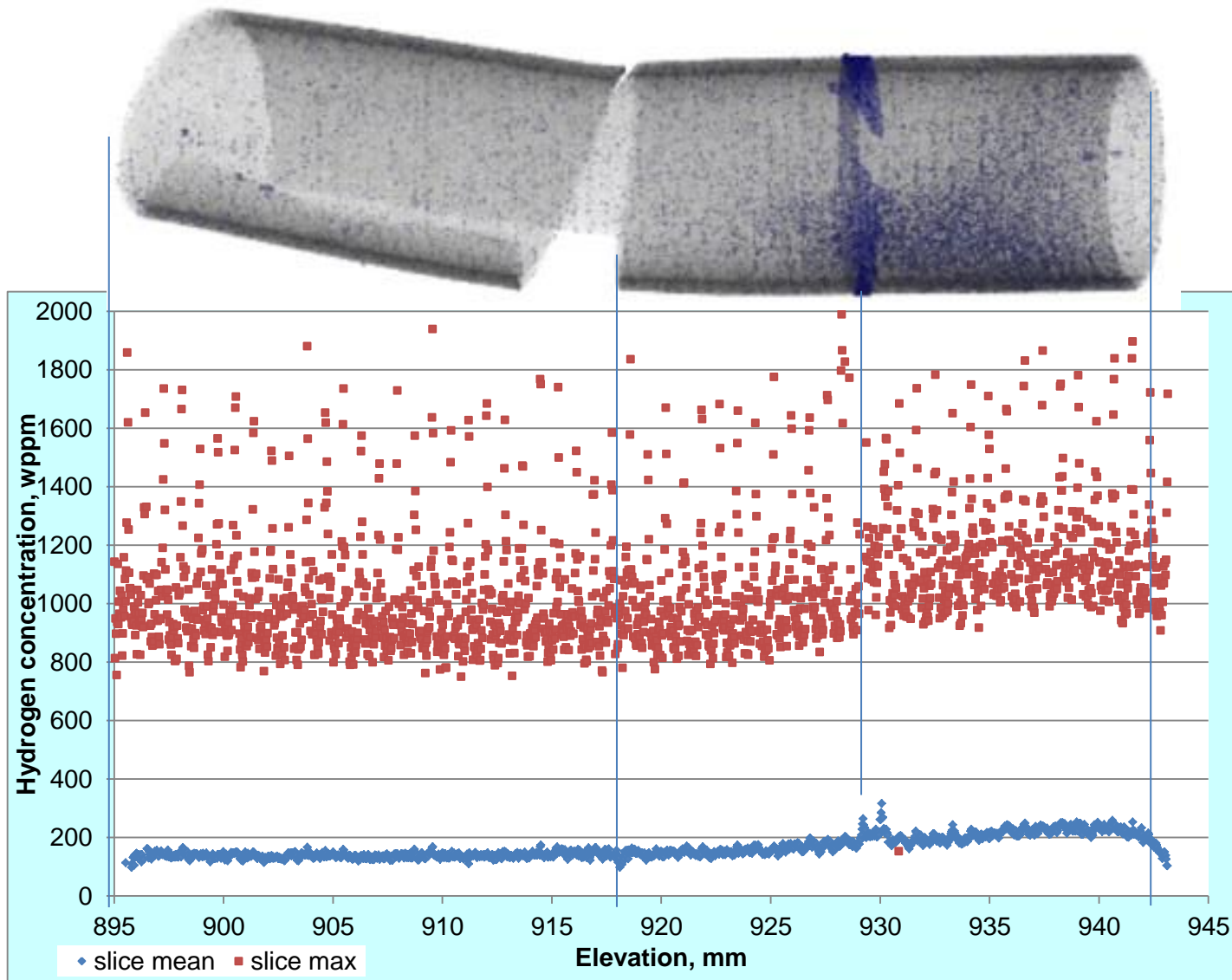


Figure 121 QUENCH-L4; correspondence between reconstruction of tomography image and plots of mean and maximal hydrogen concentrations (calculated for each cross section slice of 25.6 μm width) in rod #10: weak hydrogen band above burst opening, relative homogeneous axial distribution of hydrogen.

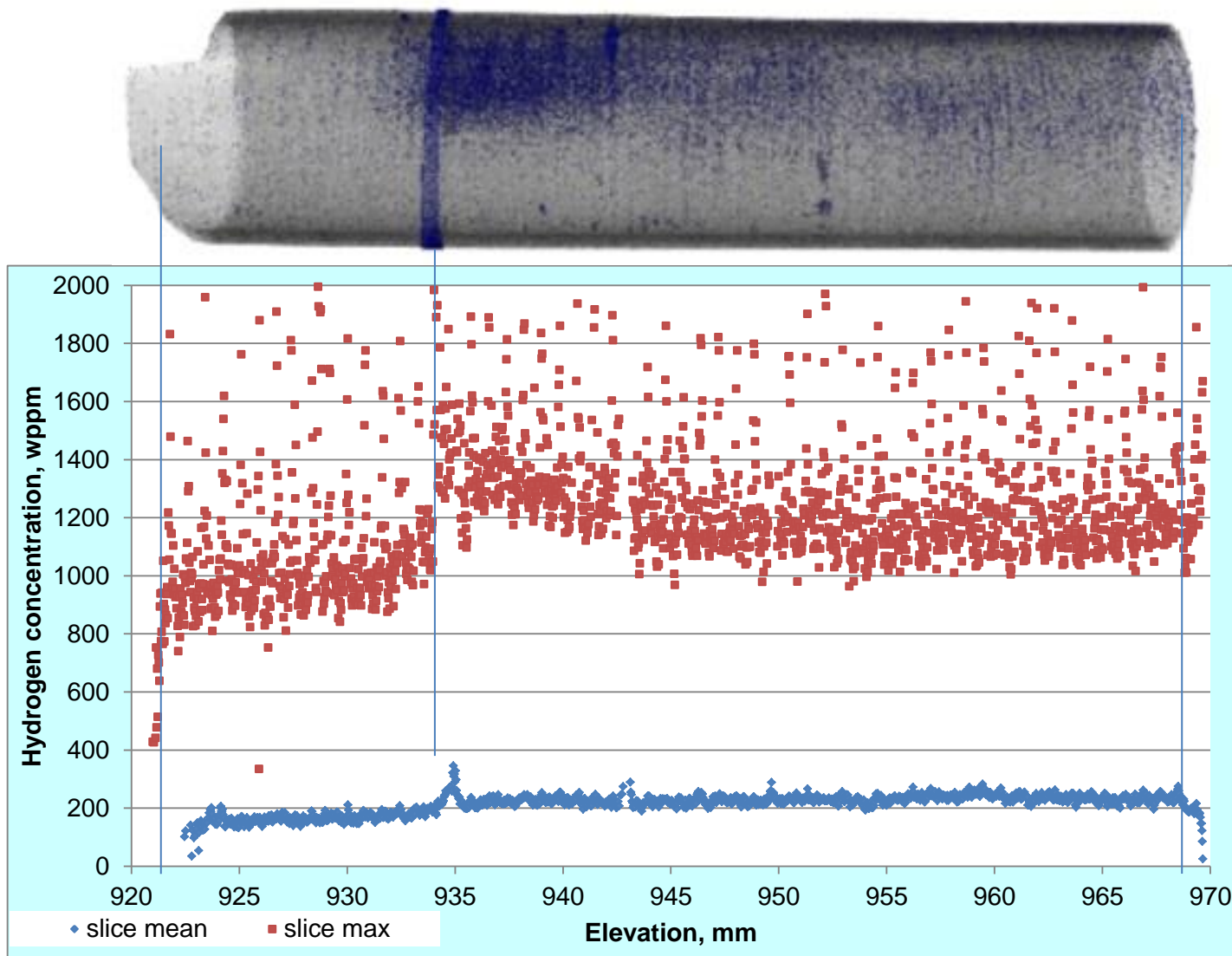


Figure 122 QUENCH-L4; correspondence between reconstruction of tomography image and plots of mean and maximal hydrogen concentrations (calculated for each cross section slice of 25.6 μm width) in rod #14: hydrogenated zone above burst opening, relative homogeneous axial distribution of hydrogen.

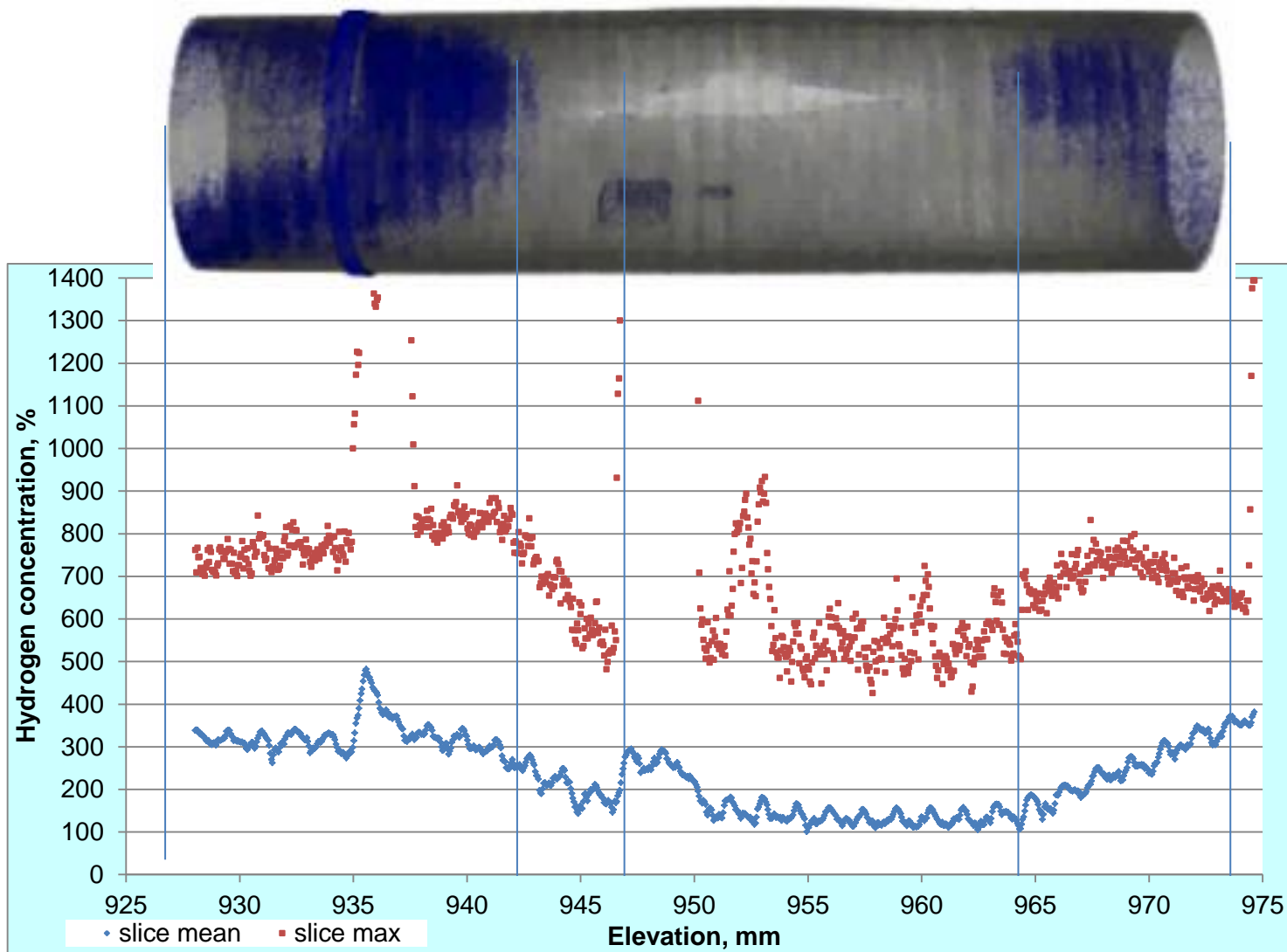


Figure 123 QUENCH-L4; correspondence between reconstruction of tomography image and plots of mean and maximal hydrogen concentrations (calculated for each cross section slice of 45.9 μm width) in rod #2: hydrogenated zone *below* burst opening.

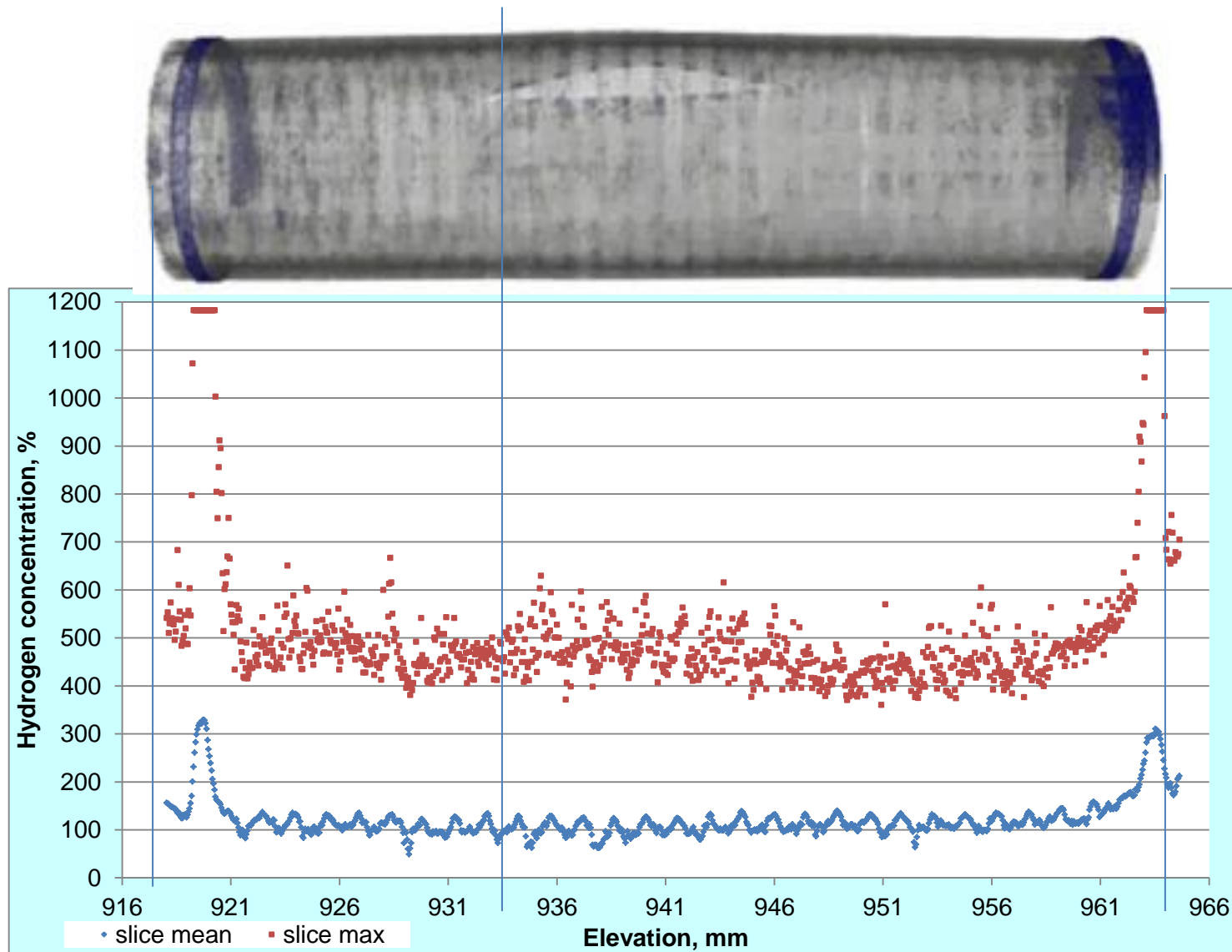


Figure 124 QUENCH-L4; correspondence between reconstruction of tomography image and plots of mean and maximal hydrogen concentrations (calculated for each cross section slice of 45.9 μm width) in rod #3: no hydrogenated zones.

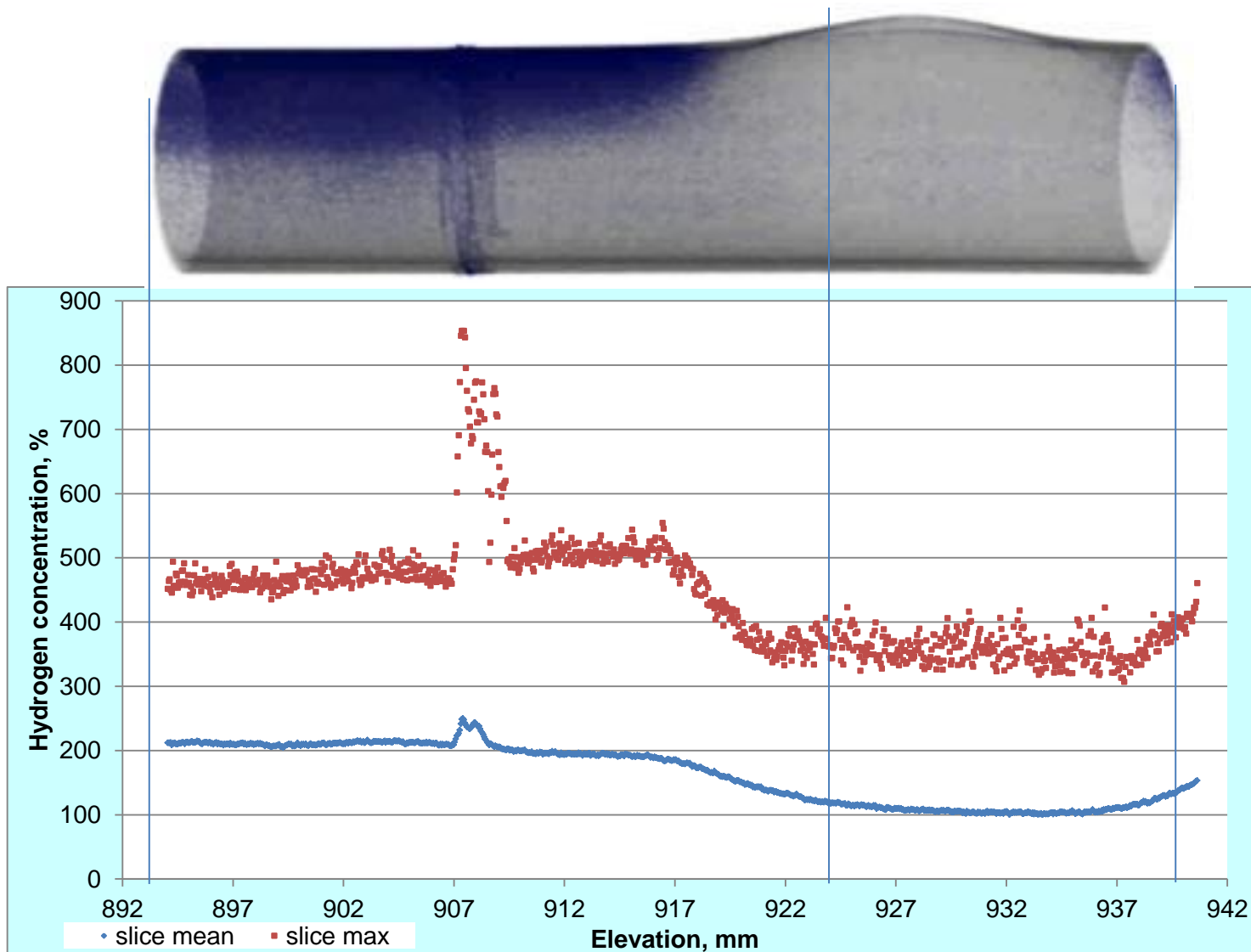


Figure 125 QUENCH-L4; correspondence between reconstruction of tomography image and plots of mean and maximal hydrogen concentrations (calculated for each cross section slice of 45.9 μm width) in rod #5: hydrogenated zone *below* burst opening.

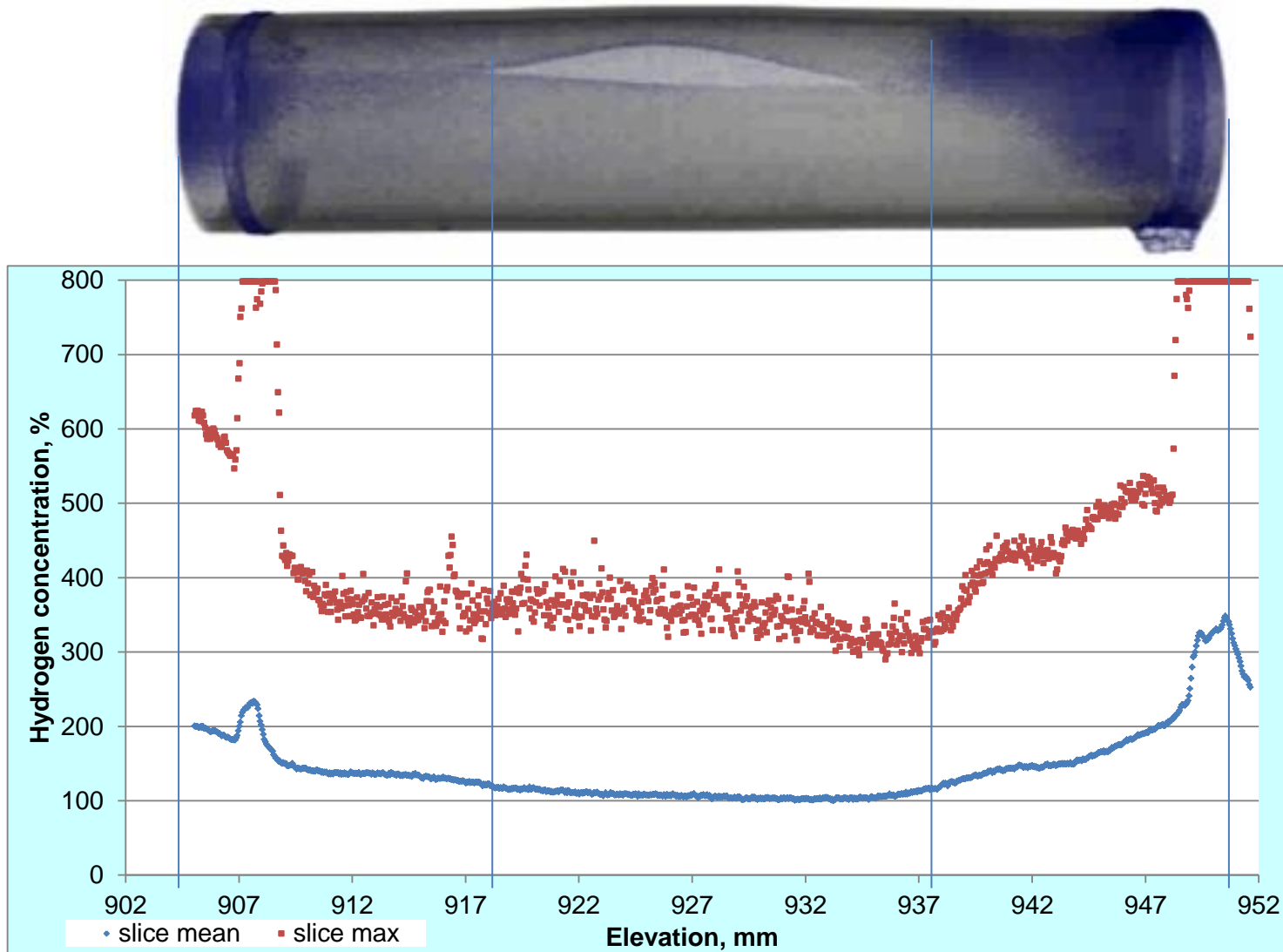


Figure 126 QUENCH-L4; correspondence between reconstruction of tomography image and plots of mean and maximal hydrogen concentrations (calculated for each cross section slice of 45.9 μm width) in rod #7: hydrogenated zone above burst opening.

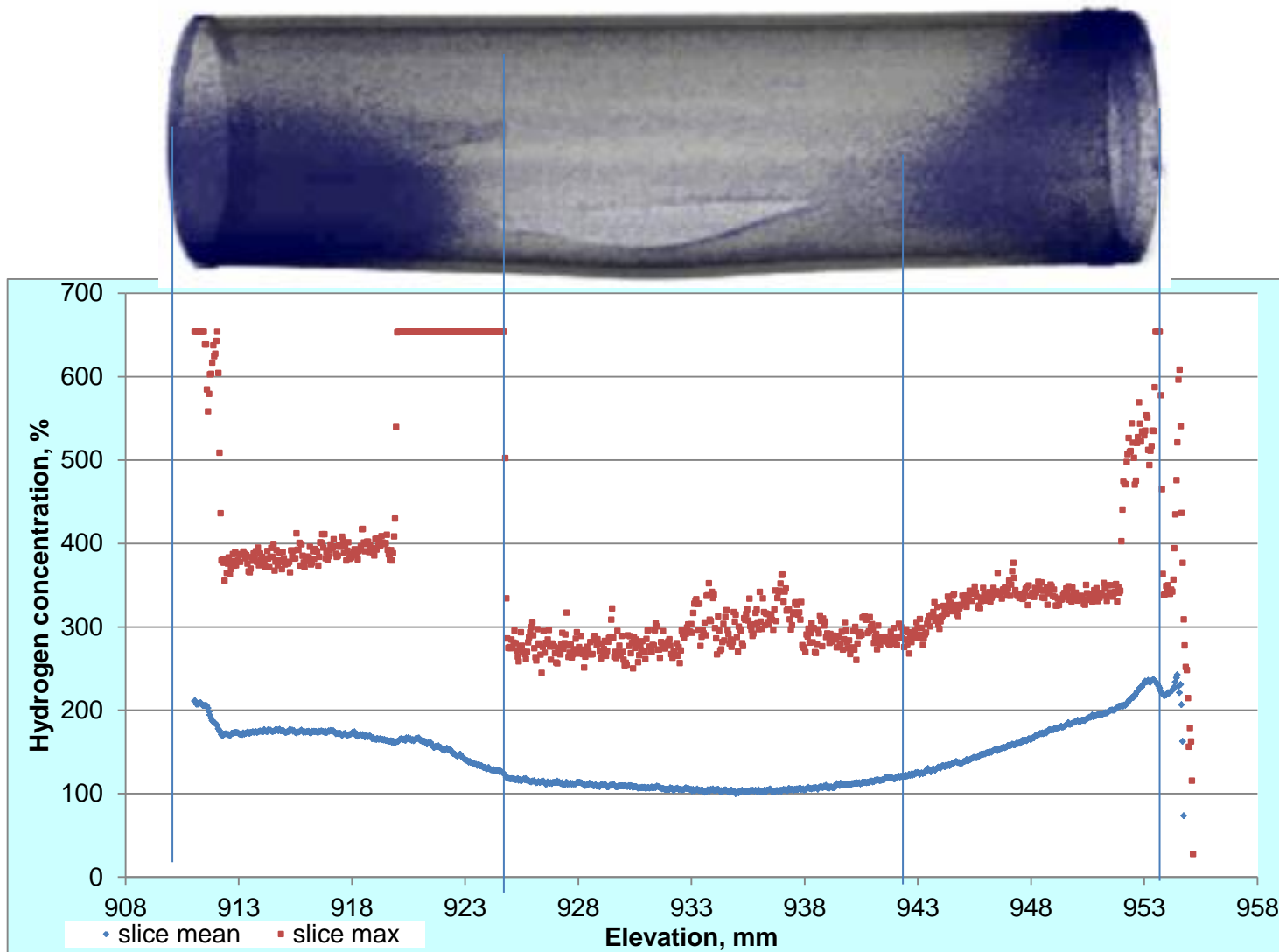


Figure 127 QUENCH-L4; correspondence between reconstruction of tomography image and plots of mean and maximal hydrogen concentrations (calculated for each cross section slice of 45.9 μm width) in rod #8: hydrogenated zones above and below burst opening.

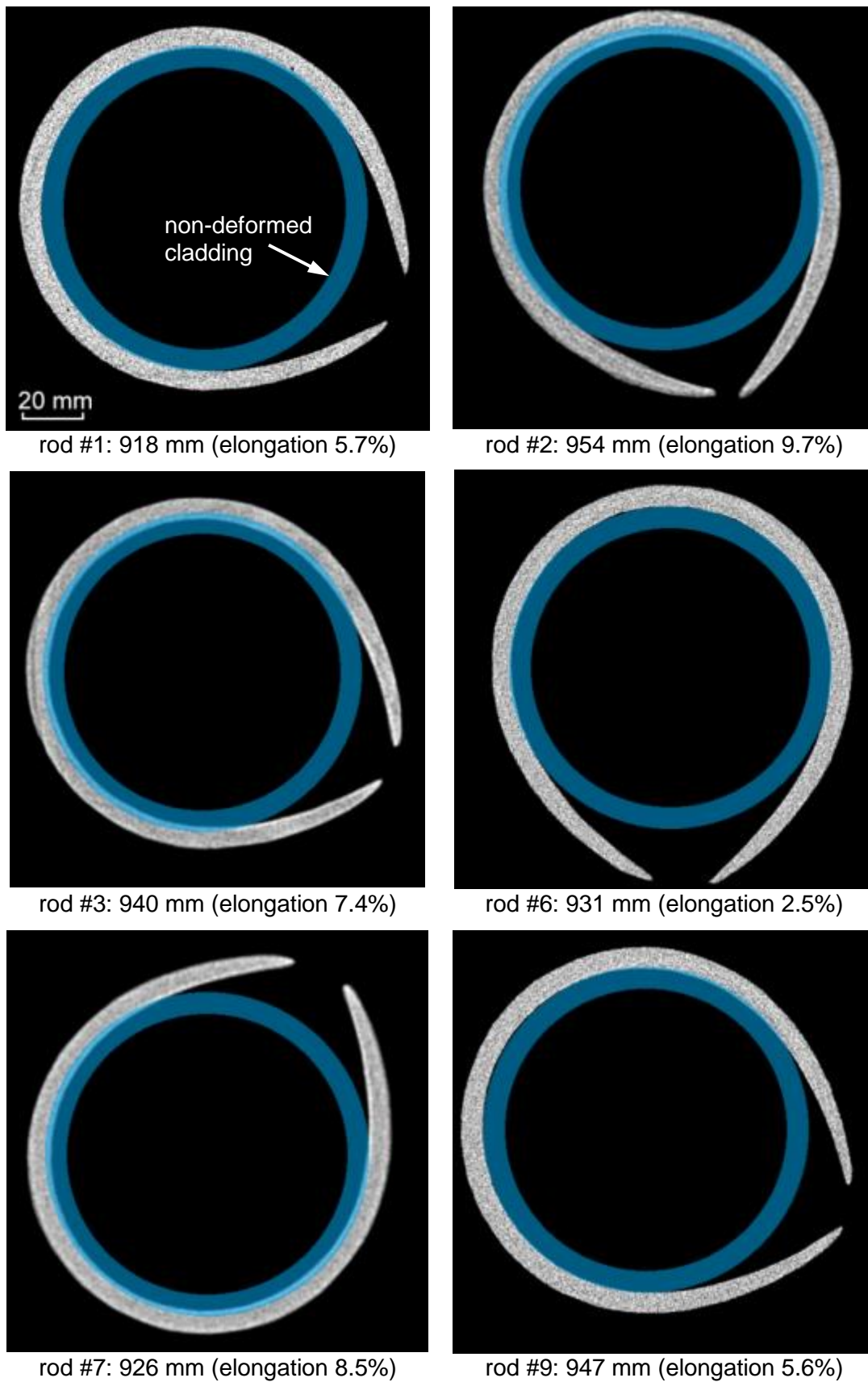


Figure 128 QUENCH-L4; Comparison of tomography images (made after tensile tests) at the axial middle of burst opening with initial (pre-test) cladding cross section (OD=10.75 mm; wall thickness 725 μm); elongation values point the deformation degree after tensile tests.

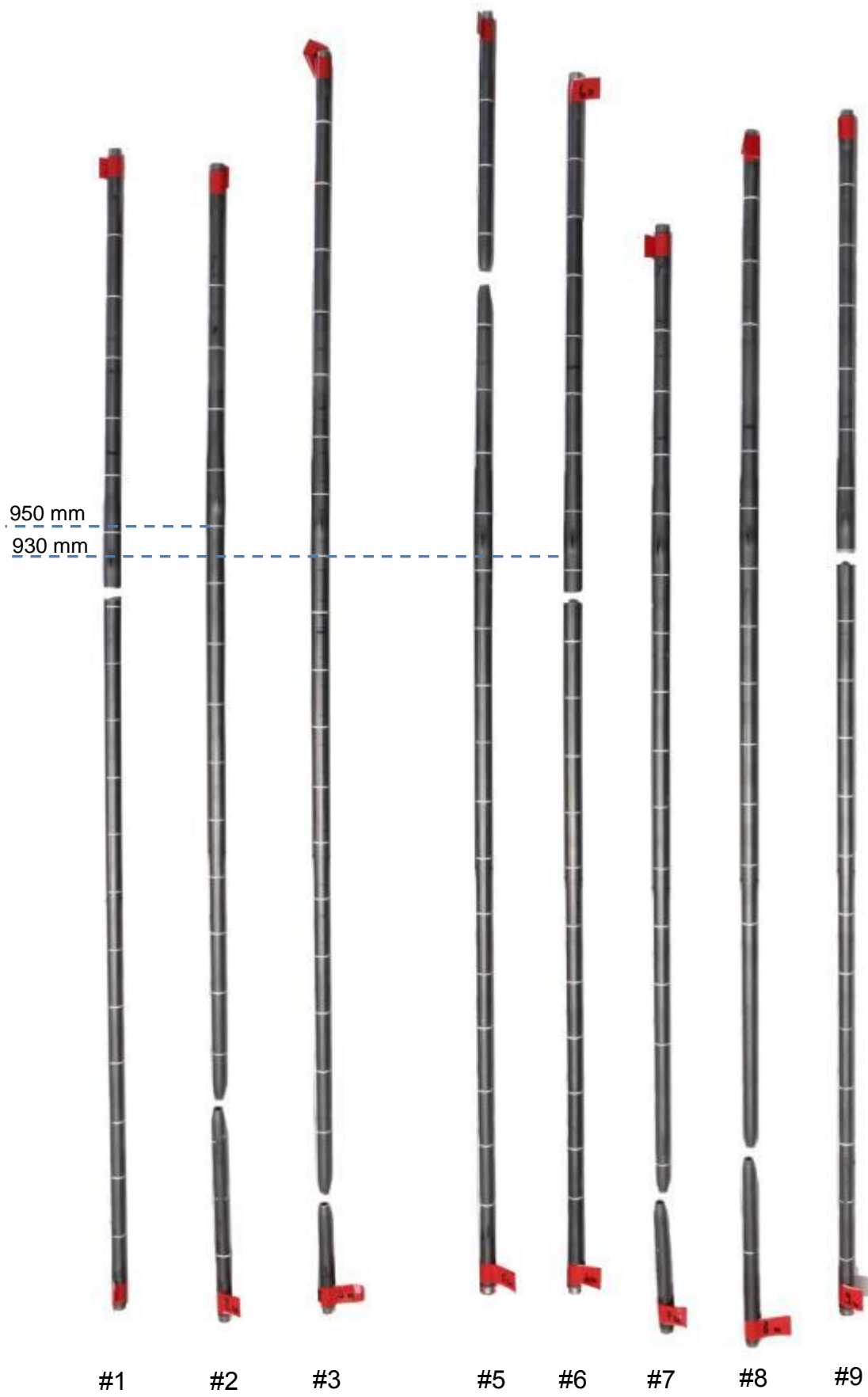


Figure 129 QUENCH-L4; Inner rods after tensile tests; ruptures due to H-embrittlement (rods 1, 6, 9) and necking (rods 2, 3, 5, 7, 8).



Figure 130 QUENCH-L4; Inner rods after tensile tests; ruptures due to H-embrittlement for rods 1, 6, 9; necking of the rods 2, 3, 5, 7, 8.

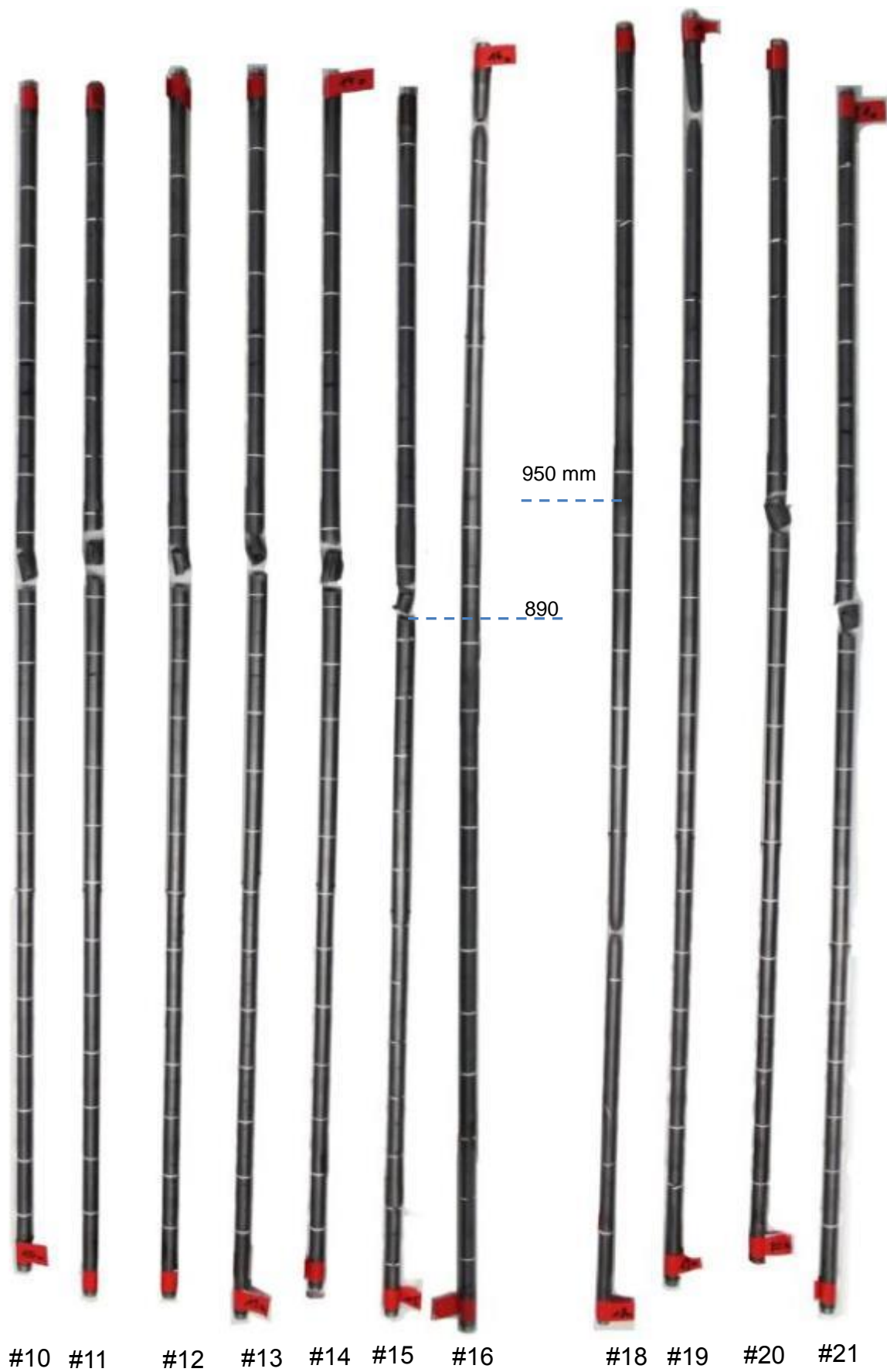


Figure 131 QUENCH-L4; Outer rods after tensile tests; ruptures due to stress concentration (rods 10-15, 20, 21) and necking (rods 16, 18, 19).



Figure 132 QUENCH-L4; Outer rods after tensile tests; ruptures due to stress concentration for the rods 10-15, 20, 21; necking of the rods 16, 18, 19.

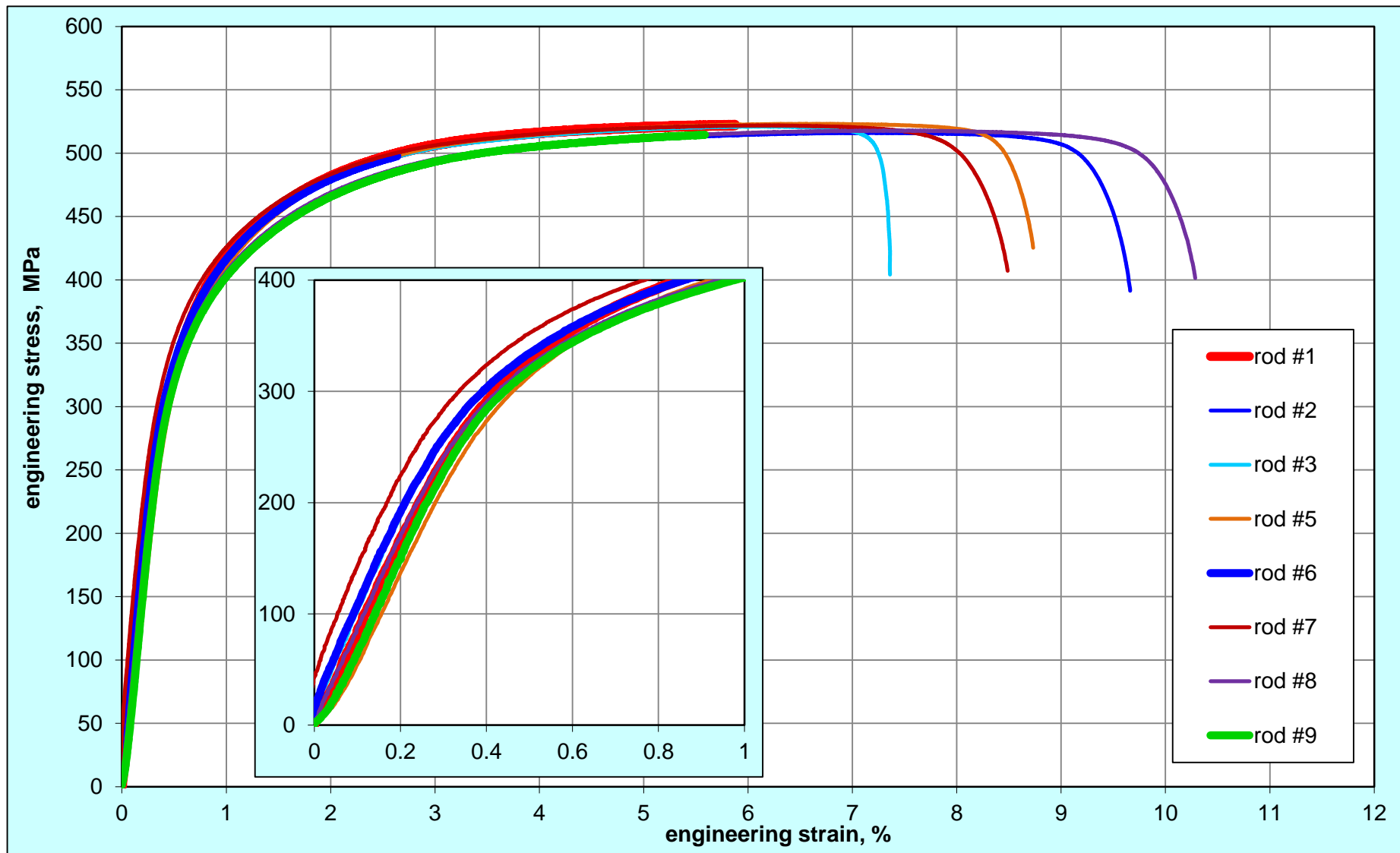


Figure 133 QUENCH-L4; Results of tensile tests with claddings of the inner rod group.

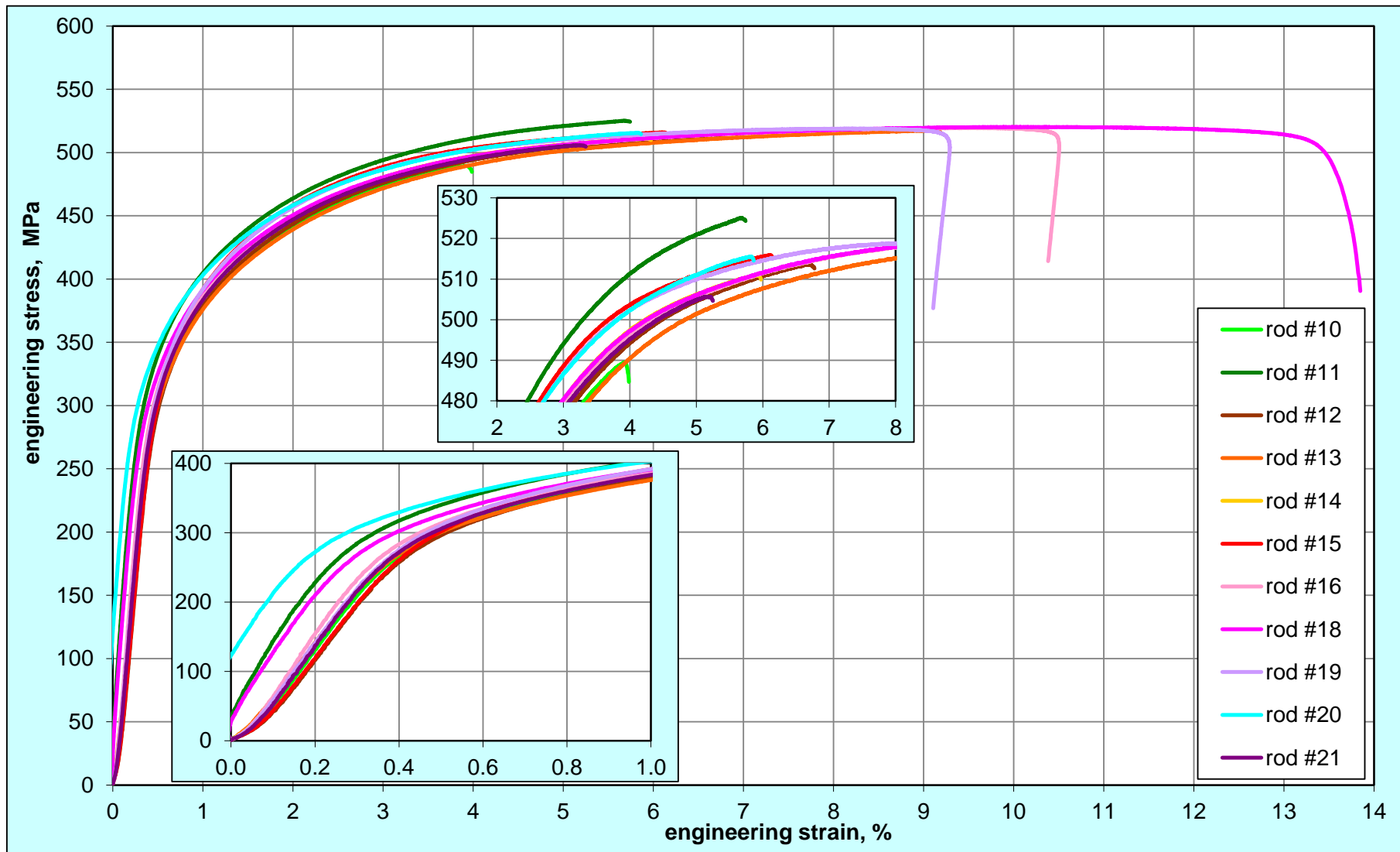


Figure 134 QUENCH-L4; Results of tensile tests with claddings of the outer rod group.

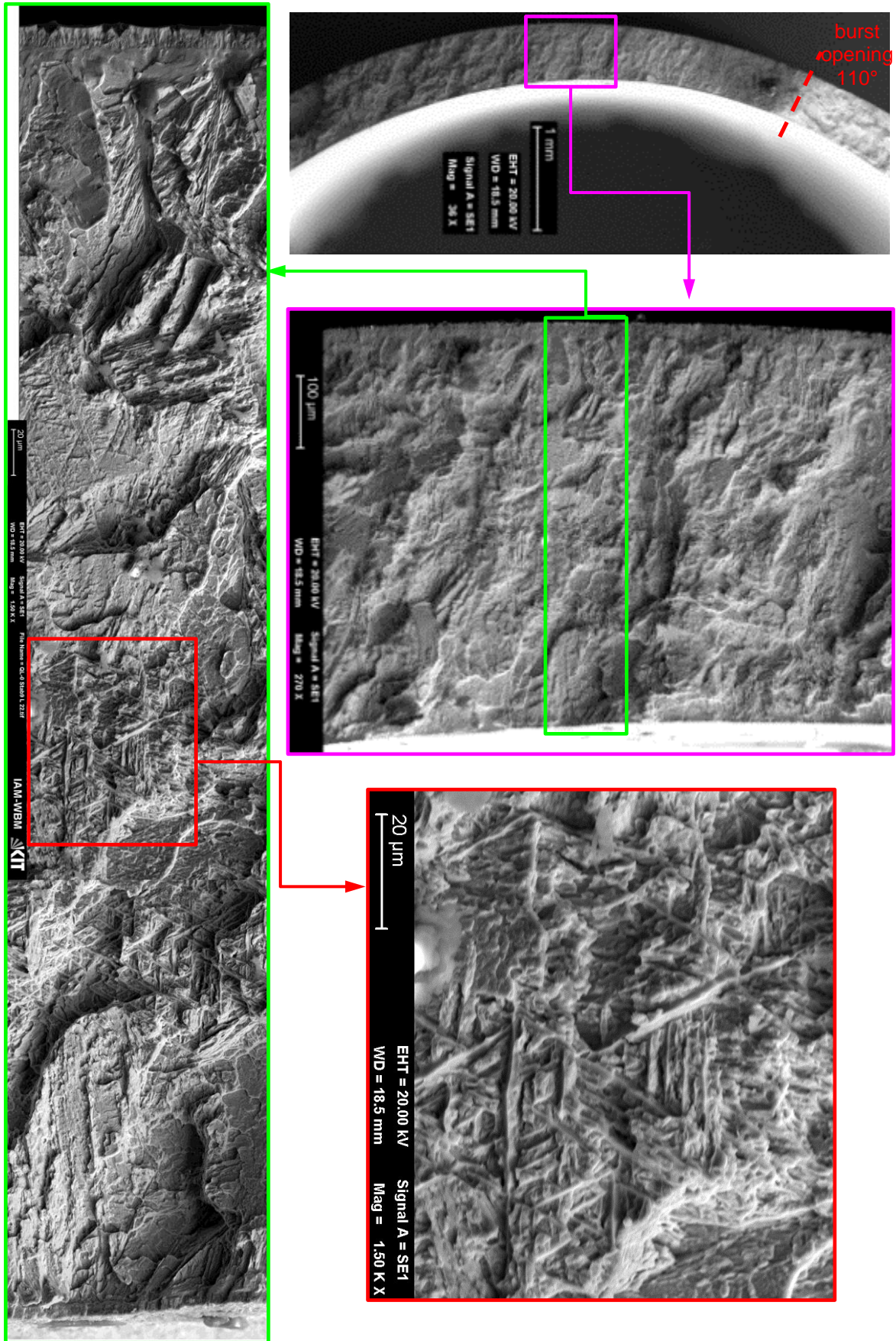


Figure 135 QUENCH-L4; SEM image of fractured surface of rod #9 at angle 90° after tensile test; top view. Brittle fracture.

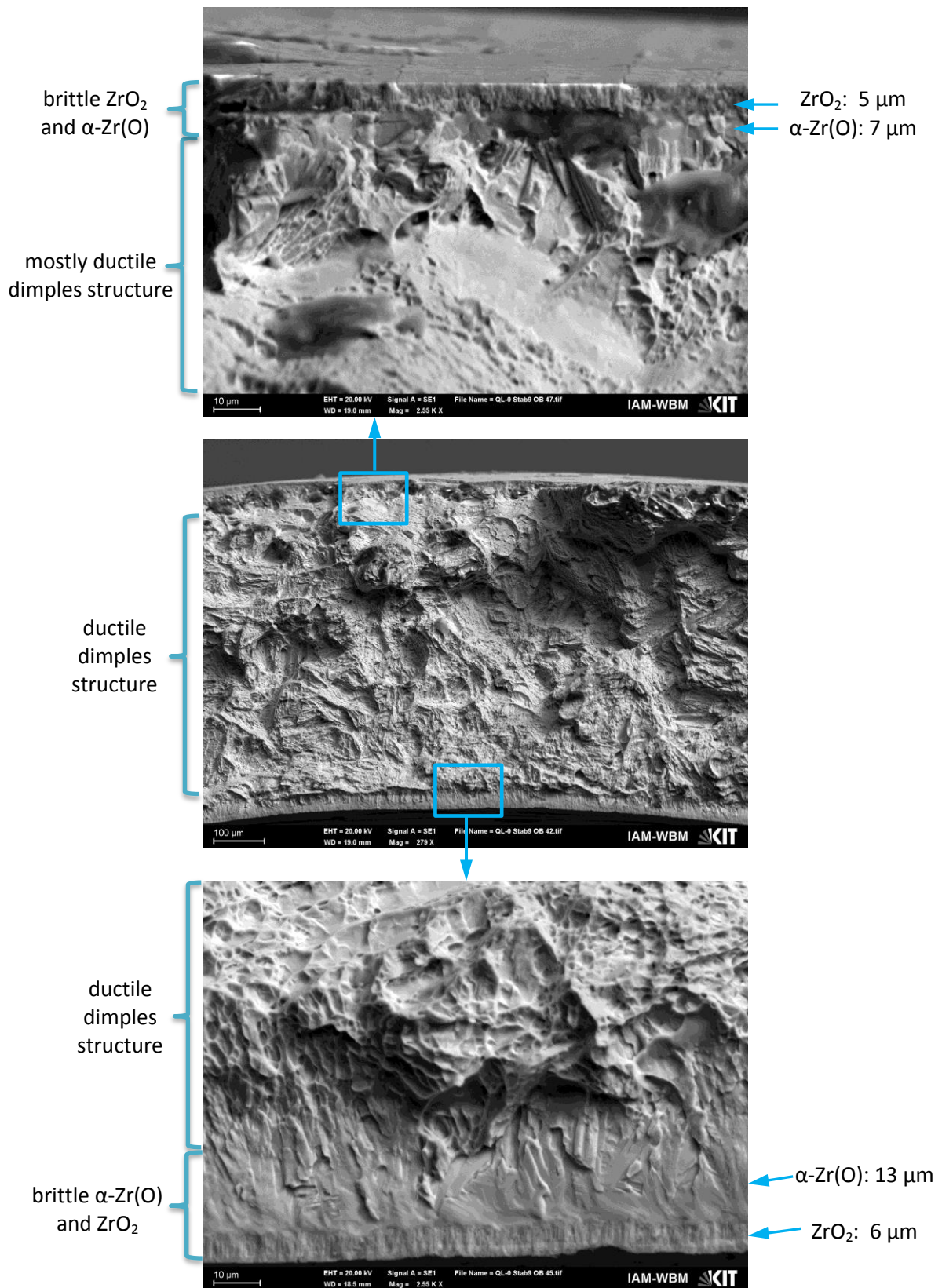


Figure 136 QUENCH-L4; SEM image of fractured surface of rod #9 at angle 200° after tensile test; top view. Ductile fracture.

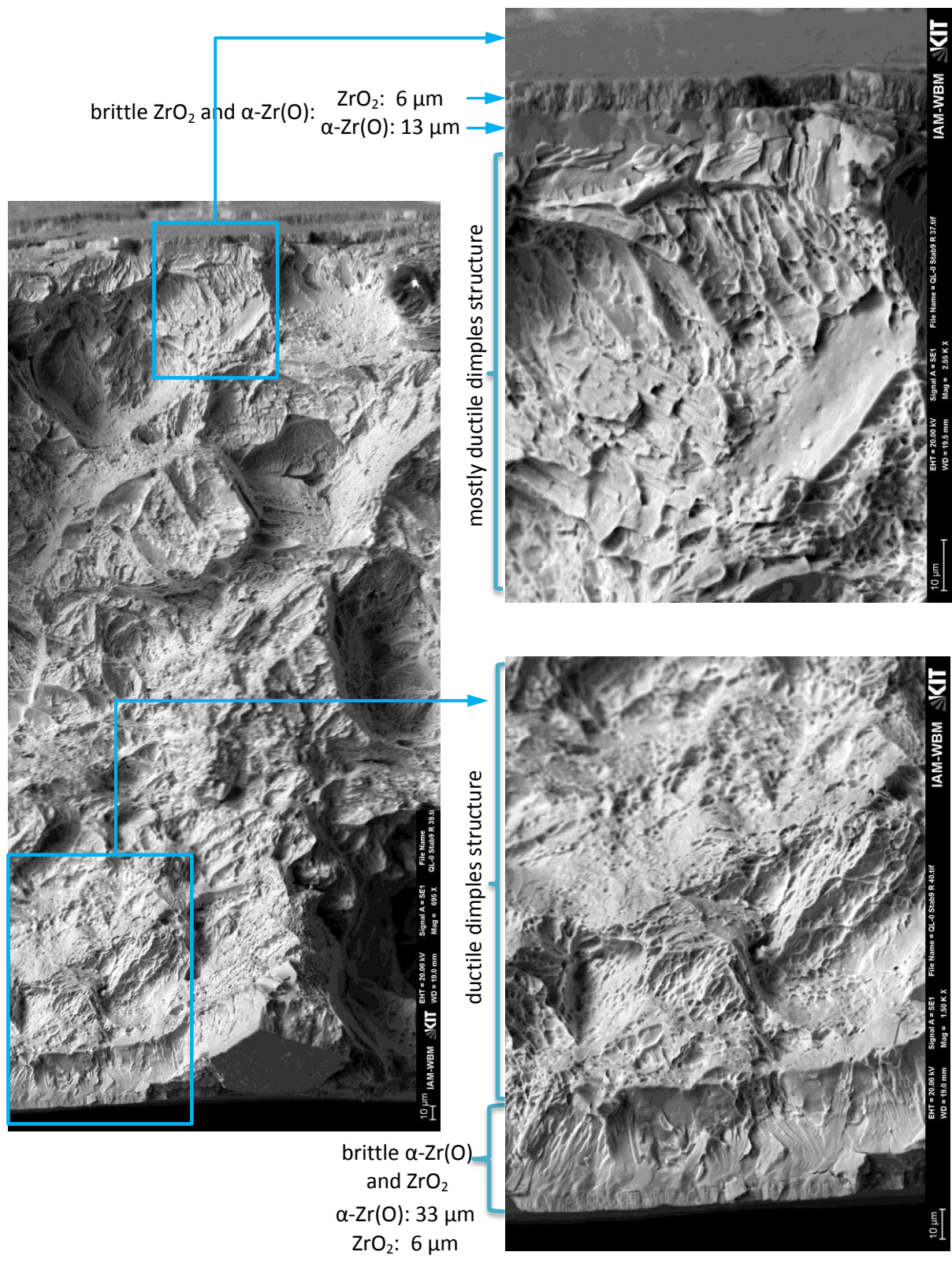


Figure 137 QUENCH-L4; SEM image of fractured surface of rod #9 at angle 290° after tensile test; top view. Ductile fracture.

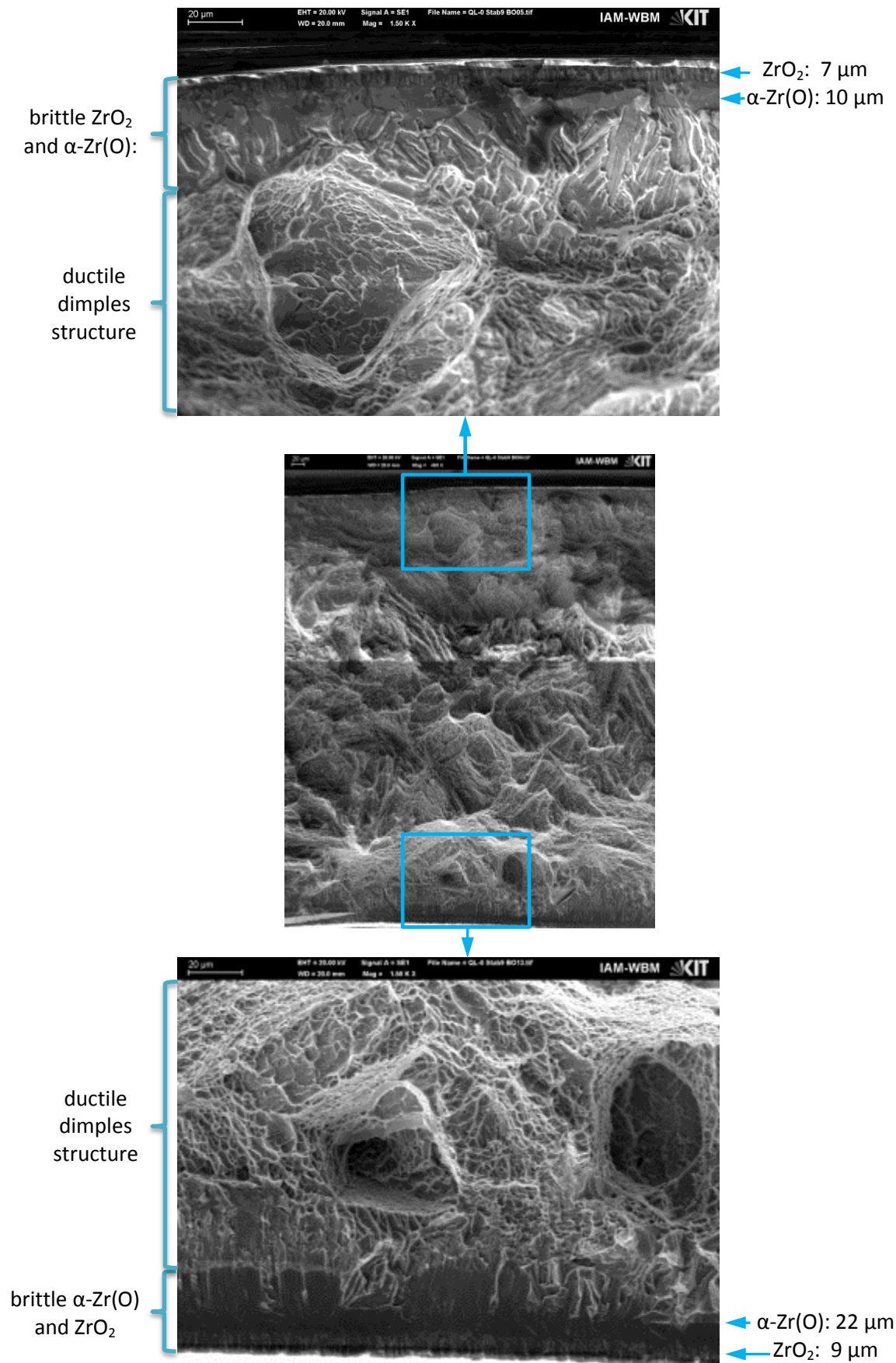


Figure 138 QUENCH-L4; SEM image of fractured surface of rod #9 at angle 20° after tensile test; top view. Ductile fracture.

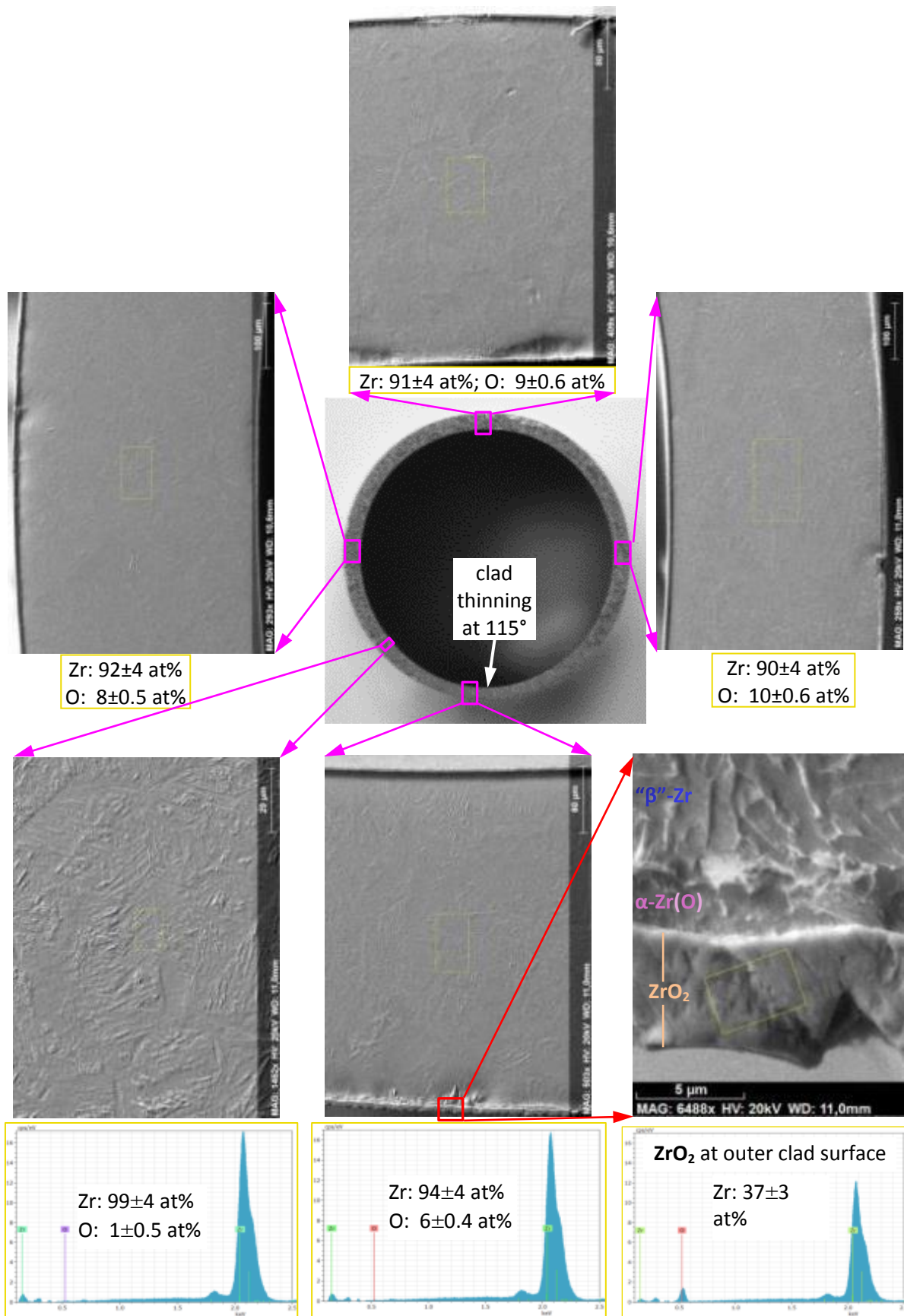
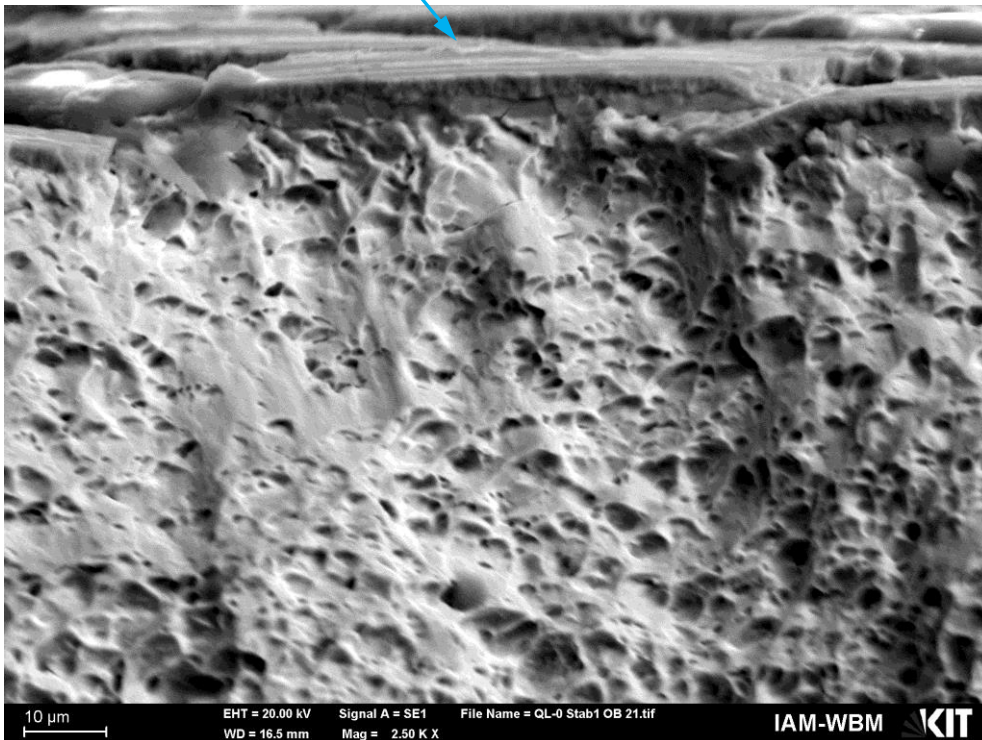


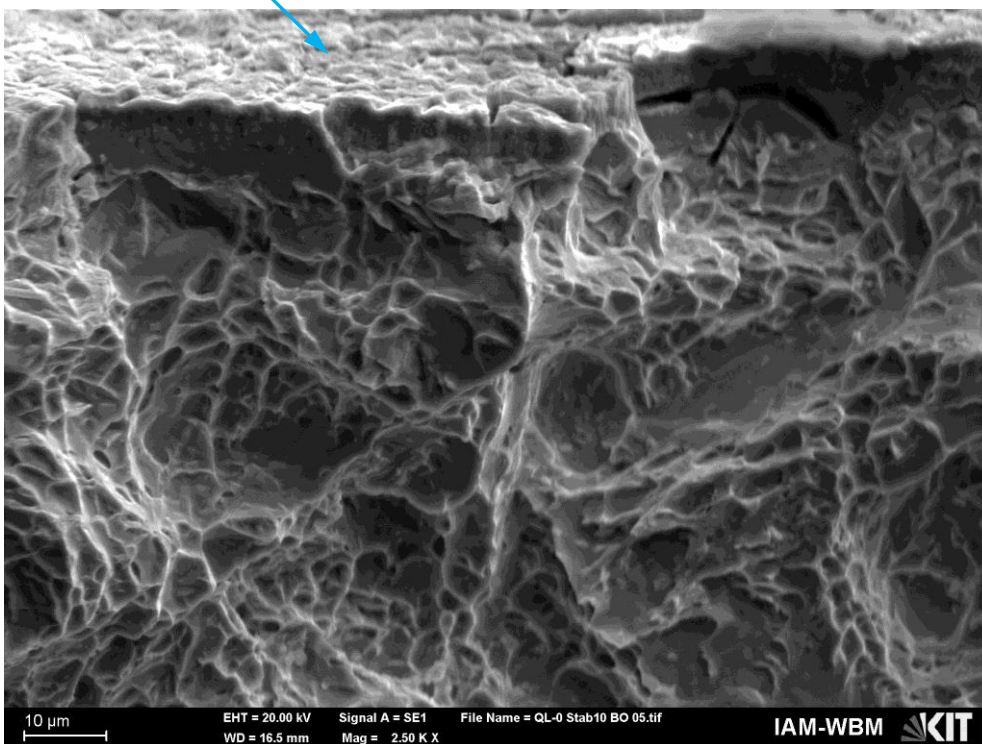
Figure 139 QUENCH-L4, Rod #9, rupture surface after tensile test (as-etched after polishing). SEM/EDX results: no oxygen in metallic part of the clad.

outer oxidised cracked surface: ZrO_2 : 5 μm , α -Zr(O): 5 μm



typical ductile dimples structure at *outer* cladding surface for all circumferential positions

inner oxidised surface: ZrO_2 : 5 μm , α -Zr(O): 5 μm



typical ductile dimples structure at *inner* cladding surface for all circumferential positions

Figure 140 QUENCH-L4; SEM images of fractured surface of rod #10 after tensile test; top view. Ductile fracture.

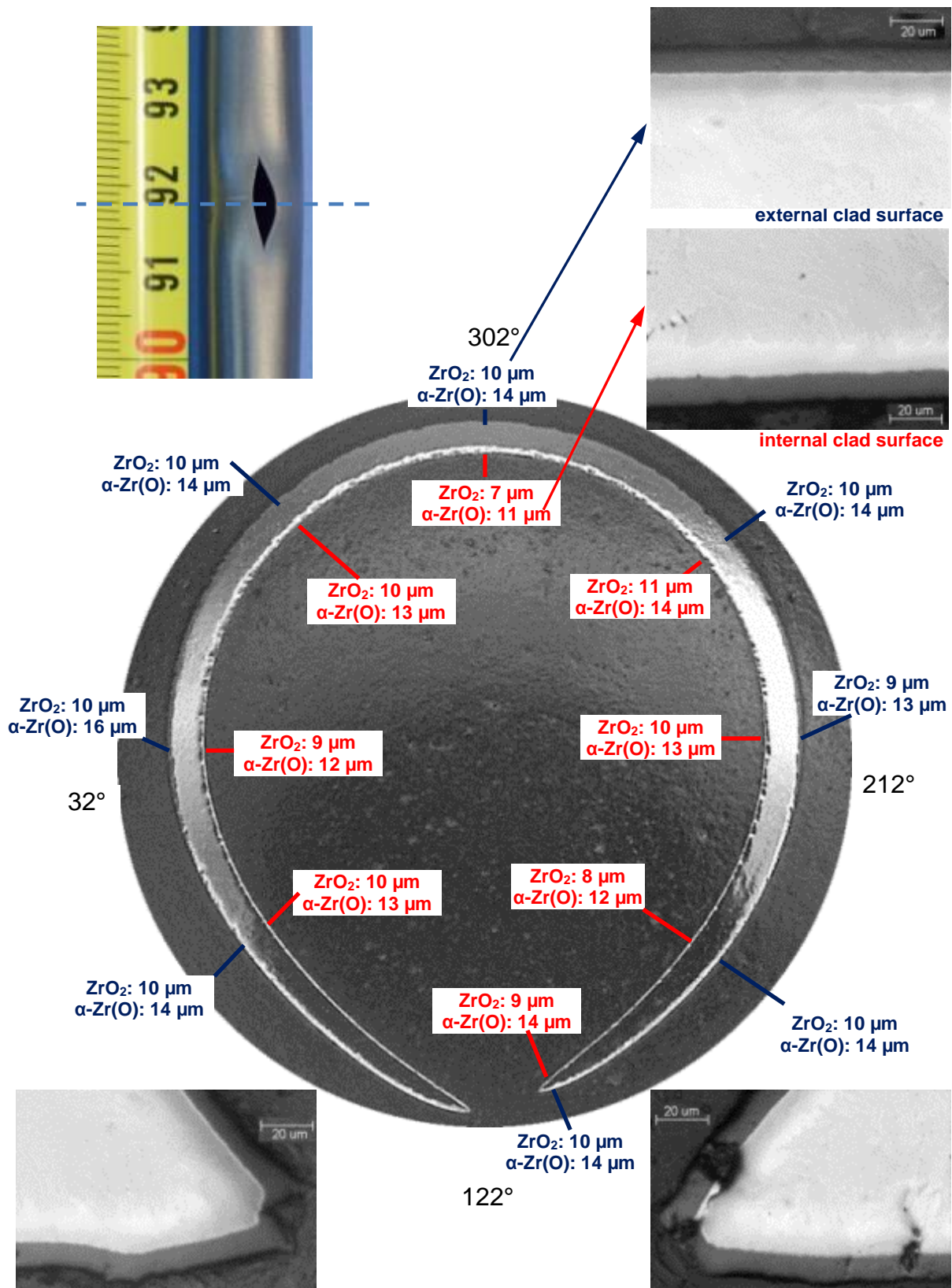


Figure 141 QUENCH-L4; Thicknesses of ZrO_2 and $\alpha-Zr(O)$ layers at outer and inner surfaces of cladding #1 at burst elevation 918 mm; top view, as polished.

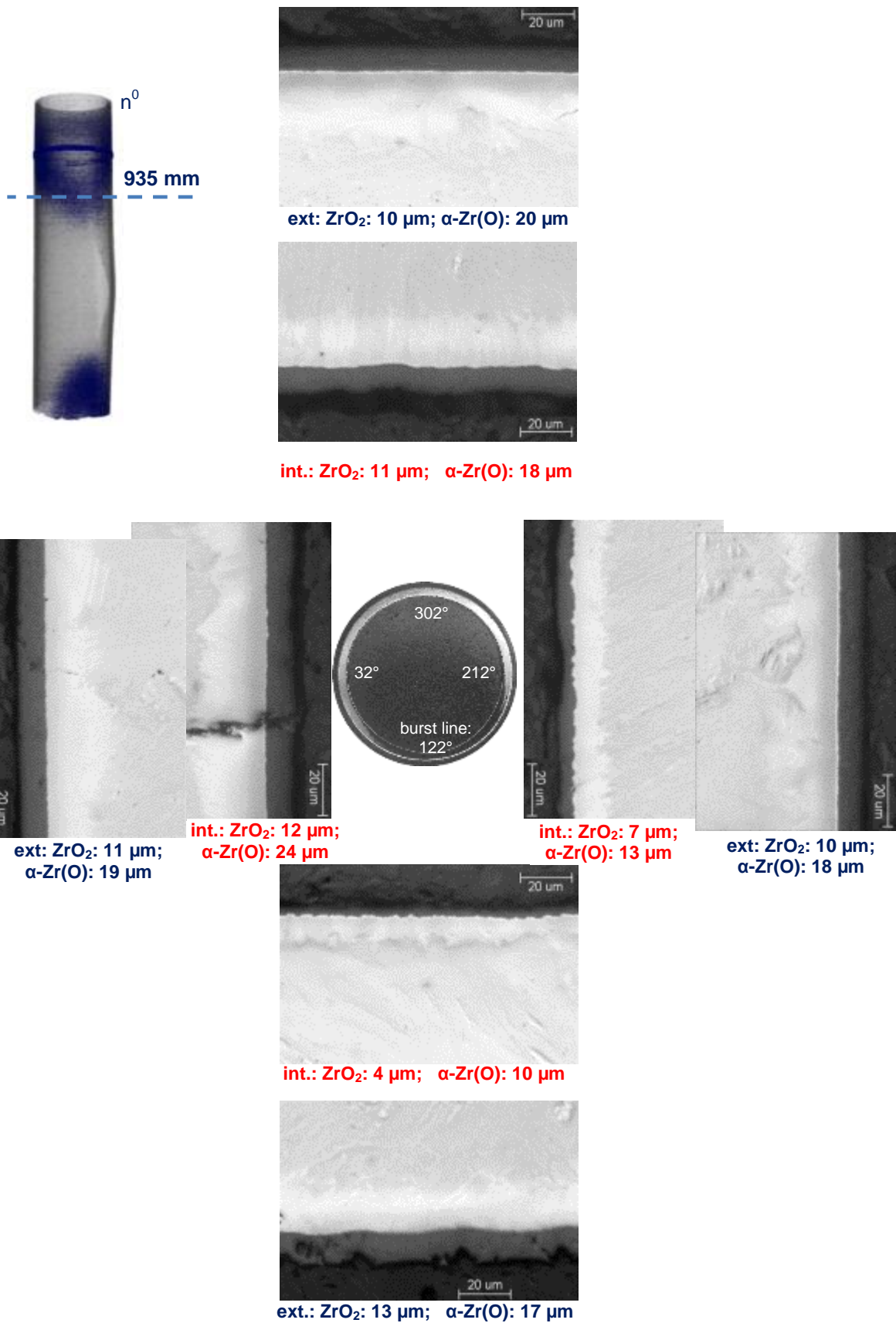


Figure 142 QUENCH-L4; Thicknesses of ZrO_2 and $\alpha-Zr(O)$ layers at outer and inner surfaces of cladding #1 above burst at bundle elevation 935 mm; top view, as polished.



Figure 143 QUENCH-L4; Thicknesses of ZrO_2 and α -Zr(O) layers at outer and inner surfaces of cladding #1 underneath burst at bundle elevation 901 mm; top view, as polished.

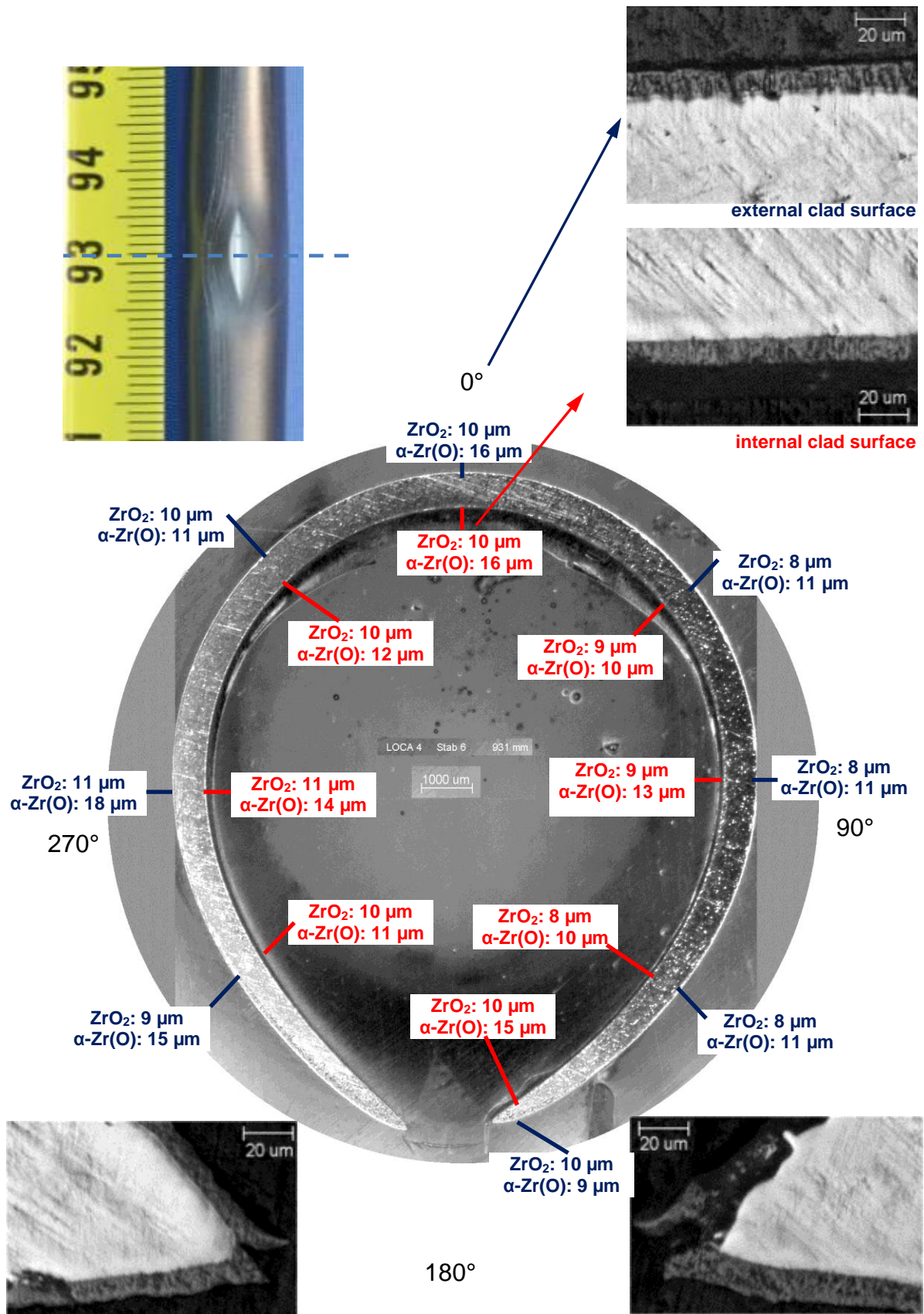


Figure 144 L4; Thicknesses of ZrO_2 and $\alpha-Zr(O)$ layers at outer and inner surfaces of cladding #6 at burst elevation 931 mm; top view, as polished.

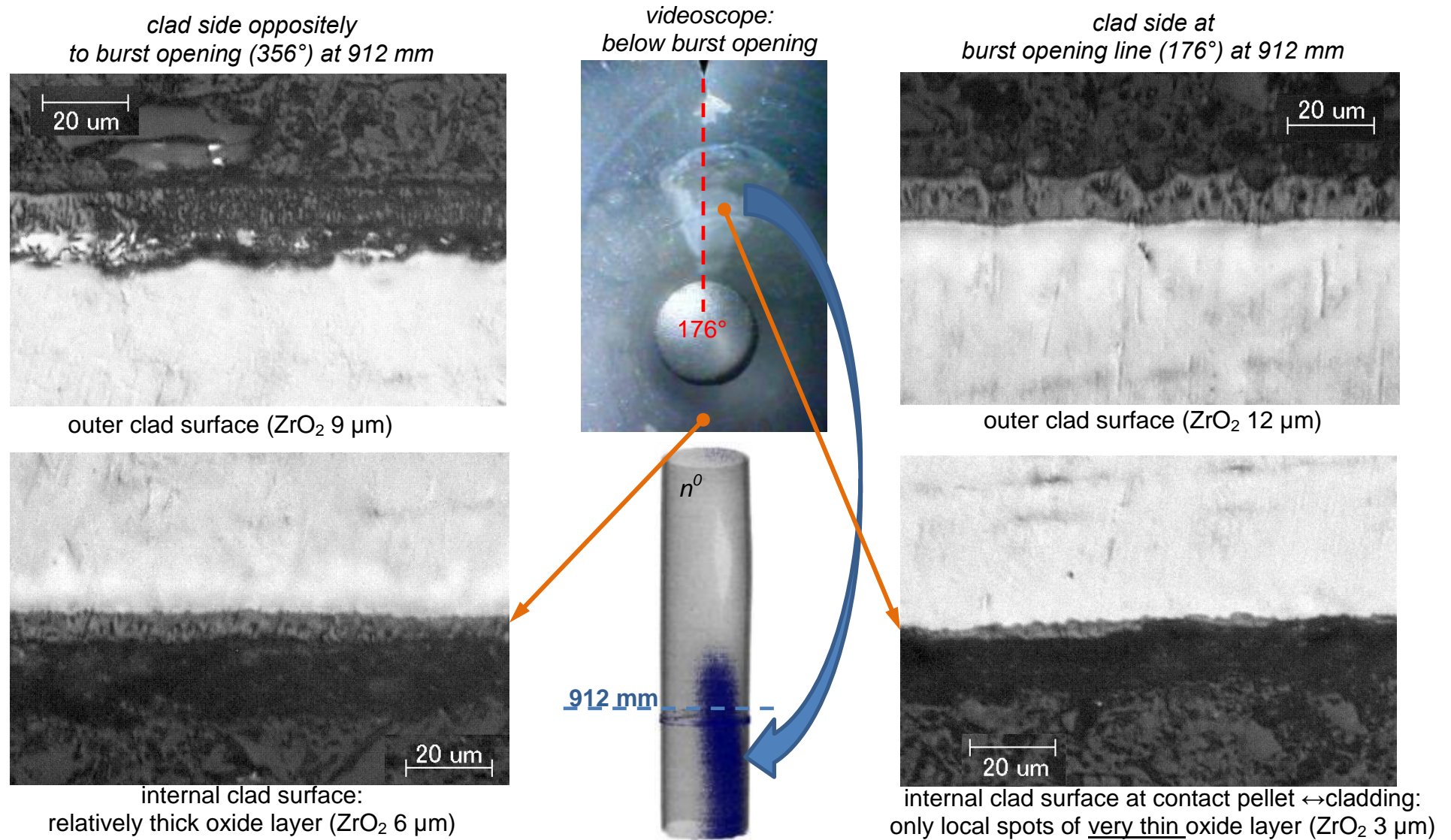


Figure 145 UENCH-L4; Correspondence between practically absence of inner oxide layer (contact clad ↔ pellet) and hydrogen spot for rod #6.

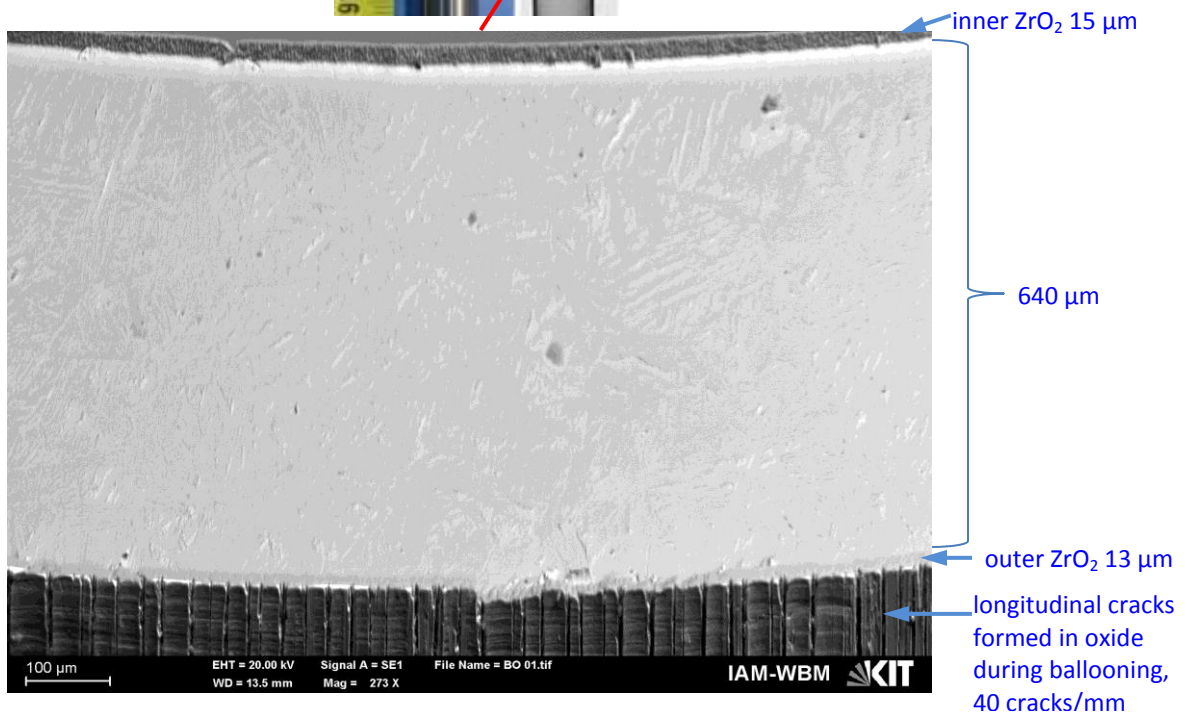
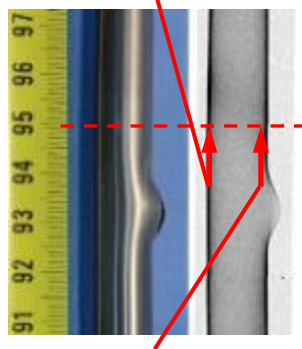


Figure 146 QUENCH-L4, Rod #8 at elevation 950 mm (12 mm above burst opening; SEM observation of cross sections (as etched) at the line of burst opening (bottom) and opposite side (top).

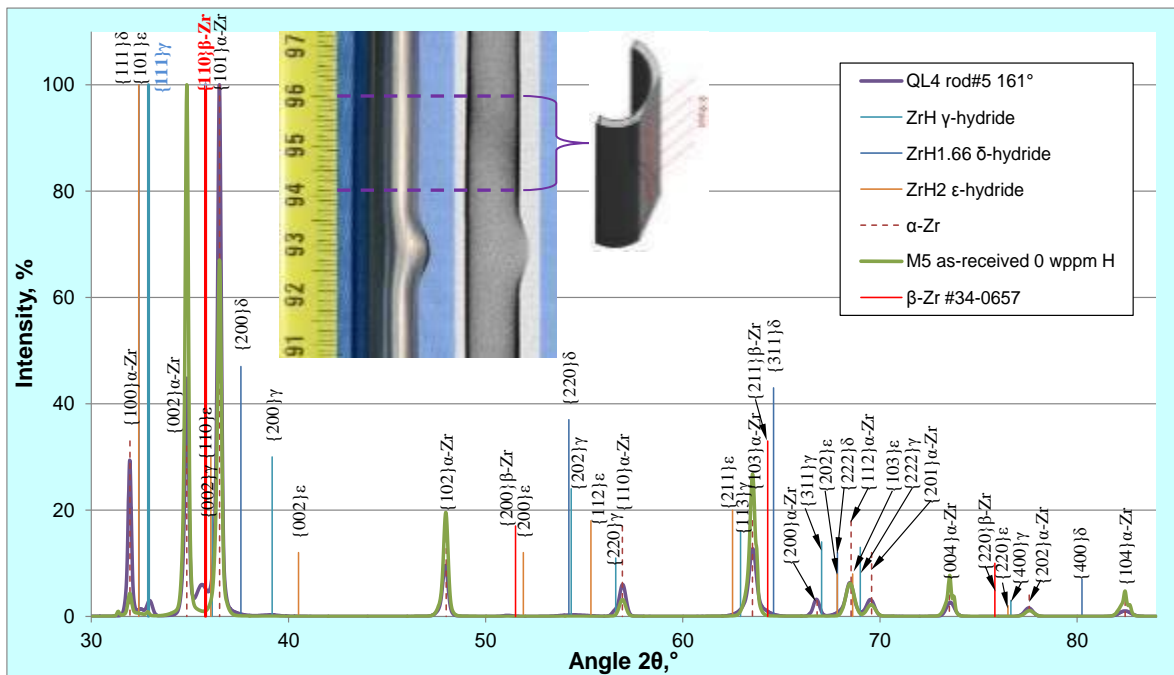


Figure 147 QUENCH-L4; XRD analysis of rod #5 at the hydrogen band on the line of the burst opening (161°); indication of {111}γ-hydrides and {110}β-Zr.

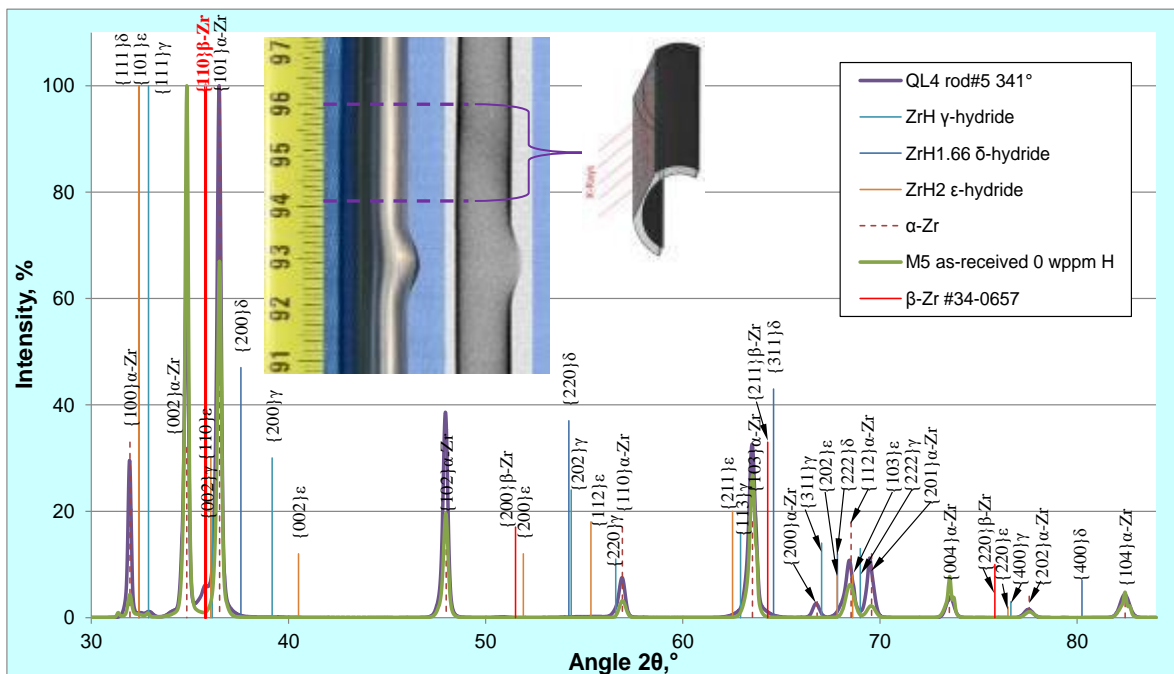


Figure 148 QUENCH-L4; XRD analysis of rod #5 at the hydrogen band on the line opposite to the burst opening (341°); indication of {110}β-Zr.

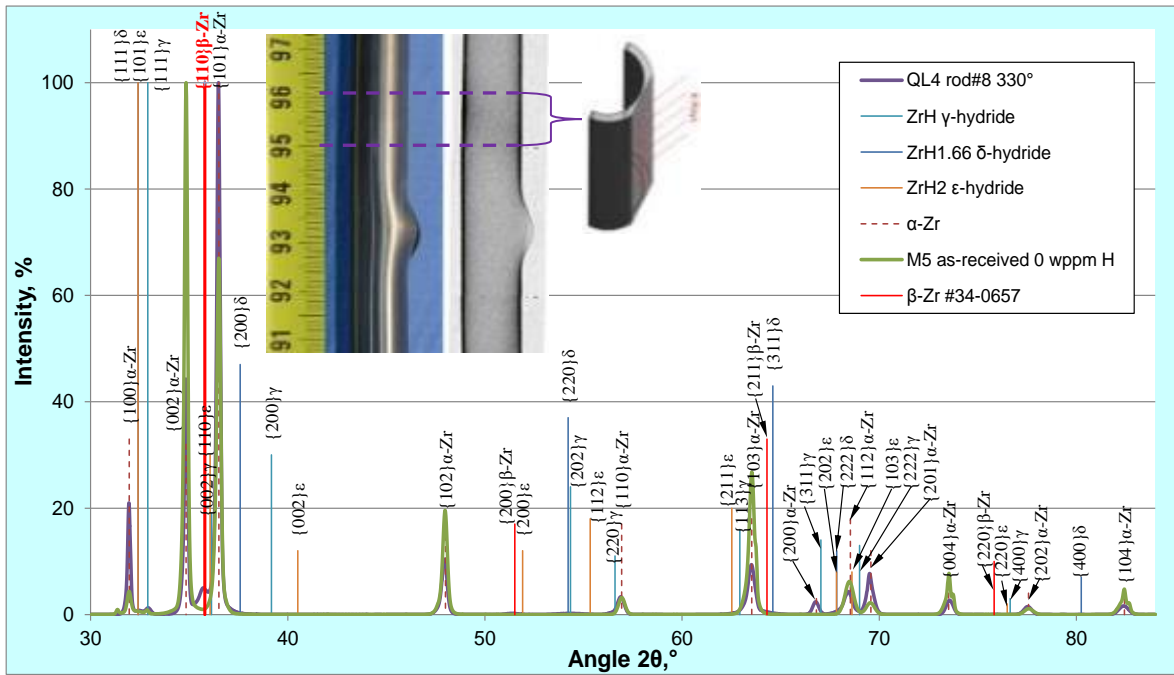


Figure 149 QUENCH-L4; XRD analysis of rod #8 at the hydrogen band on the line of burst opening (330°); indication of {110}β-Zr.

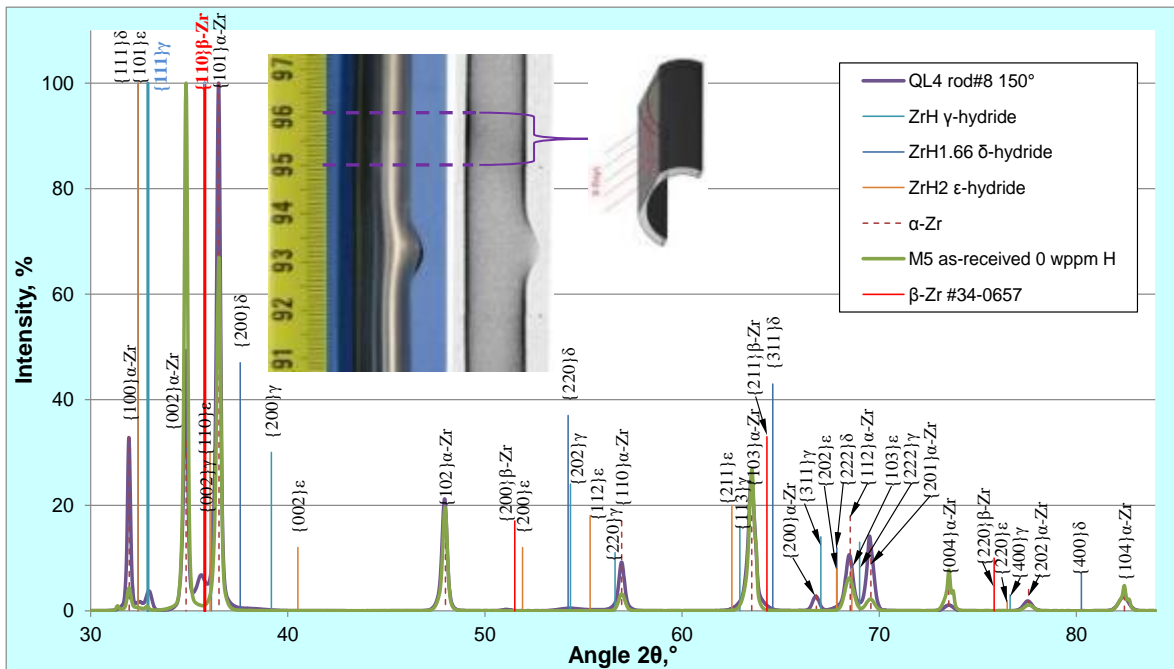


Figure 150 QUENCH-L4; XRD analysis of rod #8 at the hydrogen band on the line opposite to the burst opening (150°); indication of {111}γ-hydrides and {110}β-Zr.

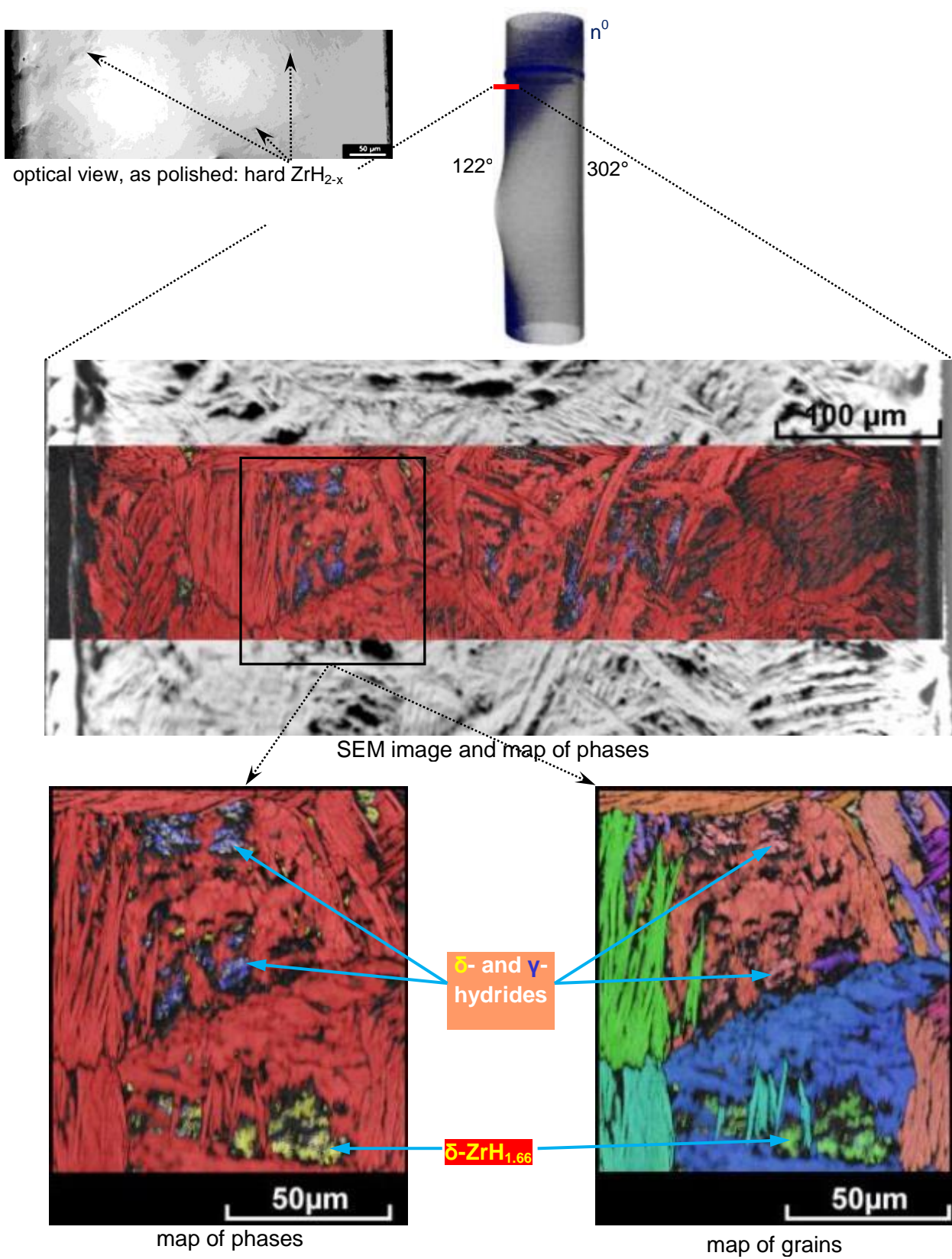


Figure 151 QUENCH-L4; EBSD analysis of δ - $ZrH_{1.66}$ and γ - ZrH hydrides (mostly intra-granular) agglomerated inside α -Zr matrix for rod #1 at elevation of 935 mm (area of hydrogen band visualized by neutron tomography) at the burst opening cladding side.

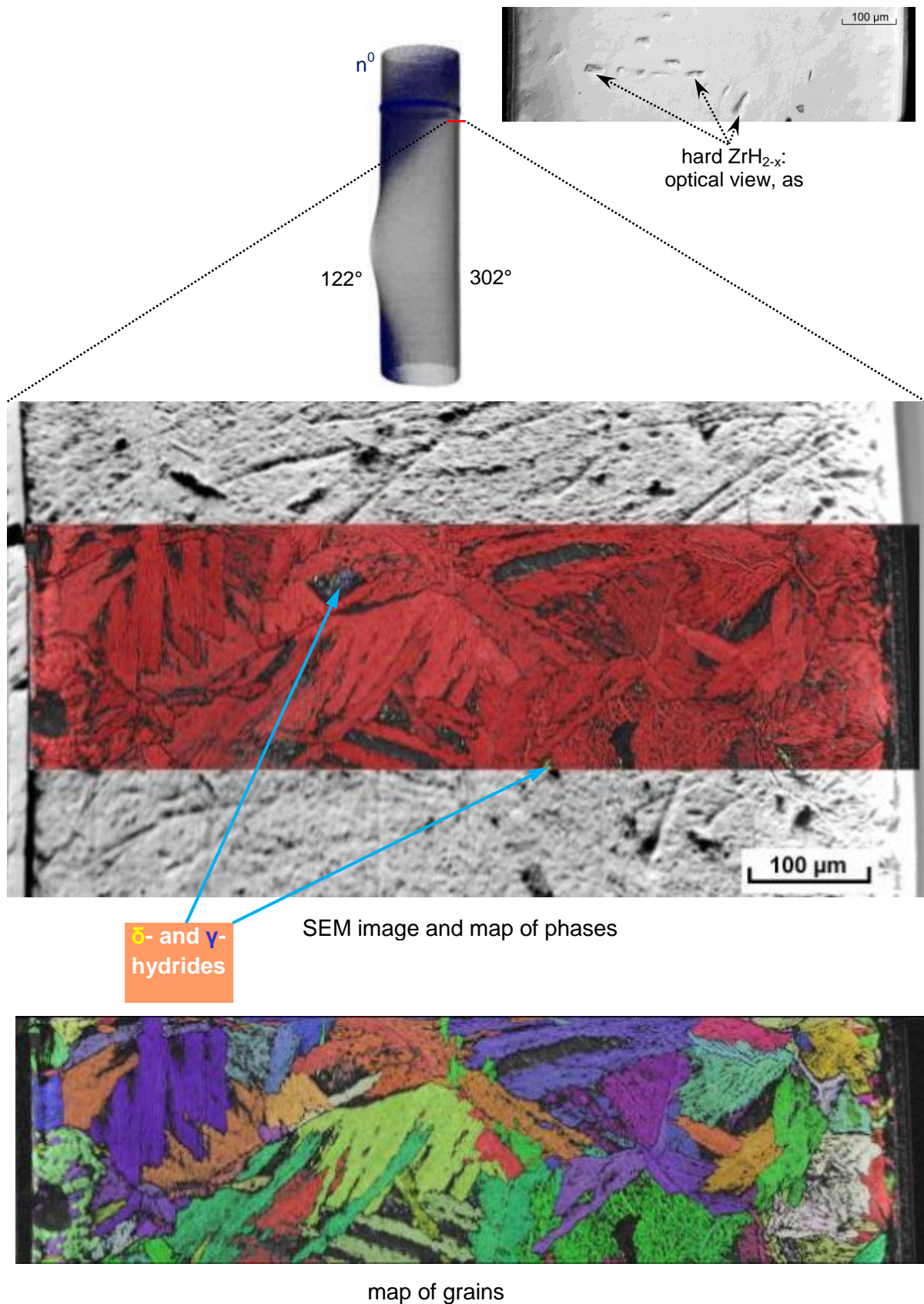


Figure 152 QUENCH-L4; EBSD analysis of δ - $ZrH_{1.66}$ and γ - ZrH hydrides (mostly intra-granular) agglomerated inside α -Zr matrix for rod #1 at elevation of 935 mm at the cladding side oppositely to the burst opening side.

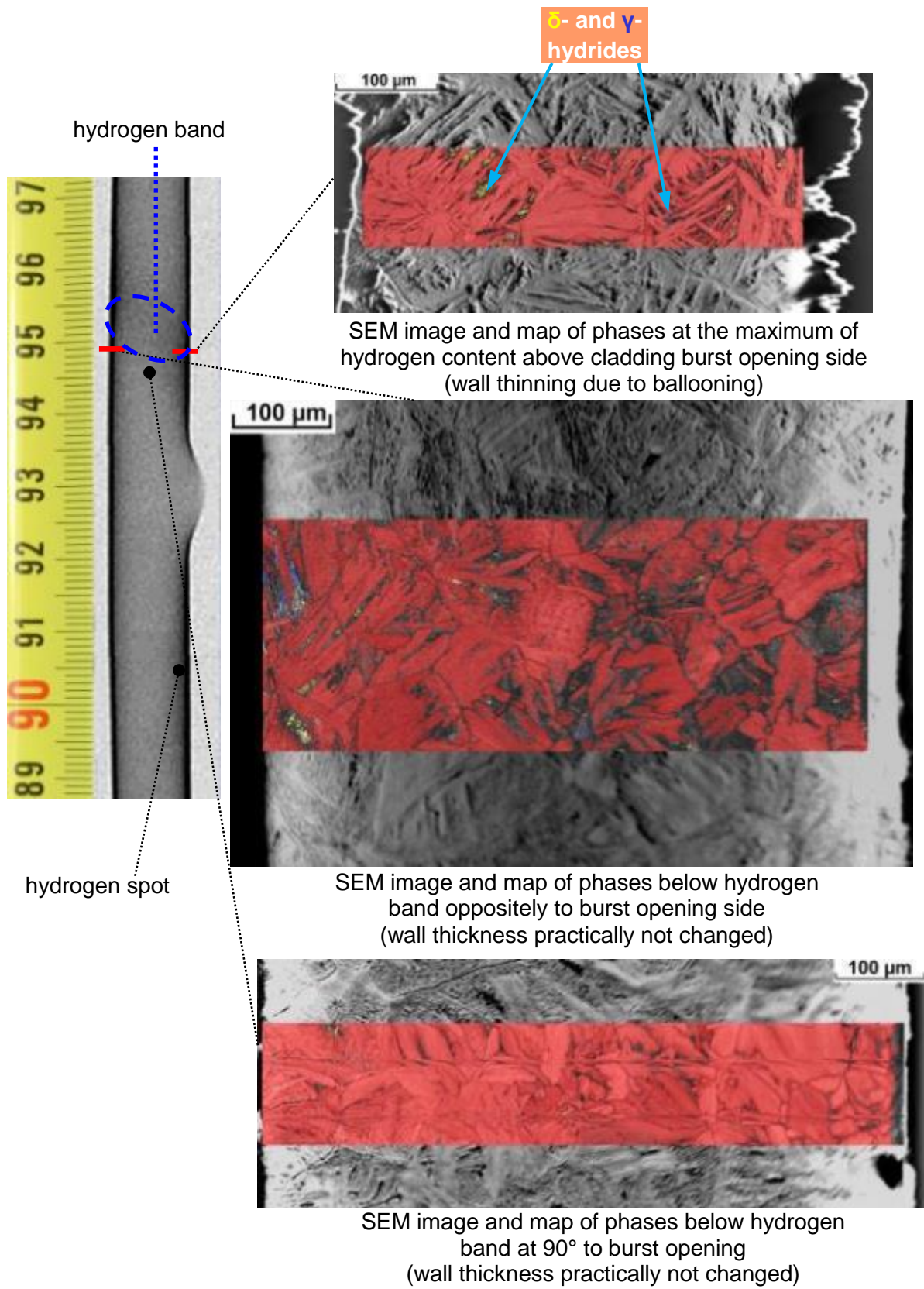
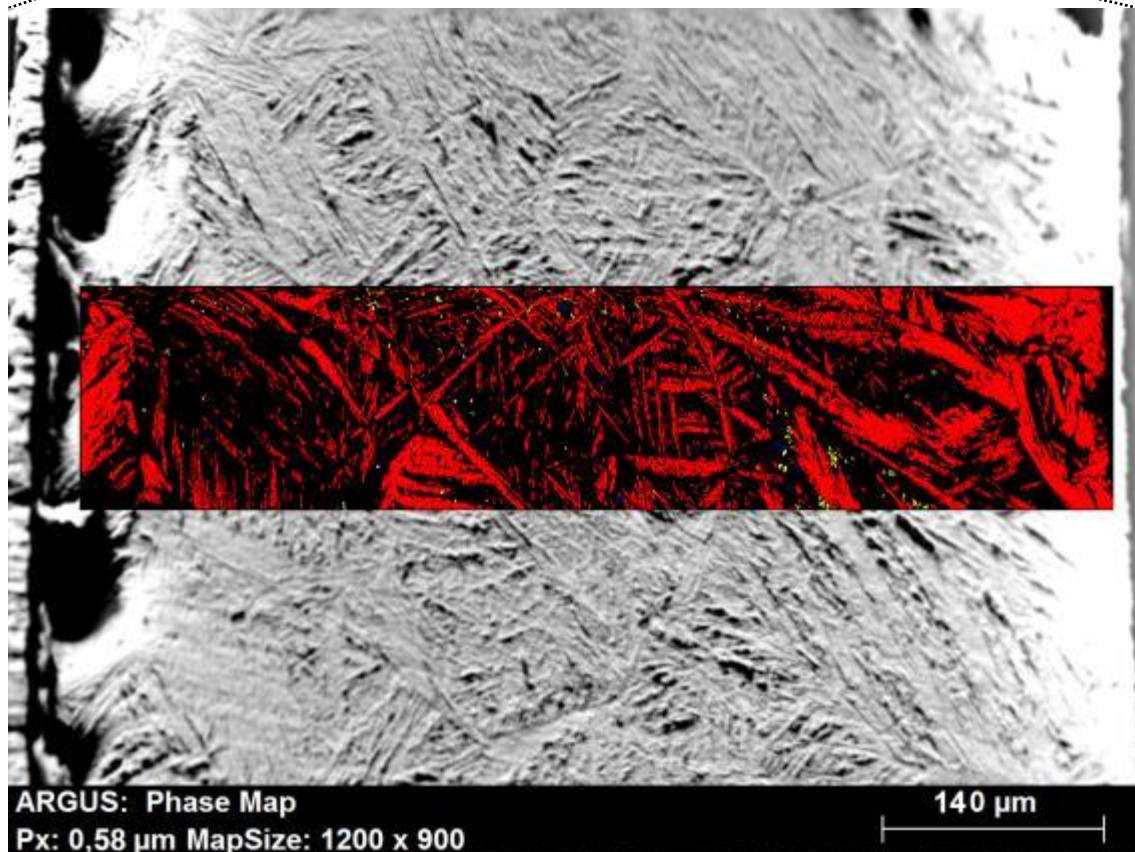
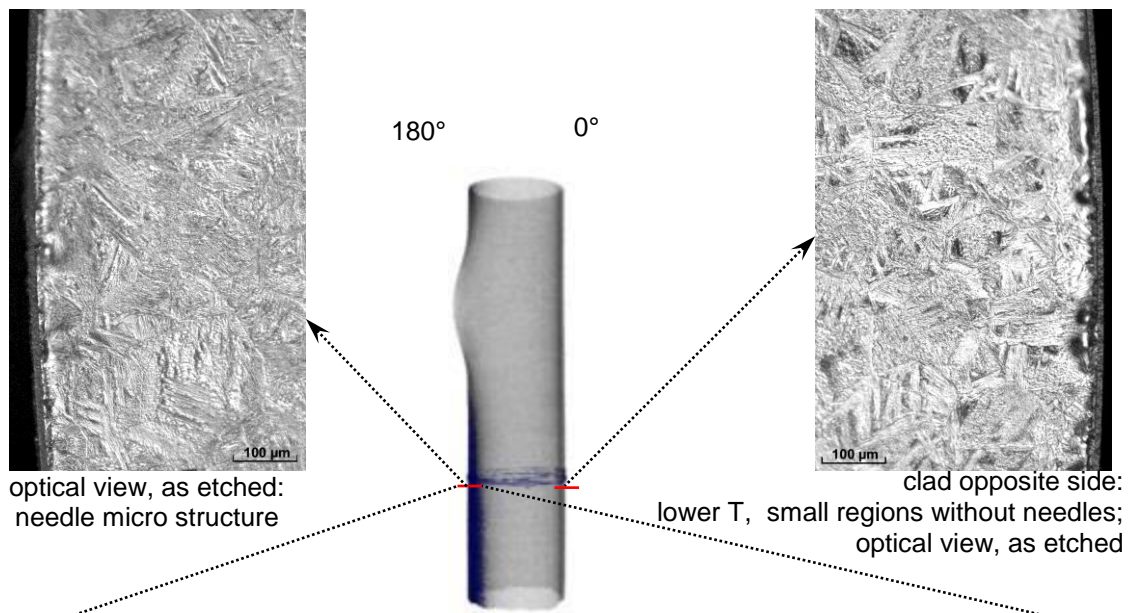


Figure 153 QUENCH-L4; EBSD analysis of δ -ZrH_{1.66} and γ -ZrH hydrides agglomerated inside α -Zr matrix for rod #5 at elevation of 950 mm.



red needles: Zr yellow points: $ZrH_{1.6}$ (δ -hydrides) blue points: ZrH (γ -hydrides)

not recognised structure: >55% of phase map

Figure 154 QUENCH-L4; EBSD analysis of cross section 911 mm of rod #6 at hydrogen spot (on the line of burst opening 20 mm below opening).

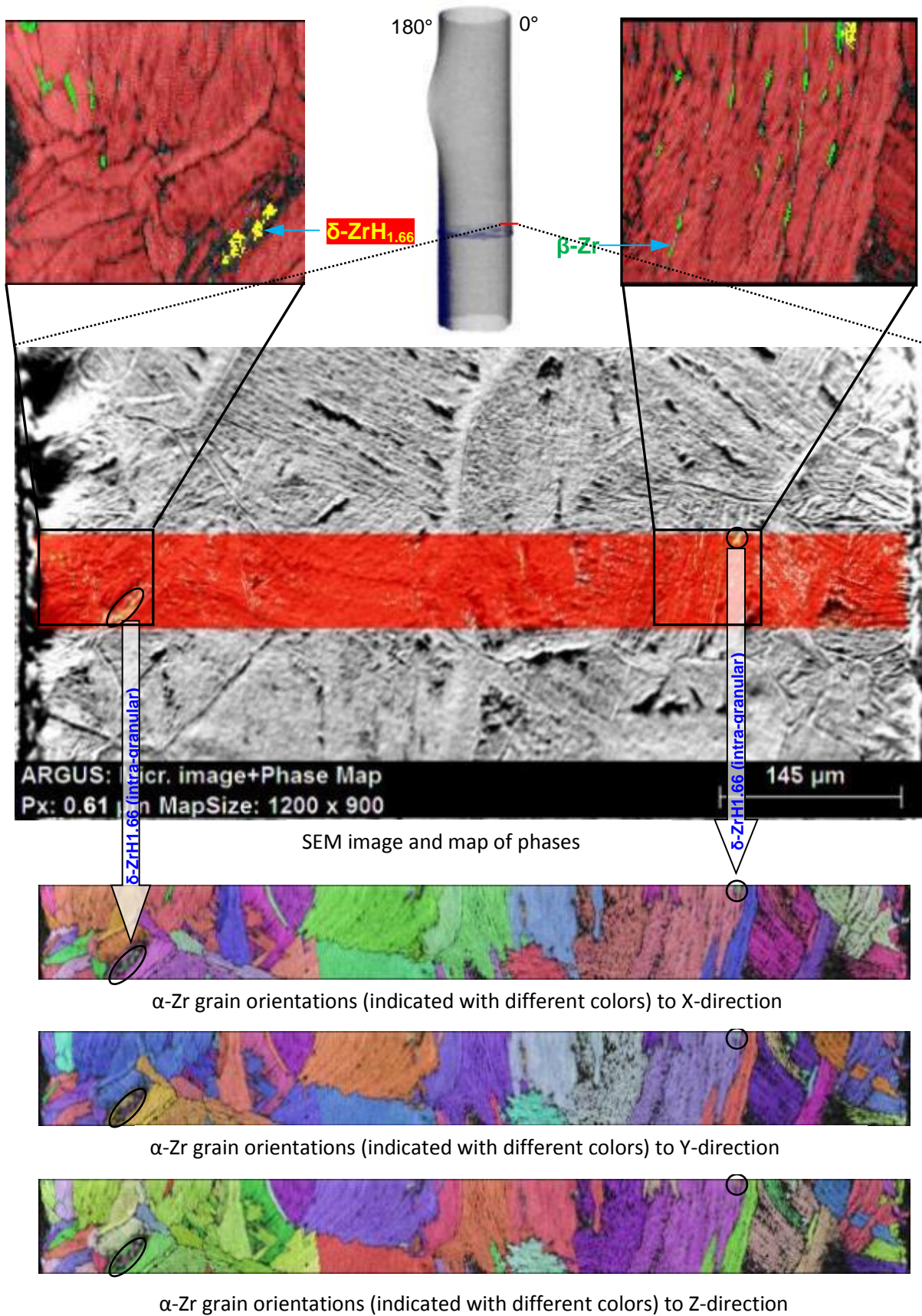


Figure 155 QUENCH-L4; EBSD analysis of $\delta\text{-ZrH}_{1.66}$ hydrides (mostly intra-granular) and $\beta\text{-Zr}$ (inter- and intra-granular) inside $\alpha\text{-Zr}$ matrix for rod #6 at elevation of 911 mm (20 mm below burst opening middle) oppositely to burst opening.

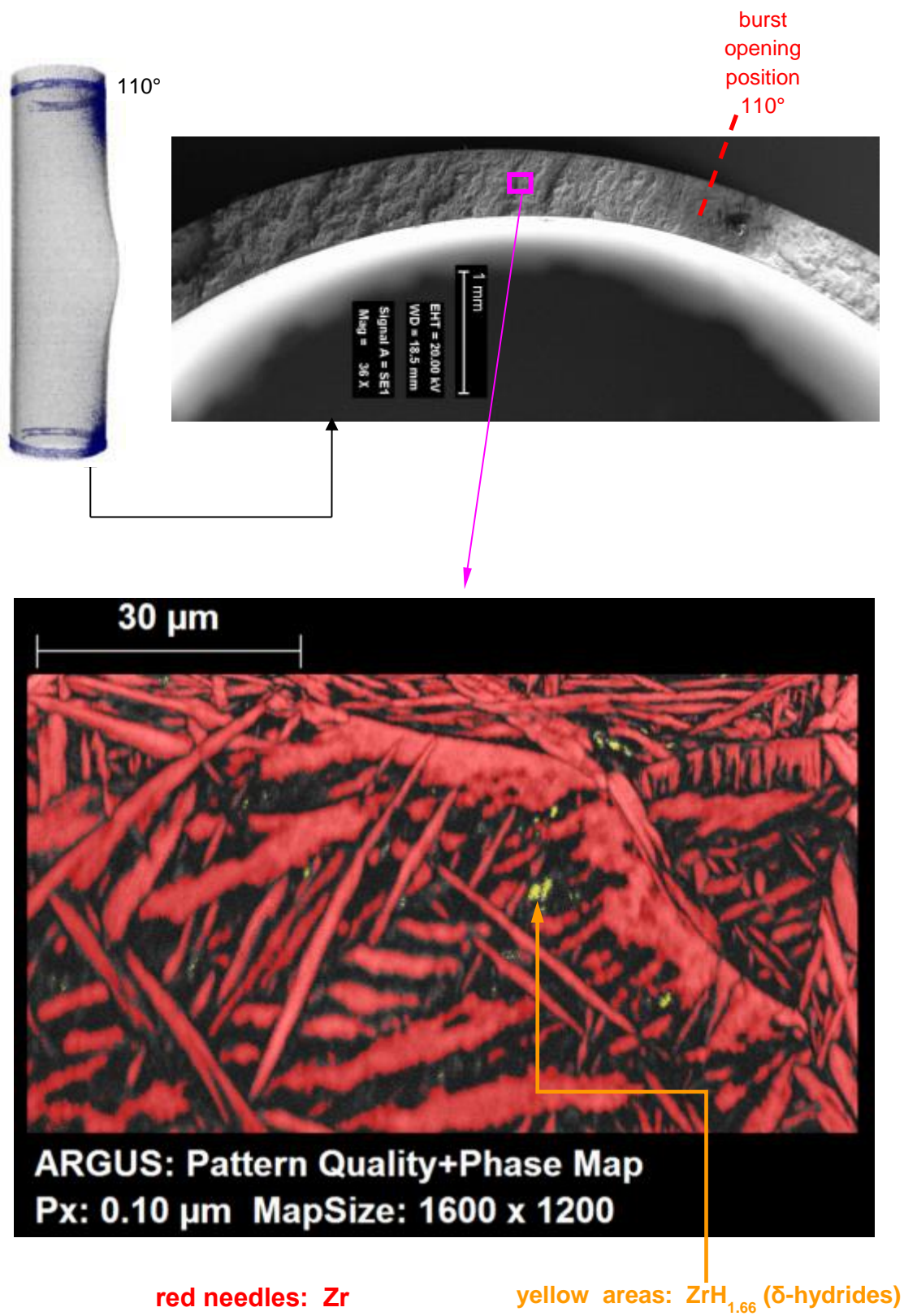



Figure 156 QUENCH-L4; EBSD analysis of fractured surface of rod #9 at hydrogen spot (on the line of burst opening 20 mm below opening; after polishing and etching).



The QUENCH-L4 experiment was performed in the framework of the QUENCH-LOCA test series. The overall objective of this bundle test series is the investigation of ballooning, burst, degree of oxidation and secondary hydrogen uptake of the cladding under representative design-basis accident conditions and their influence on the mechanical properties. For the QUENCH L4 test, M5[®] claddings pre-loaded with approximately 100 wppm hydrogen and with an outside diameter of 10.75 mm have been used. Like in all experiments of the QUENCH LOCA series, the fuel rod simulators were separately pressurized with krypton to 55 bar. The QUENCH-L4 test was performed according to a temperature/time-scenario typical for a LBLOCA in a German PWR with the same parameters as the QUENCH-L2 test with fresh not pre-hydrogenated M5[®] claddings: the maximal heat-up rate was 8 K/s; the cooling phase lasted about 120 s and was terminated by 3.3 g/s/effective rod water flooding. Similar to QUENCH-L2, a maximum temperature of about 1400 K was reached at the end of the heat-up phase at elevation 950 mm. The tangential temperature gradient across a rod was up to 30 K on the burst onset (lower than the corresponding parameter for the QUENCH L2 test). The detailed profilometry for whole length of the rods showed formation of not only main ballooning area (with burst) but also, for several rods, additional two or three ballooning regions. Cladding wall thinning from 725 μm to 450 μm due to ballooning was observed at the burst side along 50 mm below and above burst opening.). The cladding burst occurred at temperatures between 1067 and 1151 K with an average value of 1107 K (QUENCH L2: between 1050 and 1195 K, average 1138 K). The average burst opening parameters were: width 3.3 ± 0.7 mm; length 13.1 ± 1.9 mm (similar to QUENCH L2). The maximal oxide thickness at the outer cladding surface and at the inner surface around burst opening was less than 15 μm. Neutron tomography analyses showed the maximal hydrogen concentrations inside the hydrogen bands between 730 and 1520 wppm (secondary hydriding). During quenching, following the high-temperature test stages, no fragmentation of claddings was observed (residual strengths and ductility was sufficient). Tensile tests evidenced fracture at hydrogen bands: three inner rods were fractured due to this embrittlement. Maximal hydrogen concentrations measured at the fracture positions were more than 1400 wppm. Eight peripheral rods were fractured due to stress concentration at burst opening edges. All other tensile tested claddings failed after necking far away from burst region.